Report
R-19-02
January 2019

Groundwater flow and reactive transport modelling of temperate conditions

Report for the safety evaluation SE-SFL

Steven Joyce
Pete Appleyard
Lee Hartley
Vasileios Tsitsopoulos
Hannah Woollard
Niko Marsic
Magnus Sidborn
James Crawford

SVENSK KÄRNBRÄNSLEHANTERING AB

SWEDISH NUCLEAR FUEL
AND WASTE MANAGEMENT CO

Box 3091, SE-169 03 Solna
Phone +46 8 459 84 00
skb.se

SVENSK KÄRNBRÄNSLEHANTERING

ISSN 1402-3091
SKB R-19-02
ID 1566580
January 2019

Groundwater flow and reactive transport modelling of temperate conditions

Report for the safety evaluation SE-SFL

Steven Joyce, Pete Appleyard, Lee Hartley, Vasileios Tsitsopoulos, Hannah Woollard
Amec Foster Wheeler

Niko Marsic, Magnus Sidborn, James Crawford
Kemakta Konsult AB

Keywords: SFL, Repository, Safety evaluation, Groundwater, Modelling, Transport, Chemistry.

Summary

The repository for long-lived waste (SFL) will be used for disposal of Swedish long-lived low- and intermediate-level radioactive waste. Possible solutions for management and disposal of this waste were examined in the SFL concept study and a system was proposed as a basis for further assessment of post-closure safety (Elfwing et al. 2013). According to the proposed concept, SFL is designed as a deep (300–500 m depth) geological repository with two different sections:

- one waste vault for metallic waste from the nuclear power plants designed with a concrete barrier, BHK, and
- one waste vault for the waste from Studsvik Nuclear AB, Cyclife Sweden AB and AB SVAFO designed with a bentonite barrier, BHA.

The work reported here carries out groundwater flow, solute transport and geochemical calculations for a period of constant temperate climate conditions as part of the safety evaluation for SFL, SE-SFL. No site has been selected for SFL. Data from the site investigations in Laxemar in Oskarshamn municipality are chosen to obtain a detailed, realistic and coherent dataset for the evaluation. Calculations are carried out for multiple realisations of the hydrogeological properties, and cases with different geochemical reactions are compared.

The hydrogeochemical evolution of groundwater composition over the full temperate climate period is calculated in a catchment focussed equivalent continuous porous medium (ECPM) model. These calculations show that flushing by meteoric water continues to around 20 000 AD, with little change beyond that and does not penetrate much below repository depth. The groundwater composition differs little between the geochemical cases considered, although the changes are most noticeable for the lower concentration, redox -sensitive species, such as iron. Greater differences are seen between realisations, showing that groundwater composition is mostly dependent on the hydrogeological properties adopted and groundwater mixing. This is further confirmed by reference water and tracer transport studies.

The detailed flows around the vaults at selected times and particle tracking calculations are carried out in a facility focussed model with an embedded discrete fracture network (DFN) within the volume immediately surrounding the waste vaults. The waste vaults and tunnels are represented explicitly as porous medium structures with properties appropriate to the backfill materials. A more detailed, layered model of the regolith is used, with the properties of each layer calibrated against transient head measurements in the catchment focussed model. The facility focussed model explicitly represents the structural controls on flow imposed by a fracture network and so can more accurately predict transport pathways than an ECPM model and thus provide appropriate input to radionuclide transport and biosphere studies.

Performance measure calculations show little difference between the geochemical cases considered, although the differences are noticeable when using a degraded concrete backfill for the BHK vault. Greater differences in performance measures are observed between realisations, particularly where large stochastic fractures intersect the vaults. Generally, particle exit locations are consistent between geochemical cases and realisations, being governed by the catchment scale flow pattern and the locations of deformation zones. The effects of water supply wells are also considered but are found to have little effect on particle exit locations or performance measures, although there is the possibility of small amounts of contaminant entering a well, depending on its location.

Sammanfattning

Slutförvaret för långlivat avfall (SFL) kommer att användas för slutförvaring av svenskt långlivat låg- och medelaktivt radioaktivt avfall. Möjliga lösningar för hantering och slutförvaring av detta avfall av det svenska långlivade låg- och medelaktiva radioaktivt avfall utvärderades i SFL koncept-studie och ett system föreslogs för vidare utvärdering av säkerhet efter förslutning (Elfwing et al. 2013). Det föreslagna konceptet för SFL utgörs av ett djupt (300–500 m djup) geologiskt förvar med två olika bergssalar:

- En bergssal för metalliskt avfall från de svenska kärnkraftverken som utformas med en betong-barriär, BHK, och,
- En bergssal för avfall från Studsvik Nuclear AB, Cyclife Sweden AB och AB SVAFO som utformas med en bentonitbarriär, BHA.

Arbetet som presenteras här omfattar beräkningar av grundvattenflöden, transport av lösta ämnen samt geokemi, för en period med konstant tempererat klimattillstånd och utgör en del av utvärderingen av säkerhet efter förslutning för SFL, SE-SFL. Ingen plats har valts för SFL. Data från platsundersökningarna i Laxemar i Oskarshamns kommun har valts för att erhålla en detaljerad, realistisk och koherent uppsättning data för värderingen.. Beräkningar utförs för multipla realisationer av hydrogeologiska egenskaper och fall med olika geokemiska reaktioner jämförs.

Den hydrogeokemiska utvecklingen av grundvattensammansättningen under hela den tempererade klimatperioden beräknas i en avrinningsområdesfokuserad ekvivalent kontinuerligt poröst media (ECPM) modell. Dessa beräkningar visar att urspolning med meteoriskt vatten fortsätter till cirka 20 000 e.Kr., med liten förändring därefter och tränger inte ned mycket längre än förvarsdjupet. Grundvattensammansättningen skiljer sig något mellan de olika studerade geokemiska fallen, även om skillnaderna är mest märkbara vid lägre koncentrationer av redoxkänsliga specier, såsom järn. Större skillnader ses mellan olika realiseringar, vilket visar att grundvattensammansättningen är mest beroende av de antagna hydrogeologiska egenskaperna samt av blandningen av grundvatten. Detta bekräftas vidare av referensvattenanalys och partikelspårningsberäkningar.

De detaljerade grundvattenflödena beräknas runt bergssalarna vid utvalda tidpunkter och partikel-spårningsberäkningar utförs i en anläggningsfokuserad modell med ett inbäddat diskret spricknätverk (DFN) inom volymen som omger bergssalarna. Bergssalar och tunnlar är explicit representerade som porös media-strukturer med relevanta egenskaper för fyllnadsmaterialen. En mer detaljerad, flerlagersmodell av regoliten används, där egenskaperna hos varje lager kalibreras mot transienta tryckmätningar i den avrinningsområdesfokuserade modellen. Den anläggningsfokuserade modellen representerar genom DFN-modellen explicit de strukturer som kontrollerar flödet och kan därför mer exakt bestämma transportvägar jämfört med en ECPM-modell och därmed leverera lämpliga indata till radionuklidtransportberäkningar och biosfärsanalys.

Beräkningar av hydrogeologiska prestandamått visar liten skillnad mellan de studerade geokemiska fallen, även om skillnaderna är märkbara när man använder en degraderad betongfyllning i BHK. Större skillnader i hydrogeologiska prestandamått observeras mellan realiseringar, särskilt där stora stokastiska sprickor skär genom bergssalarna. Partikelutsläppsområdena är generellt sett konsistenta mellan de olika geokemiska fallen och realisationerna, då de styrs av flödesmönster och deformationszonernas placering på avrinningsområdesskala. Effekten av brunnar anses också ha liten effekt på partikelutströmningsområden eller hydrogeologiska prestandamått, även om det finns möjlighet att små mängder föroreningar kommer in i en brunn beroende på läge.

Contents

1 Introduction

1.1 Background

The repository for long-lived waste (SFL) will be used for disposal of Swedish long-lived low- and intermediate-level radioactive waste. Possible solutions for management and disposal of this waste were examined in the SFL concept study and a system was proposed as a basis for further assessment of post-closure safety (Elfwing et al. 2013). According to the proposed concept, SFL is designed as a deep (300–500 m depth) geological repository with two different sections:

- one waste vault for metallic waste from the nuclear power plants designed with a concrete barrier, BHK, and
- one waste vault for the waste from Studsvik Nuclear AB, Cyclife Sweden AB and AB SVAFO designed with a bentonite barrier, BHA.

The current stage is a safety evaluation, SE-SFL, to evaluate the long-term safety of the proposed solutions. The output from SE-SFL will inform the choice of solution to adopt for further development and planning of SFL. This document supports that evaluation.

1.2 Scope

The work reported here concerns groundwater flow and solute transport modelling under post-closure conditions during the temperate climate period as part of the safety evaluation for SFL, SE-SFL. Although no site has been chosen for SFL, information from the Laxemar site is used as an illustration, as described in the comparative safety analysis carried out during SR-Site (SKB 2010a). Specifically, the fractured rock is modelled according to the Elaborated Hydro-DFN, which was an improvement to the DFN methodology that included a borehole-specific calibration and individual calibration for each fracture set (Joyce et al. 2010).

The long-term catchment scale evolution of the site hydrogeochemistry is modelled using an equivalent continuous porous medium (ECPM) model. This model calculates the transient changes in groundwater composition due to transport processes and chemical reactions. The calculations take into account the changes in sea level and salinity over the simulation period 8000 BC to 60 000 AD. The work is based on the regional-scale (now referred to as catchment focussed) modelling methodology described in Joyce et al. (2010) and the geochemical calculations described in Gimeno et al. (2010). However, an approach is adopted which integrates the calculations of flow, solute transport and hydrogeochemistry (Joyce et al. 2014). The calculated groundwater composition also provides input to near-field modelling studies and to the solubility and sorption properties used for radionuclide transport calculations. These cases are considered:

Case 1. No chemical reactions, i.e. the groundwater composition is determined only by groundwater flow and transport/mixing processes.

Case 2. Equilibration of groundwater with calcite, quartz and amorphous iron (II) sulphide. This is the case from Gimeno et al. (2010) for a situation with significant activity of sulphate-reducing bacteria. However, the hydroxyapatite reactions are not included as they are not deemed relevant to this work (consistent with the approach in Joyce et al. 2015).

Case 3. Equilibration of groundwater with calcite, quartz and haematite. This is the case from Gimeno et al. (2010) for a situation where the redox state is not affected by sulphate-reducing bacteria. Again, the hydroxyapatite reactions are not included.

The detailed flows around the facility structures are modelled using a combined discrete fracture network (DFN) and ECPM facility focussed model using a methodology similar to that described in Joyce et al. (2010). This model uses a more detailed layered model of the regolith, with the properties of each layer calibrated against transient head measurements. The facility focussed model is used to calculate performance measures and particle pathways for use in radionuclide transport calculations and biosphere modelling.

The main objectives of the work were to:

1. Calculate the evolution of groundwater composition in the catchment focussed model for the duration of a 68 000 year temperate period, taking into account changes in land elevation and seawater salinity. The outputs are groundwater composition, pressure and density at specific time-slices for use in near-field modelling and facility focussed modelling.
2. Calculate pathways for particles released at fractures intersecting the vaults in the facility focussed model at selected time slices. The outputs are distributions of performance measures as inputs to a safety assessment, particle pathways for use in radionuclide transport calculations and particle exit locations for use in biosphere modelling.
3. Consider the effects of stochastic variability by considering multiple realisations of the DFN.
4. Consider the effects of water supply wells on particle pathways.

1.3 Report structure

The report structure is as follows:

- Chapter 1 provides background information to set the work into context.
- Chapter 2 describes the concepts and methodology used for this study. This includes modelling representations of the bedrock, soil and fractures. The methodology used for carrying out the required calculations is also covered.
- Chapter 3 describes the numerical modelling. This chapter describes the models used to perform the simulations required to calculate the quantities of interest. The calculations of the evolution of groundwater composition were performed in a catchment focussed model. Particle tracking calculations to calculate performance measures and exit locations were carried out using a facility focussed model.
- Chapter 4 presents the results. The results are illustrated by plots showing the evolution of groundwater composition calculated by the catchment focussed model. These are followed by the results of particle tracking calculations in terms of exit locations and cumulative distribution plots of performance measures. Results for different cases, times and realisations are shown.
- Chapter 5 summarises the findings and presents the conclusions.

2 Concepts and methodology

2.1 Conceptual model

In the work described here for SFL, information from the Laxemar site description was used as an example for the purposes of illustration. The model is based on that developed during SDM-Site Laxemar (SKB 2009a) and updated in Joyce et al. (2010).

2.1.1 Hydrogeology

The Laxemar-Simpevarp area is located on the Swedish east coast near Oskarshamn and around 350 km south of Stockholm (Figure 2-1). The bedrock consists of crystalline rock that has been subject to brittle deformation. The bedrock is overlaid by a thin till in the elevated areas and glaciofluvial sediments in the larger valleys. The topography is fairly flat.

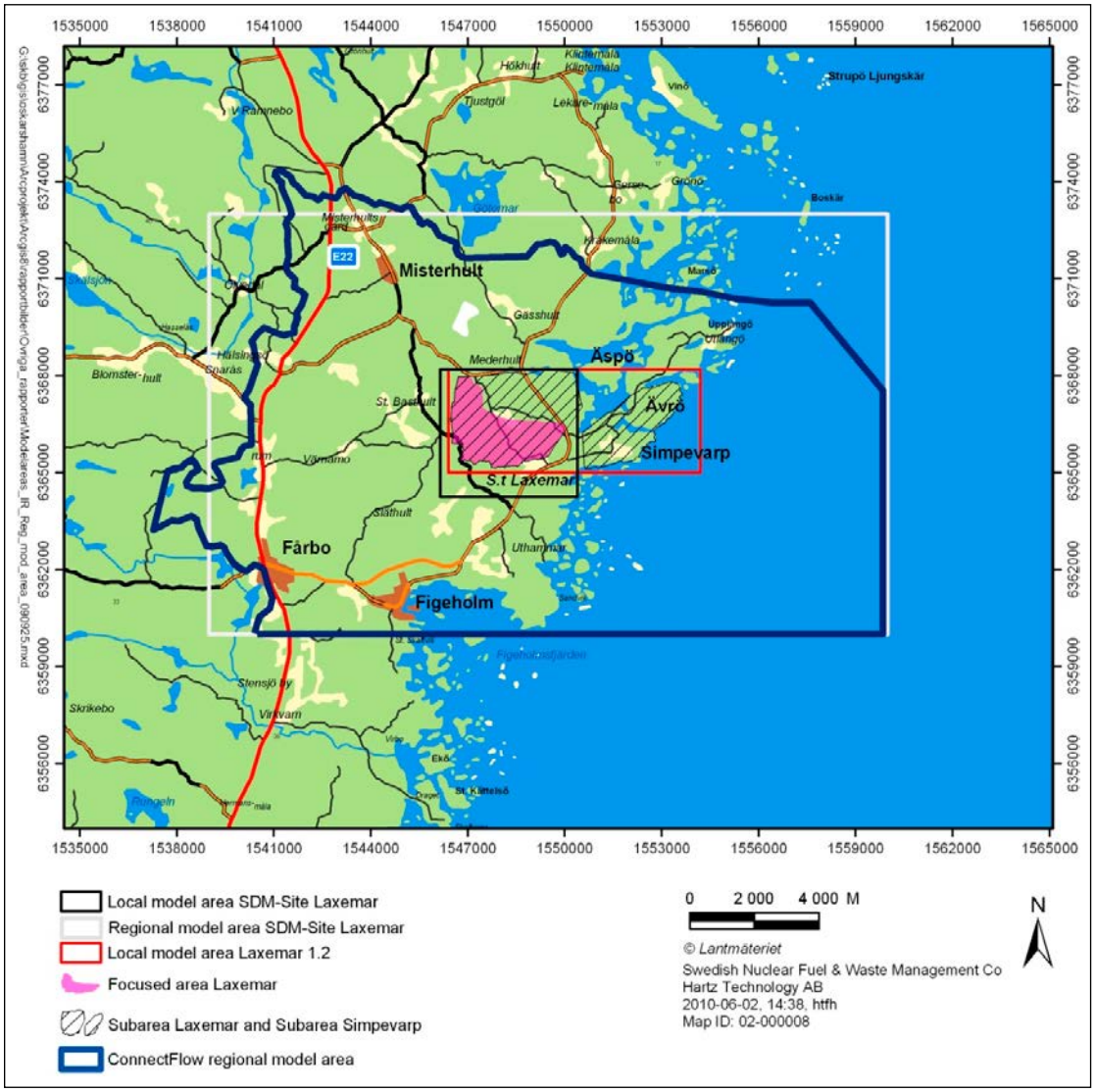

Figure 2-1. *Regional and local model areas used for SDM-Site Laxemar, now referred to as the local and facility focussed model areas, respectively (Figure 1-6 in Rhén and Hartley 2009). The choice of boundaries used for the SDM-Site regional groundwater flow simulations (using ConnectFlow) based on surface-water catchments is also shown and is now referred to as the catchment focussed model area.*

The hydrogeological conceptual model for Laxemar divides the groundwater system into three hydraulic domain types:

- HCD (Hydraulic Conductor Domain) representing deformation zones,
- HRD (Hydraulic Rock mass Domain) representing the fractured bedrock between the deformation zones,
- HSD (Hydraulic Soil Domain) representing the regolith (Quaternary deposits).

These domain types are illustrated in Figure 2-2.

The deformation zones and Quaternary deposits are generally more hydraulically conductive than the bedrock. The hydraulic conductivity tends to decrease with depth in both the deformation zones and the bedrock. The bedrock has been divided into four depth zones according to the frequency of occurrence of conductive fractures. The conceptual model is illustrated in Figure 2-3.

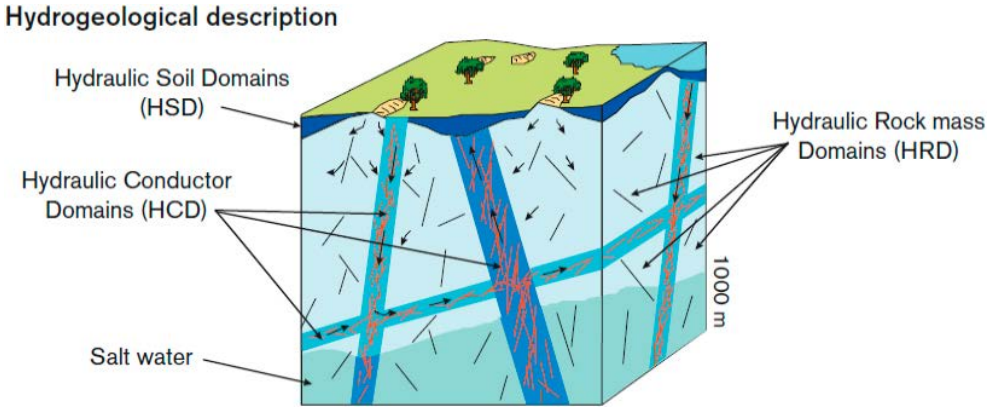

Figure 2-2. *Schematic diagram showing the division of the crystalline bedrock and the regolith (Quaternary deposits) into three hydraulic domains, HCD, HRD and HSD (Rhén et al. 2003).*

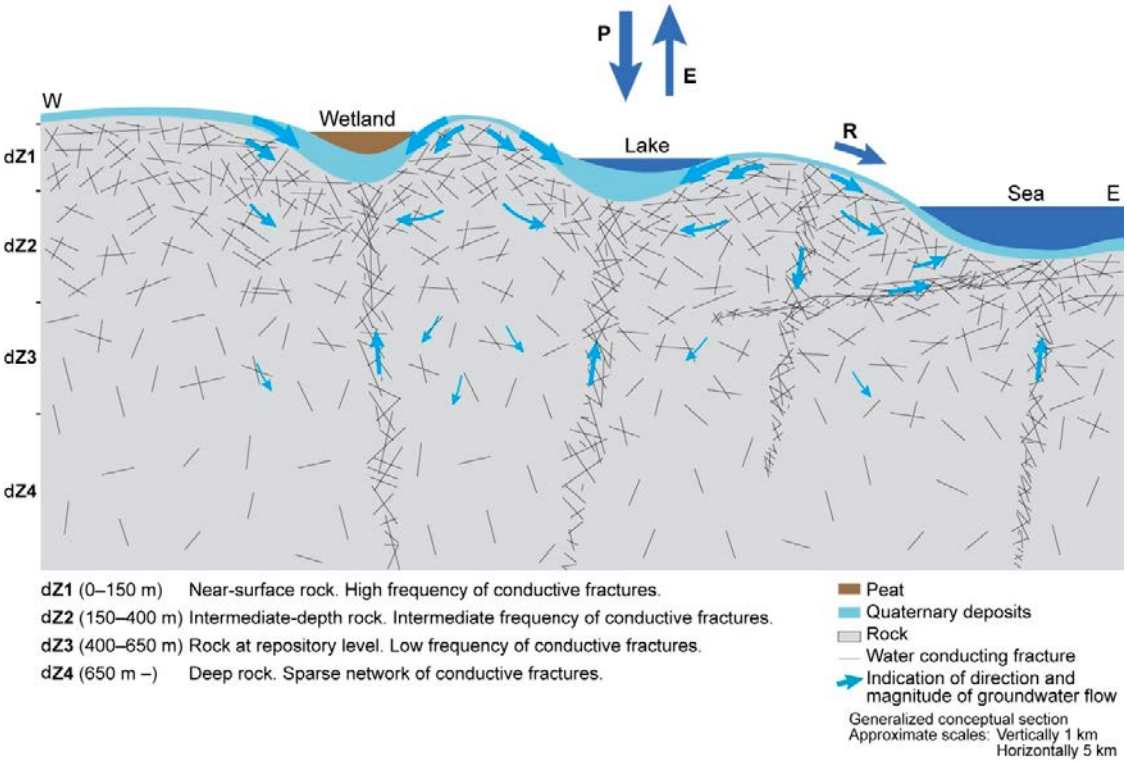

Figure 2-3. *Generalised section illustrating the conceptual model of hydrology and hydrogeology in Laxemar (Rhén and Hartley 2009). There are different horizontal (5 km) and vertical (1 km) scales and the thickness of the Quaternary deposits is exaggerated in the figure.*

The deformation zones making up the HCD show a trend of decreasing transmissivity with depth and a correlation between deformation zone size (interpreted trace length on the surface) and transmissivity. The transmissivity is also dependent on orientation (E-W zones appear more conductive due to a maximum principal stress in the WNW-ESE direction), with significant variability within each zone. An exponential relationship is used for the trend in transmissivity with depth:

$$T(z) = 10^{(a+B-z)} \quad (2\text{-}1)$$

where T is transmissivity (m^2/s), z is elevation (m.a.s.l) and the coefficients a and B are based on a linear regression of $\log_{10}(T)$ (Rhén et al. 2008). There is also significant horizontal variability in transmissivity with an overall estimated standard deviation in $\log_{10}(T)$ of 1.4. The standard deviation of $\log_{10}(T)$ within individual deformation zones is in the range 0.5 to 2.0. Interference tests have shown that dolerite dykes and deformation zones containing fault gouge can act as hydraulic barriers, although the effect is likely to be very localised for the latter. The locations of the deformation zones are shown in Figure 2-4.

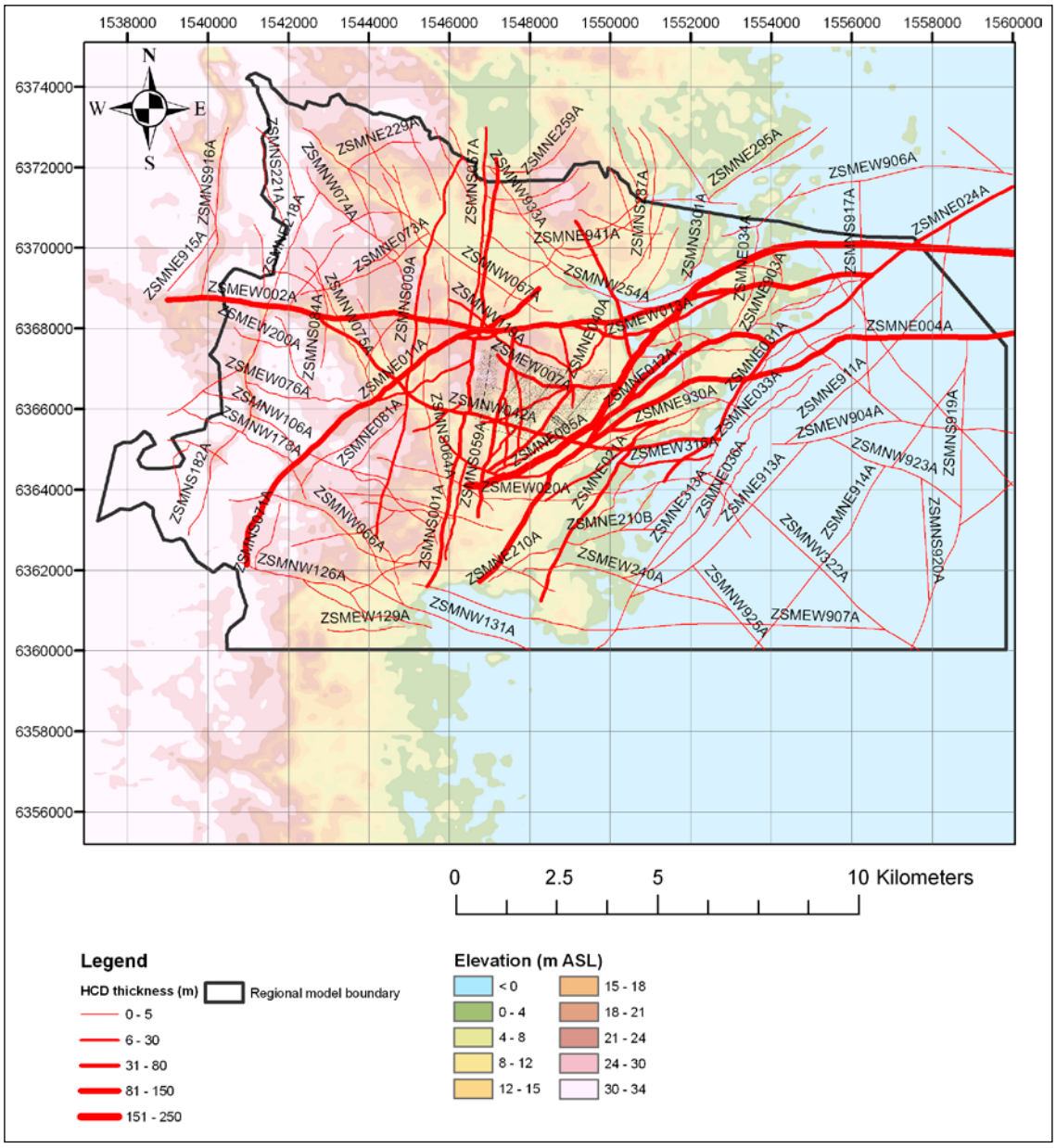

Figure 2-4. *Deformation zones included in the SDM-Laxemar deterministic deformation zone model, with interpreted thickness indicated by line width (Joyce et al. 2010).*

The fractures in the HRD have been divided into four hydraulic rock mass domains (HRD_C, HRD_EW007, HRD_N and HRD_W), as shown in Figure 2-5. Additionally, four fracture sets have been assigned: steeply-dipping ENE, WNW, N-S and sub-horizontal HZ (Rhén and Hartley 2009). The intensity of flowing fractures is highest for the WNW set, with the HZ set also being significant in the upper bedrock. There is a decrease in the intensity of flowing fractures with depth, but transmissivities are similar within a given depth interval. This leads to a decrease in effective hydraulic conductivity of the rock mass with depth, as measured by double packer test (PSS) data on 5 m, 20 m and 100 m scales. A power-law relationship has been inferred from outcrop and lineament data between intensity, *f*, and fracture size:

$$f(r) = \frac{k_r r_0^{k_r}}{r^{k_r+1}} \qquad (2\text{-}2)$$

where r is the fracture radius, r_0 is the location parameter and k_r is the shape parameter. Different size-transmissivity correlation models have been examined for Laxemar modelling (Joyce et al. 2010), but the one used for this study is the semi-correlated relationship:

$$log(T) = log(a\, r^b) + \sigma_{log(T)} N[0,1] \qquad (2\text{-}3)$$

where T is transmissivity, r is the fracture radius, a and b are constants and $N[0,1]$ is a normally distributed random deviate with a mean equal to zero and a standard deviation of 1.

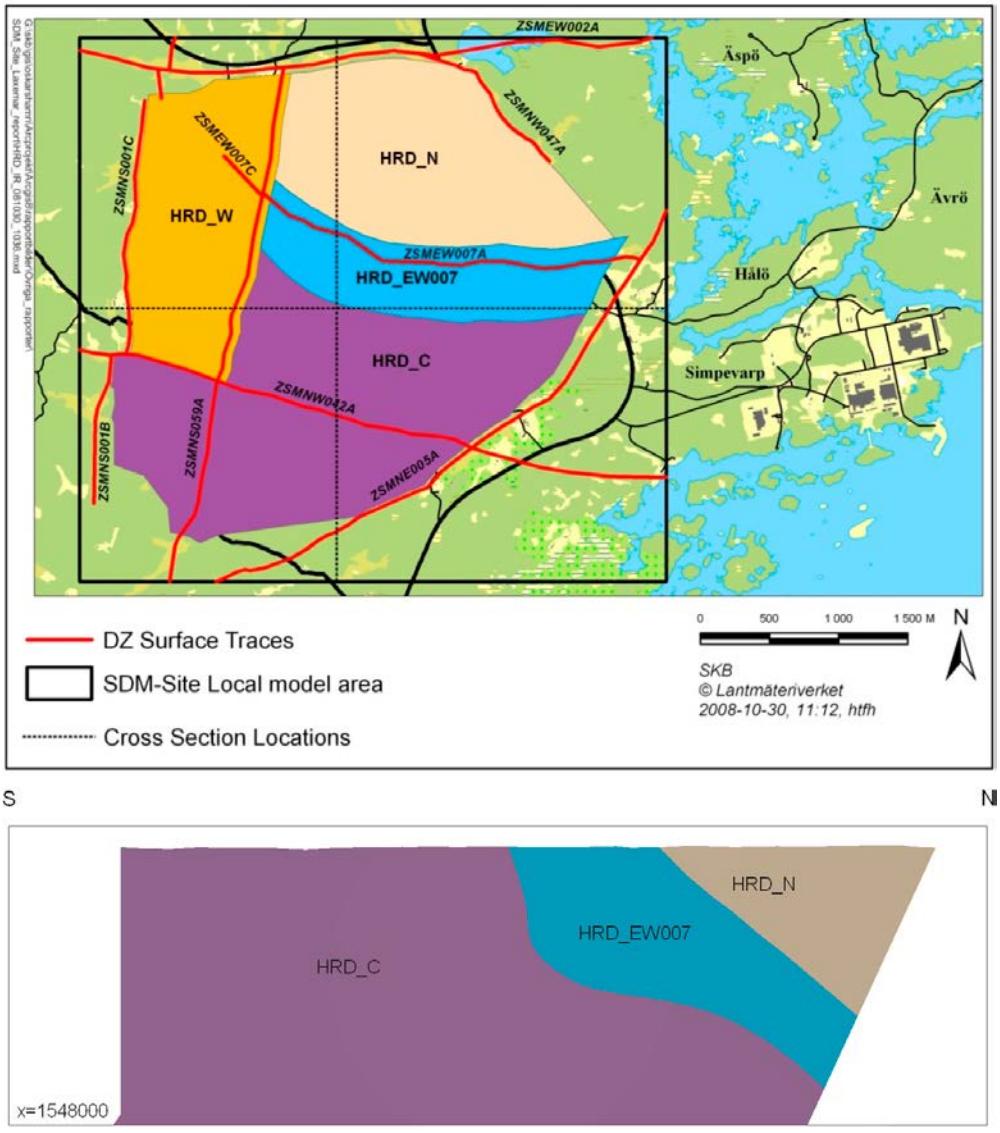

Figure 2-5. *Illustration of the SDM-Site Laxemar Hydraulic Rock mass Domain Model (Figures 3-4 and 3-5 in Rhén and Hartley 2009). Top: horizontal view. Bottom: Vertical section from south (left) to north at Easting X=154800 m. The local model area is now referred to as the facility focussed model area.*

The Quaternary deposits in the HSD have a fairly uniform stratigraphical distribution. The till in valleys is often overlain by glacial clays and often a thin layer of sand, then clay gyttja and peat. The conceptual model of the HSD (Sohlenius and Hedenström 2008) consists of six layers, denoted Z1–Z6, as shown in Figure 2-6. The distribution of layers is affected by the fact that the entire Laxemar-Simpevarp area is situated below the Weichselian previous highest shoreline and, in many areas, soil-forming processes will only have been operating for a few thousand years or the soils will have been subject to wave erosion (Sohlenius and Hedenström 2008). The HSD layers are defined as:

- Z1: a thin surface(-affected) layer,
- Z2: (fen or bog) peat,
- Z3: postglacial clay, clay gyttja/gyttja clay, gyttja or recent fluvial sediments,
- Z4: postglacial sand/gravel, glaciofluvial sediments or artificial fill,
- Z5: glacial clay,
- Z6: (glacial) till.

2.1.2 Climate evolution

The current geological period (Holocene) started at the end of the Weichselian glaciation. A simplified reference glacial cycle was defined in SR-Site for groundwater modelling purposes. This defined the end of the temperate climate period as 10 000 AD (SKB 2010b). During the temperate period, assumed to start at 8000 BC for groundwater modelling purposes, the Laxemar area is subject to post-glacial isostatic land rise, resulting in a retreating shoreline. The predicted shoreline evolution is shown in Figure 2-7 up to 60 000 AD. Beyond 20 500 AD the shoreline elevation is treated as being constant for the purposes of the modelling reported here (see also Figure 3-2 for the modelled shoreline location at selected times). The predicted salinity of the Baltic Sea is shown in Figure 2-8 up to 60 000 AD, which shows a fall in salinity over the temperate period until 2000 AD, beyond which it is treated as being constant.

Additional climate cases were also considered for SR-Site, but not included in the groundwater modelling. One such case is the global warming case, which describes a future climate development influenced by both natural climate variability and the possibility of global warming attributed directly or indirectly to human activity. The global warming case predicts that temperate conditions will dominate until around 60 000 AD. This will expose the Laxemar area to an extended period of meteoric water infiltration, which will have implications for groundwater composition and the associated safety functions (particularly those related to salinity, pH and redox conditions). It is this extended temperate period that is considered in the modelling reported here.

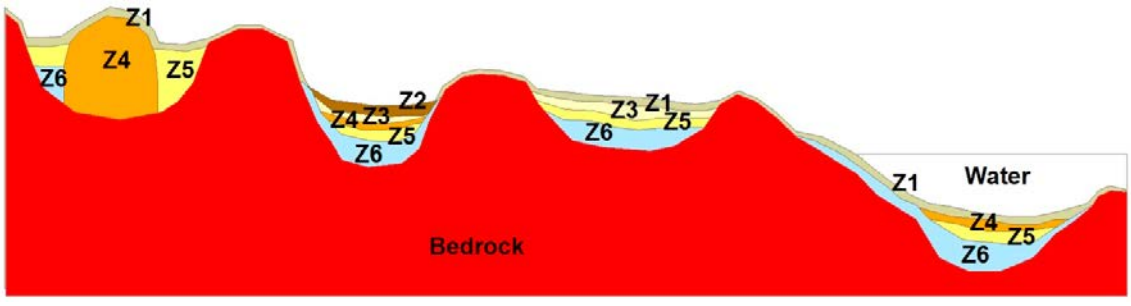

Figure 2-6. *The stratigraphical model of the Quaternary deposits in the Laxemar-Simpevarp regional model area (Sohlenius and Hedenström 2008).*

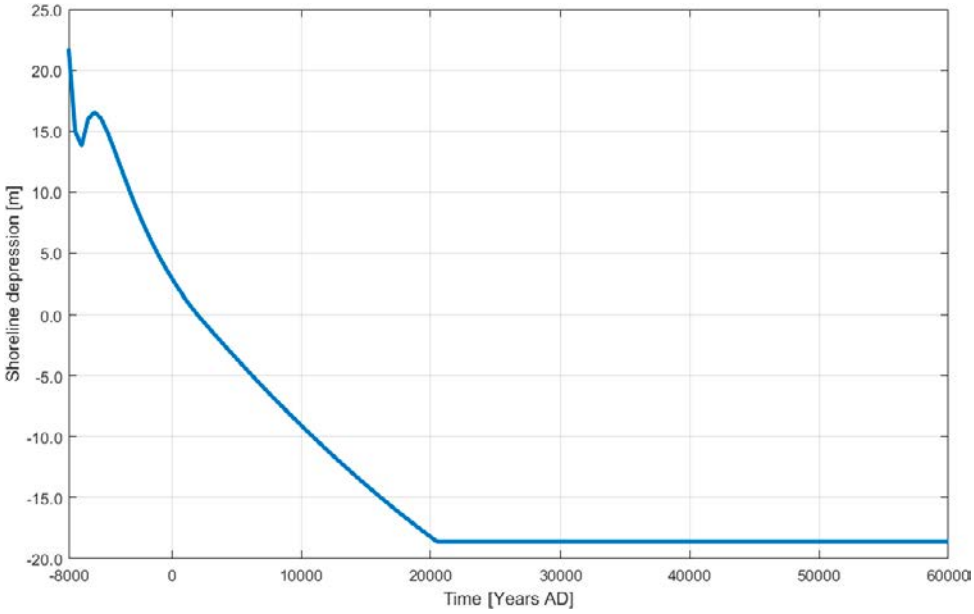

Figure 2-7. *Evolution of the shoreline.*

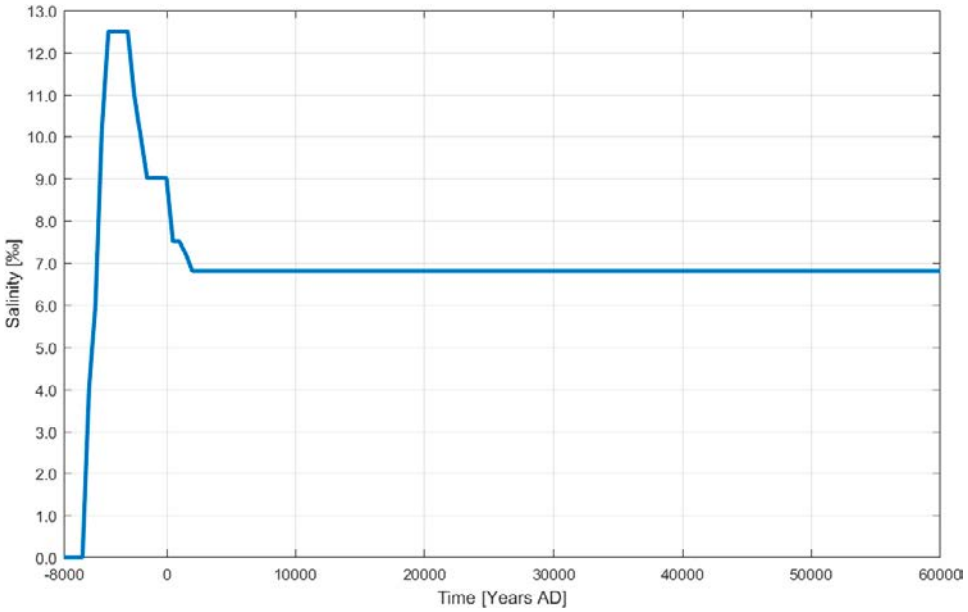

Figure 2-8. *Evolution of the salinity of the Baltic Sea along the shoreline of the Laxemar-Simpevarp area.*

2.1.3 Hydrogeochemistry

The present groundwater composition at Laxemar is the result of the mixing of, and reactions between, waters of different origins and the bedrock during a succession of glacial and interglacial periods. These waters include glacial melt-water, meteoric water, Littorina sea water and deep saline water (Rhén et al. 2009). Waters of different origin are defined in terms of reference waters (Glacial, Altered Meteoric, Interglacial, Littorina, Deep Saline), whose modelled compositions are given in Subsection 3.3.4. The meteoric water originates from both the current temperate climate period (Altered Meteoric), present at shallower bedrock depths, and from older meteoric water (Interglacial), present at greater depths, originating from periods before the last glaciation (Laaksoharju et al. 2009). Significant groundwater circulation extends to depths of around 600 m to 1 000 m, depending on topography, which determines the extent of groundwater mixing. Below these depths, the groundwater is largely stagnant and solute transport is mainly diffusion controlled. Since the last glaciation, the site has been subject to land rise due to post-glacial rebound, leading

to increasing exposure to the infiltration of meteoric water as areas of land rose above sea level. For some areas of the site, this occurred around 1 000 years ago, but other parts of the site have been exposed to meteoric water since around 8000 BC.

In the regolith, the hydrogeochemistry is dominated by weathering reactions involving carbonate and aluminosilicate dissolution, facilitated by biogenic carbon dioxide which leads to a decrease in pH (Laaksoharju et al. 2009). The redox conditions in the near-surface groundwater are highly variable due to biological activity. In the bedrock, hydrogeochemical mixing processes become a more dominant consideration, but water-rock interactions, e.g. mineral equilibration, and microbiological activity are also of significance. Below around 20 m depth, the redox conditions are reducing.

2.2 Methods and tools

The modelling reported here was carried out using ConnectFlow version 11.2 (Amec Foster Wheeler 2015). ConnectFlow is a suite of groundwater flow and transport software that can represent rock using continuous porous medium (CPM), discrete fracture network (DFN), or combined CPM/DFN concepts. An equivalent continuous porous medium (ECPM) concept based on upscaled DFN properties is also available. The modelling carried out for this study (described in Chapter 3) used DFN, CPM and ECPM representations. The main concepts and methods used for this work are summarised in the following subsections. Further details can be found in Joyce et al. (2010, 2014), Hartley and Joyce (2013) and Amec Foster Wheeler (2015).

2.2.1 Discrete fracture network (DFN) representation

The DFN concept is a representation for fractured rock that explicitly represents aspects of the structural geology and individual flows within fractures. The properties of the network are usually characterised in terms of:

- Spatial distribution (e.g. Poisson, fractal, clustered around points or deformation zones).
- Fracture intensity (and its spatial variation).
- Fracture sets distinguished by orientation.
- Fracture size (e.g. log-normal, power-law distributions).
- Transmissivity-size relationships and statistical distributions.

The properties of each fracture are primarily:

- Size.
- Orientation (strike and dip).
- Transmissivity (and potentially spatial variability within the fracture).
- Transport aperture.
- Storativity.
- Shape.

In ConnectFlow, fractures are usually rectangular, but may be right-angled triangles where a complex surface has been triangulated into many pieces (e.g. for a deformation zone). For stochastic fractures, the properties are sampled from probability distribution functions (PDF's) specified for each fracture set. The properties may be sampled independently or correlated with other properties, e.g. transmissivity and size. The PDF's and associated parameters used for this study are described in Section 3.2.

2.2.2 Continuous porous medium (CPM) representation

CPM models are considered appropriate for certain types of ground conditions, in which flow is predominantly through an interconnected network of pores in the rock matrix, such as for many sedimentary rocks, or for soils and unconsolidated deposits. The model assumes continuity in three dimensions and hence a high degree of connectivity between points in the modelling domain.

Connectivity is only reduced when very low conductivity layers or flow barriers are incorporated in the model. The flow through such domains is modelled by Darcy's law, which relates specific discharge (Darcy flux) to the driving force, i.e. the pressure gradient and/or buoyancy force.

The CPM representation is less useful for fractured rocks than for unfractured ones, as it can only represent bulk properties over large volumes. However, it can be of use for regions of a model where there are few data available on fracturing and it is appropriate to use generic bulk rock properties, e.g. in rock mass volumes far away from the repository host rock.

Where more detail is required, it is possible to nest volumes with finer discretisation within more coarsely defined volumes. Where there are disconnects in node connectivity between the sub-volumes, internal boundary conditions are applied that impose continuity of pressure and conservation of mass at the interfaces of the sub-volumes.

2.2.3 Equivalent continuous porous medium (ECPM) representation

To assess the implications of a discrete fracture network for flow and transport on the catchment scale, it is often necessary, for practical reasons, to convert the DFN model to an ECPM model with appropriate properties. The resulting parameters are a directional hydraulic conductivity tensor, fracture kinematic porosity and other transport properties (such as the fracture surface area per unit volume). In ConnectFlow, a flux-based upscaling method is used that requires several flow calculations through a DFN model in different directions (Hartley and Joyce 2013, Jackson et al. 2000).

2.2.4 Embedded CPM/DFN models

It also possible to create models with non-overlapping sub-domains that are either (E)CPM or DFN. Where sub-domains of different types meet, ConnectFlow applies internal boundary conditions that ensure continuity of pressure and conservation of mass. This type of model is appropriate for representing backfilled repository structures within a surrounding DFN below a CPM representation of the regolith. It is also useful for embedding a facility scale DFN within a catchment scale ECPM. In this case, consistency of properties can be ensured by using a facility scale DFN that is a sub-volume of the catchment scale DFN used for upscaling to the ECPM. This type of model allows the detailed, structurally-controlled flows around the repository to be represented without the computational burden of using a catchment scale DFN model.

2.2.5 Implicit fracture zones (IFZ)

The properties of large deterministic structures, such as deformation zones, in CPM or ECPM models can be represented in ConnectFlow using the implicit fracture zone (IFZ) method. This approach combines the properties of each cell in the model that is intersected by a structure with the corresponding properties of the intersecting structure, taking the volume of the cell occupied by the structure and its orientation into account (Hartley and Joyce 2013). The result of this process is to produce a spatial distribution of cell properties (hydraulic conductivity tensor, porosity and flow-wetted surface) that represents the combined influence of both the deterministic structures and bedrock stochastic fractures.

In a DFN, these deterministic structures are represented as fracture surfaces, with hydraulic properties equivalent to the structures they represent. In an embedded model, the representation changes from a fracture surface to an IFZ at the interface between the DFN and the (E)CPM.

2.2.6 Groundwater flow

Groundwater flow in ConnectFlow for a CPM or DFN is expressed in terms of Darcy's law

$$\boldsymbol{q} = -\frac{k_r \boldsymbol{k}}{\mu} \cdot (\nabla P_T - \rho \boldsymbol{g}) \tag{2-4}$$

and the equation for conservation of mass

$$\frac{\partial(\phi S \rho)}{\partial t} + \nabla \cdot (\rho \boldsymbol{q}) = 0 \tag{2-5}$$

where

- $\boldsymbol{q}$ is the specific discharge (or Darcy flux) [m/s],
- k_r is the residual permeability [m^2],
- $\boldsymbol{k}$ is the equivalent permeability tensor due to the fractures carrying the flow [m^2],
- μ is the groundwater viscosity [kg/m/s],
- P_T is the (total) pressure in the groundwater [N/m^2],
- ρ is the groundwater density [kg/m^3],
- $\boldsymbol{g}$ is the gravitational acceleration [m/s^2],
- t is the time [s],
- ϕ is the kinematic porosity due to the fractures carrying the flow [-],
- S is saturation [-].

In ConnectFlow, the pressure is usually represented in terms of "residual pressure", P_R. The residual pressure is defined with respect to the selected reference elevation and is obtained by subtracting from the total pressure the hydrostatic pressure due to a freshwater column that extends vertically from the location where the total pressure is measured to the reference elevation, i.e.

$$P_R = P_T + \rho_0 g(z - z_0) \tag{2-6}$$

where

- ρ_0 is the reference groundwater density [kg/m^3],
- z_0 is the reference elevation [m].

Also, the dependence of porosity on pressure can be expressed in terms of specific storage:

$$S_T = \rho \boldsymbol{g}(\frac{\partial \phi}{\partial P_R} + \phi \propto) \tag{2-7}$$

where

- S_T is the specific storage coefficient [m^{-1}],
- α is the fluid compressibility [m^2/N].

Equations (2-4), (2-5), (2-6) and (2-7) can then be combined into a single groundwater flow equation in terms of residual pressure and specific storage

$$\frac{S_T}{\boldsymbol{g}}\frac{\partial P_T}{\partial t} + \phi\rho\frac{\partial S}{\partial t} - \nabla \cdot \left(\rho \frac{k_r \boldsymbol{k}}{\mu}\nabla P_R\right) = 0 \tag{2-8}$$

In general, the density and viscosity of the groundwater depend on temperature, pressure and total salinity. Temperature and salinity are in turn transported by the groundwater. When the variations in temperature or solute concentration with time are large enough to produce significant changes in density or viscosity, it is necessary to couple the solution of the groundwater flow problem to that of the heat or solute transport problem. For this study, transport of heat is not included, but a fixed (in time) depth-dependent temperature field is applied. The spatially varying temperature is taken into account, along with the salinity and pressure, when calculating groundwater density and viscosity (Kestin et al. 1981) and equilibration reactions.

2.2.7 Solute transport

ConnectFlow calculates solute transport in a CPM using the advection-dispersion equation

$$\frac{\partial(\phi\rho c)}{\partial t} + \nabla \cdot (\rho \boldsymbol{q} c) = \nabla \cdot (\phi\rho \boldsymbol{D} \cdot \nabla c) \tag{2-9}$$

where

- c is the solute mass fraction in the groundwater flowing through the fractures [-],
- $\boldsymbol{D}$ is the (effective) dispersion tensor [m^2/s].

The dispersion tensor is given by

$$\boldsymbol{D} = \frac{D_m}{\tau}\delta_{ij} + \alpha_T v\delta_{ij} + (\alpha_L - \alpha_T)\frac{v_i v_j}{v} \quad (2\text{-}10)$$

where

- D_m is the molecular diffusion coefficient for solute [m^2/s],
- τ is the tortuosity [-],
- δ_{ij} is the Kronecker delta [-],
- α_T is the transverse dispersion length of solute [m],
- α_L is the longitudinal dispersion length of solute [m],
- v is the magnitude of the fluid velocity [m/s],
- v_i and v_j are components of the fluid velocity [m/s].

Values of the parameters used for this study are given in Section 3.3.2.

For a single transported component, Equations (2-4), (2-5) and (2-9) can be solved in ConnectFlow as a coupled set of equations. However, for the transport of many components, it is not usually practicable to solve the full set of coupled equations simultaneously. In this case, sequential iteration can be used as an operator splitting method to solve each groundwater flow and transport equation separately within each time step. Multiple iterations of the sequence of calculations can be carried out for increased accuracy at the expense of computational time, but normally a single iteration is sufficient for a system that is evolving slowly relative to the time step size (Joyce et al. 2015).

2.2.8 Rock matrix diffusion (RMD)

Rock matrix diffusion (RMD) is the process of migration of solutes from fractured rock into the less mobile water within the rock matrix over long time periods. A rock matrix diffusion method that is compatible with the calculation of chemical reactions, based on a finite volume approach, has been used in CPM solute transport calculations for this study (Joyce et al. 2014). This method divides the rock matrix into separate cells and calculates the transport of components from one cell to the next at each time step before carrying out chemical reactions. RMD is represented by an additional term in Equation (2-9):

$$\frac{\partial(\phi\rho c)}{\partial t} + \nabla\cdot(\rho\boldsymbol{q}c) = \nabla\cdot(\phi\rho\boldsymbol{D}\cdot\nabla c) + \sigma\rho D_i\left.\frac{\partial c'}{\partial w}\right|_{w=0} \quad (2\text{-}11)$$

and

$$\frac{\alpha\partial(\rho c')}{\partial t} = \frac{\partial}{\partial w}\left(\rho D_i\frac{\partial c'}{\partial w}\right) \quad (2\text{-}12)$$

where

- D_i is the intrinsic diffusion coefficient of the matrix [m^2/s],
- σ is the fracture surface area per unit volume [m^{-1}],
- w is the distance from the fracture into the rock matrix [m],
- c' is the solute mass fraction in the groundwater in the rock matrix [-],
- α is the capacity factor of the matrix [-].

2.2.9 Hydrogeochemical calculations

ConnectFlow is able to combine groundwater flow and transport calculations with hydrogeochemical calculations, i.e. reactive transport (Joyce et al. 2014). At each time step, the mass fractions of components are updated based on the results of chemical reaction calculations. The chemical reactions are calculated by the iPhreeqc version 2.18 software library (Charlton and Parkhurst 2011), which encapsulates and provides access to the widely used PHREEQC geochemical software (Parkhurst and Appelo 1999). The data produced by iPhreeqc are used to calculate the mass fractions of components for the next time step in ConnectFlow. Figure 2-9 shows a flow diagram describing the reactive transport system in ConnectFlow. Chemical reactions are calculated for both the fractures and the rock matrix.

The chemical calculations are based on a set of thermodynamic constraints defined in a separate database. The thermodynamic database used in this study is basically the same as the one used in the calculations performed by Gimeno et al. (2010) (see SKB 2009b). Additional equilibrium constraints with mineral phases FeS(ppt) and haematite, have been added to the database to include the reactions used in this study.

The mineral reactions considered are:

- Quartz: $SiO_2 + 2H_2O = Si(OH)_4$ $\quad\quad$ logK = −3.746
- Calcite: $CaCO_3 + H^+ = Ca^{2+} + HCO_3^-$ $\quad\quad$ logK = 1.849
- FeS(ppt): $FeS + H^+ = Fe^{2+} + HS^-$ $\quad\quad$ logK = −3.00
- Haematite: $Fe(OH)_3 + 3H^+ = Fe^{3+} + 3H_2O$ $\quad\quad$ logK = −1.10

All the reactions are considered to be at equilibrium, i.e. kinetic effects are not considered, and charge balance is maintained.

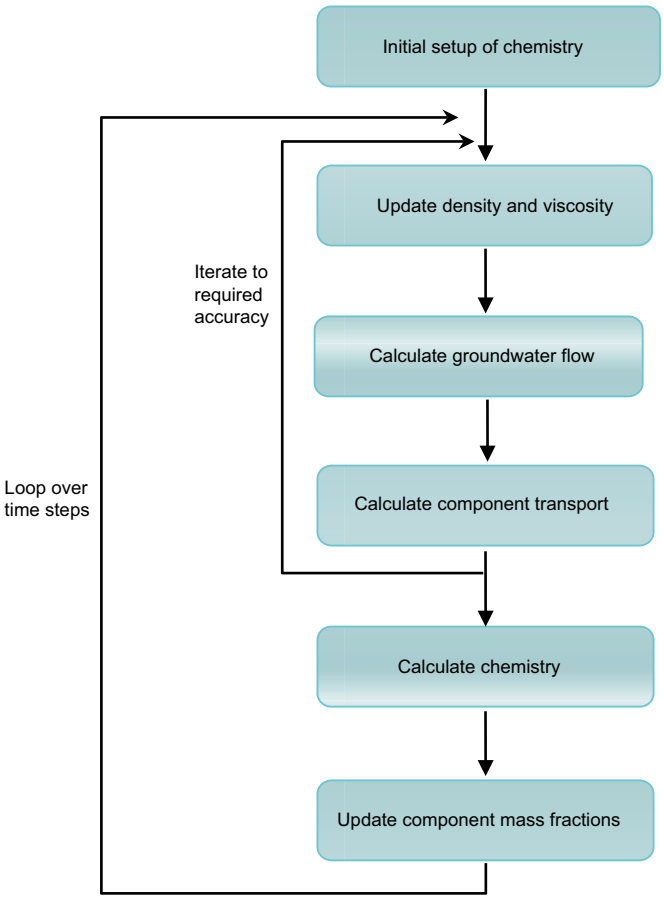

Figure 2-9. *Flow diagram of reactive transport within ConnectFlow.*

2.2.10 Particle tracking

Particle tracking is used to calculate solute migration pathways, typically starting from the repository. Paths can be tracked with the downstream groundwater flow field to identify contaminant transport pathways and discharge areas, or upstream to identify pathways for recharge.

In the CPM, ConnectFlow deterministically tracks particles following the discretised flow field. In the DFN, a library of potential flow paths is constructed between so-called transport nodes, which are evenly spaced along each fracture intersection. The library is used to stochastically calculate the path taken by each particle using flux-weighted random path selection at each transport node. For this study, the ConnectFlow approximate particle tracking approach was used. In this approach, there is only one transport node per fracture intersection and the flux-weightings are based on the bulk flows calculated between pairs of intersections on each fracture. The approximate particle tracking approach is robust and fast enough to be used with the large models considered in this study.

For embedded models, particles may switch back and forth between parts of the domain represented by the deterministic CPM concept and the stochastic DFN concept according to the flow field. The overall path for a particle is stochastic if any part of it is within the DFN.

2.2.11 Performance measures

Particle tracking in the facility focussed model can be used to calculate performance measures that provide input to repository safety assessments. The performance measures considered for this study are only calculated in the DFN part of the model and are defined as:

- Equivalent flow rate [m^3/y], Q_{eq}, at the release point from the vault into a single fracture (Equation B-8).
- Equivalent flux [m^2/y], U, at the release point from the vault into a single fracture (Equation B-10).
- Path length [m], $L = \sum_i \delta l_i$, where δl_i is the length [m] of path step i.
- Travel time [y], $t = \sum_i \frac{e_{t,i} w_i \delta l_i}{Q_i}$, where $e_{t,i}$ is the transport aperture [m] of the fracture containing step i, w_i is the flow width [m] between the pair of intersections for the step and Q_i is the flow rate [m^3/y] between the pair of intersections.
- Flow-related transport resistance [y/m], $F = \sum_i \frac{2 w_i \delta l_i}{Q_i} = \sum_i \frac{2 t_i}{e_{t,i}}$. This is a measure of the potential for retention and retardation of radionuclides within the rock.

Further details on the performance measures can be found in Appendix B and Joyce et al. (2010).

3 Modelling

The models used in this study are based on the Elaborated Hydro-DFN case used for the Laxemar temperate climate period modelling as part of the SR-Site site comparison project (Joyce et al. 2010). Changes have been made to support reactive transport modelling, to extend the simulated period to 60 000 AD and to provide an alternative model of the regolith. The main features of the models are summarised in the following sections.

3.1 Description of modelled cases

Three different model cases are considered, see Table 3-1. These cases are selected to explore some of the uncertainties in the hydrogeochemical reactions that are thought to occur at the Laxemar site. Case 1 includes no chemical reactions and simply transports the chemical components. Case 2 and Case 3 include chemical reactions with different mineral phases and correspond to reactions used for SR-Site (Gimeno et al. 2010). The effect of cation exchange is neglected for all cases in the present study.

In the two cases where chemical reactions are included, the reference waters are initially equilibrated with the mineral phases and charge balanced by adjusting the chloride concentration, as necessary. Equilibrium conditions are assumed for all chemical reactions and the equilibration reactions with the selected minerals are then repeated for each time step using the updated compositions from the transport calculations. An initial amount of 10.0 moles of each mineral per kilogram of water (the PHREEQC default) is specified that allows for effectively unlimited dissolution. This means that the included minerals are assumed to be abundant in the geosphere at the site, which is not necessarily true. However, since the presence of specific minerals does not have a significant effect on the modelling results (seen by comparing Case 1 with the other cases) then more comprehensive and site-specific data will not be needed in order to provide more accurate simulation results.

Table 3-1. Description of modelled cases.

Name	Description
Case 1	**No chemical reactions.** No chemical speciation, mineral equilibrium reactions, or cation-exchange reactions are included in this case. Therefore, the spatial and temporal distribution of groundwater components is determined by transport processes only (i.e. matrix diffusion and advection affected by dispersion and mixing of reference waters), which are modelled in terms of the individual components of the reference waters. For the temperate climate period at repository depth, the main process is the gradual replacement of mainly Littorina/Deep Saline water with Altered Meteoric water (see Table 3-7). This leads to a reduction in salinity and an increase in the concentration of bicarbonate, reported here in terms of total inorganic carbon. Comparing the results from Case 1 with the remaining cases allows for an evaluation of the effects of the chemical reactions considered relative to the simplified case of solute transport and mixing of waters with different compositions. This case can also be used for backward comparison with SR-Site results, since the hydrogeological modelling performed there did not include chemical reactions. In addition, a sensitivity study is performed using Case 1, to address the sensitivity of the palaeo-hydrogeological calibration to the hydraulic properties of the HRD. In this analysis, four additional realisations of the DFN (making a total of five HRD realisations) were used to derive the spatially varying properties of the HRD for Case 1. **Tracer simulations.** The first HRD realisation of the Case 1 model (r1) was also used in a separate analysis in which chemical tracer components (non-reacting and non-sorbing) were used to track the mixing of the different reference waters. The only change made to the Case 1 model is that a unique chemical tracer was added to each of the five existing reference waters. By using tracers, the mixing of reference waters can be tracked and analysed readily in the post-processing of the simulation results. This is currently not possible without the addition of tracers, since the identification of reference waters is lost at the start of the simulation (only the separate chemical components are kept track of), due to the included subsequent reactive transport processes. The results from the tracer simulations can be used to estimate the degree of dispersion within the hydrogeological model.
Case 2	**Equilibration of groundwater with calcite, quartz and amorphous iron (II) sulphide.** This is the "base case" from Gimeno et al. (2010) for a situation with significant activity of sulphate-reducing bacteria. However, the hydroxyapatite reactions are not included as they are not deemed relevant to this work. The evolution of groundwater composition for this case is due to the transport and mixing of components originating from different reference waters. However, the concentrations of reacting species are modified by the chemical reactions considered for this case, which include equilibration of groundwater and matrix porewater with calcite, quartz and amorphous iron (II) sulphide. Chemical reactions are calculated for both the fractures and the rock matrix. It was expected that the reactions would have an effect on pH, pE, and the concentrations of total inorganic carbon, calcium, silicon, sulphur and iron. The concentrations of non-reacting species such as chloride and sodium should be the same as for Case 1, except possibly with very minor differences caused by slight changes in groundwater density, due to dissolution or precipitation of solutes, which might affect the transport of components.
Case 3	**Equilibration of groundwater with calcite, quartz and iron (III) oxyhydroxide.** This is the "base case" from Gimeno et al. (2010) for a situation where the redox state is not affected by sulphate-reducing bacteria. Again, the hydroxyapatite reactions are not included. The evolution of groundwater composition for this case is also due to the transport and mixing of components originating from different reference waters. However, a different set of chemical reactions are considered for this case, which include equilibration of groundwater with calcite, quartz and iron (III) oxyhydroxide. This is the same as Case 2, except that iron (III) oxyhydroxide has replaced amorphous iron (II) sulphide. Chemical reactions are calculated for both the fractures and the rock matrix. It was expected that the reactions would have an effect on pH, pE, and the concentrations of total inorganic carbon, calcium, sulphur, silicon and iron. Since only reactions involving iron and sulphur are different between Case 2 and Case 3, it was expected that only the results for pE and the concentrations of iron and sulphur would differ significantly between these two cases. The concentrations of non-reacting species should be very similar for all cases.

3.2 Representation of fractures

3.2.1 Hydraulic Conductor Domain (HCD)

The deformation zones in the HCD were represented by triangulated surfaces with assigned hydraulic properties and thicknesses. They were incorporated into the model using the IFZ method (Subsection 2.2.5). The properties of the deformation zones were either treated deterministically or stochastically. Both methods incorporate the depth trend described in Subsection 2.1.1. The stochastic HCD uses the same geometry for each realisation, but calculates depth-dependent stochastic properties, conditioned on borehole measurements (Joyce et al. 2010), with a standard deviation in $\log_{10}(T)$ of 1.4, assuming a log-normal independently sampled distribution.

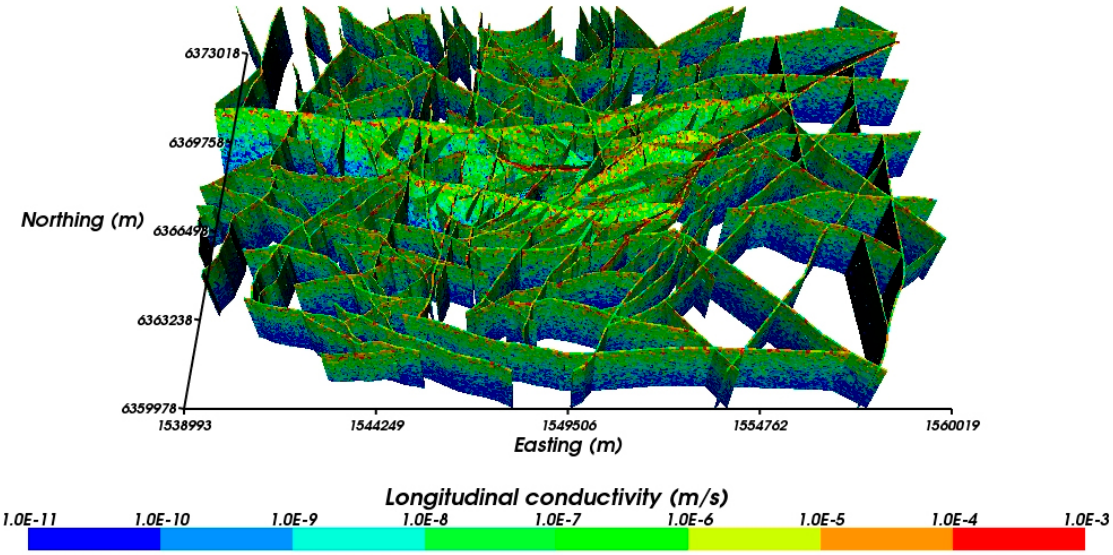

Figure 3-1. *One realisation of the modelled stochastic HCD coloured by hydraulic conductivity (Figure 4-2 in Joyce et al. 2010).*

3.2.2 Hydraulic Rock Domain (HRD)

The HRD used the Elaborated Hydro-DFN specification detailed in Joyce et al. (2010). The parameters required for the relationships described in Subsection 2.1.1 for each rock mass domain, depth zone and fracture set are given in Table 3-2 to Table 3-5. Fracture intensity was based on open and partly open fractures. The orientations were represented by a univariate Fisher distribution (Fisher 1953), parameterised by a mean plunge and trend, along with a concentration. The transmissivity model assumed a semi-correlation (SC) between size and transmissivity. Isolated fractures were removed as they will not contribute to groundwater flow.

Table 3-2. Elaborated Hydro-DFN parameters for HRD_C for a fixed r_0 of 0.038 m (Table E-1 in Joyce et al. 2010).

Depth zone (metres above sea level)	Set	Orientation set pole: (trend, plunge), conc.	Fracture radius model power-law (k_r, r_0)	Intensity P_{32} (m^2/m^3) of open fractures	Transmissivity model T (m^2/s) (a, b, σ)
−150 to 0 (DZ1)	ENE	(155.1, 3.4), 9.6	(2.70, 0.038)	0.52	SC: (2×10^{-7}, 0.7, 0.4)
	WNW	(204, 1.6), 12.0	(2.49, 0.038)	0.95	SC: (2×10^{-7}, 0.9, 0.6)
	N-S	(270.2, 8.4), 7.8	(2.80, 0.038)	0.54	SC: (8×10^{-8}, 0.5, 0.4)
	SubH	(46.3, 84.7), 12.0	(2.59, 0.038)	1.20	SC: (6×10^{-8}, 0.7, 0.5)
−400 to −150 (DZ2)	ENE	(155.1, 3.4), 9.6	(3.00, 0.038)	0.47	SC: (6×10^{-7}, 0.7, 0.9)
	WNW	(204, 1.6), 12.0	(2.44, 0.038)	0.55	SC: (1×10^{-8}, 0.5, 0.7)
	N-S	(270.2, 8.4), 7.8	(2.91, 0.038)	0.63	SC: (1×10^{-8}, 0.7, 0.2)
	SubH	(46.3, 84.7), 12.0	(2.87, 0.038)	0.71	SC: (3.5×10^{-8}, 1.2, 0.9)
−650 to −400 (DZ3)	ENE	(155.1, 3.4), 9.6	(2.87, 0.038)	0.38	SC: (8×10^{-8}, 0.8, 0.6)
	WNW	(204, 1.6), 12.0	(2.54, 0.038)	0.74	SC: (3×10^{-9}, 0.8, 0.6)
	N-S	(270.2, 8.4), 7.8	(2.87, 0.038)	0.47	SC: (6×10^{-9}, 0.4, 0.4)
	SubH	(46.3, 84.7), 12.0	(3.00, 0.038)	0.58	SC: (2×10^{-7}, 0.8, 0.7)
−1 000 to −650 (DZ4)	ENE	(155.1, 3.4), 9.6	(2.96, 0.038)	0.46	SC: (1×10^{-8}, 0.7, 0.4)
	WNW	(204, 1.6), 12.0	(3.00, 0.038)	0.73	SC: (3×10^{-7}, 0.7, 0.4)
	N-S	(270.2, 8.4), 7.8	(3.00, 0.038)	0.25	SC: (1×10^{-8}, 0.7, 0.4)
	SubH	(46.3, 84.7), 12.0	(2.97, 0.038)	0.35	SC: (1×10^{-7}, 0.7, 0.4)

Table 3-3. Elaborated Hydro-DFN parameters for HRD_EW007 for a fixed r_0 of 0.038 m (Table E-2 in Joyce et al. 2010).

Depth zone (metres above sea level)	Set	Orientation set pole: (trend, plunge), conc.	Fracture radius model power-law (k_r, r_0)	Intensity P_{32} (m^2/m^3) of open fractures	Transmissivity model T (m^2/s) (a, b, σ)
−150 to 0 (DZ1)	ENE	(162.8, 1.4), 10.7	(2.77, 0.038)	0.55	SC: (3.0×10^{-8}, 0.6, 0.4)
	WNW	(25.3, 0.2), 16.4	(2.30, 0.050)	1.01	SC: (3.0×10^{-8}, 0.6, 0.3)
	N-S	(88.9, 3.9), 8.8	(2.53, 0.038)	0.33	SC: (1.0×10^{-7}, 0.8, 0.3)
	SubH	(138.7, 81.3), 9.7	(2.76, 0.038)	1.72	SC: (2.3×10^{-7}, 0.8, 0.5)
−400 to −150 (DZ2)	ENE	(162.8, 1.4), 10.7	(2.83, 0.038)	0.60	SC: (2.0×10^{-7}, 0.6, 0.6)
	WNW	(25.3, 0.2), 16.4	(2.41, 0.038)	1.15	SC: (3.0×10^{-8}, 0.6, 0.4)
	N-S	(88.9, 3.9), 8.8	(2.60, 0.038)	0.54	SC: (3.0×10^{-7}, 0.8, 0.4)
	SubH	(138.7, 81.3), 9.7	(2.84, 0.038)	0.82	SC: (5.0×10^{-8}, 0.8, 0.4)
−650 to −400 (DZ3)	ENE	(162.8, 1.4), 10.7	(2.93, 0.038)	0.69	SC: (1.0×10^{-8}, 0.5, 0.2)
	WNW	(25.3, 0.2), 16.4	(2.62, 0.038)	1.43	SC: (1.2×10^{-7}, 0.3, 0.2)
	N-S	(88.9, 3.9), 8.8	(3.00, 0.038)	0.64	SC: (8.0×10^{-8}, 0.4, 0.2)
	SubH	(138.7, 81.3), 9.7	(2.99, 0.038)	0.92	SC: (1.5×10^{-7}, 0.7, 0.3)
−1 000 to −650 (DZ4)	ENE	(162.8, 1.4), 10.7	(2.96, 0.038)	0.33	SC: (1.0×10^{-8}, 0.7, 0.4)
	WNW	(25.3, 0.2), 16.4	(3.00, 0.038)	0.89	SC: (3.0×10^{-7}, 0.7, 0.4)
	N-S	(88.9, 3.9), 8.8	(3.00, 0.038)	0.21	SC: (1.0×10^{-8}, 0.7, 0.4)
	SubH	(138.7, 81.3), 9.7	(2.97, 0.038)	0.80	SC: (1.0×10^{-7}, 0.7, 0.4)

Table 3-4. Elaborated Hydro-DFN parameters for HRD_W for a fixed r_0 of 0.038 m (Table E-3 in Joyce et al. 2010).

Depth zone (metres above sea level)	Set	Orientation set pole: (trend, plunge), conc.	Fracture radius model power−law (k_r, r_0)	Intensity P_{32} (m^2/m^3) of open fractures	Transmissivity model T (m^2/s) (a, b, σ)
−150 to 0 (DZ1)	ENE	(340.3, 1.2), 15	(2.59, 0.038)	0.44	SC: (2.1×10^{-8}, 0.7, 0.6)
	WNW	(208.9, 2.2), 10.9	(2.54, 0.038)	0.61	SC: (7.0×10^{-8}, 0.8, 1.0)
	N−S	(272.8, 12.0), 11.5	(2.52, 0.038)	0.54	SC: (4.0×10^{-8}, 0.7, 0.8)
	SubH	(277.1, 84.3), 11.1	(2.50, 0.038)	1.03	SC: (8.0×10^{-8}, 0.7, 0.7)
−400 to −150 (DZ2)	ENE	(340.3, 1.2), 15	(2.54, 0.038)	0.28	SC: (2.2×10^{-9}, 0.5, 0.4)
	WNW	(208.9, 2.2), 10.9	(2.65, 0.038)	0.38	SC: (1.5×10^{-8}, 0.5, 1.2)
	N−S	(272.8, 12.0), 11.5	(3.00, 0.038)	0.40	SC: (5.0×10^{-9}, 0.4, 0.3)
	SubH	(277.1, 84.3), 11.1	(2.72, 0.038)	0.50	SC: (1.2×10^{-7}, 0.7, 1.2)
−650 to −400 (DZ3)	ENE	(340.3, 1.2), 15	(3.00, 0.038)	0.17	SC: (3.0×10^{-9}, 0.6, 0.4)
	WNW	(208.9, 2.2), 10.9	(2.61, 0.038)	0.33	SC: (1.5×10^{-8}, 0.5, 0.3)
	N−S	(272.8, 12.0), 11.5	(2.53, 0.038)	0.30	SC: (5.0×10^{-8}, 0.2, 0.2)
	SubH	(277.1, 84.3), 11.1	(2.72, 0.038)	0.38	SC: (2.0×10^{-7}, 0.8, 0.8)
−1 000 to −650 (DZ4)	ENE	(155.1, 3.4), 9.6	(3.00, 0.038)	0.12	SC: (1.0×10^{-8}, 0.7, 0.4)
	WNW	(208.9, 2.2), 10.9	(3.00, 0.038)	0.09	SC: (3.0×10^{-8}, 0.7, 0.4)
	N−S	(272.8, 12.0), 11.5	(2.53, 0.038)	0.14	SC: (1.0×10^{-8}, 0.7, 0.4)
	SubH	(277.1, 84.3), 11.1	(3.00, 0.038)	0.65	SC: (3.0×10^{-8}, 0.7, 0.4)

Table 3-5. Elaborated Hydro-DFN parameters for HRD_N for a fixed r_0 of 0.038 m.

Depth zone (metres above sea level)	Set	Orientation set pole: (trend, plunge), conc.	Fracture radius model power−law (k_r, r_0)	Intensity P_{32} (m^2/m^3) of open fractures	Transmissivity model T (m^2/s) (a, b, σ)
−150 to 0 (DZ1)	ENE	(342.2, 0.2), 15.8	(2.50, 0.038)	0.41	SC: (1.0×10^{-7}, 0.6, 0.6)
	WNW	(209.8, 1.6), 14.6	(2.30, 0.038)	0.92	SC: (2.0×10^{-7}, 0.7, 0.8)
	N−S	(271.3, 3.8), 10.3	(2.50, 0.038)	0.46	SC: (1.0×10^{-7}, 0.7, 1.0)
	SubH	(238.9, 81.5), 12.7	(2.70, 0.038)	1.35	SC: (2.0×10^{-7}, 0.7, 1.0)
−400 to −150 (DZ2)	ENE	(342.2, 0.2), 15.8	(2.80, 0.038)	0.41	SC: (1.0×10^{-7}, 0.6, 0.8)
	WNW	(209.8, 1.6), 14.6	(2.40, 0.038)	0.54	SC: (2.0×10^{-7}, 0.6, 0.6)
	N−S	(271.3, 3.8), 10.3	(2.80, 0.038)	0.39	SC: (1.0×10^{-7}, 0.4, 0.4)
	SubH	(238.9, 81.5), 12.7	(2.75, 0.038)	1.28	SC: (3.0×10^{-7}, 0.6, 0.6)
−650 to −400 (DZ3)	ENE	(342.2, 0.2), 15.8	(2.60, 0.038)	0.26	SC: (1.0×10^{-7}, 0.5, 0.7)
	WNW	(209.8, 1.6), 14.6	(2.40, 0.038)	0.36	SC: (1.0×10^{-7}, 0.5, 0.5)
	N−S	(271.3, 3.8), 10.3	(2.60, 0.038)	0.25	SC: (5.0×10^{-8}, 0.3, 0.3)
	SubH	(238.9, 81.5), 12.7	(2.70, 0.038)	0.41	SC: (5.0×10^{-8}, 0.4, 0.4)
−1 000 to −650 (DZ4)	ENE	(342.2, 0.2), 15.8	(2.90, 0.038)	0.35	SC: (5.0×10^{-9}, 0.6, 0.4)
	WNW	(209.8, 1.6), 14.6	(2.80, 0.038)	0.45	SC: (5.0×10^{-8}, 0.6, 0.4)
	N−S	(271.3, 3.8), 10.3	(2.95, 0.038)	0.08	SC: (5.0×10^{-9}, 0.6, 0.4)
	SubH	(238.9, 81.5), 12.7	(2.95, 0.038)	0.07	SC: (1.0×10^{-7}, 0.6, 0.4)

3.3 Catchment focussed model description

The catchment focussed model uses an ECPM concept to represent the larger-scale evolution of groundwater flow and solute transport over a catchment scale domain and for long time periods. It simulates both the past and the future evolution of groundwater composition due to changes in land elevation and varying composition of infiltrating water. Although the vaults are not explicitly present in this model, greater refinement is used around the vault locations to provide a more detailed ECPM representation and more accurate calculations of groundwater composition within this volume for near-field modelling. The catchment focussed model is also used to provide groundwater density and pressure values at specified time slices for use in the facility focussed model.

3.3.1 Model domain and discretisation

The model grid is approximately 21 km by 13 km in horizontal extent and extends from the ground surface to a depth of around 2.2 km. The upstream boundaries of the model correspond to significant surface-water divides (Rhén and Hartley 2009) and the downstream boundary represents the eventual shoreline position during the current temperate period (Figure 3-2). A facility volume is defined around the volume selected as an example for the SE-SFL, approximately 4.2 km across and 1.3 km deep. Within the facility volume, the finite element grid cells are 30 m square horizontally. Outside the facility volume the grid cells are a constant 60 m square horizontally. Around the vaults themselves there is an additional refined volume (the repository volume) that is 600 m square and 60 m thick that uses 5 m cells. Internal boundary conditions ensure continuity of pressure and flow where there are discontinuities in the grid at the boundaries of the embedded refined volumes. The cells are approximately cubes, except in the soil domain, where an approximately 1 m vertical cell size is used. The upper layers of the model are also mapped sub-parallel to the surface topography which causes some adjustment of cell height. There are around 2.2 million cells in the model in total. A close-up view of the grid is shown in Figure 3-3.

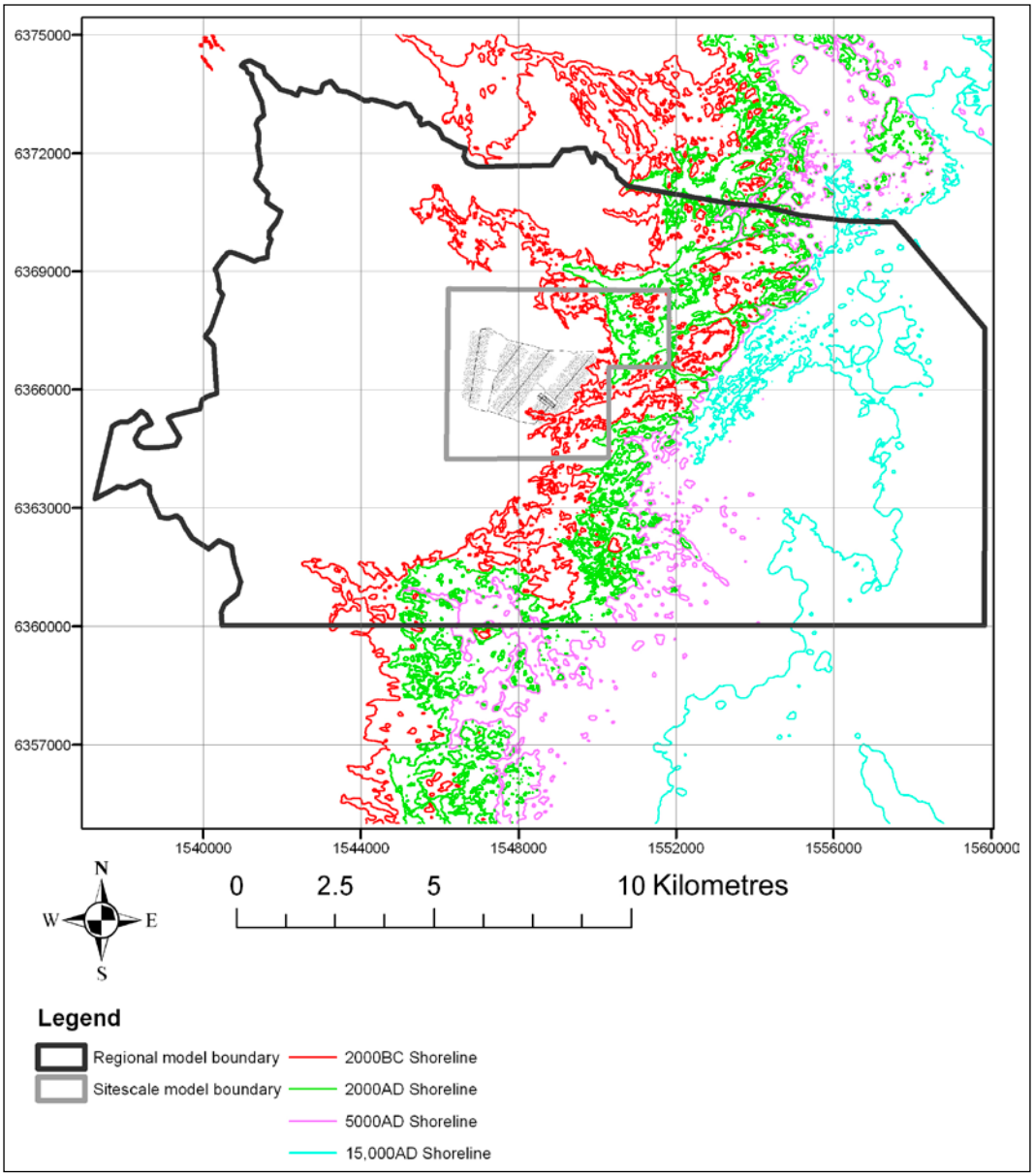

Figure 3-2. *Shoreline location at different times (red = 2000 BC, green = 2000 AD, purple = 5000 AD and blue = 15 000 AD) presented within the regional-scale area (black), now referred to as the catchment scale area (reproduced from Joyce et al. 2010). The Laxemar repository structures from the SR-Site comparison study are shown in grey within the site-scale model area, now referred to as the facility focussed model area.*

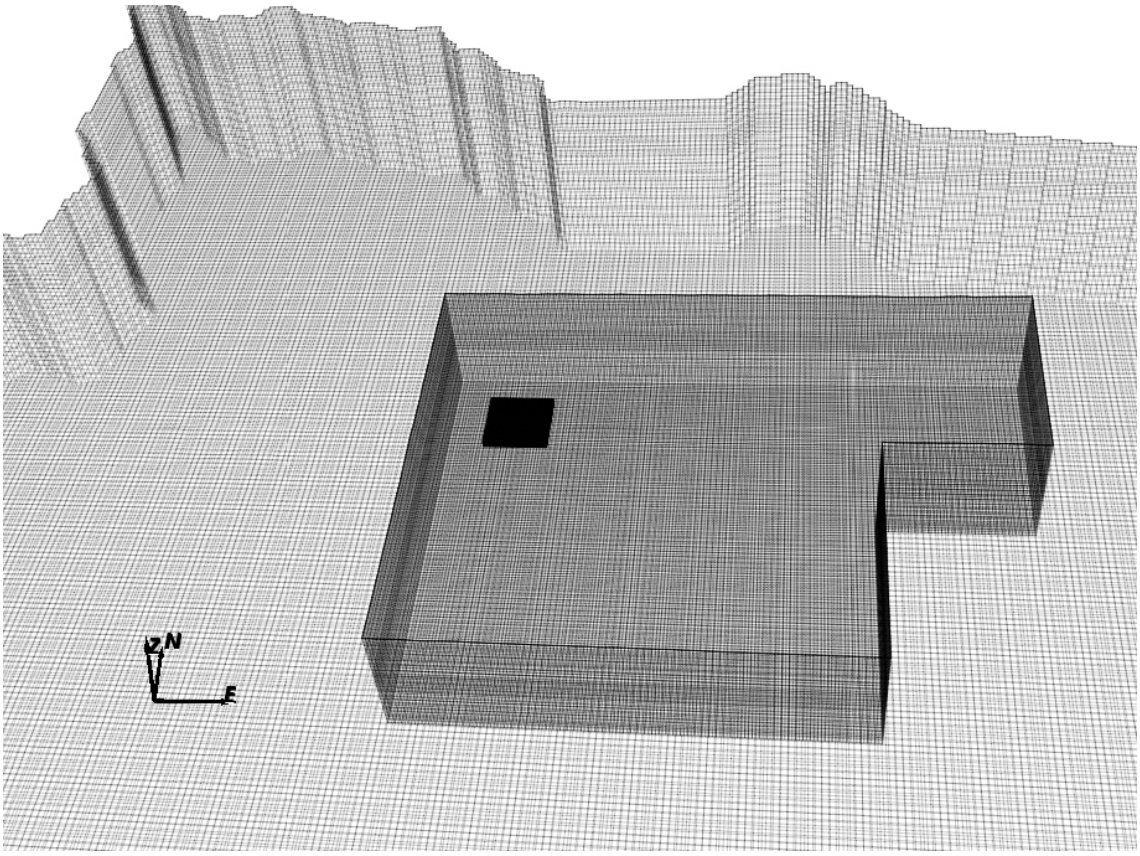

Figure 3-3. *Wireframe view of the facility volume (dark grey) within the catchment focussed model grid (light grey). The black square corresponds to the volume selected as an example for the SE-SFL.*

3.3.2 Hydraulic and transport properties

The catchment focussed model used an equivalent continuous porous medium (ECPM) representation, whose hydraulic properties were derived from the upscaling of a discrete fracture network (DFN) representing the Hydraulic Rock mass Domain (HRD), combined with the application of deformation zone properties using the implicit fracture zone method (IFZ), as described in Subsection 2.2.5. The DFN is the Elaborated Hydro-DFN described in Joyce et al. (2010) and summarised in Section 3.1. Only fractures with side lengths between 10 m and 1 km were included. The model includes the deformation zone model (HCD) with deterministic properties (including a depth trend) and realisation 1 of the HRD (denoted r1). Four additional realisations of the HRD (denoted r2 to r5) were also used. The vertical component of the upscaled hydraulic conductivity for one realisation is shown in Figure 3-4. The large-scale changes in hydraulic conductivity in different areas of the model are due to differences in properties between the four hydraulic rock mass domains. There is also a clear reduction in hydraulic conductivity with depth due to the fall off in fracture intensity.

For solute transport, the longitudinal dispersion length is set to 60 m in the catchment volume and 30 m in the facility volume. The transverse dispersion length is set to 20 m in the catchment volume and 10 m in the facility volume. The molecular diffusion coefficient of solute in the fractures is 1.0×10^{-9} m^2/s. Rock matrix diffusion is included with a matrix porosity (capacity factor), σ, of 8.0×10^{-3} and an intrinsic diffusion coefficient, D_i, of 5.0×10^{-14} m^2/s. Five finite volume cells per finite element cell were used to represent the matrix, with cell size increasing with distance into the matrix.

The Hydraulic Soil Domain (HSD) used for the catchment focussed model is consistent with that used in Joyce et al. (2010) and is represented by four 1 m deep layers. These layers are a simplified representation of the soil domain, whose properties are consistent, in an average sense, with the underlying stratigraphic model used in the near-surface hydrogeological modelling for SDM-Site Laxemar (Bosson et al. 2009). The vertical and horizontal components of the HSD hydraulic conductivity are different, i.e. the hydraulic conductivity is anisotropic. The horizontal component of the conductivity tensor is based on the arithmetic mean of the hydraulic properties of the original stratigraphy, whereas the vertical component is based on its harmonic mean. Further details can be found in Rhén et al. (2009).

An alternative HSD model used only for the facility focussed modelling has six layers that match the stratigraphy of the near-surface hydrogeological modelling for SDM-Site Laxemar (Bosson et al. 2009). This provides greater consistency between the bedrock hydrogeological models and the near-surface models when considering particle exit locations. An example slice through this HSD is shown in Figure 3-5. This approach was not used for the catchment focussed model, as the extra complexity is not appropriate when considering the large-scale, long term evolution of groundwater composition, which is not significantly influenced by the details of the near-surface hydrogeological representation.

For both HSD models, changes were made to the stratigraphy on a cell by cell basis compared to that used for the near-surface hydrogeological modelling. These changes are consistent with those used for SDM-Site Laxemar (Rhén et al. 2009, Rhén and Hartley 2009):

1. If the soil type is z1 and has a thickness of less than 5.0 m then it is changed to z6.
2. If the soil type is z6 and has a thickness greater than 5.0 m then it is changed to z1.

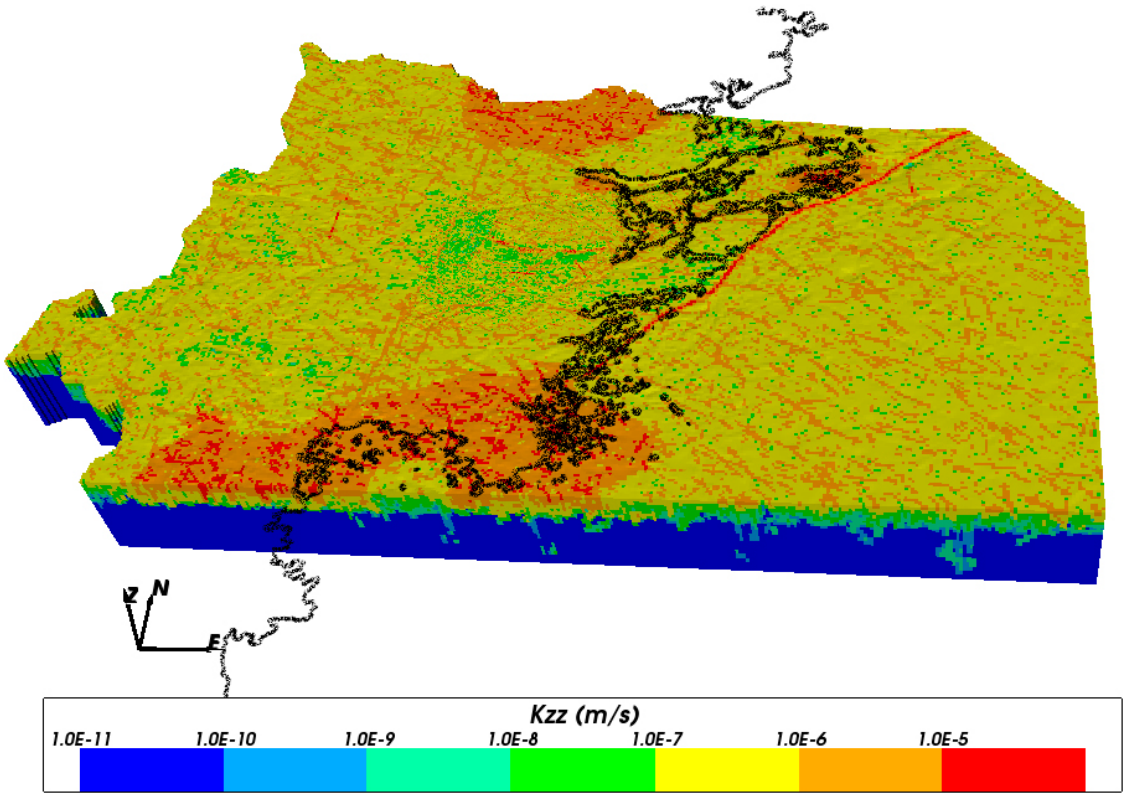

Figure 3-4. *Catchment focussed model coloured by the vertical component of hydraulic conductivity for realisation r1. The regolith has been removed. The present-day shoreline is shown in black.*

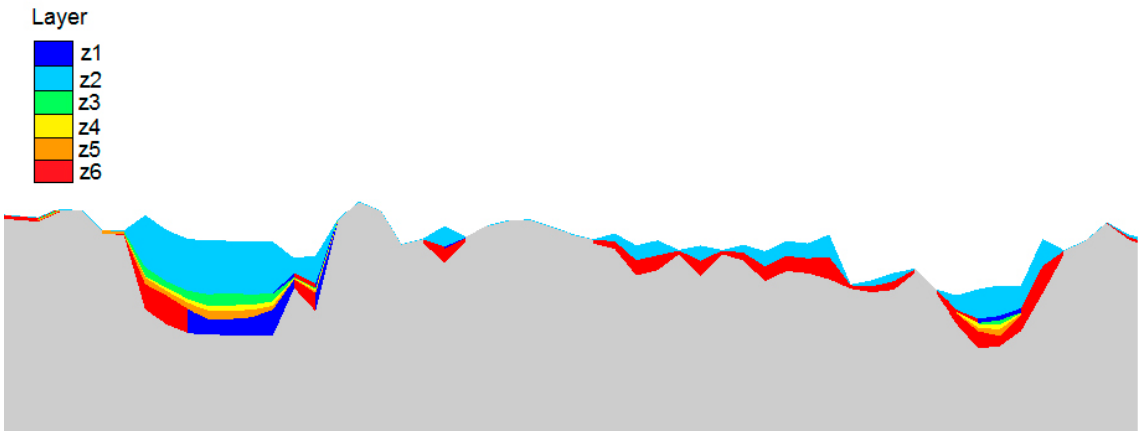

Figure 3-5. *HSD layers on a west-east slice above the repository volume. The bedrock is shown in grey. The vertical scale is exaggerated by a factor of 10.*

3.3.3 Near-surface hydrogeological modelling

To obtain suitable properties for the alternative HSD model that was used for the facility focussed modelling, a calibration exercise was carried out to try and match head measurements in groundwater monitoring (SSM) wells and percussion-drilled (HLX) boreholes. Both the mean head values and the time-varying head values were calibrated against using the catchment focussed ECPM model.

The top surface boundary condition used for the calibration leads to recharge or discharge of water depending on the calculated head relative to the ground surface elevation:

$$R = \begin{cases} R_0(x,y), & h \le z - \delta \\ -R_0(x,y)\dfrac{(h-z)}{\delta}, & h > z - \delta \end{cases} \tag{3-1}$$

where R is the groundwater recharge rate [m/s], R_0 is the maximum recharge rate [m/s], h is groundwater head [m], z is the surface elevation [m] and δ, is a small number representing the depth [m] over which the model switches from recharge to discharge (taken to be 0.05 m in this case). Where recharge occurs, the maximum recharge rate, R_0, is spatially and temporally varying. The recharge rates were supplied on a series of regular spatial grids exported at 5-day intervals from a surface hydrogeology model (Bosson et al. 2009). Where no recharge data were available for a location, the mean spatial recharge for the current time was used. The sides and the bottom of the model specify zero flux of water. The calculations for the calibration were freshwater only and so the salinity was zero throughout the model.

The transient evolution of groundwater pressure was simulated over the time period from October 2003 to December 2007 in 5-day time steps, i.e. 1540 days in total. The initial condition was the steady-state solution for the specified boundary conditions at the initial time. A variable saturation model was used, with the saturation, S, and relative permeability, k_r, varying according to a Van Genuchten relationship:

$$k_r = \sqrt{S_\alpha}\left[1 - \left(1 - S_\alpha^{\gamma/(\gamma-1)}\right)^{(\gamma-1)/\gamma}\right]^2 \tag{3-2}$$

$$S = S_{res} + (1 - S_{res})\left(\frac{1}{1 + \left({}^{-P_T}/_{P_E}\right)^{\gamma}}\right)^{(\gamma-1)/\gamma} \tag{3-3}$$

$$S_\alpha = \frac{S - S_{res}}{1 - S_{res}} \tag{3-4}$$

where γ is a constant, S_{res} is residual saturation [-], P_T is the total pressure [N/m^2], and P_E is the capillary entry pressure [N/m^2]. The parameters used are given in Table 3-6.

Table 3-6. Parameters for calculating variable saturation using a Van Genuchten model.

Parameter	Value
S_{res}	0.1
γ	3.0
P_E	4.0×10^4 N/m^2

The transient pressure response to temporal changes in recharge depends on the assigned values of permeability, storage coefficient and porosity Equation (2-5). Initially, these were set to values equivalent to those used in Bosson et al. (2009) for the HSD and to those used in Joyce et al. (2010) for the bedrock. The parameters were then varied to improve the match to the measured mean and transient heads at the locations of the HLX boreholes and SSM monitoring wells (shown in Figure 3-6 and Figure 3-7, respectively). Figure 3-6 also shows the location of core-drilled KLX boreholes not used in the calibration exercise.

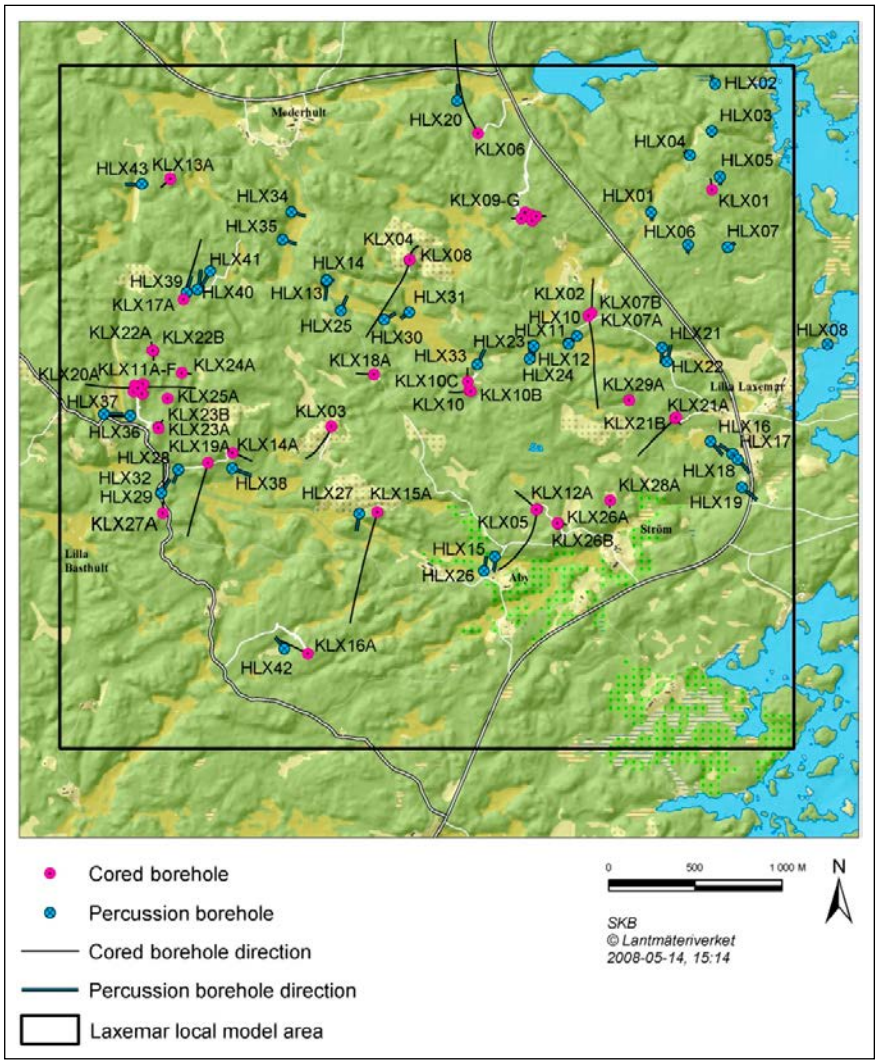

Figure 3-6. *Core-drilled (KLX) and percussion-drilled (HLX) boreholes within and close to the Laxemar local model area, now referred to as the facility focussed model area (reproduced from Figure 3-3 in Rhén and Hartley 2009).*

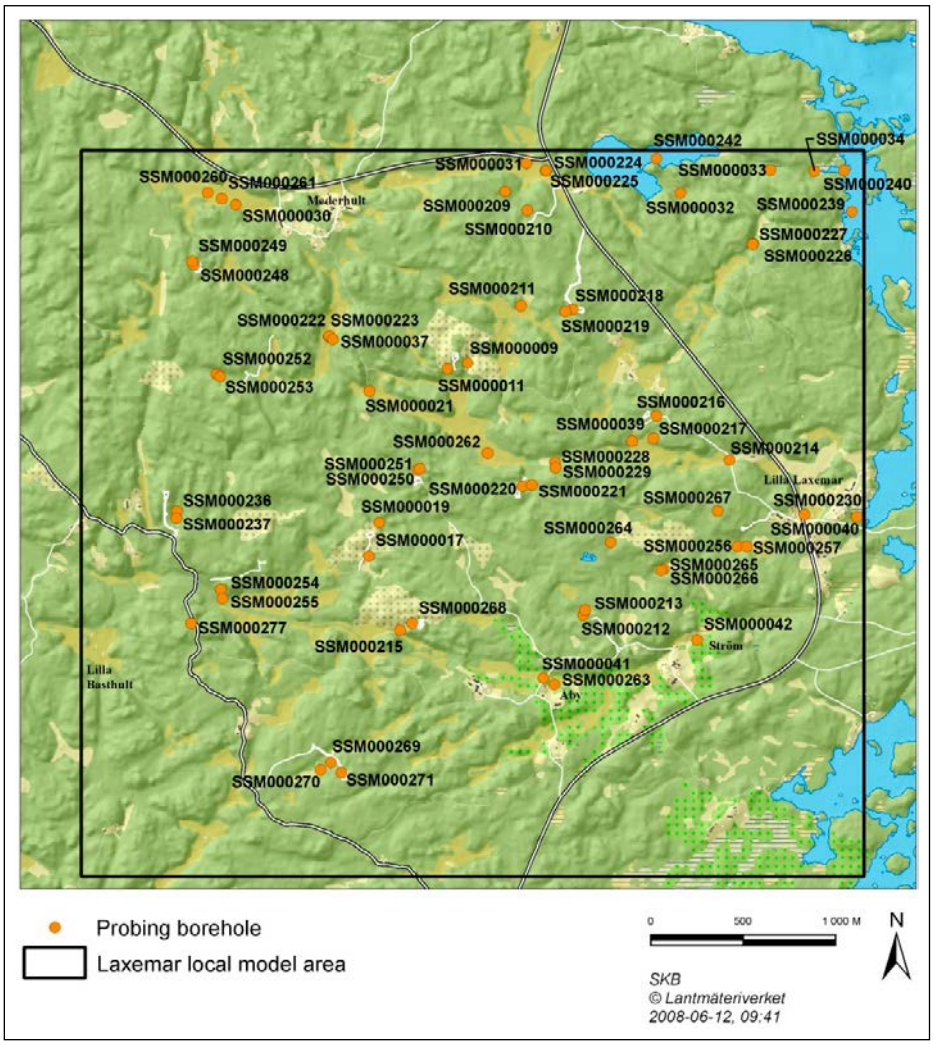

Figure 3-7. *Groundwater monitoring wells within and close to the Laxemar local model area, now referred to as the facility focussed model area (reproduced from Figure 3-5 in Rhén and Hartley 2009).*

3.3.4 Hydrogeochemical initial and boundary conditions

For simulating the catchment scale evolution of hydrogeochemistry, the initial conditions (see Figure 3-10) and boundary conditions used were the same as those in Joyce et al. (2010), except that reference water fractions were replaced by the equivalent mass fractions of the individual solutes given in Table 3-7.

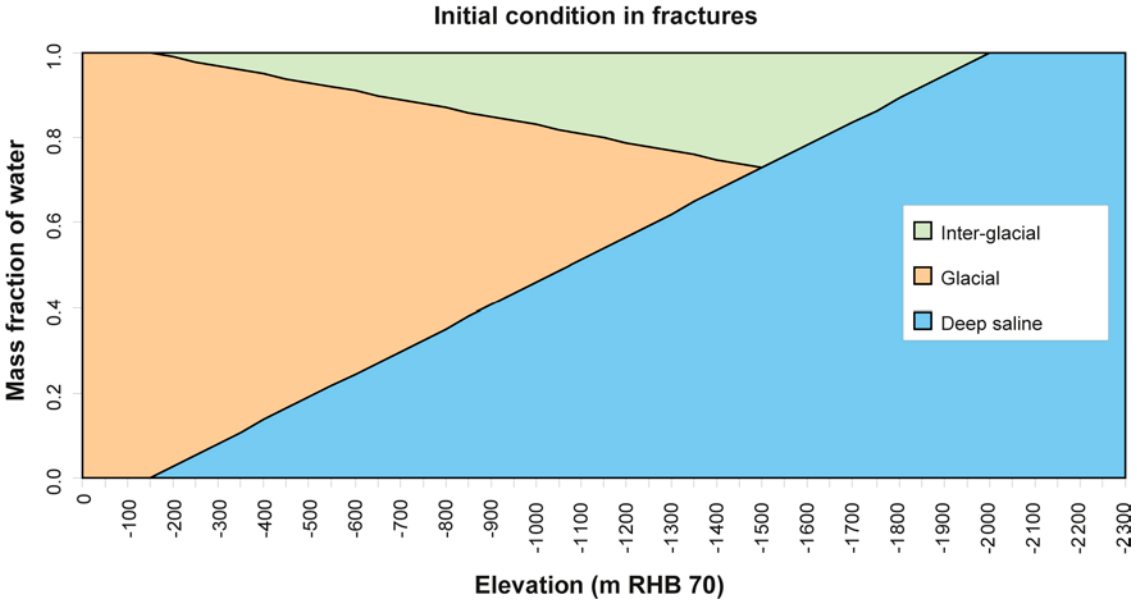

Figure 3-8. *Initial conditions for the fracture water at 8000 BC (reproduced from Rhén et al. 2009).*

Table 3-7. Relation of reference water compositions modified from Gimeno et al. (2010) to component mass fractions for implementation in ConnectFlow calculations.

	Deep Saline	Littorina	Altered Meteoric	Glacial	Inter−glacial
pH	8.000	7.952	7.842	9.300	7.909
pe	−4.448	−4.424	−1.046	−5.260	−3.160
Component mass fractions [kg/kgs]					
Al	1.847×10^{-10}	8.695×10^{-9}	5.477×10^{-9}	1.405×10^{-7}	7.753×10^{-9}
Br	3.080×10^{-4}	2.220×10^{-5}	0.000	0.000	3.430×10^{-5}
C	4.102×10^{-7}	1.931×10^{-5}	5.114×10^{-5}	1.023×10^{-6}	1.890×10^{-6}
Ca	1.836×10^{-2}	1.530×10^{-4}	7.150×10^{-6}	2.879×10^{-6}	1.585×10^{-3}
Cl	4.452×10^{-2}	6.641×10^{-3}	1.532×10^{-5}	7.963×10^{-7}	4.738×10^{-3}
F	1.523×10^{-6}	4.899×10^{-7}	3.850×10^{-6}	0.000	0.000
Fe	1.380×10^{-8}	7.861×10^{-7}	1.000×10^{-7}	4.469×10^{-8}	7.361×10^{-10}
K	2.980×10^{-5}	1.340×10^{-4}	2.970×10^{-6}	4.000×10^{-7}	4.001×10^{-6}
Li	4.417×10^{-6}	6.999×10^{-8}	1.100×10^{-8}	0.000	0.000
Mg	2.018×10^{-6}	4.479×10^{-4}	3.600×10^{-6}	1.000×10^{-7}	2.001×10^{-6}
Mn	1.333×10^{-7}	0.000	5.800×10^{-8}	0.000	0.000
Na	8.104×10^{-3}	3.673×10^{-3}	1.100×10^{-4}	1.700×10^{-7}	1.440×10^{-3}
S	2.879×10^{-4}	2.975×10^{-4}	1.195×10^{-5}	1.701×10^{-7}	1.252×10^{-4}
Si	2.298×10^{-6}	3.555×10^{-6}	3.801×10^{-6}	4.676×10^{-6}	3.620×10^{-6}
Sr	3.208×10^{-4}	2.680×10^{-6}	0.000	0.000	0.000

3.3.5 Evolution of hydrogeochemistry

Calculations of variable density groundwater flow and solute transport were carried out for the simulation period of 8000 BC to 60 000 AD in constant 20-year time steps. An efficient multi-component sequential iteration method was used to transport each component individually and partially decouple the transport and flow calculations within each individual time step, although changes in flow, composition and fluid density affect conditions in the next time step (Joyce et al. 2014). For those cases involving chemical reactions, the reactions were calculated at each time step. For reasons of efficiency, chemical reactions were only calculated at locations where the mass fraction of any component had changed by at least 2 % since the last time chemical reactions were calculated at that location. The 2 % calculation threshold was chosen, based on scoping simulations, to provide good efficiency without impacting the quality of the results.

A finite volume implementation of the rock matrix diffusion method was used for this study, which also allowed equilibration of chemical species to occur in the rock matrix. Five rock matrix cells, which increased linearly in size with distance from the fracture, were used for each model grid cell. Using smaller cells close to the fracture increases accuracy where the solute concentrations are changing most rapidly.

3.4 Facility focussed model description

The facility focussed model covers the same domain as the catchment focussed model, but replaces the facility volume around the vaults with a DFN representation. It also explicitly represents the repository structures within the model. The model allows detailed flows around the repository to be simulated, accounting for the structural constraints imposed by fractures. Particle tracking calculations are then used to obtain performance measures relevant to a safety assessment and to determine possible discharge locations for radionuclides released from the vaults.

3.4.1 Model domain and discretisation

The model grid covers the same domain as the catchment focussed model described in Subsection 3.3.1. A DFN replaces the ECPM in a facility scale volume, approximately 4.2 km across and 1.3 km deep, as shown in Figure 3-10 and Figure 3-11. This DFN is part of the same DFN used to generate the ECPM, but includes additional fractures with side lengths down to 0.7 m in the volume (280 m square and 83 m thick, shown in blue in Figure 3-9) immediately around the vaults within the repository volume. An increased resolution, with a 30 m horizontal cell size, is used for the ECPM part of the model, with further refinement added, where necessary, around the repository to represent the vault and tunnel geometry. The cells are approximately cubes, except when constrained by the vault or tunnel geometry and in the upper parts of the model. The upper layers of the model are mapped sub-parallel to the surface topography and to surfaces that define the boundaries between soil layers, as described in Subsection 3.3.2. This surface mapping causes some adjustment of cell height. A CPM representation is used for the vaults and tunnels, but planar surfaces are used to represent the more complicated geometry of the ramp and shaft, with properties equivalent to those of the backfilled structures (transmissivity equal to hydraulic conductivity multiplied by structure width) (Figure 3-12). There are around 7.3 million (E)CPM cells and 2.2 million fractures in the model in total. Fractures with side lengths greater than 20 m are tessellated into approximately 20 m tessellates. There are approximately 5 million fracture tessellates in total.

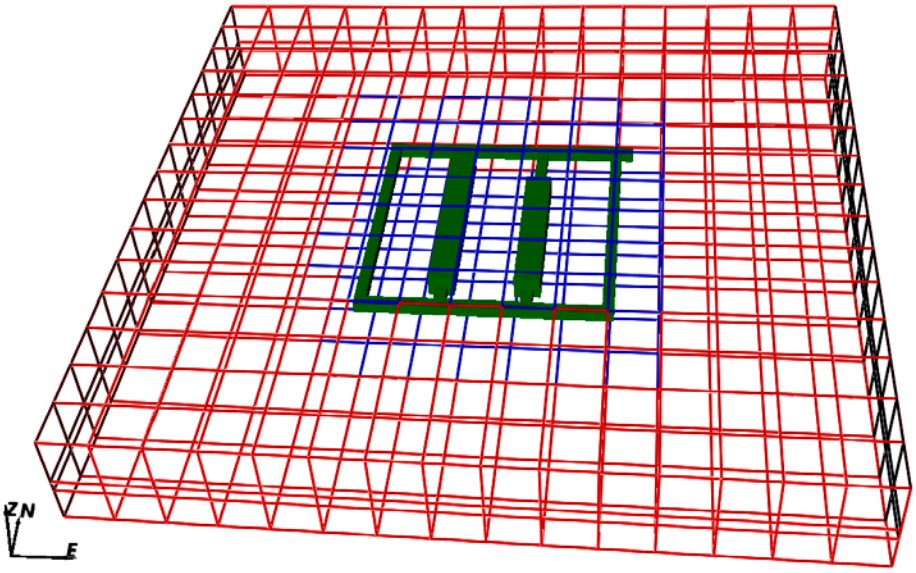

Figure 3-9. *Fracture generation region around the repository structures. Fractures with side lengths down to 0.7 m are generated in the blue region and down to 3.0 m within the red region. The vaults and tunnels are shown in green.*

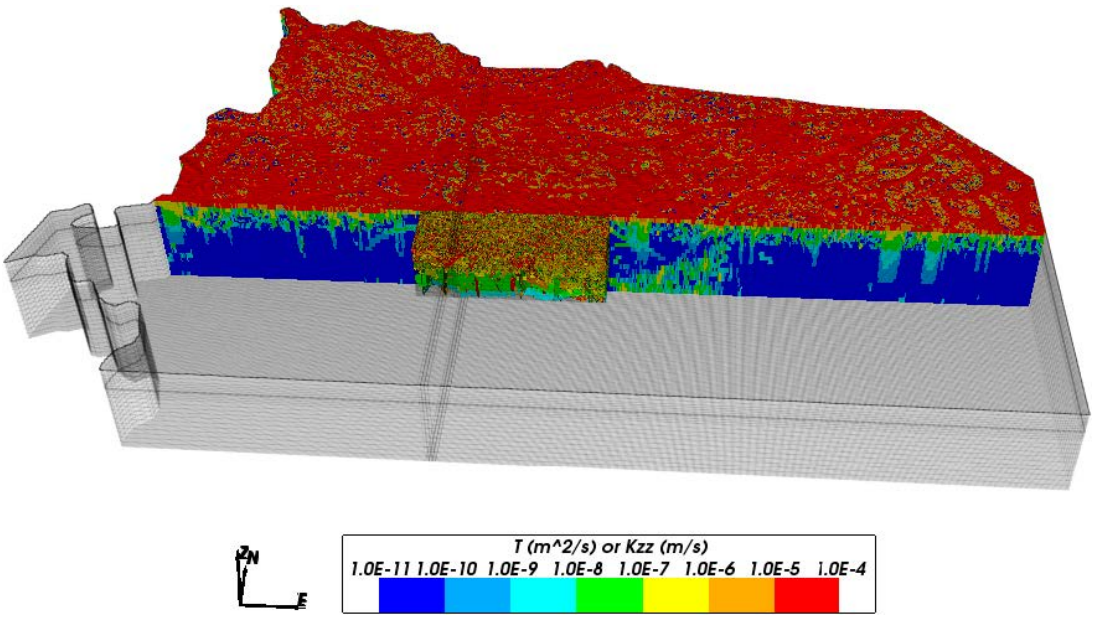

Figure 3-10. *Facility focussed model coloured by transmissivity [m^2/s] (for the DFN) or the vertical component of hydraulic conductivity [m/s] (for the ECPM). Some of the ECPM has been removed to reveal the DFN.*

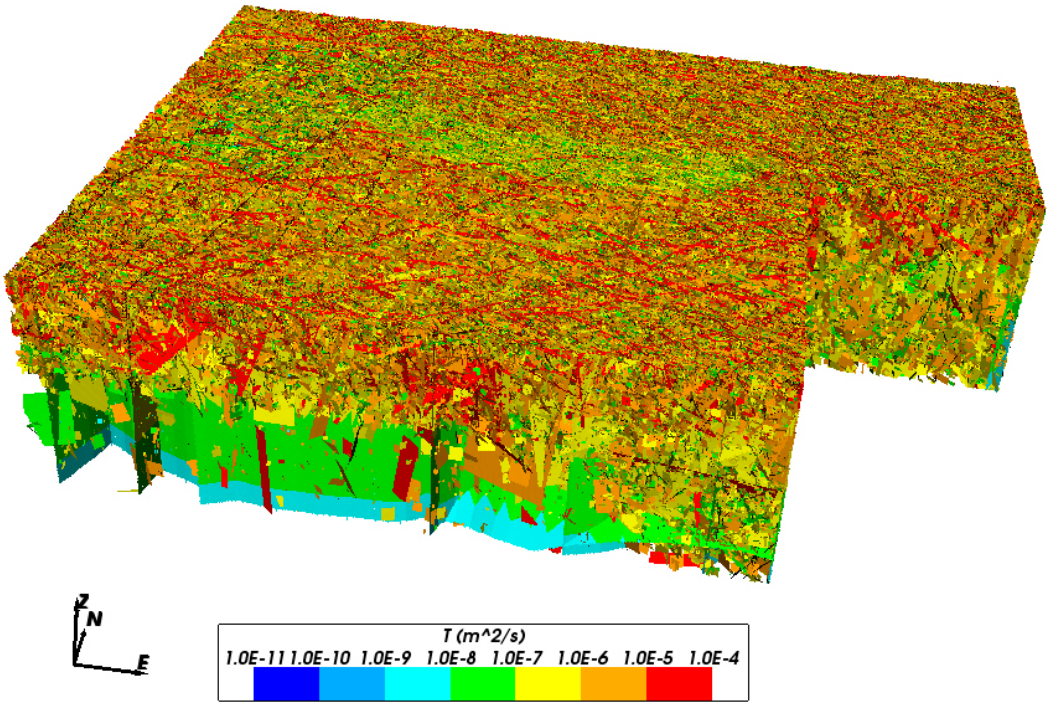

Figure 3-11. *Facility focussed DFN coloured by transmissivity [m^2/s].*

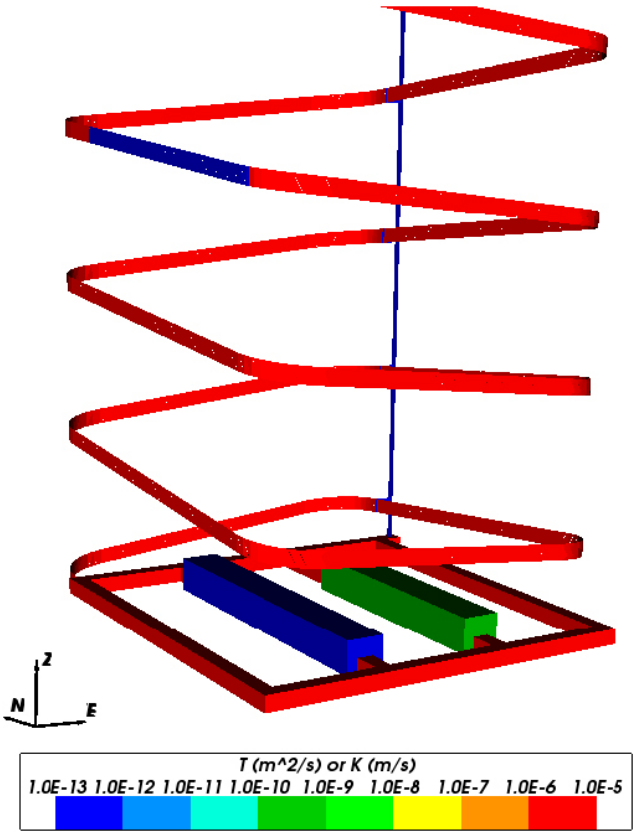

Figure 3-12. *Repository structures coloured by transmissivity [m^2/s] (for the ramp and shaft) or hydraulic conductivity [m/s] for the vaults and tunnels. The BHA vault (bentonite backfill) is blue and the BHK vault (concrete backfill) is green. A bentonite seal is shown in blue part way up the ramp.*

3.4.2 Hydraulic and transport properties

The facility focussed model uses a DFN representation of the fractured bedrock, embedded within an equivalent porous medium (ECPM) representation, whose hydraulic properties are derived from the upscaling of the DFN representing the Hydraulic Rock mass Domain (HRD), combined with the application of deformation zone properties using the implicit fracture zone method (IFZ), as described in Subsection 2.2.5. The DFN is the Elaborated Hydro-DFN described in Joyce et al. (2010) and summarised in Section 3.1. Fractures with side lengths between 10 m and 1 km are included throughout the model, with fractures down to 0.7 m around the vaults. Five realisations are used. The first uses an HCD with deterministic properties (including a depth trend) and realisation 1 of the HRD (denoted r1). Each of the other four is a different realisation of an HCD with stochastic properties and a realisation of the HRD (denoted r2 to r5) consistent with the approach used for the SR-Site site comparison project (Joyce et al. 2010). Heterogeneity within the deformation zones is likely to be an important influence on hydraulic properties and so stochastic variability is an important consideration for the HCD, as well as the HRD, for a DFN representation. The effect is not considered in the catchment focussed ECPM as the heterogeneity would be largely averaged out on the scale of the model cells. The use of a deterministic HCD for realisation r1, however, allows direct comparison between the DFN and ECPM representations. The HRD fractures with side lengths greater than 10 m are the same as those used for the catchment focussed model for the corresponding realisations. The properties of the ECPM are as described in Subsection 3.3.2.

The alternative HSD model was used for the facility focussed modelling, see Subsection 3.3.2. The properties of the soil types were calibrated, as described in Subsection 3.3.3, to give the values in Subsection 4.1.2. These correspond to Case 6_4c and are reproduced in Table 3-8. The soil types z1 to z6 represent the layers of the regolith. The bracketed types in Table 3-8 refer to sub-types that exist in parts of some layers. As part of the calibration, the hydraulic conductivity of the upper bedrock (above −150 m elevation) was increased by a factor of 50 in the ECPM parts of the model relative to the catchment focussed model. There is no corresponding modification of the properties of the DFN as these represent the fractured bedrock explicitly and have been separately calibrated against borehole data.

The hydraulic properties of the repository structures are given in Table 3-9. The bentonite seals are present at points in the ramp. A variant of Case 1 considers a degraded concrete backfill for the BHK vault with a hydraulic conductivity of 1.0×10^{-7} m/s.

Table 3-8. Calibrated HSD parameters for the facility focussed model, where K_h and K_v are the horizontal and vertical components of hydraulic conductivity, respectively and ϕ is the kinematic porosity.

Soil type	K_h [m/s]	K_v [m/s]	ϕ [−]
z1	4.0×10^{-2}	4.0×10^{-3}	0.75
z1 (peat)	1.5×10^{-4}	1.5×10^{-5}	1.0
z1 (shingle)	5.0×10^{-1}	5.0×10^{-2}	1.0
z1 (sand)	2.5×10^{-1}	2.5×10^{-2}	1.0
z2	1.5×10^{-4}	1.5×10^{-5}	1.0
z3	5.0×10^{-6}	5.0×10^{-7}	0.15
z3 (gyttja)	5.0×10^{-7}	2.5×10^{-7}	0.15
z4	5.0×10^{-1}	5.0×10^{-2}	1.0
z4 (glaciofluvial sediments)	2.5×10^{-2}	2.5×10^{-3}	1.0
z4 (postglacial sand)	1.5×10^{-1}	1.5×10^{-2}	1.0
z4 (postglacial gravel)	5.0×10^{-1}	5.0×10^{-2}	1.0
z4 (artificial fill)	2.0×10^{-3}	2.0×10^{-4}	0.25
z5	5.0×10^{-7}	5.0×10^{-8}	0.15
z6	2.0×10^{-3}	2.0×10^{-4}	0.25

Table 3-9. Hydraulic properties of the repository structures, where K is the hydraulic conductivity and ϕ is the kinematic porosity.

Material	K [m/s]	ϕ [−]
Access tunnel backfill	1.0×10^{-5}	0.30
BHK vault backfill	8.3×10^{-10}	0.11
BHA vault backfill	1.0×10^{-13}	0.43
Bentonite seals	1.0×10^{-13}	0.43

3.4.3 Initial and boundary conditions

The initial conditions for the facility focussed model are the pressure and density values imported from the catchment focussed model for the relevant time slice and realisation and interpolated onto the fractures and (E)CPM cells.

The boundary conditions fix the pressure on the top surface of the model to the initial values. Additional boundary conditions ensure consistency of pressure and flux between the DFN and (E) CPM regions of the model. There is no flow of groundwater through the sides and bottom of the model. The top surface boundary condition assumes constant conditions for the duration of the period considered for the particle tracking. This simplification makes the calculations more practicable and is unlikely to affect the results for the particles with the shortest travel times, which are the ones of most relevance to a safety assessment. The no-flow boundary conditions on the sides are consistent with the catchment focussed model and correspond to natural flow-divides. The no-flow bottom boundary is a reasonable approximation given the very limited groundwater flow at depth.

3.4.4 Calculation of steady-state pressure and particle tracking

The facility focussed model calculates a steady-state, density dependent, pressure solution that is consistent with the applied boundary conditions and initial conditions that are imported for each time slice. Due to the computational demands of these simulations, it was only possible to carry out the calculations for a limited number of time slices during the timescale of interest. The resulting groundwater flow field is consistent with the boundary pressures and the spatial distribution of the imported groundwater densities. Fully saturated, closed repository conditions were assumed.

Particles were released from the vault surfaces at each location where a fracture intersects the vault. Ten particles per vault intersection were released. The particles were tracked from the vaults to the ground surface using the approach described in Subsection 2.2.10. Performance measures were calculated as described in Subsection 2.2.11. In addition, particles were released from the same locations and tracked backwards through the flow field to the recharge locations for groundwater entering the vaults. Only particles at locations where the flow direction is from the vault to the fracture (or *vice versa* for backward particle tracks) are retained. Additionally, it is possible for some particles to become stuck before they exit the model due to numerical reasons (i.e. very small flows cannot be resolved with sufficient numerical accuracy), particularly in stagnant flow regions, for instance where there are dead-end clusters of fractures with no through-flow of groundwater.

4 Results

4.1 Calibration of near-surface hydrogeological modelling

A sensitivity analysis was performed using the catchment focussed hydrogeological model to improve the match to the measured mean and transient heads at the locations of the groundwater monitoring (SSM) wells and percussion drilled (HLX) boreholes. Maps of the locations of the HLX boreholes (and core-drilled KLX boreholes) and SSM wells at the Laxemar site are shown in Figure 3-6 and Figure 3-7, respectively. In the analysis, the permeability, specific storage coefficient and porosity were varied in the soil and rock The specific storage coefficient and porosity only affect the transient calibration, both having an effect on the amplitude and the phase of the head response with time, but the porosity is more important in the partially saturated zone and the specific storage coefficient has more of an effect in the saturated zone. The other properties, including those relating to saturation, were not varied. As a starting point, the parameter settings used in Joyce et al. (2010) were selected, as shown in Table 4-2 and Table 4-3. The catchment focussed model for the calibration uses the alternative, layered, HSD representation described in Subsection 3.3.2. Although this HSD representation was not used in the catchment focussed modelling of the evolution of groundwater composition, it was used for the more detailed facility focussed modelling.

4.1.1 Presentation of results

The results of the near-surface hydrogeological calibration are presented as average groundwater level plots across all boreholes and transient head plots for selected boreholes. In all plots, a comparison between measured heads, either averaged or transient, and the calculated head values, is made. In addition, the calibrated properties are compared to the original SR-Site model properties and presented in tables (see Table 4-2 and Table 4-3).

4.1.2 Sensitivity analysis

Table 4-1 shows a description and hydraulic properties of the sensitivity cases presented in the report. For each case, the analysed sensitivity parameter is specified and the domain (HSD, HCD or HRD) to which it was applied. In addition, the magnitude of the parameter change compared to the SR-Site model (here called the base case) is specified together with the expected effect on model results. During the sensitivity analysis, many cases (approximately 90) were completed, but only the most relevant are reported here (Table 4-1). Note that the cases seek to examine the sensitivity of the model calibration to the hydraulic parameters rather than to necessarily obtain the best fit, and so parameter values may fall outside physically appropriate ranges in some cases.

Table 4-2 and Table 4-3 show the properties used in the SR-Site comparison project (Joyce et al. 2010), and adopted for the catchment focussed modelling of groundwater composition for SFL in the current work, and the properties obtained for what is considered the best calibration (Case 6_4c), and adopted for the SFL facility focussed modelling (described in Section 3.4), Note that the SDM (Rhén and Hartley 2009), and later SR-Site, increased the porosity of the HSD by a calibration factor of 5 (up to a maximum of 1.0) for each soil type. This factor 5 is retained for the current work and is included in the porosity values in Table 4-3. Due to the non-linearities introduced into the calculations by variable saturation, achieving numerical convergence is challenging and in some cases the desired convergence criteria were not fully achieved. Only cases that converged successfully were selected for reporting. Cases that showed very little or no effect on the model results are also not reported. The selected cases include the ones giving the best match (calibration) to measured heads, both averaged and transient. In addition, a set of sensitivities are selected to demonstrate the effect of changing a specific parameter and/or domain.

Generally, when properties are applied to the HSD it is done uniformly for all soils, i.e. no difference is made between the different soil layers or soil materials within layers. Similarly, when the permeabilities are changed, generally no attempt is made to separate the horizontal (K_h) and vertical (K_v) permeabilities. Only in a few sensitivity cases, which are not presented here, were tests performed changing only one of the principal permeability components, but the results were not improved significantly. The reason for this somewhat simplified analysis was to reduce the number of sensitivity cases initially, considering that a more rigorous calibration attempt was not in the scope of this project.

The hydrogeological model has a depth trend applied to the rock properties. The uppermost layer of the bedrock, assigned to material types HCD1 (for cells intersected by deformation) zones or HRD1 (for cells between deformation zones) reaches from the bottom of the soil layers down to a depth of −150 metres above sea level. This meant that changing the parameter values in these domains affected quite a large volume of the model and hence potentially had a great impact on the measured heads. Note that due to the casing of the upper part of the KLX boreholes, the upper ~50 m of bedrock is not well characterised and so there is some uncertainty associated with the hydraulic parameters assigned.

Table 4-1. Description and hydraulic properties of presented sensitivity cases.

Case name	Sensitivity	Domain	Changes made compared to SR-Site	Expected effect on model results
Case_6_4c	Permeability and Storage	HSD HCD1 HRD1	• Kh and Kv increased by a factor of 50. • Ss set to 1.0×10^{-12} m^{-1}.	Increasing the permeability in the top layers of the model is expected to lower the calculated heads and thereby improve the calibration on measured heads in both SSM wells and HLX boreholes. Decreasing the storage is expected to improve the transient head response in the boreholes by making the model respond faster to changes in recharge.
Case_6_7c	Porosity	HSD	• Same as Case_6_4c but with porosity decreased by a factor of 50.	Decreasing the porosity in the HSD is expected to improve the transient head response mainly in the shallower SSM wells by making the model respond faster to changes in recharge.
Case_8_1c	Permeability	HSD	• Kh and Kv increased by a factor of 50.	Increasing the permeability in the soil layers of the model is expected to lower the calculated heads and thereby improve the calibration on measured heads, in particular for the shallower wells and boreholes.
Case_8_2c	Permeability	HCD1	• Kh and Kv increased by a factor of 50.	Increasing the permeability in the top hydraulic conductor domain of the model (0 to −150 m) is expected to lower the calculated heads and thereby improve the calibration on measured heads, in particular for the deeper boreholes.
Case_8_3c	Permeability	HRD1	• Kh and Kv increased by a factor of 50.	Increasing the permeability in the top hydraulic rock domain of the model (0 to −150 m) is expected to lower the calculated heads and thereby improve the calibration on measured heads, in particular for the deeper boreholes.
Case_8_4c	Storage	HSD HCD1 HRD1	• Ss set to 1.0×10^{-12} m^{-1}.	Decreasing the storage is expected to improve the transient head response in the boreholes by making the model respond faster to changes in recharge.

Table 4-2. Hydraulic properties for SR-Site and Case 6-4c, where K_h and K_v are the horizontal and vertical components of hydraulic conductivity, respectively.

	SR-Site		Case 6_4c	
Material	**K_h [m/s]**	**K_v [m/s]**	**K_h [m/s]**	**K_v [m/s]**
z1	8.0×10^{-4}	8.0×10^{-5}	4.0×10^{-2}	4.0×10^{-3}
z1 (peat)	3.0×10^{-6}	3.0×10^{-7}	1.5×10^{-4}	1.5×10^{-5}
z1 (shingle)	1.0×10^{-2}	1.0×10^{-3}	5.0×10^{-1}	5.0×10^{-2}
z1 (sand)	5.0×10^{-3}	5.0×10^{-4}	2.5×10^{-1}	2.5×10^{-2}
z2	3.0×10^{-6}	3.0×10^{-7}	1.5×10^{-4}	1.5×10^{-5}
z3	1.0×10^{-7}	1.0×10^{-8}	5.0×10^{-6}	5.0×10^{-7}
z3 (gyttja)	1.0×10^{-8}	5.0×10^{-9}	5.0×10^{-7}	2.5×10^{-7}
z4	1.0×10^{-2}	1.0×10^{-3}	5.0×10^{-1}	5.0×10^{-2}
z4 (glaciofluvial sediments)	5.0×10^{-4}	5.0×10^{-5}	2.5×10^{-2}	2.5×10^{-3}
z4 (postglacial sand)	3.0×10^{-3}	3.0×10^{-4}	1.5×10^{-1}	1.5×10^{-2}
z4 (postglacial gravel)	1.0×10^{-2}	1.0×10^{-3}	5.0×10^{-1}	5.0×10^{-2}
z4 (artificial fill)	4.0×10^{-5}	4.0×10^{-6}	2.0×10^{-3}	2.0×10^{-4}
z5	1.0×10^{-8}	1.0×10^{-9}	5.0×10^{-7}	5.0×10^{-8}
z6	4.0×10^{-5}	4.0×10^{-6}	2.0×10^{-3}	2.0×10^{-4}
HCD1	upscaled	upscaled	upscaled × 50	upscaled × 50
HRD1	upscaled	upscaled	upscaled × 50	upscaled × 50

Table 4-3. Hydraulic properties for SR-Site and Case 6-4c, where ϕ is the kinematic porosity and S_s is the specific storage coefficient.

	SR−Site		Case 6_4c	
Material	**ϕ [−]**	**S_s [m^{-1}]**	**ϕ [−]**	**S_s [m^{-1}]**
z1	0.75	1.0×10^{-3}	0.75	1.0×10^{-12}
z1 (peat)	1.0	5.0×10^{-2}	1.0	1.0×10^{-12}
z1 (shingle)	1.0	2.5×10^{-2}	1.0	1.0×10^{-12}
z1 (sand)	1.0	2.5×10^{-2}	1.0	1.0×10^{-12}
z2	1.0	5.0×10^{-2}	1.0	1.0×10^{-12}
z3	0.15	6.0×10^{-3}	0.15	1.0×10^{-12}
z3 (gyttja)	0.15	6.0×10^{-3}	0.15	1.0×10^{-12}
z4	1.0	2.5×10^{-2}	1.0	1.0×10^{-12}
z4 (glaciofluvial sediments)	1.0	2.5×10^{-2}	1.0	1.0×10^{-12}
z4 (postglacial sand)	1.0	2.5×10^{-2}	1.0	1.0×10^{-12}
z4 (postglacial gravel)	1.0	2.5×10^{-2}	1.0	1.0×10^{-12}
z4 (artificial fill)	0.25	1.0×10^{-3}	0.25	1.0×10^{-12}
z5	0.15	2.5×10^{-2}	0.15	1.0×10^{-12}
z6	0.25	1.0×10^{-3}	0.25	1.0×10^{-12}
HCD1	upscaled × 5	1.0×10^{-12}	upscaled × 5	1.0×10^{-12}
HRD1	upscaled × 5	1.0×10^{-12}	upscaled × 5	1.0×10^{-12}

4.1.3 Average groundwater levels

In Figure 4-1 and Figure 4-2, a comparison of measured heads in percussion drilled boreholes (HLX) with results for the base case, is presented. The 77 HLX boreholes are divided into two groups in order to improve visibility in the presentation. The field data are plotted as mean point water heads in the bedrock with error bars to show the range of values at different measurement times. The figures clearly show that the modelled heads (blue markers), based on soil properties used in the SR-Site study (here called the base case) are consistently higher than the measured point water heads (red markers) in the bedrock. An over-prediction of head was also found in SDM-site (Rhén and Hartley 2009).

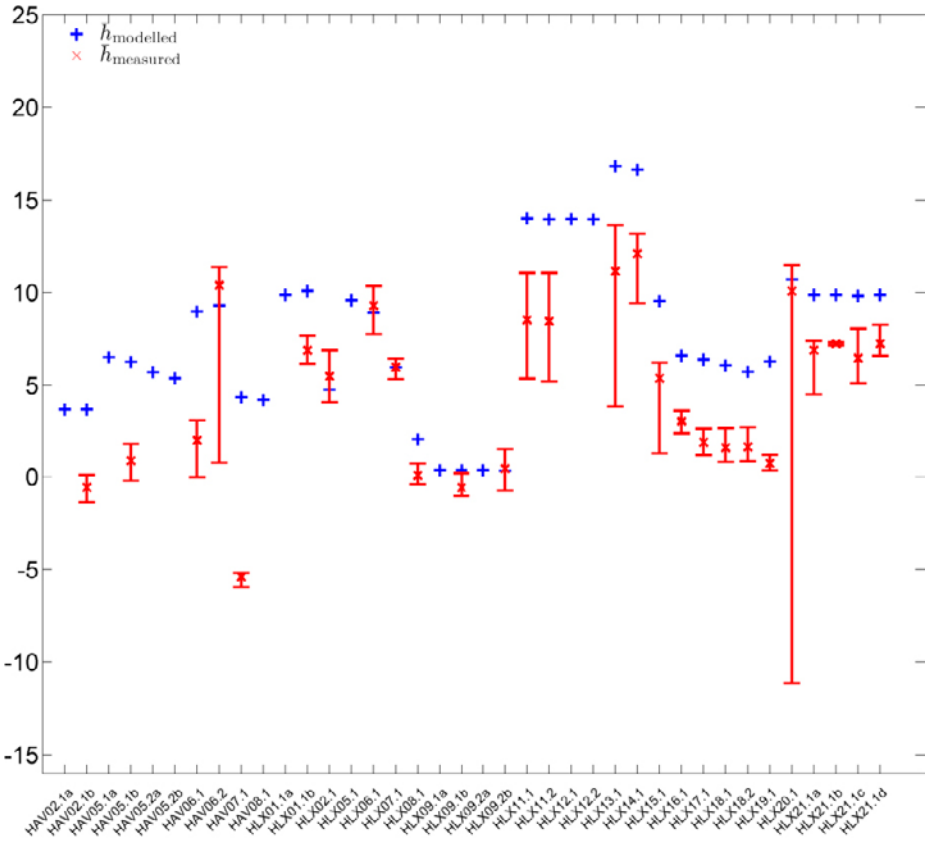

Figure 4-1. *Comparison of measured heads in the first set of percussion-drilled boreholes (HLX) with the results from the base case. The field data are plotted as mean point water heads in the bedrock with error bars to show the range of values at different measurement times.*

In Appendix A, Table A-1 and Table A-2 show the calculated mean absolute error (MAE) and mean error (ME) for each HLX borehole for the base case. The head difference varies greatly between the different boreholes, but generally reaches up to 5 m and in a few cases even more. For almost all boreholes the calculated ME is negative, confirming that the modelled heads are higher that the measured. The fact that MAE is equal to the absolute value of ME, in many boreholes, only shows that the modelled head falls outside the entire range of measured head values. The mean head difference for all HLX boreholes is −3.5 m.

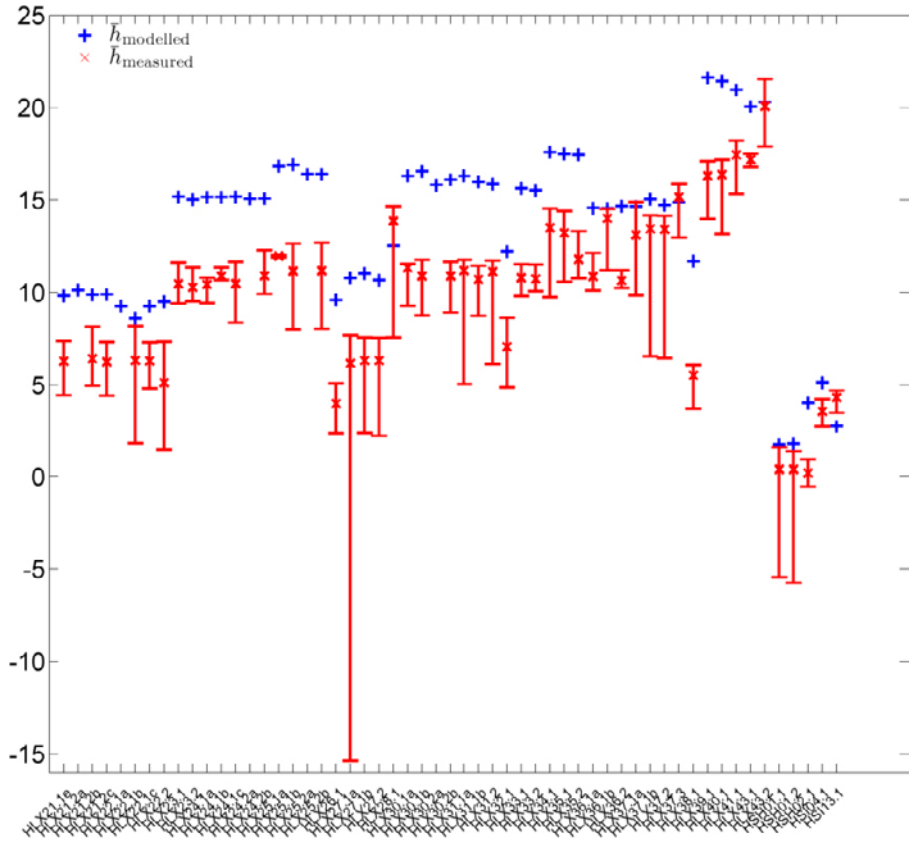

Figure 4-2. *Comparison of measured heads in the second set of percussion-drilled boreholes (HLX) with the results from the base case. The field data are plotted as mean point water heads in the bedrock with error bars to show the range of values at different measurement times.*

In Figure 4-3 and Figure 4-4, a comparison of measured heads in groundwater monitoring wells (SSM) with results for the base case, is presented. The 76 SSM wells are divided into two groups of 38 well each to improve visibility in the presentation. The field data are plotted as mean point water heads in the soil with error bars to show the range of values at different measurement times. The ground elevation (black line) and bedrock elevation (green line) are shown for reference. Again, the figures show that the modelled heads (blue markers), using the SR-Site properties, are consistently higher than the measured point water heads (red markers) in the soil.

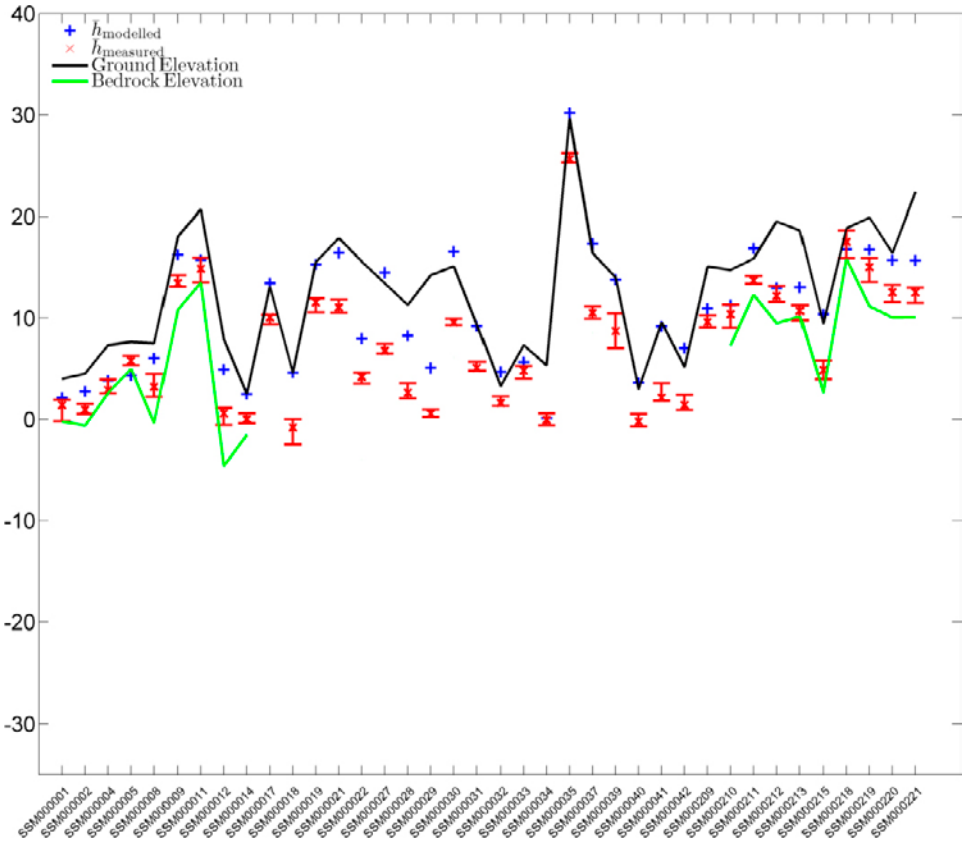

Figure 4-3. *Comparison of measured heads in the first set of groundwater monitoring wells (SSM) with the results from the base case. The field data are plotted as mean point water heads in the soil with error bars to show the range of values at different measurement times. The ground elevation (black line) and bedrock elevation (green line) are shown for reference.*

For a small number of wells, the modelled heads appear to be a little (less than 1 m) above the ground elevation. This is an effect of the rather coarse discretisation of the top surface. The borehole coordinates are accurate, but the top surface is represented using a 30 by 30 m grid (in the x and y direction) with the corner node elevations of the surface elements interpolated from a DEM on 20 m scale. This inevitably leads to discrepancies between reality and the model representation, in particular when the estimated elevation point does not coincide with the element corners. However, this issue is only likely to be significant at locations where the surface elevation is changing rapidly, i.e. at a steep incline.

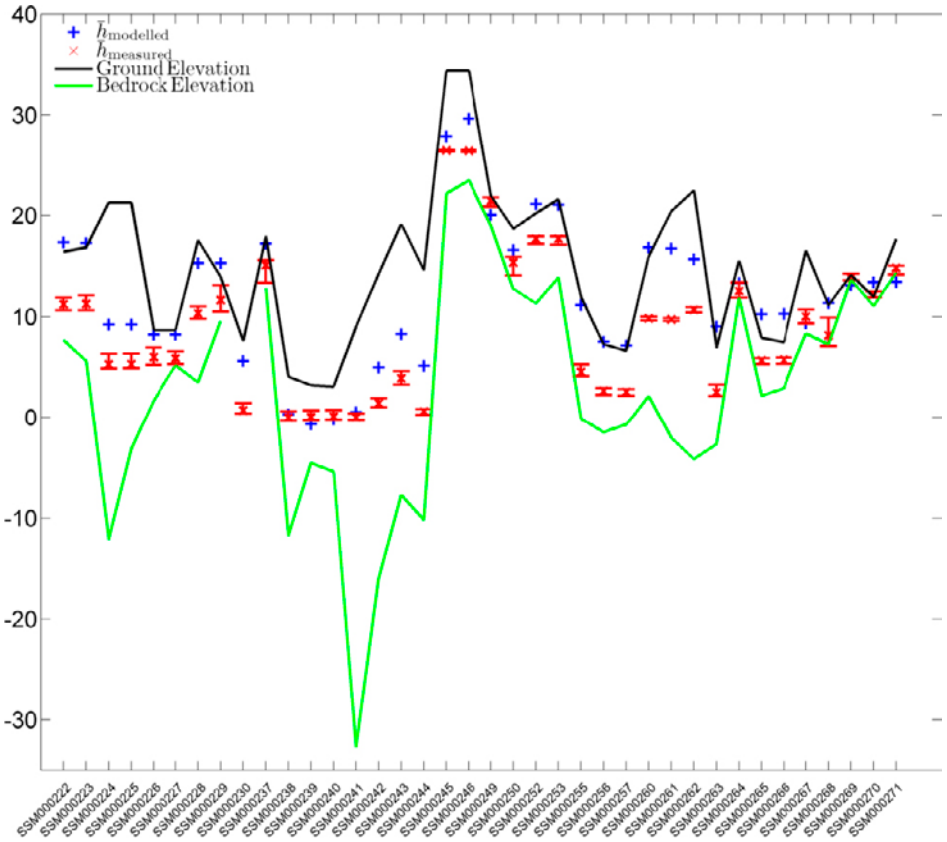

Figure 4-4. *Comparison of measured heads in the second set of groundwater monitoring wells (SSM) with the results from the base case. The field data are plotted as mean point water heads in the soil with error bars to show the range of values at different measurement times. The ground elevation (black line) and bedrock elevation (green line) are shown for reference.*

In Appendix A, Table A-3 and Table A-4 show the calculated mean absolute error (MAE) and mean error (ME) for each SSM well for the base case. The head difference varies more between the SSM wells than between the HLX boreholes, but the range is broadly the same and the head difference generally lies within 5 m with a few exceptions. For almost all boreholes, the calculated ME is negative, confirming that the modelled heads are higher than the measured. The mean head difference for all SSM wells is −3.0 m.

In Figure 4-5 through Figure 4-8, the corresponding results are shown for Case 6_4c, which, among the sensitivity cases that were performed, is considered to be the overall best match to measured values in the soil and rock, both averaged and transient (shown later in the report). The figures clearly show that the heads are considerably lower than in the base case. Since the changes made to the SR-Site properties are applied uniformly for all soil types together, it is difficult to achieve borehole specific optimisation. Instead, the heads tend to change similarly and in the same direction for all boreholes.

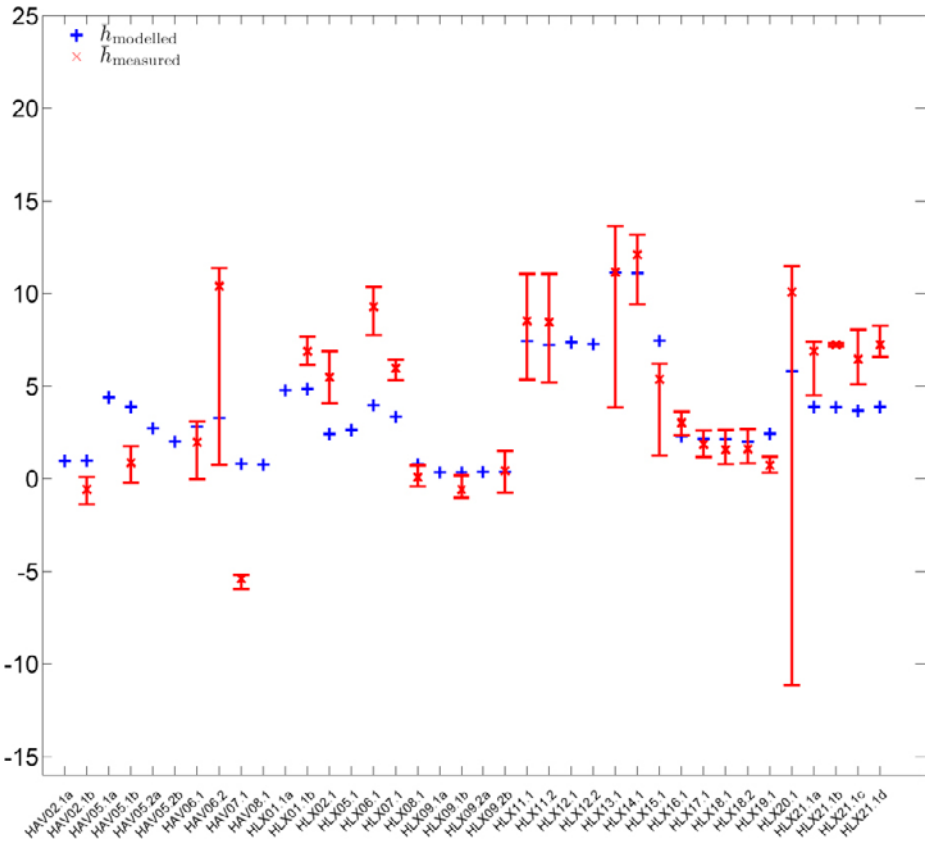

Figure 4-5. *Comparison of measured heads in the first set of percussion-drilled boreholes (HLX) with the results of Case 6_4c. The field data are plotted as mean point water heads in the bedrock with error bars to show the range of values at different measurement times.*

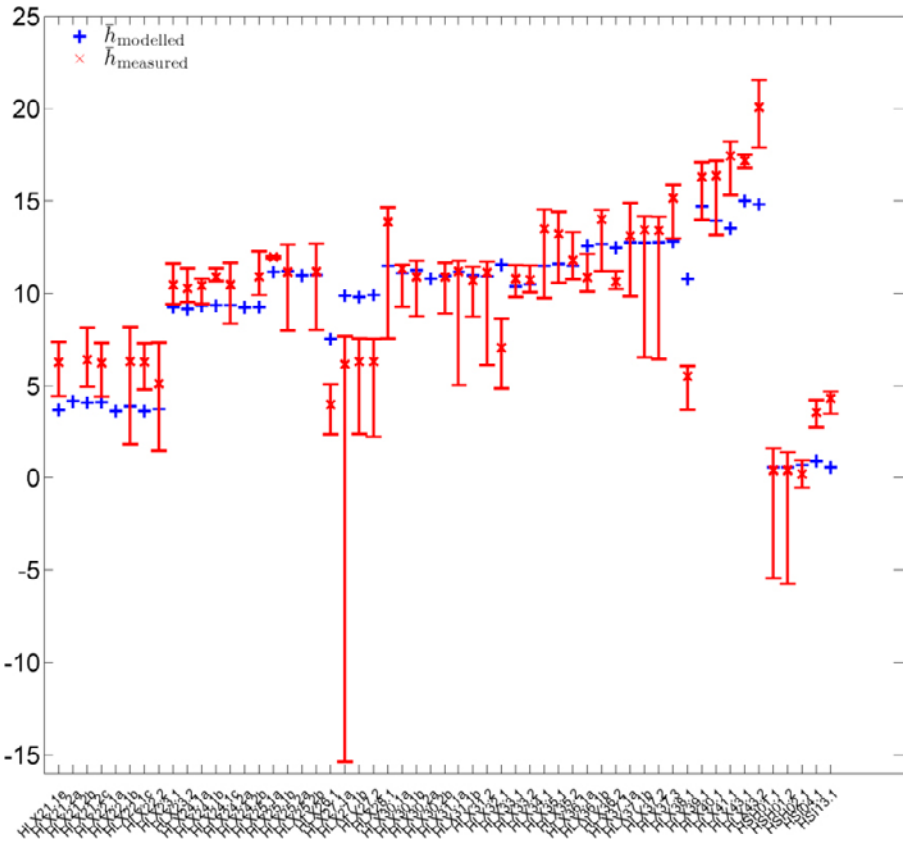

Figure 4-6. *Comparison of measured heads in the second set of percussion-drilled boreholes (HLX) with the results of Case 6_4c. The field data are plotted as mean point water heads in the bedrock with error bars to show the range of values at different measurement times.*

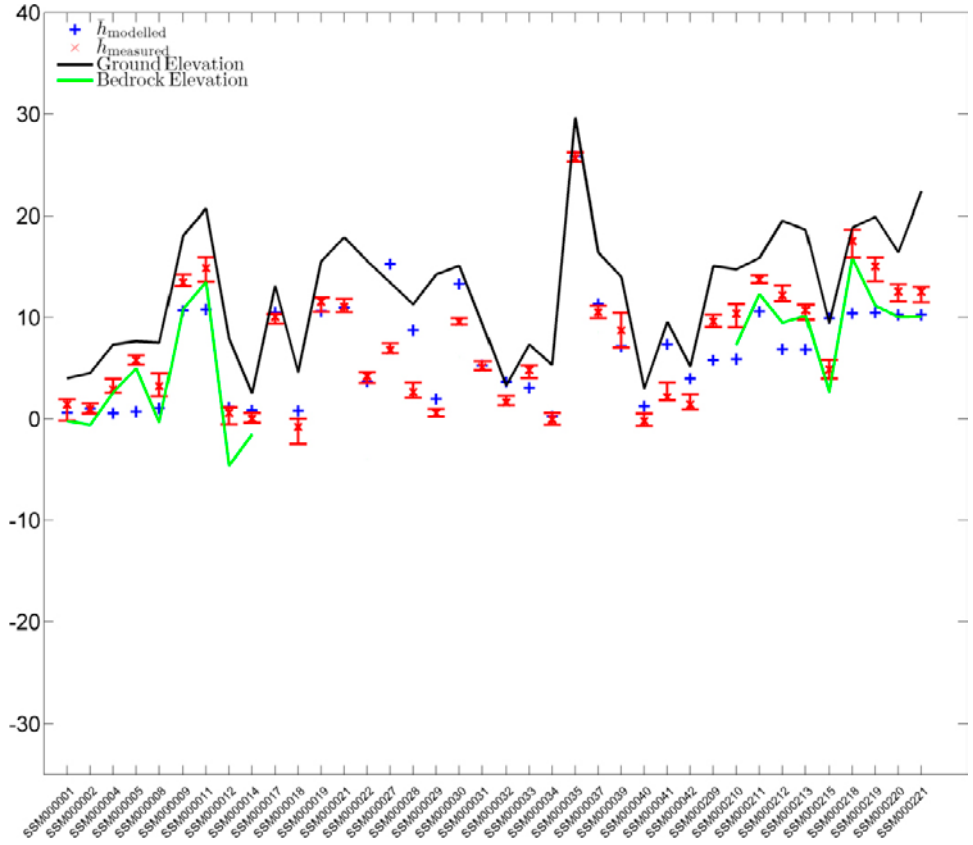

Figure 4-7. *Comparison of measured heads in the first set of groundwater monitoring wells (SSM) with the results of Case 6_4c. The field data are plotted as mean point water heads in the soil with error bars to show the range of values at different measurement times.*

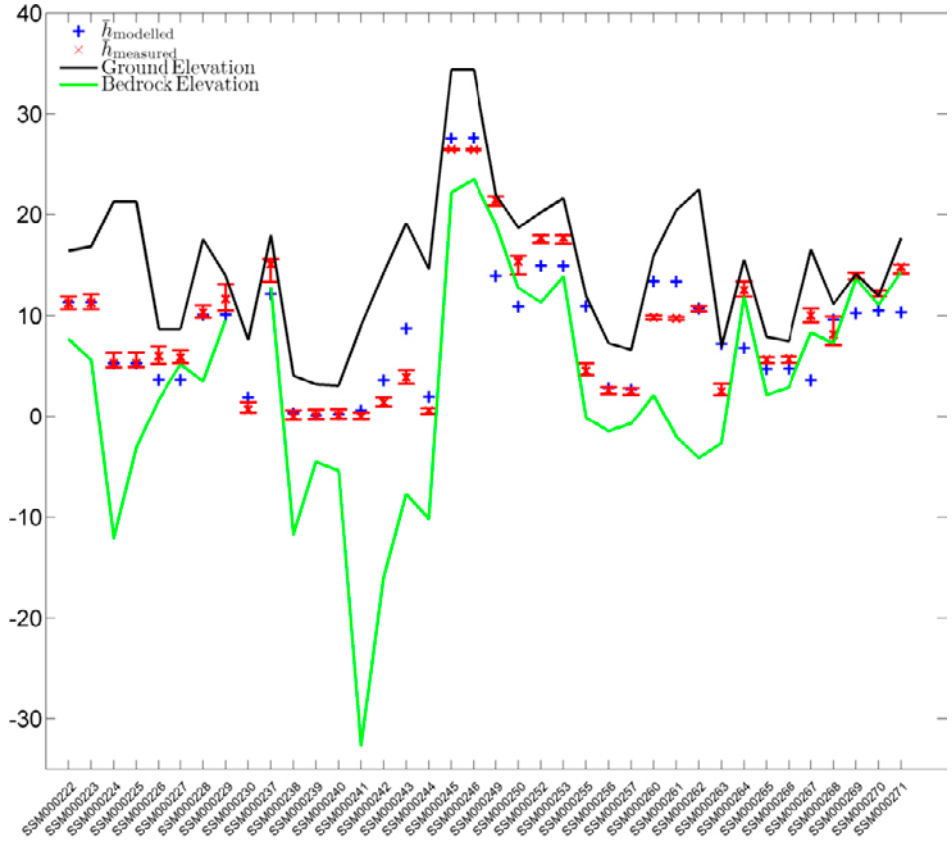

Figure 4-8. *Comparison of measured heads in the second set of groundwater monitoring wells (SSM) with the results of Case 6_4c. The field data are plotted as mean point water heads in the soil with error bars to show the range of values at different measurement times.*

Figure 4-9 and Figure 4-10 show modelled average heads, over the simulated time period of 1 540 days, compared with measured head ranges in the first set of percussion-drilled boreholes (HLX) for a selection of the sensitivity cases. In each figure, the results from the base case are included for comparison.

Figure 4-9 shows results for sensitivity Case 8_1c, Case 8_2c and Case 8_3c, in which the effect of increased permeability in the HSD, HCD and HRD respectively, is analysed. Given the applied magnitude of change (a factor of 50), it is clear that the effect is most pronounced for changes made to the HSD. Increasing the permeability in the HCD has no effect on the measured heads in the HLX boreholes. For the HRD, a minor improvement on the calibration can be seen. Note that these conclusions apply to the specified change and that there also may be combined effects if the properties are changed for more than one domain at the same time.

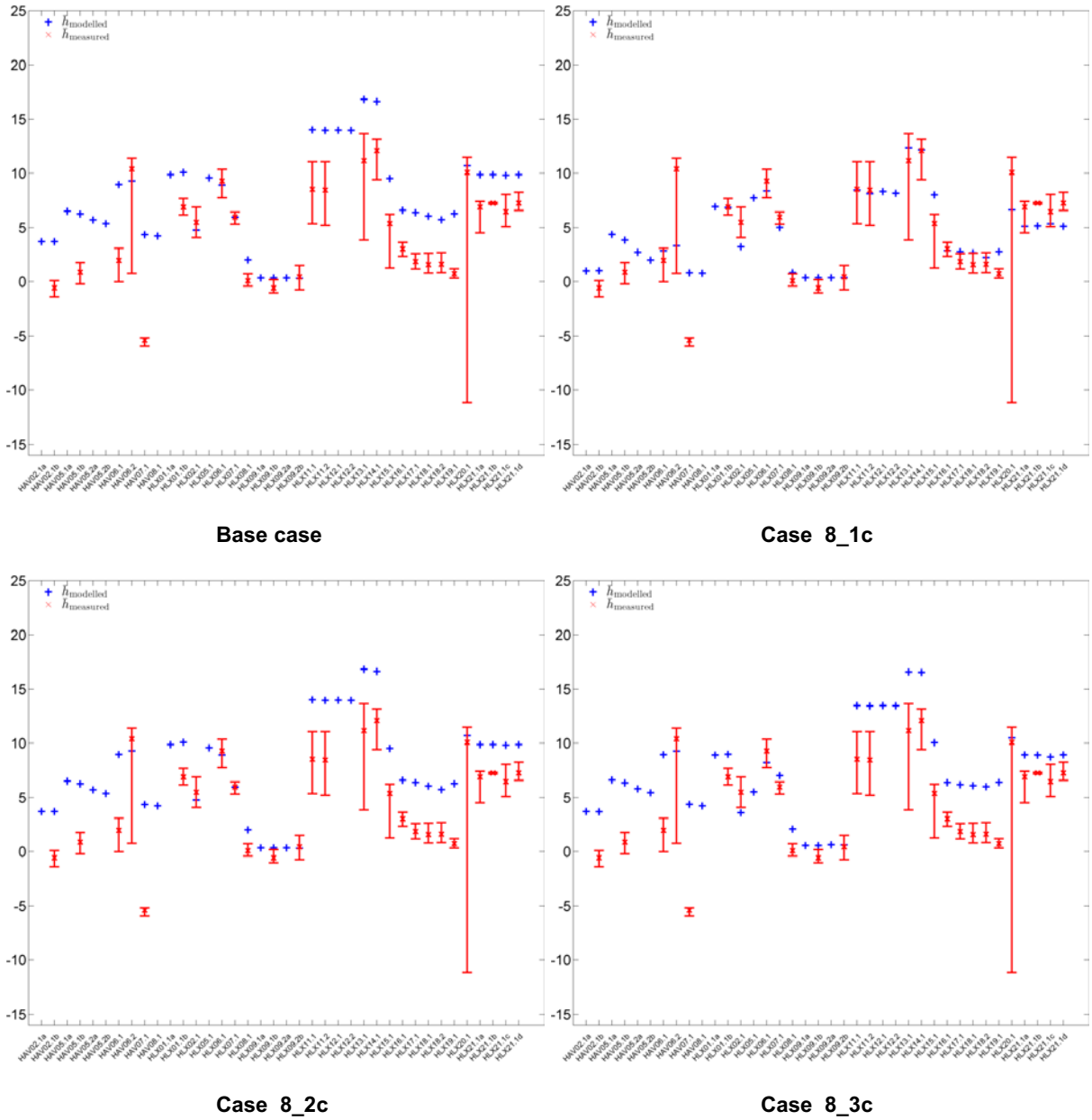

Figure 4-9. *Modelled average heads (blue markers) compared with measured head ranges (red markers) for the first set of percussion-drilled boreholes (HLX).*

Figure 4-10 shows results for sensitivity Case 8_4c, Case 6_4c and Case 6_7c, compared with the base case. In Case 8_4c, only the storage was changed compared with the base case. As expected, no effect can be seen in the calculated heads. Changing the storage only affects the dynamics of the system so any changes in results are expected to appear in the transient head response in the boreholes, primarily deeper holes drilled into the rock. The same discussion is applicable when comparing Case 6_7c to Case 6_4c. The only difference between these two cases is the decreased porosity in Case 6_7c. No difference is seen between the two cases. In the same way as for the storage, the porosity is also expected to mainly affect the transient response in the boreholes, but in the case of porosity the changes should be most significant for the shallower SSM wells drilled in the soil.

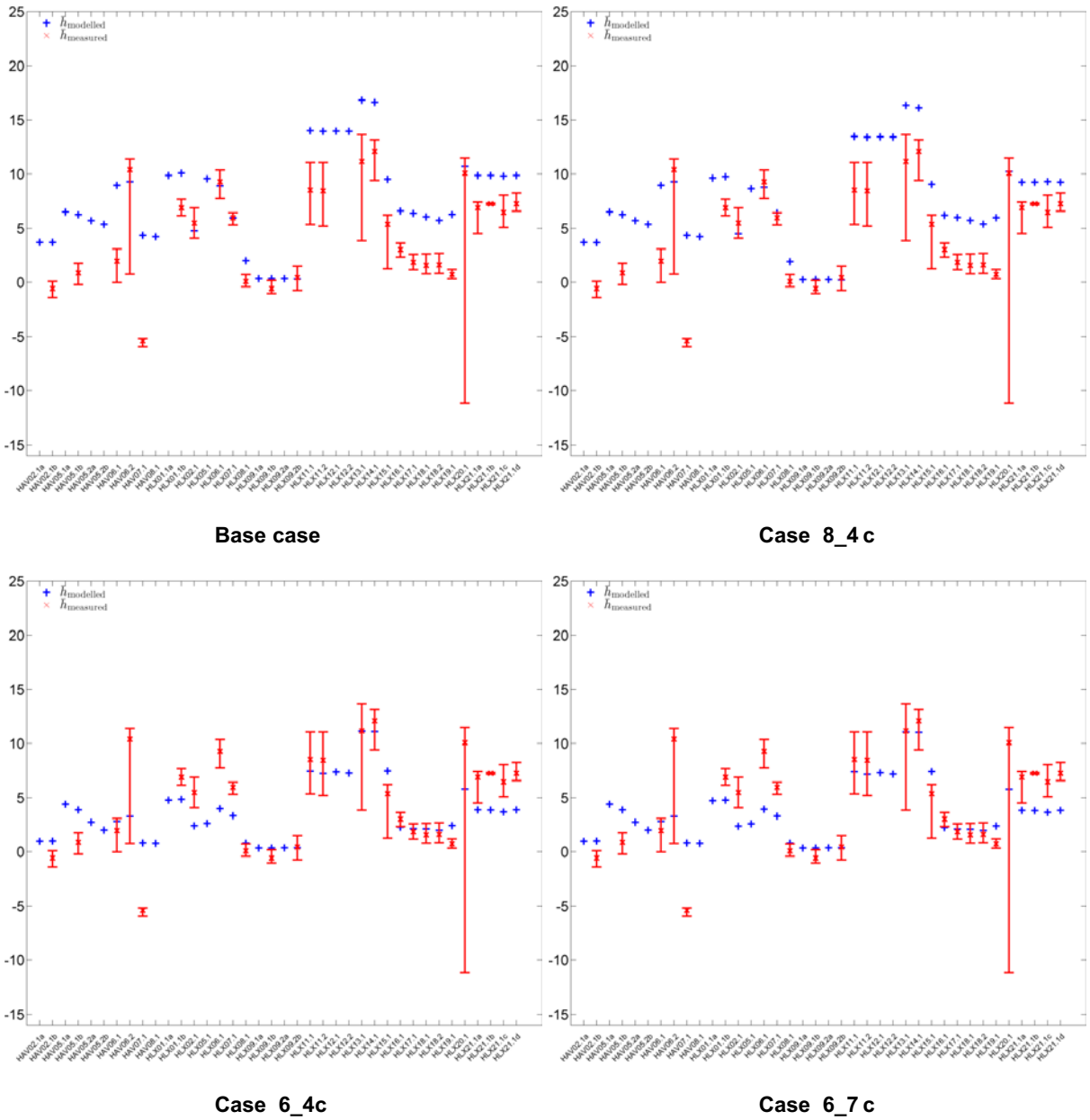

Figure 4-10. *Modelled average heads (blue markers) compared with measured head ranges (red markers) for the first set of percussion-drilled boreholes (HLX).*

Figure 4-11 and Figure 4-12 show modelled average heads, over the simulated time period of 1 540 days, compared with measured head ranges in the second set of percussion-drilled boreholes (HLX) for the same selection of sensitivity calculations as in the previous set of figures, as discussed above. The same reasoning as before applies.

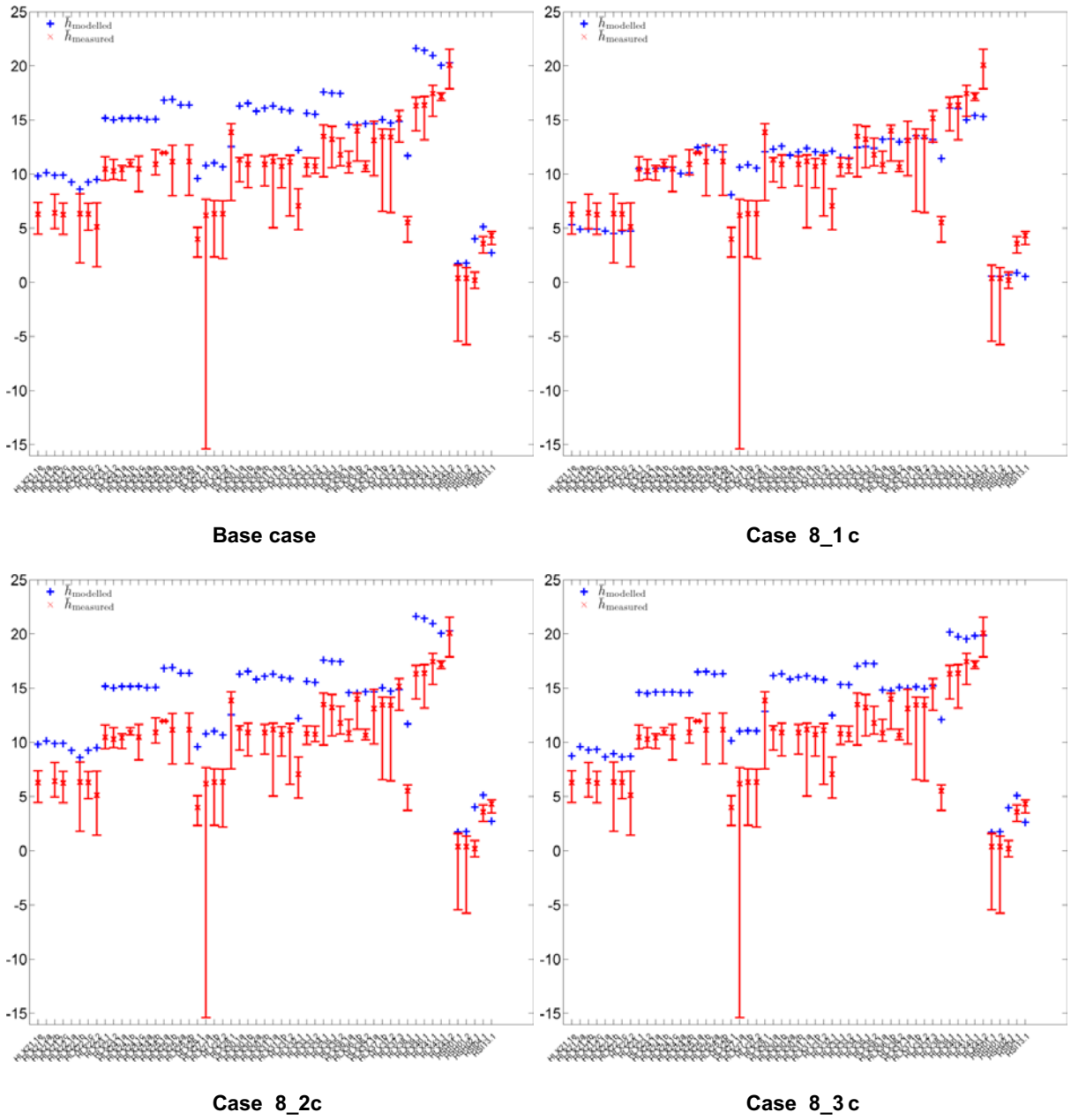

Figure 4-11. *Modelled average heads (blue markers) compared with measured head ranges (red markers) for the second set of percussion-drilled boreholes (HLX).*

Figure 4-13 and Figure 4-14 show modelled average heads, over the simulated period of 1 540 days, compared with measured head ranges in the first set of groundwater monitoring wells (SSM) for a selection of sensitivity calculations. In each figure, the results from the base case are included for comparison.

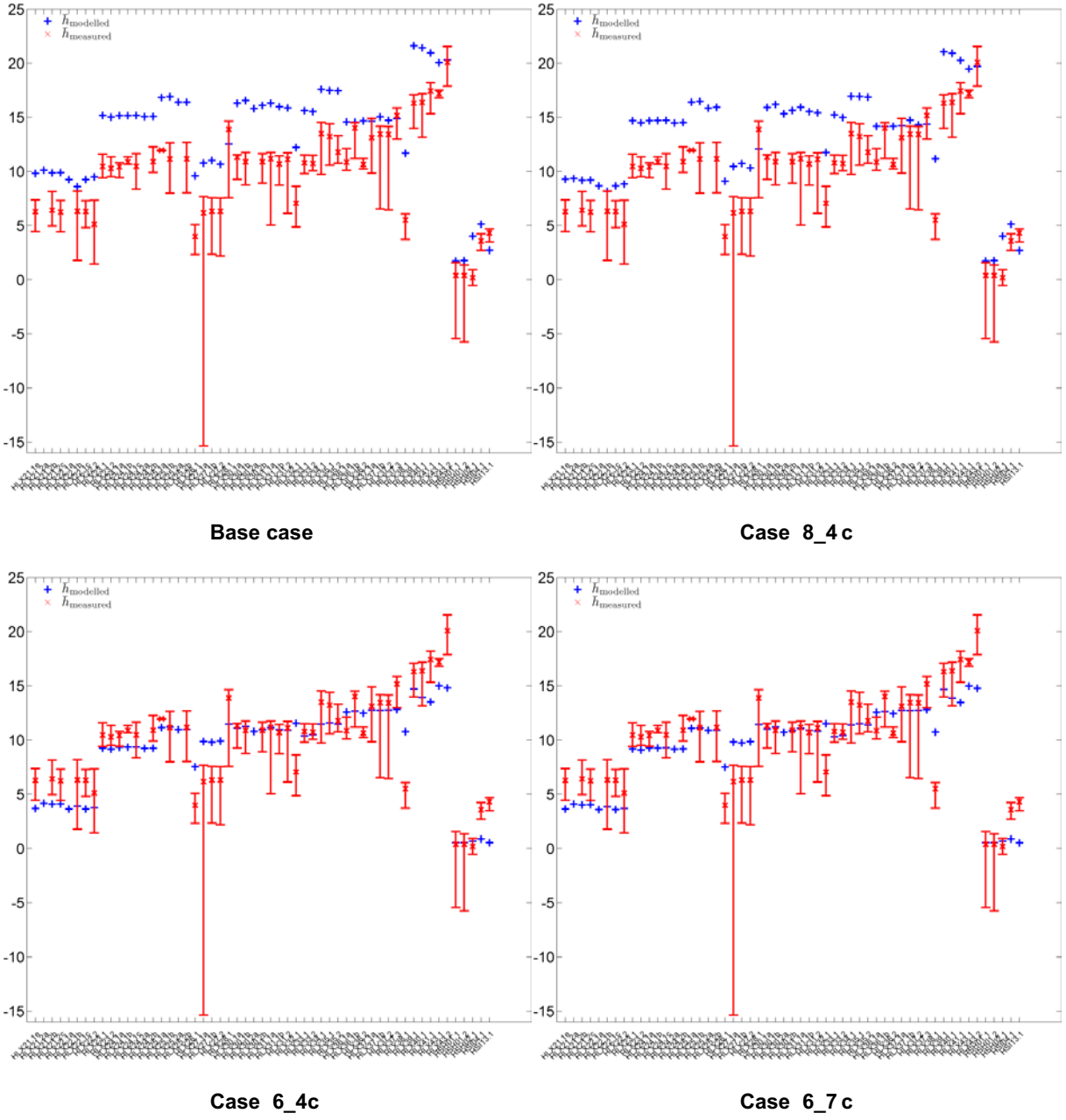

Figure 4-12. *Modelled average heads (blue markers) compared with measured head ranges (red markers) for the second set of percussion-drilled boreholes (HLX).*

Figure 4-13 shows results for sensitivity Case 8_1c, Case 8_2c and Case 8_3c, in which the effect of increased permeability in the HSD, HCD and HRD respectively, is analysed. Again, it is clear that the effect is most pronounced for changes made to the HSD. Increasing the permeability in the HCD has no effect on the measured heads in the HLX boreholes (with the changes made here at least). For the HRD, a minor improvement in the calibration can be seen.

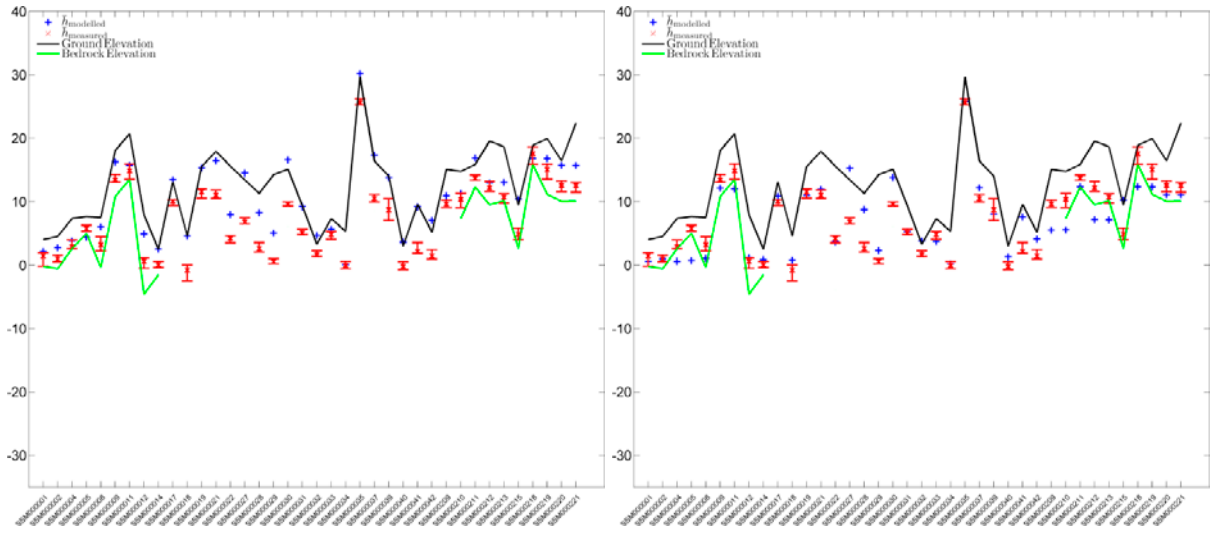

Base case

Case 8_1c

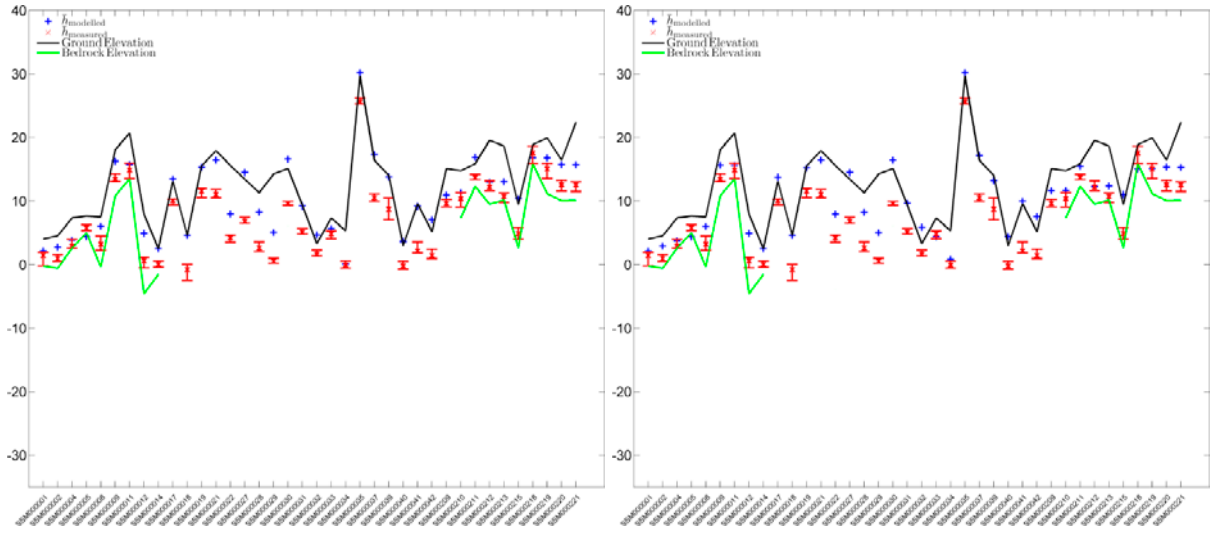

Case 8_2c

Case 8_3c

Figure 4-13. *Modelled average heads (blue markers) compared with measured head ranges (red markers) for the first set of groundwater monitoring wells (SSM). The black line indicates ground elevation and the green line indicates bedrock elevation.*

Figure 4-14 show results for sensitivities Case 8_4c, Case 6_4c and Case 6_7c compared to the base case. In Case_8_4c, only the storage was changed compared with the base case. Again, only minor effects can be seen in the calculated heads. Changing the storage only affects the dynamics of the system so any changes in results are expected to appear in the transient head responses in the boreholes. The same discussion as before, applies when comparing Case 6_7c to Case 6_4c and no difference is seen between the two cases. In the same way as for the storage, the porosity is also expected to mainly affect the transient response in the boreholes.

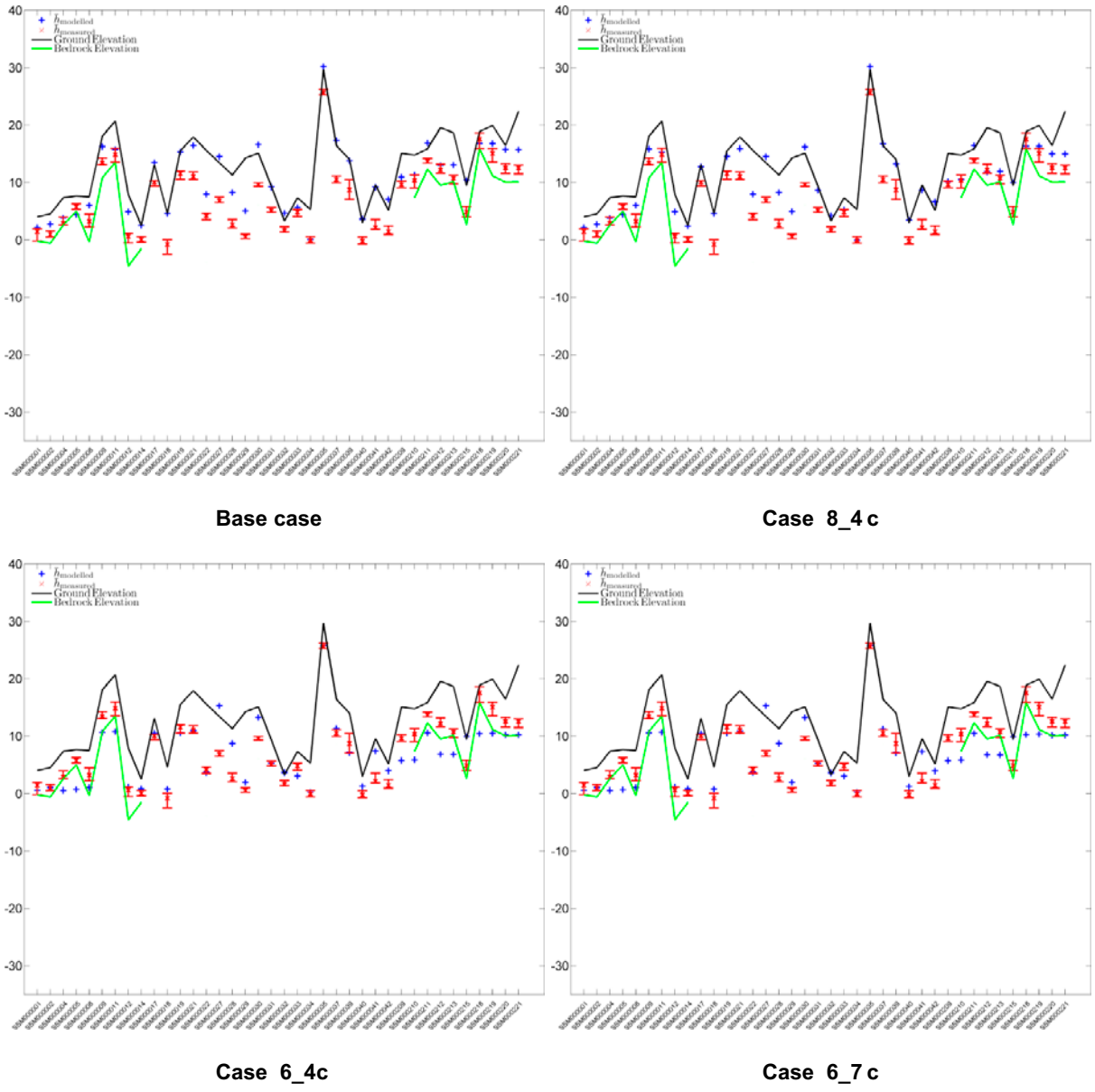

Figure 4-14. *Modelled average heads (blue markers) compared with measured head ranges (red markers) for the first set of groundwater monitoring wells (SSM). The black line indicates ground elevation and the green line indicates bedrock elevation.*

Figure 4-15 and Figure 4-16 show modelled average heads, over the simulated time period of 1 540 days, compared with measured head ranges in the second set of groundwater monitoring wells (SSM) for the same selection of sensitivity calculations as in calculations described above. The same reasoning as before applies.

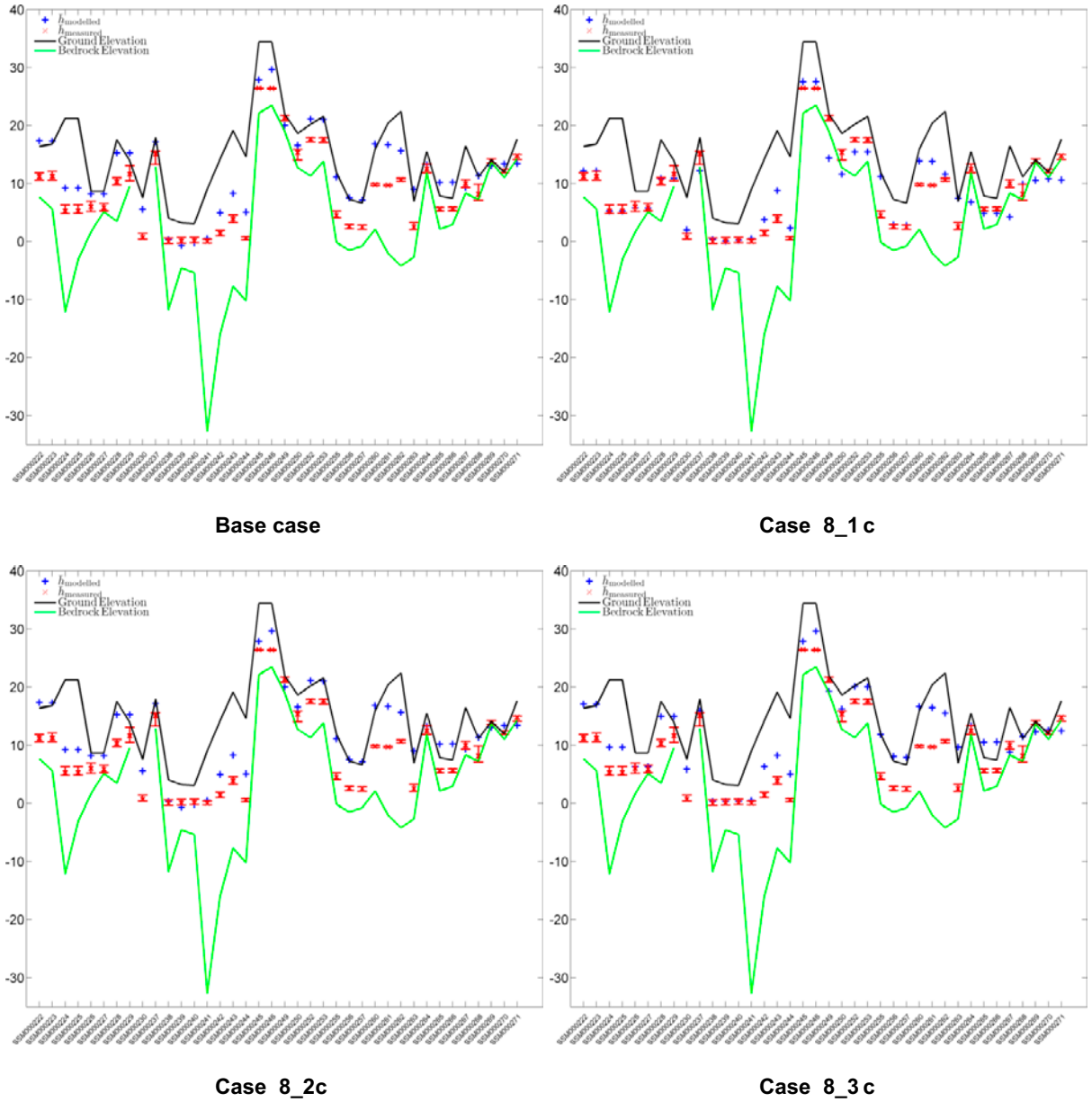

Figure 4-15. *Modelled average heads (blue markers) compared with measured head ranges (red markers) for the second set of groundwater monitoring wells (SSM). The black line indicates ground elevation and the green line indicates bedrock elevation.*

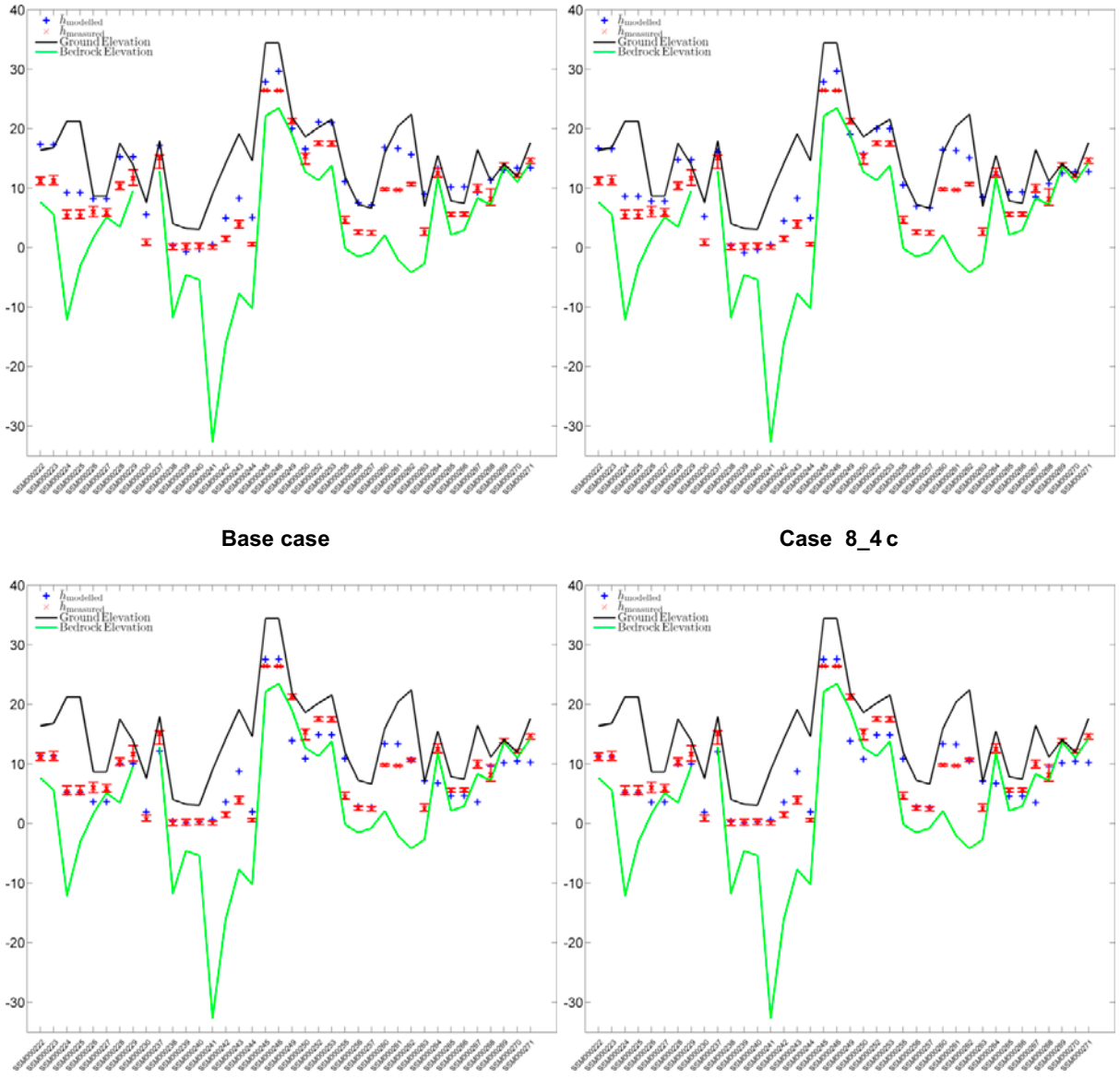

Figure 4-16. *Modelled average heads (blue markers) compared with measured head ranges (red markers) for the second set of groundwater monitoring wells (SSM). The black line indicates ground elevation and the green line indicates bedrock elevation.*

4.1.4 Transient evolution of groundwater levels

Figure 4-17 through Figure 4-22 show the modelled transient head response compared with the measured heads in the percussion drilled boreholes HLX06.1, HLX08.1 and HLX09.2b, respectively. In each figure, the results for the base case are compared with results for a selection of sensitivity cases. In all figures, the average recharge is shown for comparison.

Figure 4-17, Figure 4-19 and Figure 4-21 show results for Case 8_1c, Case 8_2c and Case 8_3c, in which the effect of increased permeability in the HSD, HCD and HRD respectively, is analysed. It is clear that the modelled transient head response is not as fast as the measured head response, and just follows the overall decline in recharge over the simulation period. There are some indications that the modelled heads follow the varying recharge but the modelled head curves are much flatter. As expected, there is not much difference in head response between the sensitivity cases, apart from the differences in average head levels which are explained by the changes in permeability.

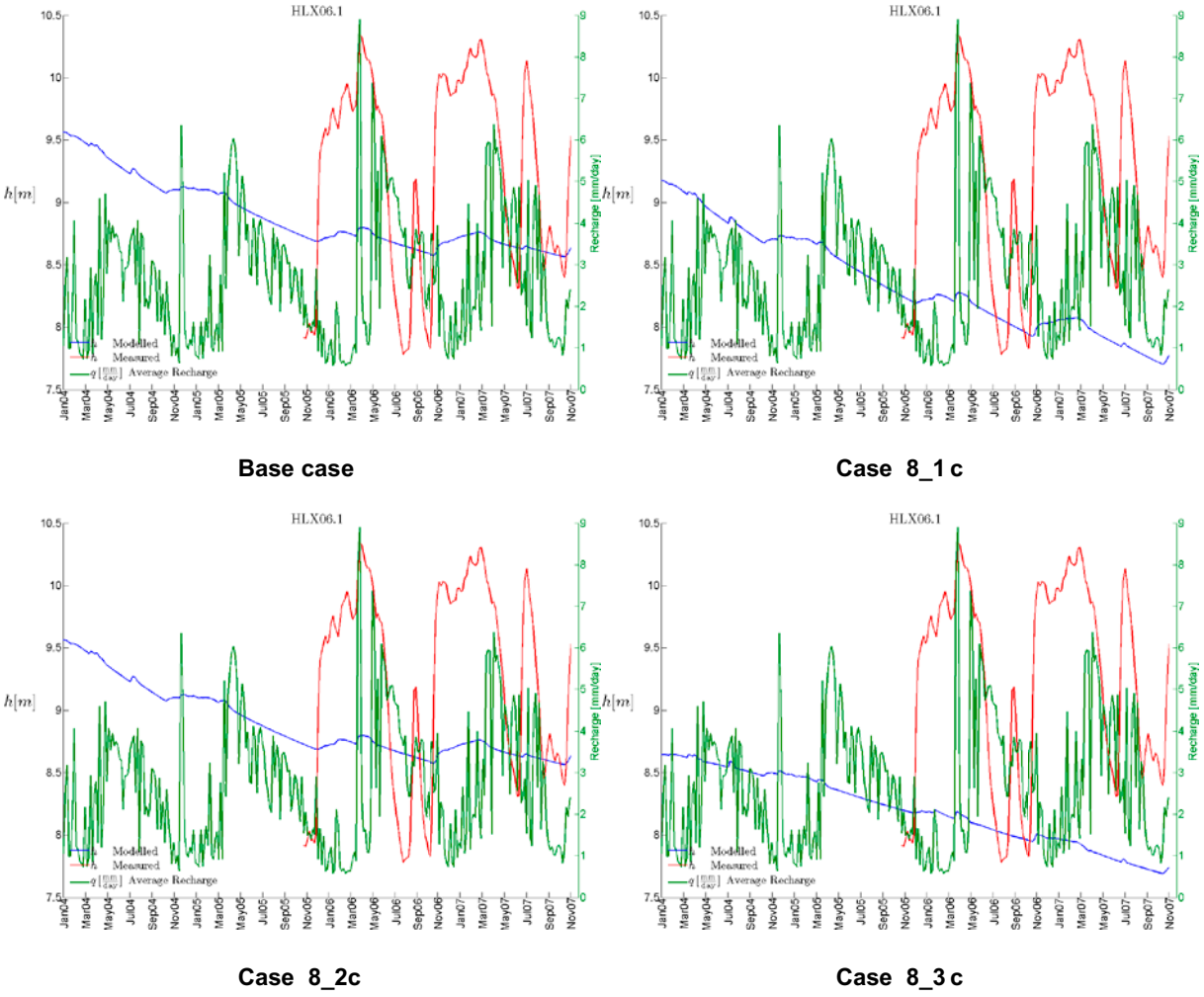

Figure 4-17. *Modelled transient head response (blue line) compared with measured heads (red line) in HLX06.1. The average recharge is shown in green for comparison.*

Figure 4-18, Figure 4-20 and Figure 4-22 show results for Case 8_4c, Case 6_4c and Case 6_7c, compared with the base case. In Case 8_4c, where the storage was decreased compared with the base case, the modelled transient head response is improved significantly, in particular in HLX06.1 and HLX09.2b. The response now follows the measured heads even if the average head values are about 1 m lower. Changing the storage apparently has the desired effect on the transient head responses in the percussion-drilled boreholes. On the other hand, the change in storage does not seem to affect all boreholes to the same degree. When the results are compared for Case 6_4c and Case 6_7c for HLX06.1, HLX08.1 and HLX09.2b, it is clear that changing the porosity in the soil layers has no effect on the transient head responses in the percussion-drilled boreholes, which is in line with expectations.

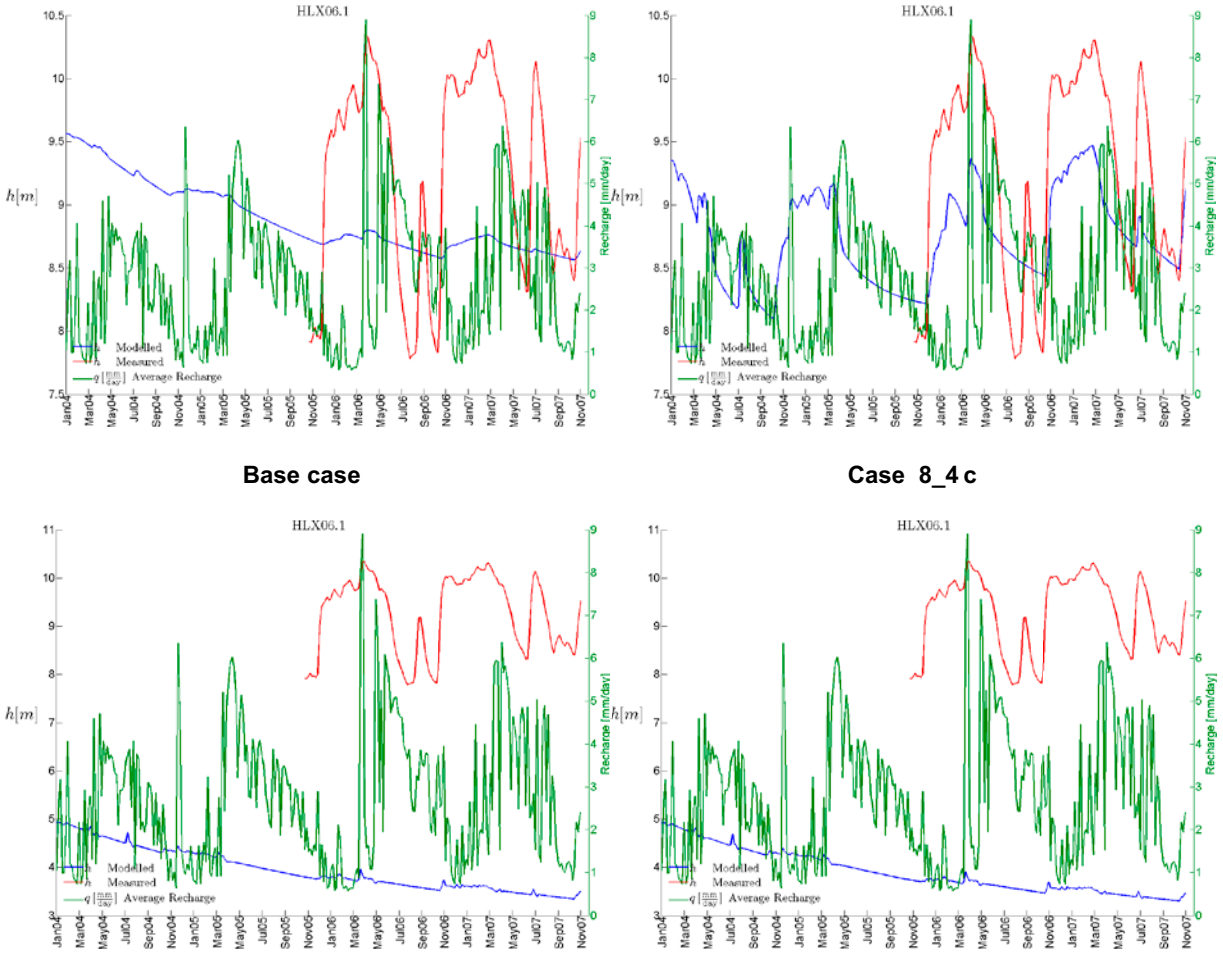

Figure 4-18. *Modelled transient head response (blue line) compared with measured heads (red line) in HLX06.1. The average recharge is shown in green for comparison.*

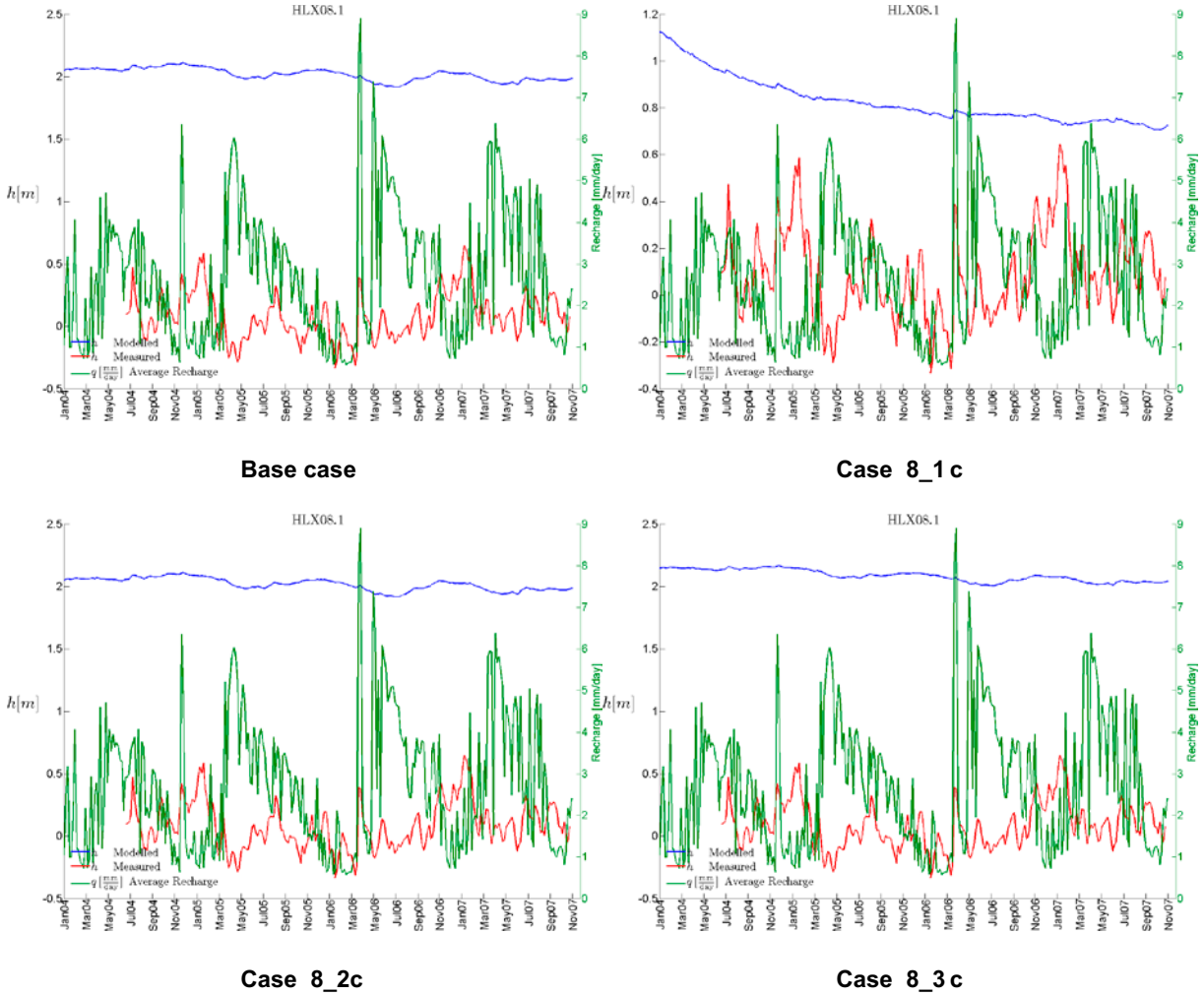

Figure 4-19. *Modelled transient head response (blue line) compared with measured heads (red line) in HLX08.1. The average recharge is shown in green for comparison.*

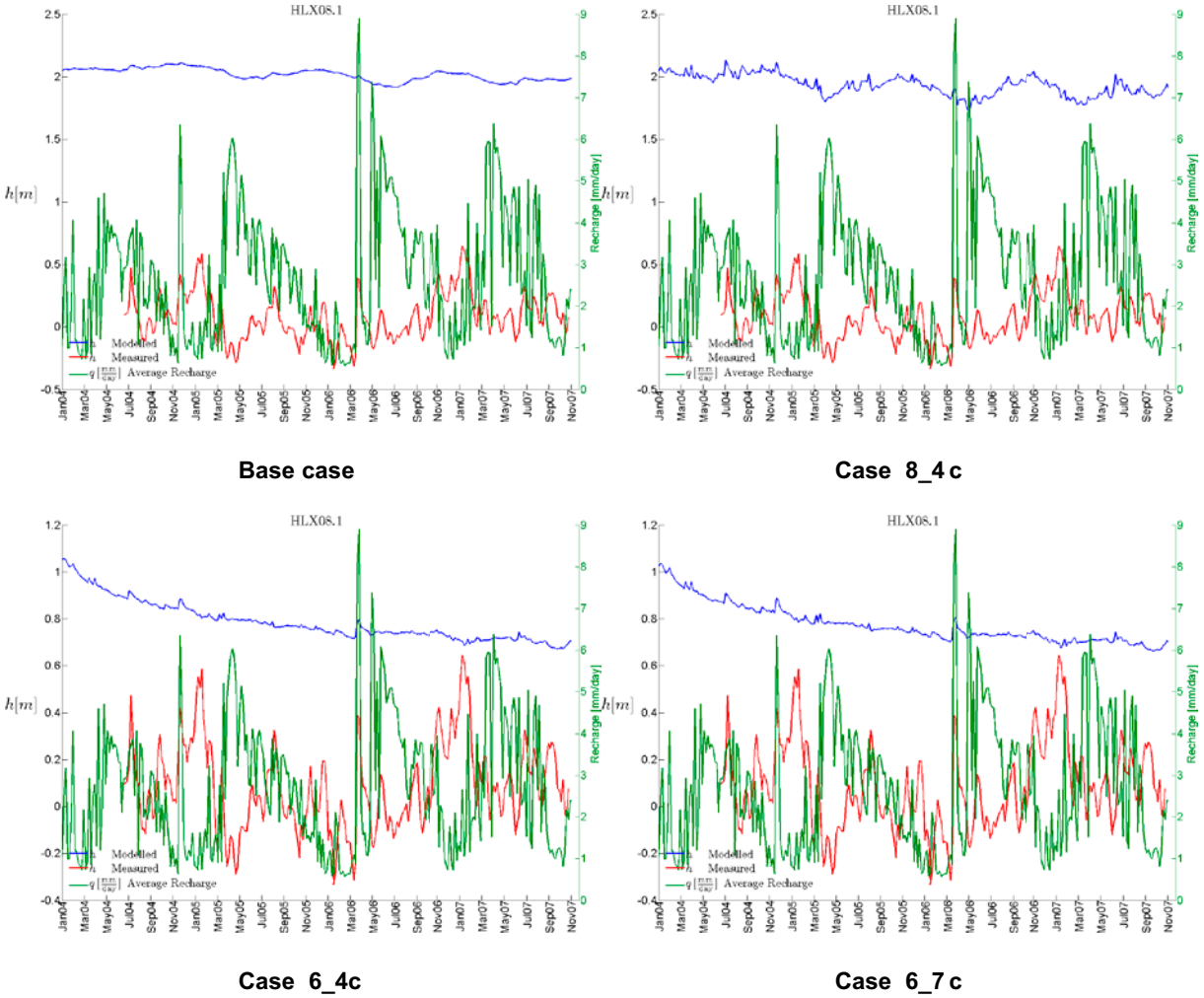

Figure 4-20. *Modelled transient head response (blue line) compared with measured heads (red line) in HLX08.1. The average recharge is shown in green for comparison.*

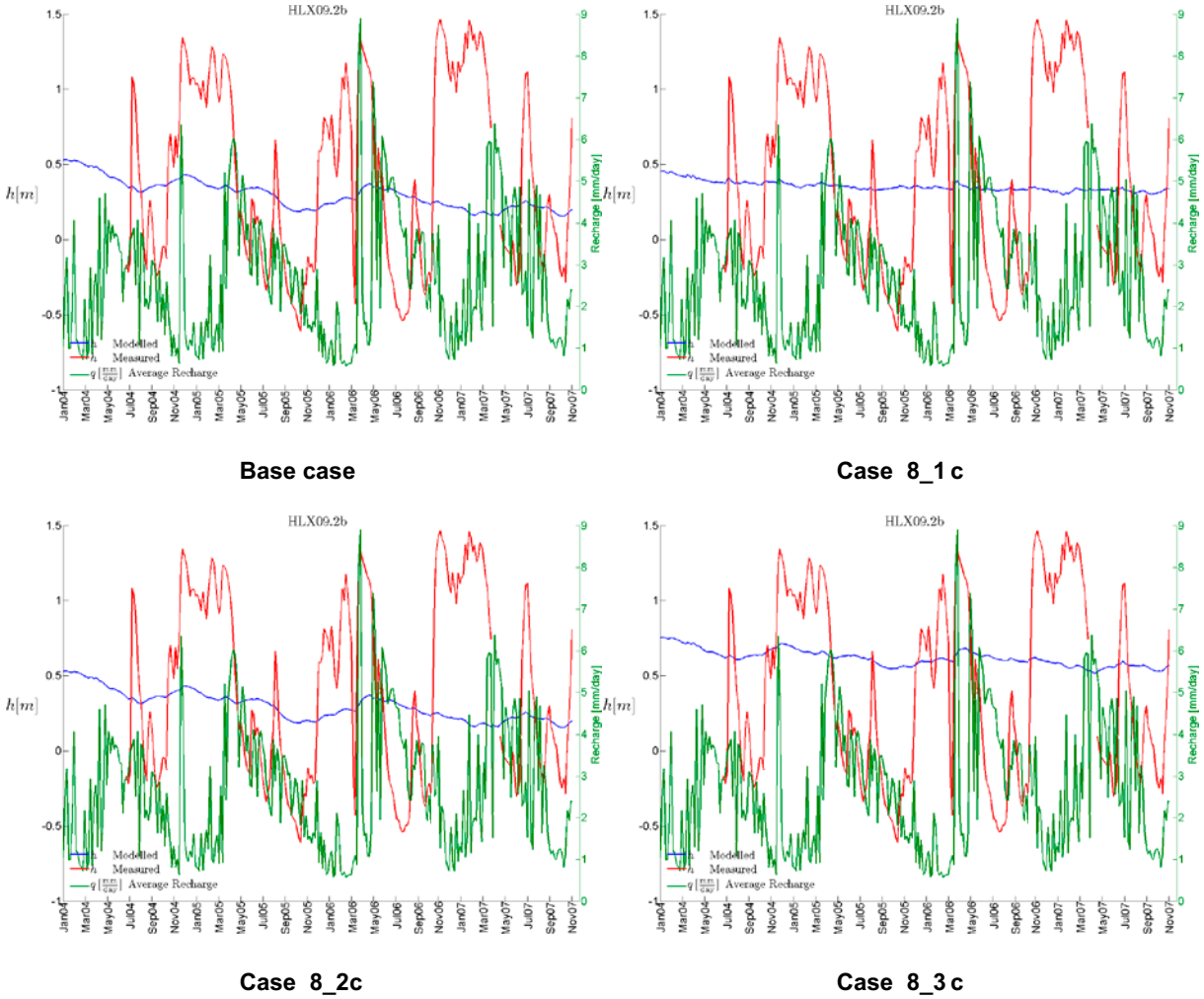

Figure 4-21. *Modelled transient head response (blue line) compared with measured heads (red line) in HLX09.2b. The average recharge is shown in green for comparison.*

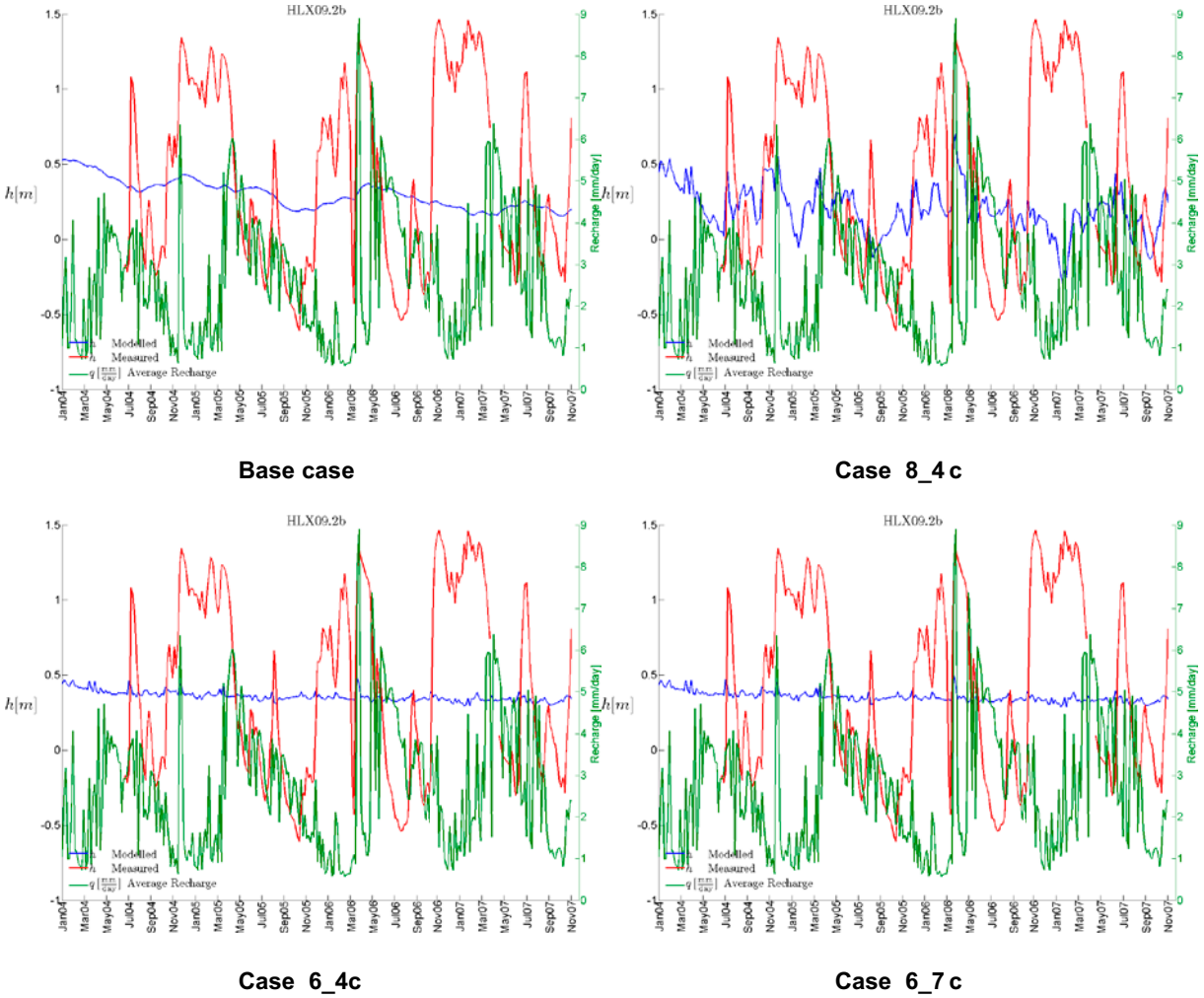

Figure 4-22. *Modelled transient head response (blue line) compared with measured heads (red line) in HLX09.2b. The average recharge is shown in green for comparison.*

Figure 4-23 through Figure 4-26 show the modelled transient head response compared with the measured heads in the groundwater monitoring wells SSM000012 and SSM000022, respectively. In each figure, the results for the base case are compared with results for a selection of sensitivity cases. In all figures, the average recharge is shown for comparison.

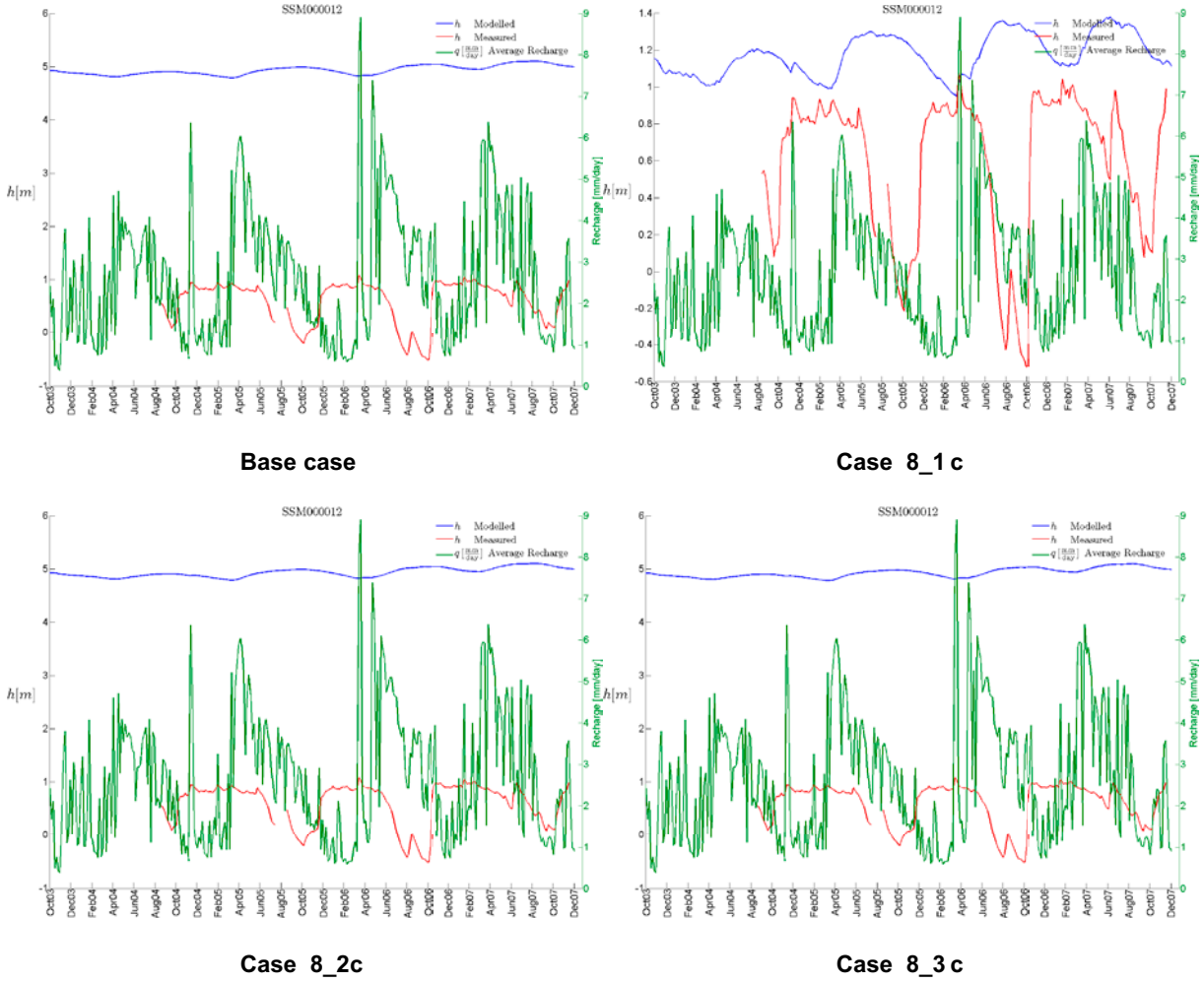

Figure 4-23. *Modelled transient head response (blue line) compared with measured heads (red line) in SSM000012. The average recharge is shown in green for comparison.*

Figure 4-23 and Figure 4-25 show results for Case 8_1c, Case 8_2c and Case 8_3c. As seen before, the results show that decreasing the permeability does not affect the transient head response in the shallow wells. There is seemingly an improvement for Case 8_1c, but this is only a scale effect caused by the change in average modelled heads leading to a magnified vertical axis. Looking closely at the other cases, the same pattern in the modelled response curve can be seen, even if the vertical scale is not optimal. The modelled response is not quite as dynamic as the measured, but the periodicity is the same. The modelled response is however delayed by a few months compared with the measured head response, indicating excessive inertia in the system.

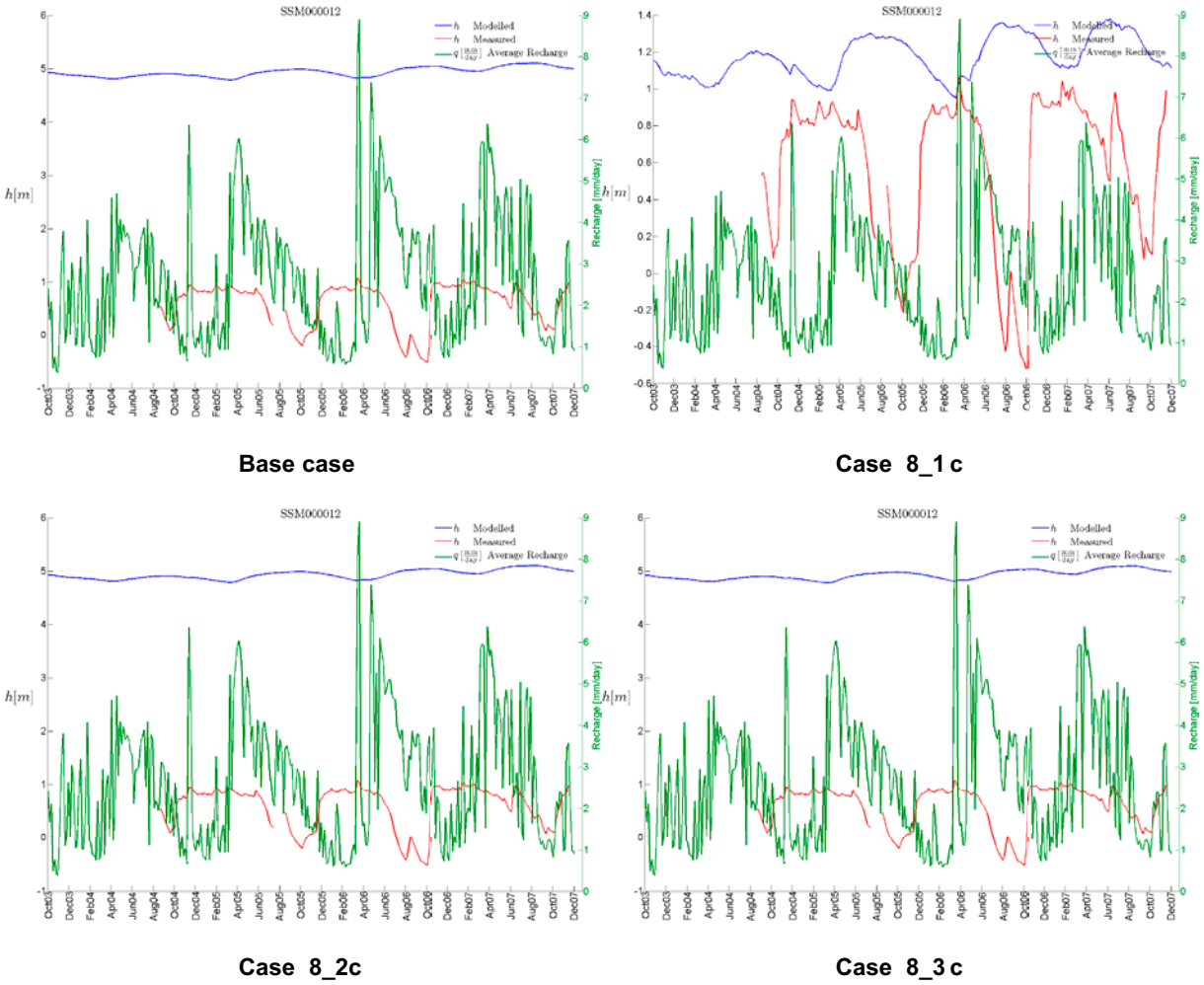

Figure 4-24. *Modelled transient head response (blue line) compared with measured heads (red line) in SSM000012. The average recharge is shown in green for comparison.*

Figure 4-24 and Figure 4-26 show results for Case 8_4c, Case 6_4c and Case 6_7c compared with the base case. The results for Case 8_4c show that decreasing the storage in the HCD and HRD does not have any impact on the shallow SSM wells. Looking at Case 6_4c and Case 6_7c, it is clear that the decrease in porosity (which is the only difference between the two cases) does not affect the transient head response. It could be that the change in porosity is not big enough. However, comparing these two cases with the base case, it is clear that by combining an increase in permeability with a decrease in storage, i.e. increasing the hydraulic diffusivity, it is possible to improve both the match between modelled and measured heads as well as the transient head responses.

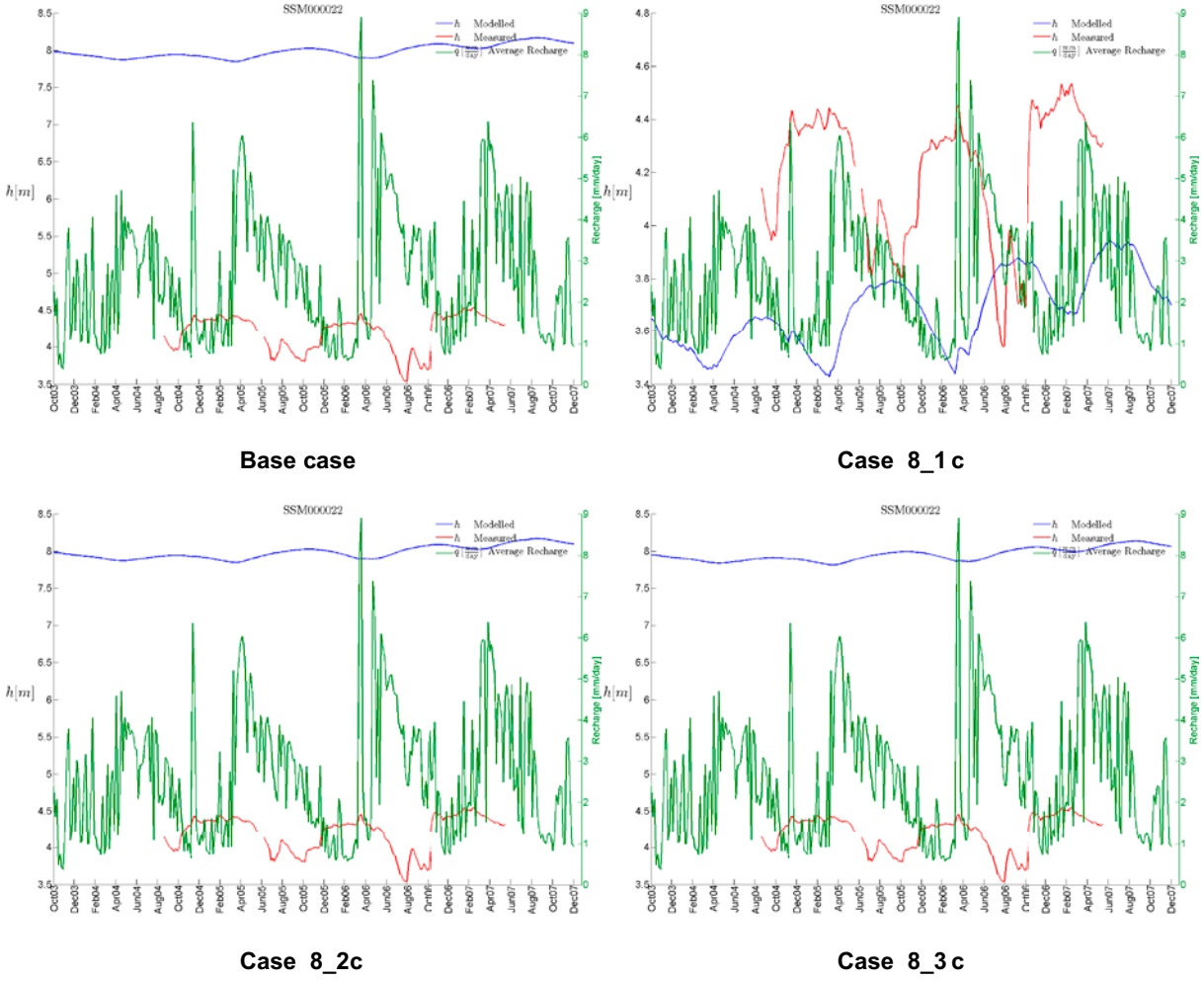

Figure 4-25. *Modelled transient head response (blue line) compared with measured heads (red line) in SSM000022. The average recharge is shown in green for comparison.*

The sensitivity analysis performed here has shown that the calibration on measured heads in percussion-drilled boreholes (HLX) and groundwater monitoring wells (SSM) can be improved. Compared with the SR-Site model, a better match to measured heads has been achieved and updated physical properties (with higher permeability in the soil and upper bedrock and lower storativity) have been produced for the soil and upper bedrock of the hydrogeological model. Further work would be required to achieve a fully calibrated model with properties within expected physical ranges.

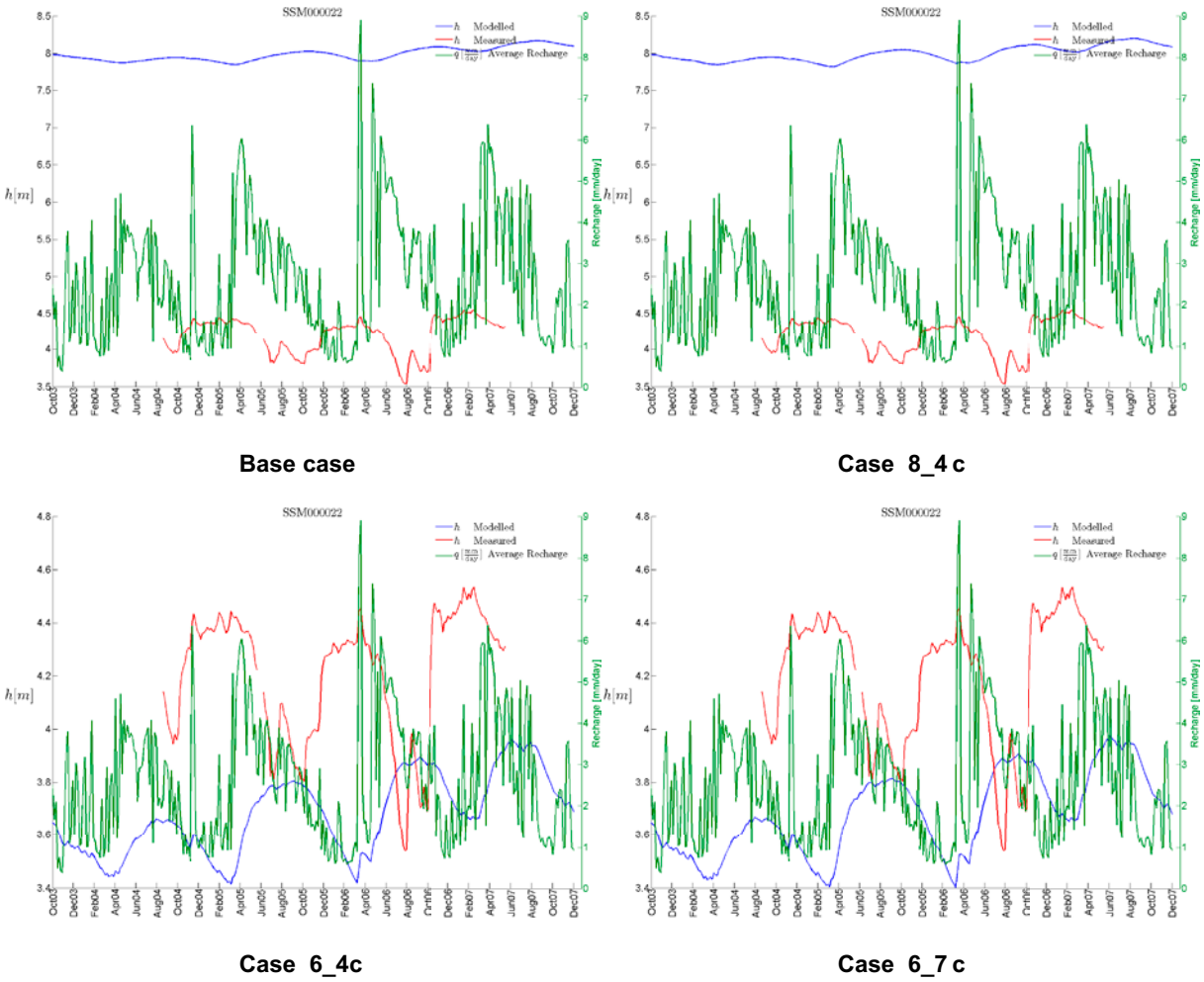

Figure 4-26. *Modelled transient head response (blue line) compared with measured heads (red line) in SSM000022. The average recharge is shown in green for comparison.*

4.2 Reference water evolution

4.2.1 Presentation of results

Results are presented to illustrate the evolution of the reference waters in the wider catchment scale context during an extended period of temperate climate conditions. The results are given at several times during the extended temperate climate period to illustrate the evolution over that period. In the presentation of the results from the tracer simulations (mixing of reference waters), times from the start of the simulated transient (8000 BC) are shown to capture the entire hydro-chemical evolution. The interval between selected times is smaller at earlier times when the site is evolving more quickly.

The results from the tracer simulations using Case 1 are presented first in the following sections. The reason for this is that the information from the mixing of reference waters is useful in the analysis and discussion of the reactive transport modelling results from Case 2 and Case 3. A set of slices through the model is used to visualise the mixing process and catchment scale evolution of the reference waters. The slices are coloured by mixing fractions of each reference water, so that the sum of all reference water fractions at a given point in time and space should be equal to one. The results are visualised using the following slice definition:

- A catchment scale vertical slice in the W-E direction, through the centre of the repository volume. For context, the refined volume and repository vaults are shown in white, although the vaults are not represented in the full ECPM model. The slice shows the entire model down to an elevation of −2 164 m. The selected time periods for this slice are 7980 BC, 5000 BC, 4000 BC, 2000 BC, 0 AD, 2000 AD, 5000 AD, 10 000 AD, 20 000 AD and 60 000 AD.

4.2.2 Mixing fractions of reference waters

Figure 4-27 through Figure 4-31 show the evolution of the reference waters Deep Saline, Littorina, Altered Meteoric, Glacial and Inter-glacial, as mixing fractions on vertical slices (from west to east) through the repository volume for Case 1, HRD realisation 1. In each figure, from top to bottom, results for 7980 BC, 5000 BC, 4000 BC, 2000 BC, 0 AD, 2000 AD, 5000 AD, 10 000 AD, 20 000 AD and 60 000 AD, are shown. In addition, the refined volume and repository vaults are shown in white for orientation.

Initially, the groundwater composition of the model is a mixture of Deep Saline, Glacial and Inter-glacial waters. The groundwater is fully Glacial down to an elevation of −150 metres above sea level, where Deep Saline and Inter-glacial water are present, with linearly increasing fractions with depth. The initial fraction of Glacial water correspondingly decreases below −150 metres above sea level and is absent below −1 500 metres above sea level. The fraction of Deep Saline water increases from −150 metres above sea level down to −2 000 metres above sea level, where the groundwater is fully Deep Saline. Between −150 metres above sea level and −2 000 metres above sea level, Inter-glacial water is present in fractions of 0 to 0.3. See Figure 3-8 for a visualisation of the initial conditions for the fracture water at 8000 BC.

Figure 4-27 shows that the Deep Saline water initially is distributed as intended in the applied initial conditions with its concentration increasing linearly with depth below −150 metres above sea level. Over time, the distribution of Deep Saline water is somewhat affected by flushing, due to infiltrating Altered Meteoric water penetrating from the top. However, due to the higher density of the Deep Saline water, it does not mix readily with the other reference waters. The distribution of Deep Saline water therefore does not change much over time and Deep Saline water is predicted to contribute the largest mass fraction at depth even at 60 000 AD.

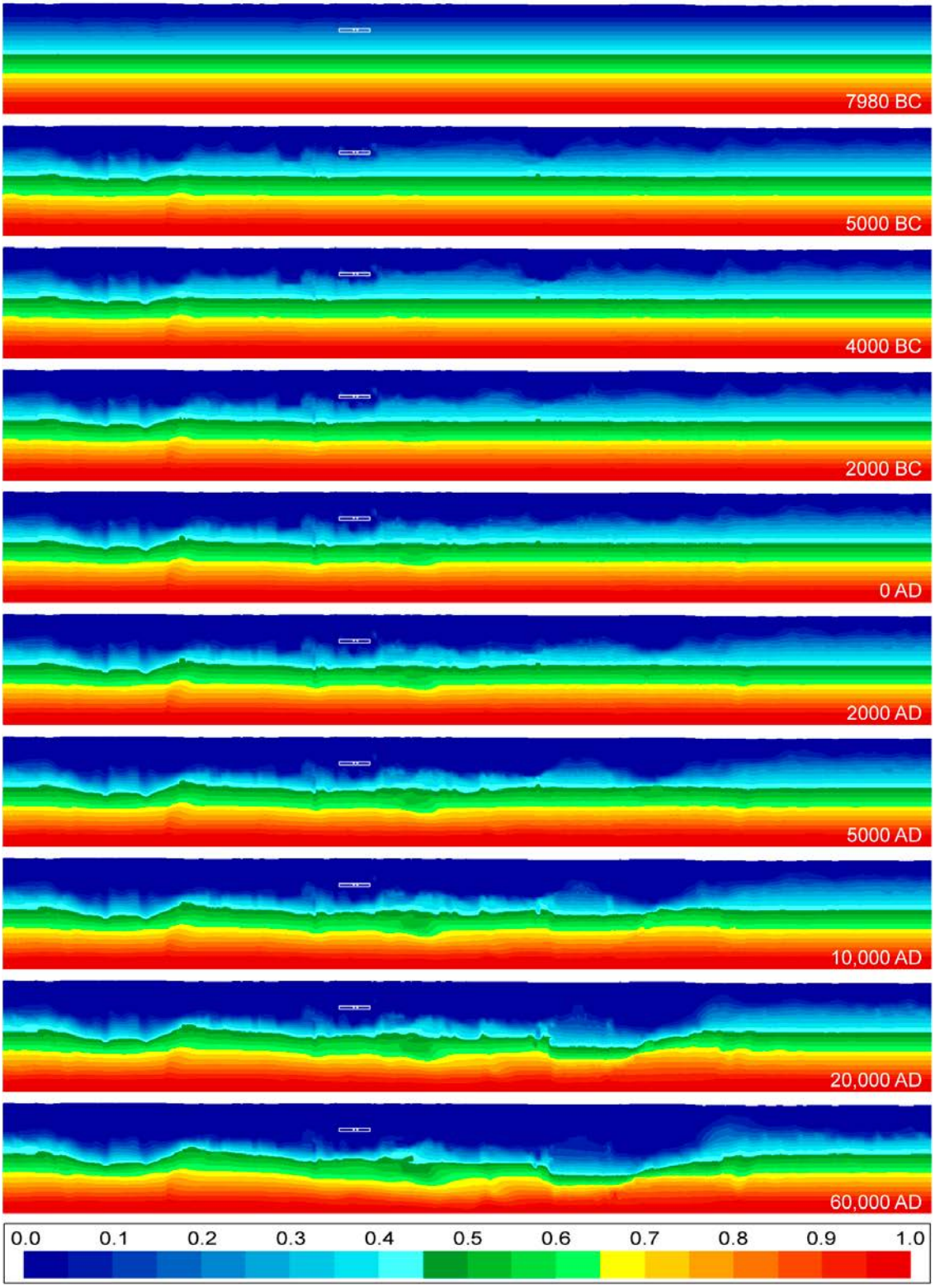

Figure 4-27. *Evolution of Deep Saline water shown as mixing fractions on vertical W-E slices through the repository volume for Case 1, HRD realisation 1, for dates (from top to bottom) 7980 BC, 5000 BC, 4000 BC, 2000 BC, 0 AD, 2000 AD, 5000 AD, 10 000 AD, 20 000 AD and 60 000 AD. The refined volume and repository vaults are shown in white.*

Figure 4-28 shows the distribution of Littorina water, which initially is not present in the model. Littorina water is introduced gradually in the eastern parts of the region (i.e. the location of the sea) from around 6000 BC. The salinity of the Littorina water increases from zero up to a maximum concentration of 12.5 ‰ salinity between 4000 BC and 2000 BC. As the heavier Littorina water penetrates downwards, forming a sharp front, it replaces the older Glacial water at the top. After 2000 BC, the salinity of the sea water drops to the present-day value of 6.8 ‰ and the fraction of Littorina water gradually decreases. The Littorina water is in turn replaced by infiltrating Altered Meteoric water, see Figure 4-29. Even though Littorina water penetrates down to an elevation of −700 metres above sea level at the deepest, it never reaches the repository volume due to its location inland, situated further west than the Littorina front. By 20 000 AD the coastline has moved south east out of the model domain and it is predicted that areas with a significant Littorina water fraction are more or less absent from the model domain.

Figure 4-29 shows the distribution of Altered Meteoric water. At 5000 BC, no land areas have yet risen above sea level within the model domain and therefore precipitation (Altered Meteoric) has not yet started to infiltrate through the top surface. However, at 4000 BC, it is evident that land covers a substantial part of the model domain and that Altered Meteoric water has started to replace the Glacial water at the top, see Figure 4-30. This process, with Altered Meteoric water replacing Glacial and Littorina water at shallower depths, continues throughout the simulated period. At the later stages in time, after 20 000 AD, there is virtually no Glacial or Littorina water remaining within the model domain.

Figure 4-30 shows the distribution of Glacial water. Again, it is clear that Glacial water initially fills the upper parts of the model domain. Then from 5000 BC, Littorina water starts flushing out the less dense Glacial water in the eastern parts of the model domain. From about 4000 BC, Altered Meteoric water starts to flush out Glacial water on-shore, as soon as land has started appearing in the higher western parts of the region. It can be seen in the time slices shown in Figure 4-30, that even though Glacial water is being flushed from the top of the model domain, there is still a fraction of Glacial water left at around depths of 600–1 100 m, indicating that flushing at great depths is a rather slow process.

Figure 4-31 shows the distribution of Inter-glacial water. Initially, Inter-glacial water is present at fractions of up to 0.3 at elevations between −300 and −1 800 metres above sea level. As the flushing processes progress with time, the fraction of Inter-glacial water gradually increases as this reference water diffuses out of the rock matrix.

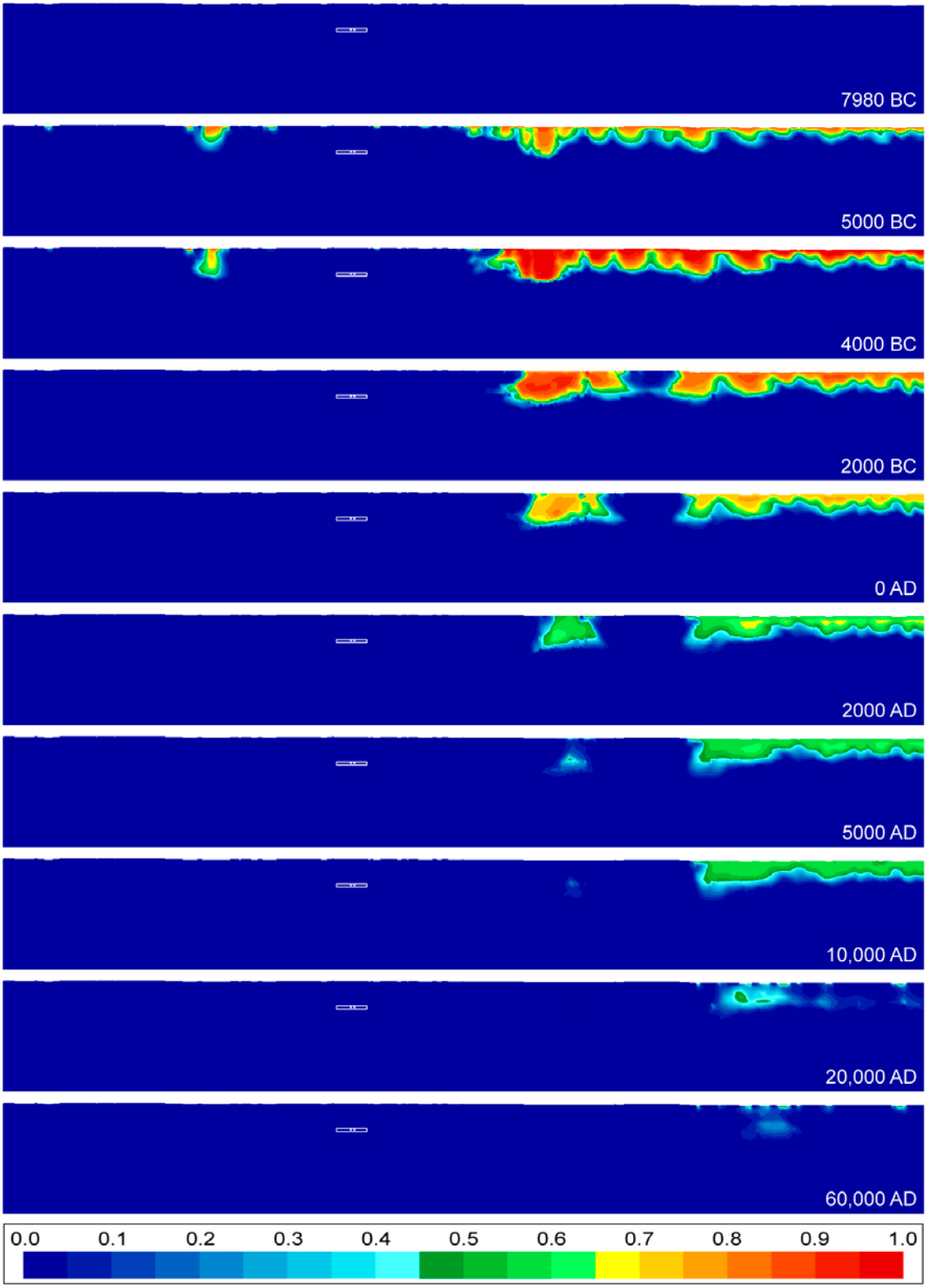

Figure 4-28. *Evolution of Littorina water shown as mixing fractions on vertical W-E slices through the repository volume for Case 1, HRD realisation 1, for dates (from top to bottom) 7980 BC, 5000 BC, 4000 BC, 2000 BC, 0 AD, 2000 AD, 5000 AD, 10 000 AD, 20 000 AD and 60 000 AD. The refined volume and repository vaults are shown in white.*

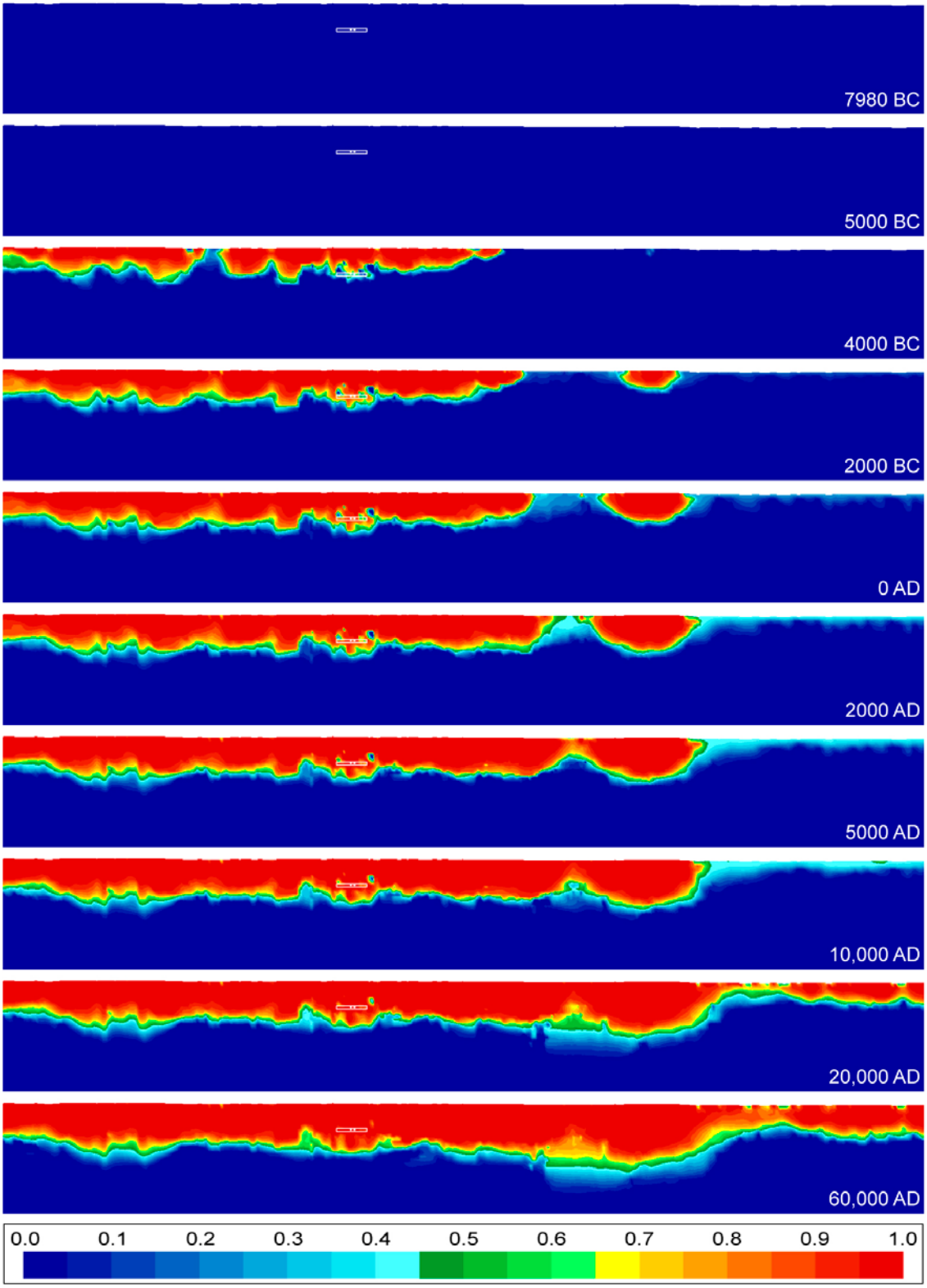

Figure 4-29. *Evolution of Altered Meteoric water shown as mixing fractions on vertical W-E slices through the repository volume for Case 1, HRD realisation 1, for dates (from top to bottom) 7980 BC, 5000 BC, 4000 BC, 2000 BC, 0 AD, 2000 AD, 5000 AD, 10 000 AD, 20 000 AD and 60 000 AD. The refined volume and repository vaults are shown in white.*

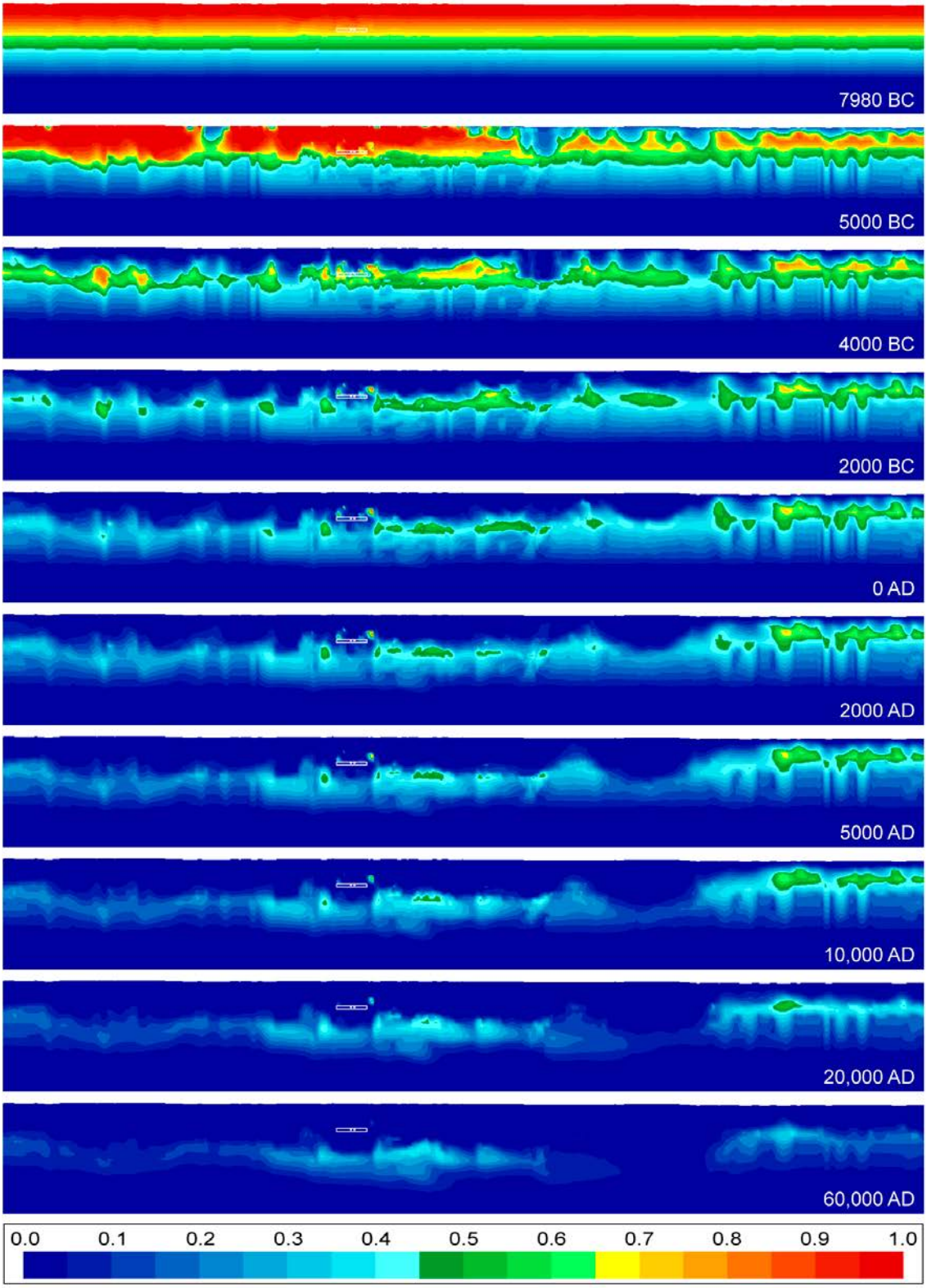

Figure 4-30. *Evolution of Glacial water shown as mixing fractions on vertical W-E slices through the repository volume for Case 1, HRD realisation 1, for dates (from top to bottom) 7980 BC, 5000 BC, 4000 BC, 2000 BC, 0 AD, 2000 AD, 5000 AD, 10 000 AD, 20 000 AD and 60 000 AD. The refined volume and repository vaults are shown in white.*

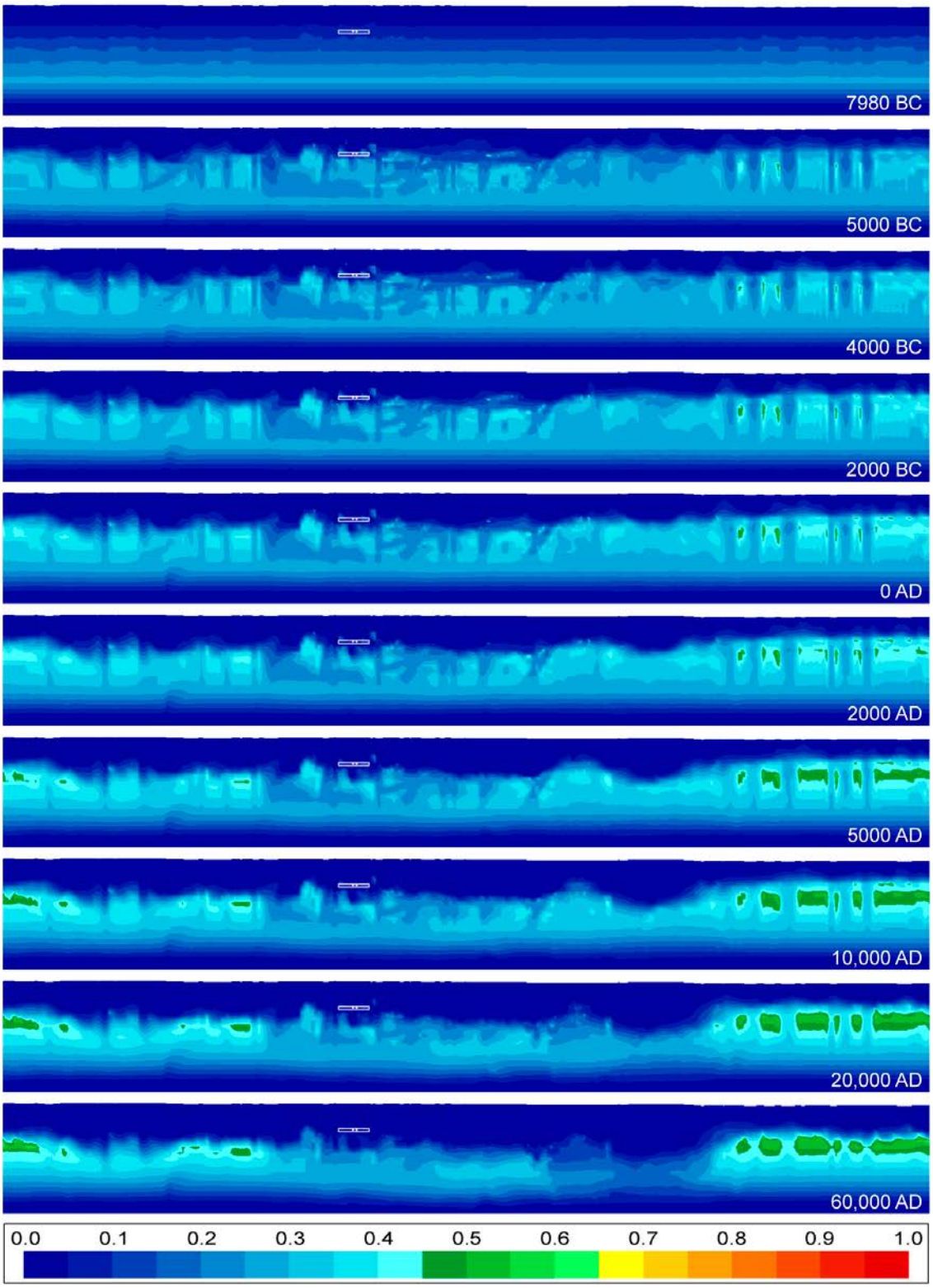

Figure 4-31. *Evolution of Inter-glacial water shown as mixing fractions on vertical W-E slices through the repository volume for Case 1, HRD realisation 1, for dates (from top to bottom) 7980 BC, 5000 BC, 4000 BC, 2000 BC, 0 AD, 2000 AD, 5000 AD, 10 000 AD, 20 000 AD and 60 000 AD. The refined volume and repository vaults are shown in white.*

4.3 Catchment focussed evolution of hydrogeochemistry

4.3.1 Presentation of results

Results are presented to illustrate the evolution of the groundwater composition and specific chemical conditions within the proposed repository volume and in the wider catchment scale context during an extended period of temperate climate conditions. The results are given at several times during the extended temperate climate period to illustrate the evolution over that period. For the presentation of reactive transport results (basic chemical parameters), results before the present time (2000 AD) are not included in the report, although the full evolution of groundwater composition from the initial conditions specified in Section 3.3.4 at 8000 BC is calculated. The interval between selected times is smaller at earlier times when the site is evolving more quickly.

The results from the reactive transport simulations (including Case 1, but without tracers) are reported in separate subsections for each of a selection of the basic chemical parameters; total dissolved solids (TDS), chloride, magnesium, sodium, pH, calcium, inorganic carbon, pE, sulphur/sulphide, and iron, using a combination of box and whisker plots and slices coloured in relation to selected chemical parameters.

Box and whisker plots are used to show comparisons of statistical distributions for the three modelled cases, for each basic chemical parameter. The chemical constituents of the groundwater are presented as total concentrations in grams per litre of solution, g/L.

In Case 1 no chemical reactions are included. Therefore, results are not shown for pH, pE, sulphide and iron for Case 1, since these chemical parameters are not relevant without chemical reactions.

For Case 3, only results for pE, sulphur and iron are shown, since, as expected, these are the only parameters that show any differences in values compared with Case 2.

The data underlying the box and whisker plots has been sampled on a regular grid of points within the refined part of the model corresponding to the repository volume between elevations −530 m and −470 m. Horizontally, the points reside within a domain with the following corner coordinates (1546690, 6367490); (1547290, 6367490); (1547290, 6366890); (1546690, 6366890). The points correspond to the corner nodes of the elements within the refined volume. The element size is 5 m cubed, which makes a total of 190 333 points. The statistical measures are the median, the 25th and 75th percentiles, the mean and the 5th and 95th percentiles.

The box and whisker plots show results for the selected time slices; 2000 AD, 3000 AD, 5000 AD, 10 000 AD, 20 000 AD, 30 000 AD, 40 000 AD, 50 000 AD and 60 000 AD.

In the respective subsection relating to each basic chemical parameter, a set of slices through the model is used to visualise the catchment scale evolution of the groundwater composition for the different cases. The slices are coloured in relation to pH, pE and the selected chemical constituents shown as mass fractions in kilograms per kilogram of solution, kg/kgs. Note that TDS and sulphide are not visualised using slices since these chemical parameters are not directly available in the ConnectFlow visualisation tool. The results are visualised using three main slices;

- A vertical catchment scale slice in the W-E direction, through the centre of the repository volume. For context, the refined volume and repository vaults are shown in white. The slice shows the model only down to an elevation of -1100 m and the vertical scale has been magnified by a factor 4 to improve the image resolution. The selected dates for this slice are 2000 AD, 5000 AD, 10 000 AD, 20 000 AD and 60 000 AD.
- A horizontal catchment scale slice through the centre of the repository volume at an elevation of −500 m. For context, the refined volume is shown in black and the shoreline is shown in white up to 20 000 AD. The selected dates for this slice are 2000 AD, 5000 AD, 10 000 AD, 20 000 AD, 40 000 AD and 60 000 AD;
- A close-up view of a horizontal slice through the centre of the repository volume at an elevation of −500 m. For context, the refined volume and repository vaults are shown in black. The selected dates for this slice are 2000 AD, 5000 AD, 10 000 AD, 20 000 AD, 40 000 AD and 60 000 AD.

A consistent value range is used for each chemical parameter within each presented slice type to allow for easy comparison between the cases and between the times considered. However, to improve visibility and resolution, the values range was changed for some of the chemical parameters presented in the close-up view slices, but still kept consistent between the cases.

4.3.2 TDS

Figure 4-32 shows a comparison of statistical distributions of total dissolved solids (TDS) for the three modelled cases. As expected, the TDS shows a gradual decrease over time, as the more dilute Altered Meteoric water infiltrates from the top, gradually diluting the slightly more saline water composition at repository depth at 2000 AD. Temporal changes are most prominent during the first 20 000 years after which the average salinity in the repository volume levels out, with a slightly decreasing spatial variability with time. This tendency is also shown for the reference water evolution in Figure 4-27 through Figure 4-31 (panes 6 through 10 for the time span 2000 AD to 60 000 AD). There are very small differences in the TDS evolution between Case 1 (transport and mixing of groundwater components only) and Cases 2 and 3 where chemical reactions in the water phase and with rock minerals are included. This indicates that the evolution of the salinity is only to a minor extent influenced by chemical reactions. Instead, the results suggest that the TDS evolution in the repository volume is controlled mainly by the transport and mixing of solutes. Also, on a catchment scale, the TDS evolution for Cases 2 (Figure 4-35 and Figure 4-36) and 3 (not shown) is visually identical to Case 1 (Figure 4-33 and Figure 4-34) where chemical reactions are not included. This further supports the conclusion that the evolution of groundwater salinity is transport-controlled, not only in the repository volume but also on a catchment scale.

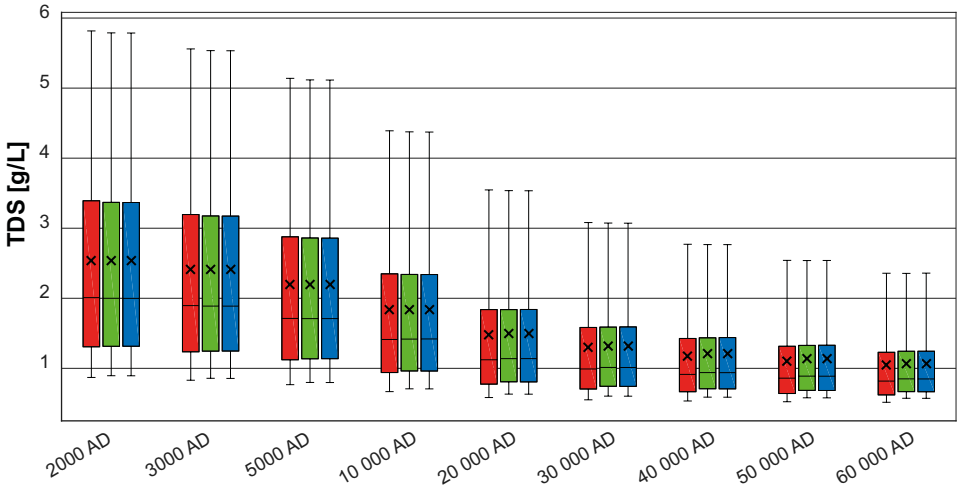

Figure 4-32. *Box and whisker plot showing a comparison of statistical distributions of TDS for the three cases (Case 1 – red, Case 2 – green, Case 3 – blue) on a regular grid of points within the repository volume between elevations −530 m and −470 m. The statistical measures are the median, the 25th and 75th percentiles (box), the mean (cross) and the 5th and 95th percentiles (whiskers).*

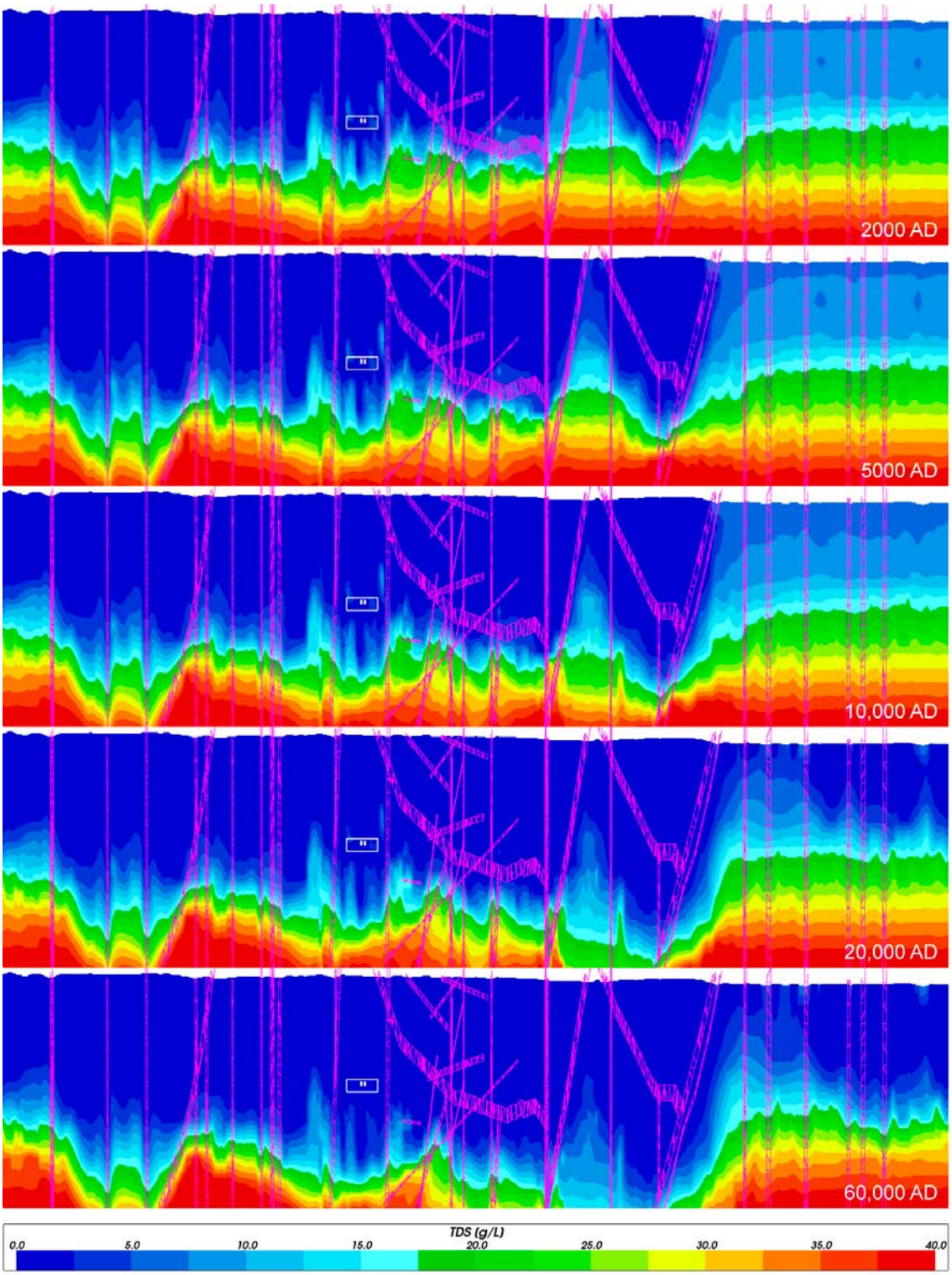

Figure 4-33. *Values of TDS on vertical W-E catchment scale slices through the repository volume for Case 1, for dates (from top to bottom) 2000 AD, 5000 AD, 10 000 AD, 20 000 AD and 60 000 AD. The refined volume and repository vaults are shown in white. The deformation zones are superimposed in purple. Model shown down to an elevation of -1100 m. Vertical scale has been magnified by a factor of 4.*

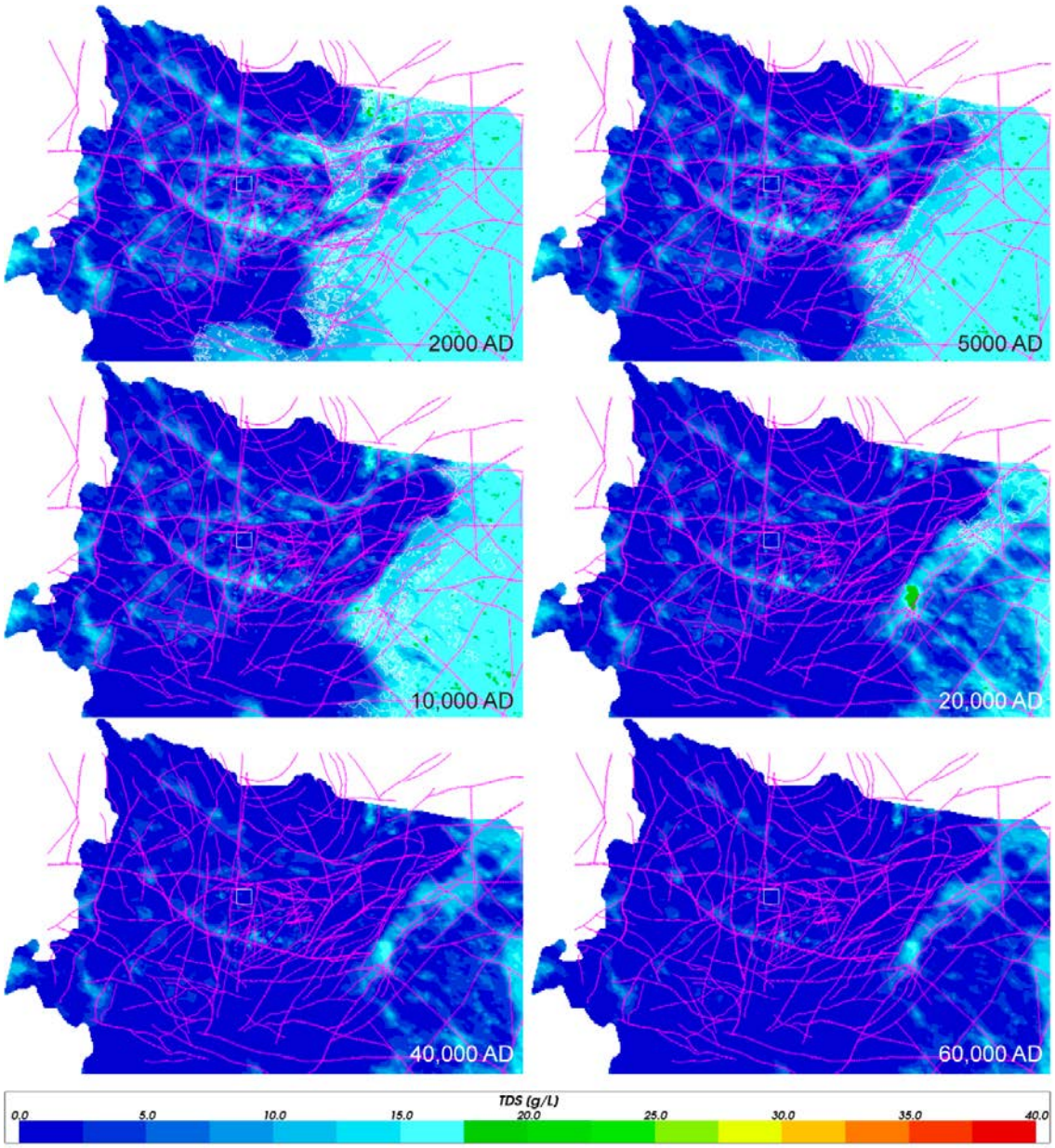

Figure 4-34. *Values of TDS on horizontal catchment scale slices at an elevation of -500 m through the repository volume for Case 1, for dates (from left to right, top to bottom) 2000 AD, 5000 AD, 10 000 AD, 20 000 AD, 40 000 AD and 60 000 AD. The refined volume and the shoreline (up to 20 000 AD) are shown in white. The deformation zones are superimposed in purple.*

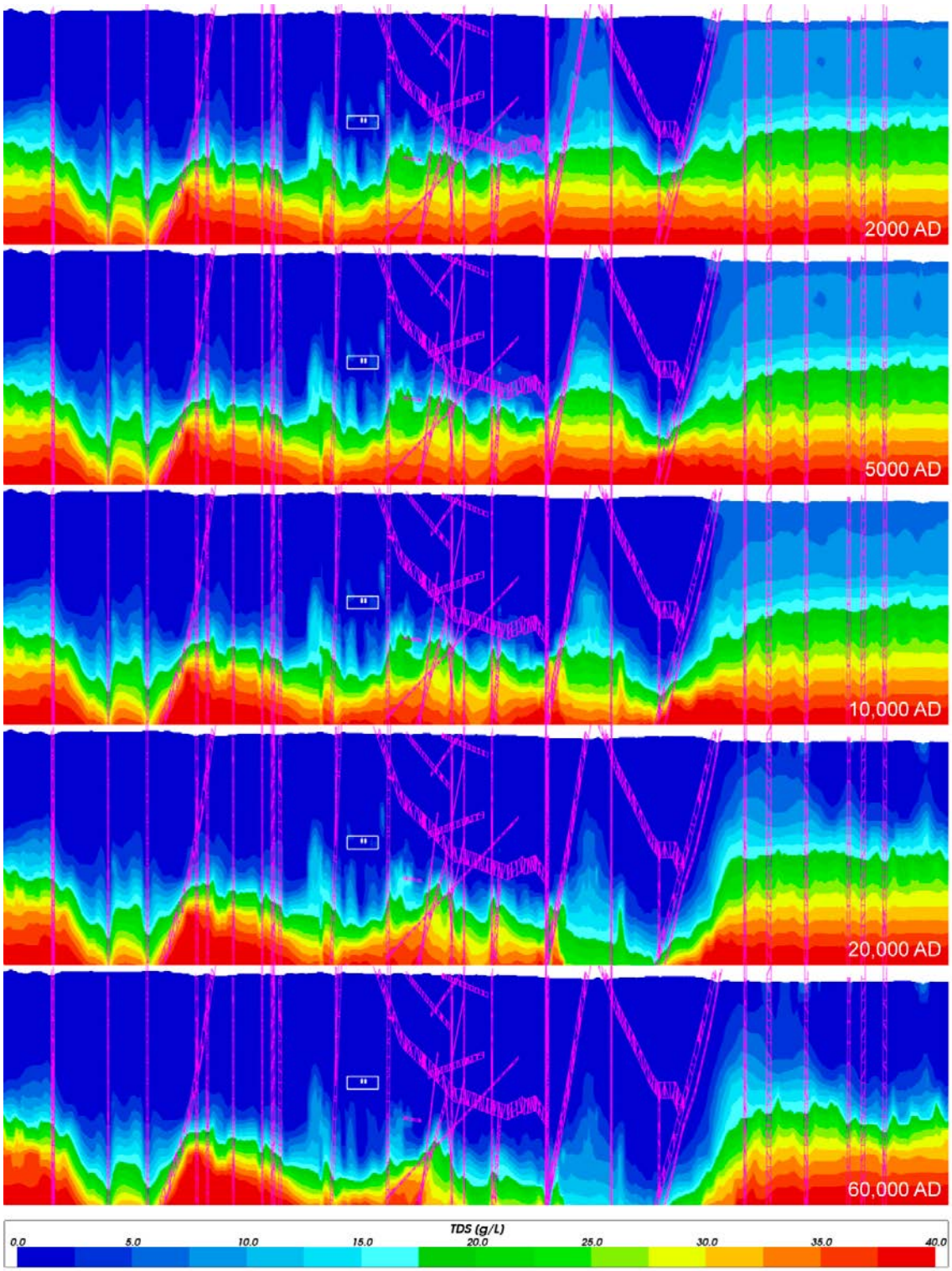

Figure 4-35. *Values of TDS on vertical W-E catchment scale slices through the repository volume for Case 2, for dates (from top to bottom) 2000 AD, 5000 AD, 10 000 AD, 20 000 AD and 60 000 AD. The refined volume and repository vaults are shown in white. The deformation zones are superimposed in purple. Model shown down to an elevation of -1100 m. Vertical scale has been magnified by a factor of 4.*

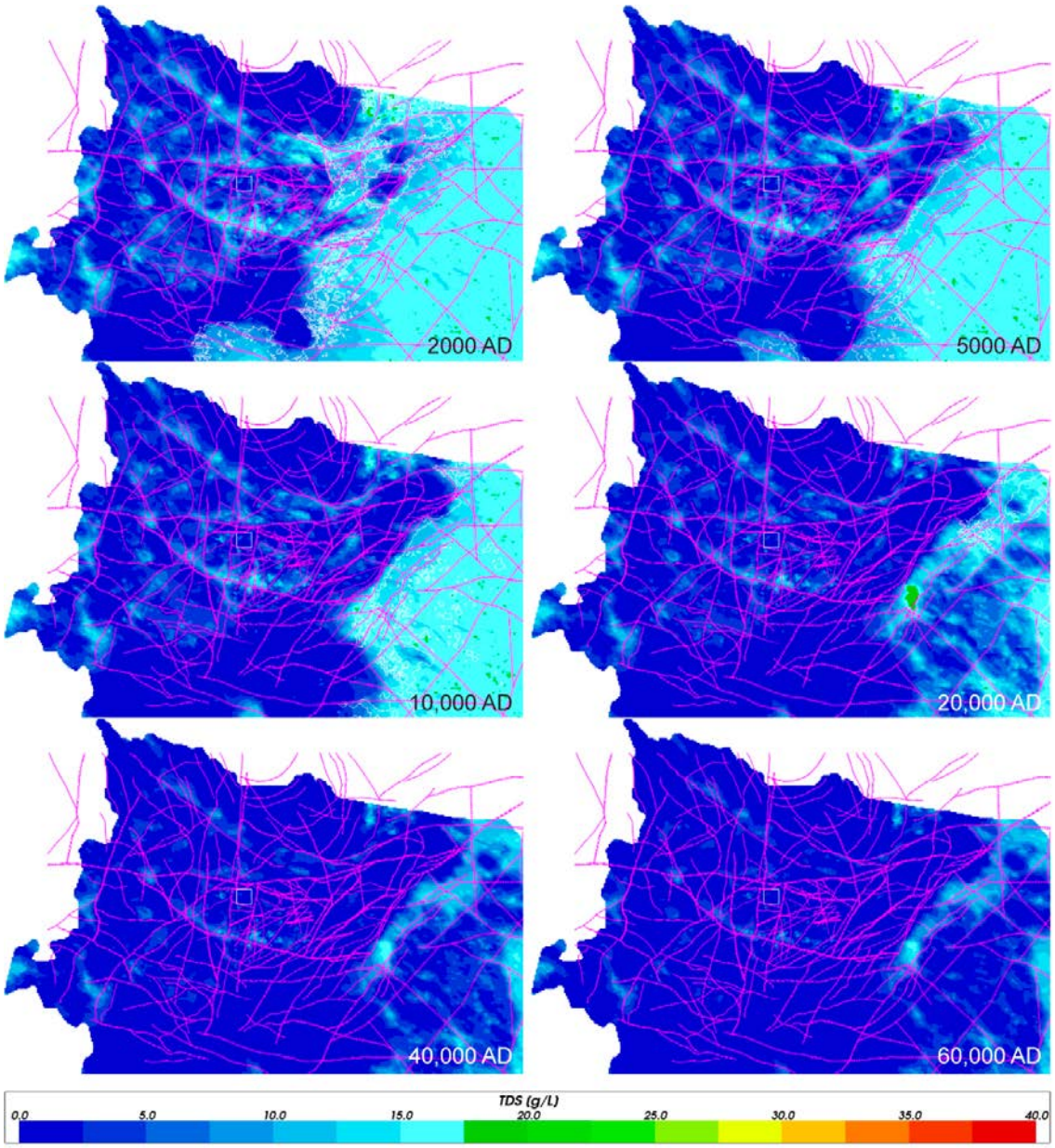

Figure 4-36. *Values of TDS on horizontal catchment scale slices at an elevation of -500 m through the repository volume for Case 2, for dates (from left to right, top to bottom) 2000 AD, 5000 AD, 10 000 AD, 20 000 AD, 40 000 AD and 60 000 AD. The refined volume and the shoreline (up to 20 000 AD) are shown in white. The deformation zones are superimposed in purple.*

The effect of hydraulically conductive zones on the catchment scale is visible in Figure 4-33 and Figure 4-34 (Case 1), and Figure 4-35 and Figure 4-36 (Case 2). These figures indicate a relatively large degree of spatial heterogeneity within the catchment scale domain where dilute areas coincide with the deformation zones included in the model (shown in purple). East of the repository volume in the area below the sea (right side of the vertical slices in Figure 4-33 and Figure 4-35), upconing of more saline groundwater along fracture zones is evident up to 20 000 AD as the shoreline is retreating due to land rise until it reaches the boundary of the catchment focussed model. Beyond 20 000 AD, the shoreline is outside the catchment scale domain and the model is unchanging apart from continued infiltration of Altered Meteoric water. It should be noted that deterministic deformation zones explicitly represented in the model only partly explain the spatial variability.

The network of connected fractures, stochastically generated in each fracture set realization, is also important and is the main reason for the spatial variability in the repository volume, which is not intersected by deterministic deformation zones (see the small rectangle indicating the location of the repository volume in the slice figures). At repository depth, the spatial heterogeneity of salinity gradually decreases with time as seen from the horizontal slices in Figure 4-34 (Case 1) and Figure 4-36 (Case 2).

Penetration of dilute water is delayed by the retardation effects of rock matrix diffusion and by buoyancy effects caused by the presence of water with higher salinity below repository depth. A high salinity at depth is maintained by the fixed composition boundary condition on the bottom surface of the model, which is consistent with the site conceptual understanding. These effects limit the changes in groundwater composition caused by penetration of Altered Meteoric water beyond 20 000 AD.

4.3.3 Chloride

Figure 4-37 shows a comparison of statistical distributions of total chloride concentrations for the three modelled cases. As expected, the spatial and temporal evolution of chloride concentrations coincides with the TDS evolution shown in Subsection 4.3.2. A general trend with a gradual decrease in chloride concentration with time is seen in the repository volume as Altered Meteoric water infiltrates from the top boundary, diluting the groundwater dominating in the repository volume at 2000 AD. The average concentration levels-out at later times after approximately 20 000 years. Also, the spatial variability decreases with time. After 20 000 years, the shoreline is displaced outside the catchment scale domain, with infiltration of altered meteoric water everywhere at the top boundary where there is recharge.

As for the TDS, no significant differences are seen between Cases 1 (transport and mixing of groundwater components only) and Cases 2 and 3, where chemical reactions are included. This shows that the evolution of the chloride concentration is controlled by the transport and mixing of solutes, since chloride is not involved in any of the chemical reactions considered. Also, on a catchment scale (Figure 4-38 through Figure 4-43), no significant differences between the modelled cases can be seen and the influence of hydraulically conductive deformation zones is the same as discussed for salinity in Subsection 4.3.2.

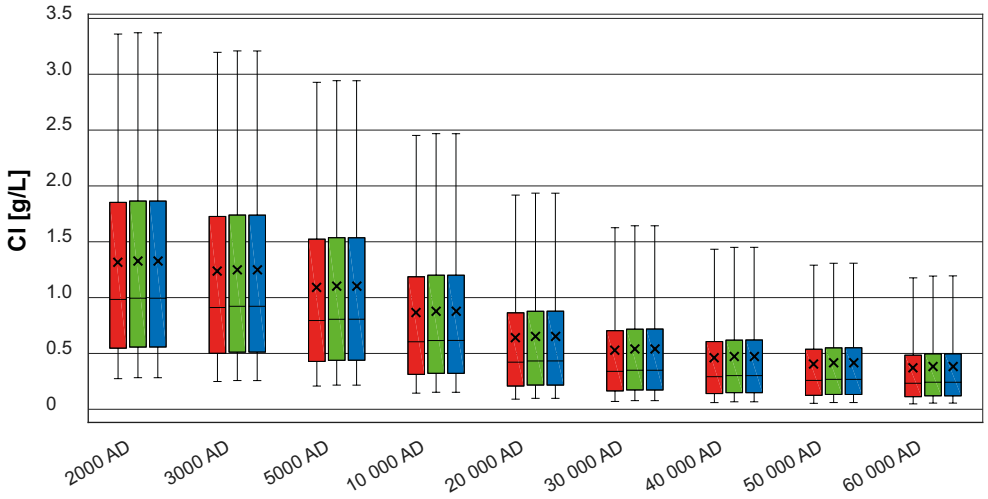

Figure 4-37. *Box and whisker plot showing a comparison of statistical distributions of total chloride concentrations for the three cases (Case 1 – red, Case 2 – green, Case 3 – blue) on a regular grid of points within the repository volume between elevations −530 m and −470 m. The statistical measures are the median, the 25th and 75th percentiles (box), the mean (cross) and the 5th and 95th percentiles (whiskers).*

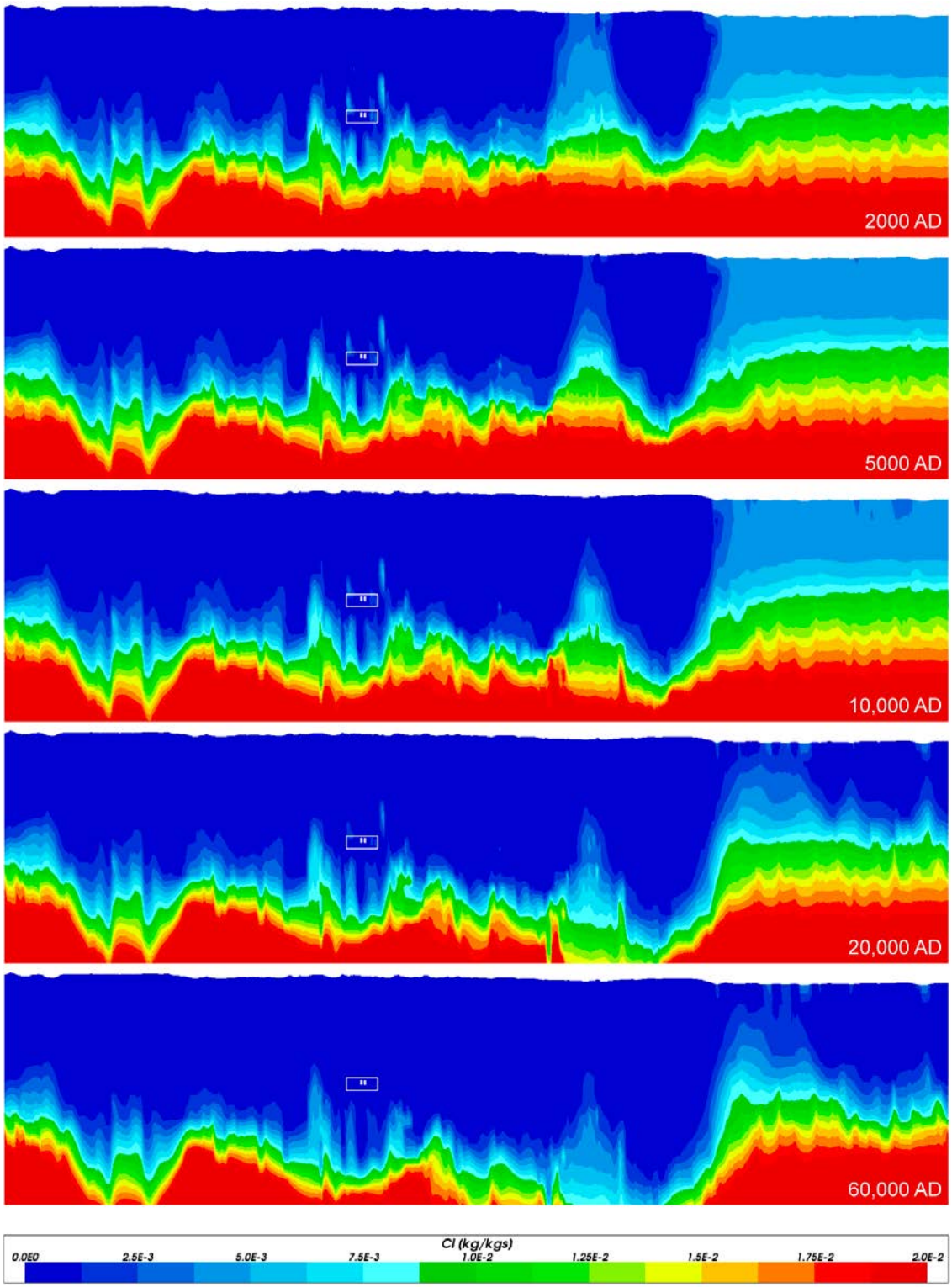

Figure 4-38. *Total chloride mass fractions on vertical W-E catchment scale slices through the repository volume for Case 1, for dates (from top to bottom) 2000 AD, 5000 AD, 10 000 AD, 20 000 AD and 60 000 AD. The refined volume and repository vaults are shown in white. Model shown down to an elevation of −1 100 m. Vertical scale has been magnified by a factor of 4.*

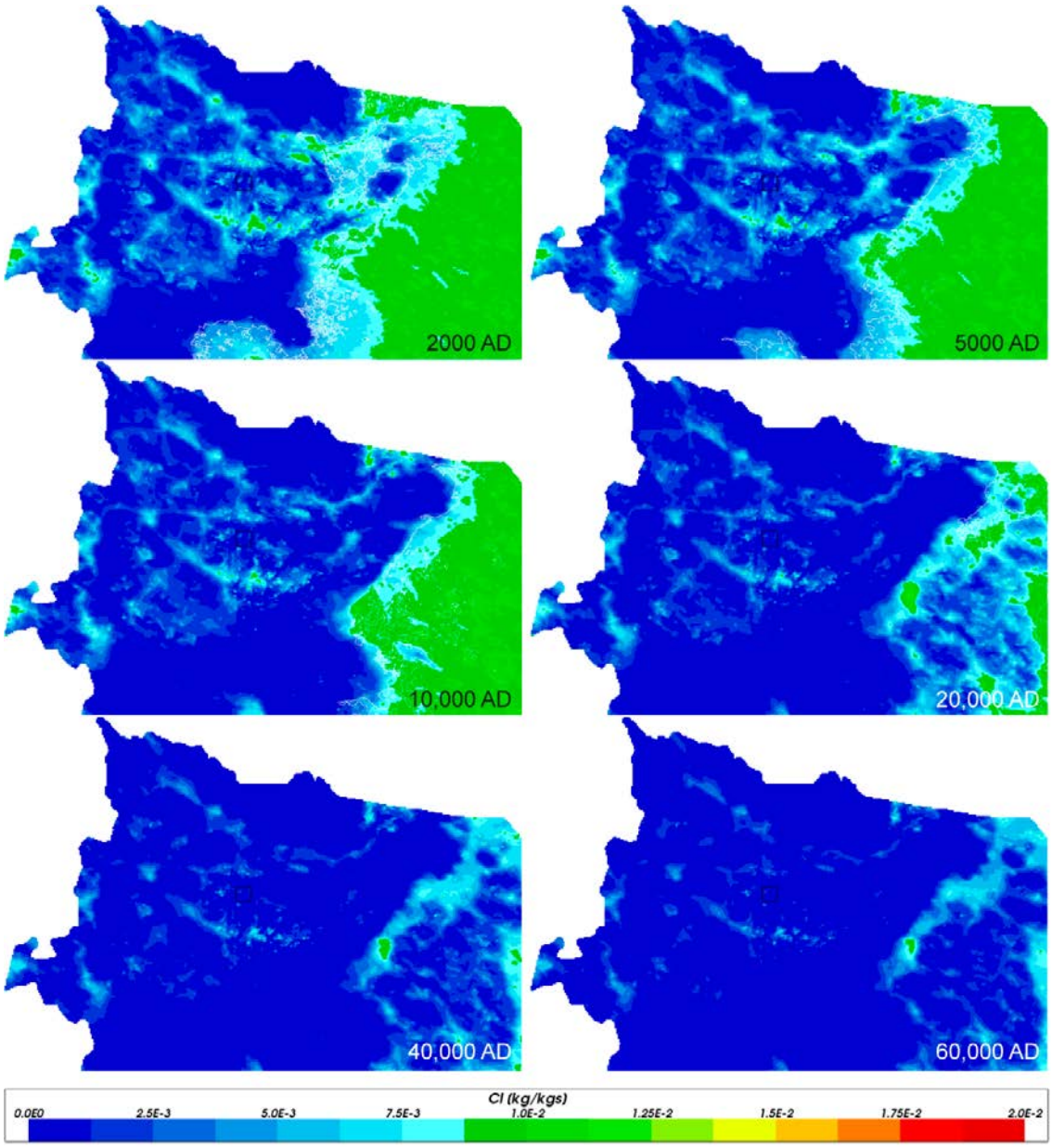

Figure 4-39. *Total chloride mass fractions on horizontal catchment scale slices at an elevation of −500 m through the repository volume for Case 1, for dates (from left to right, top to bottom) 2000 AD, 5000 AD, 10 000 AD, 20 000 AD, 40 000 AD and 60 000 AD. The refined volume is shown in black and the shoreline is shown in white up to 20 000 AD.*

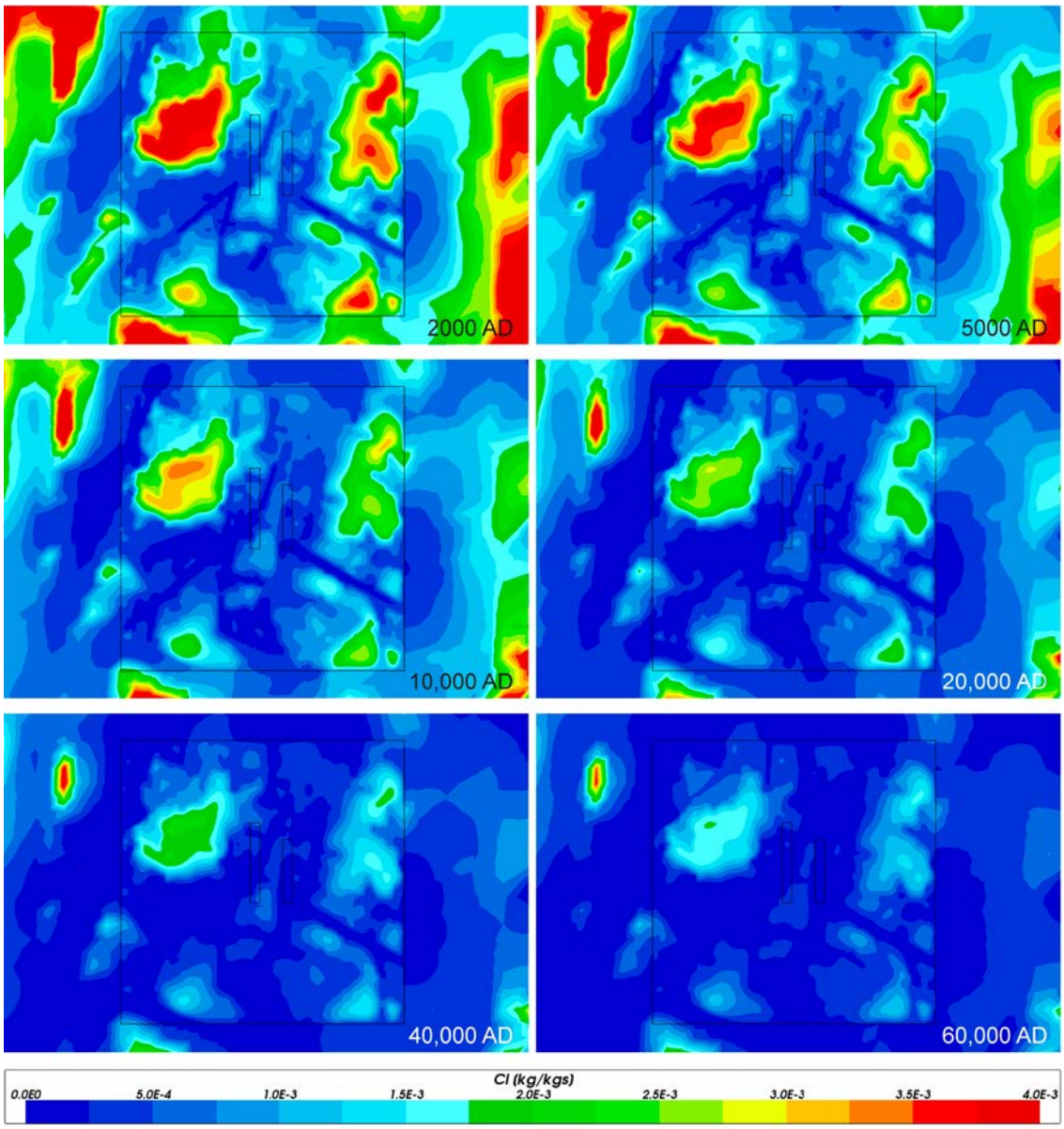

Figure 4-40. *Close-up view of total chloride mass fractions on horizontal slices at an elevation of −500 m through the repository volume for Case 1, for dates (from left to right, top to bottom) 2000 AD, 5000 AD, 10 000 AD, 20 000 AD, 40 000 AD and 60 000 AD. The refined volume and repository vaults are shown in black.*

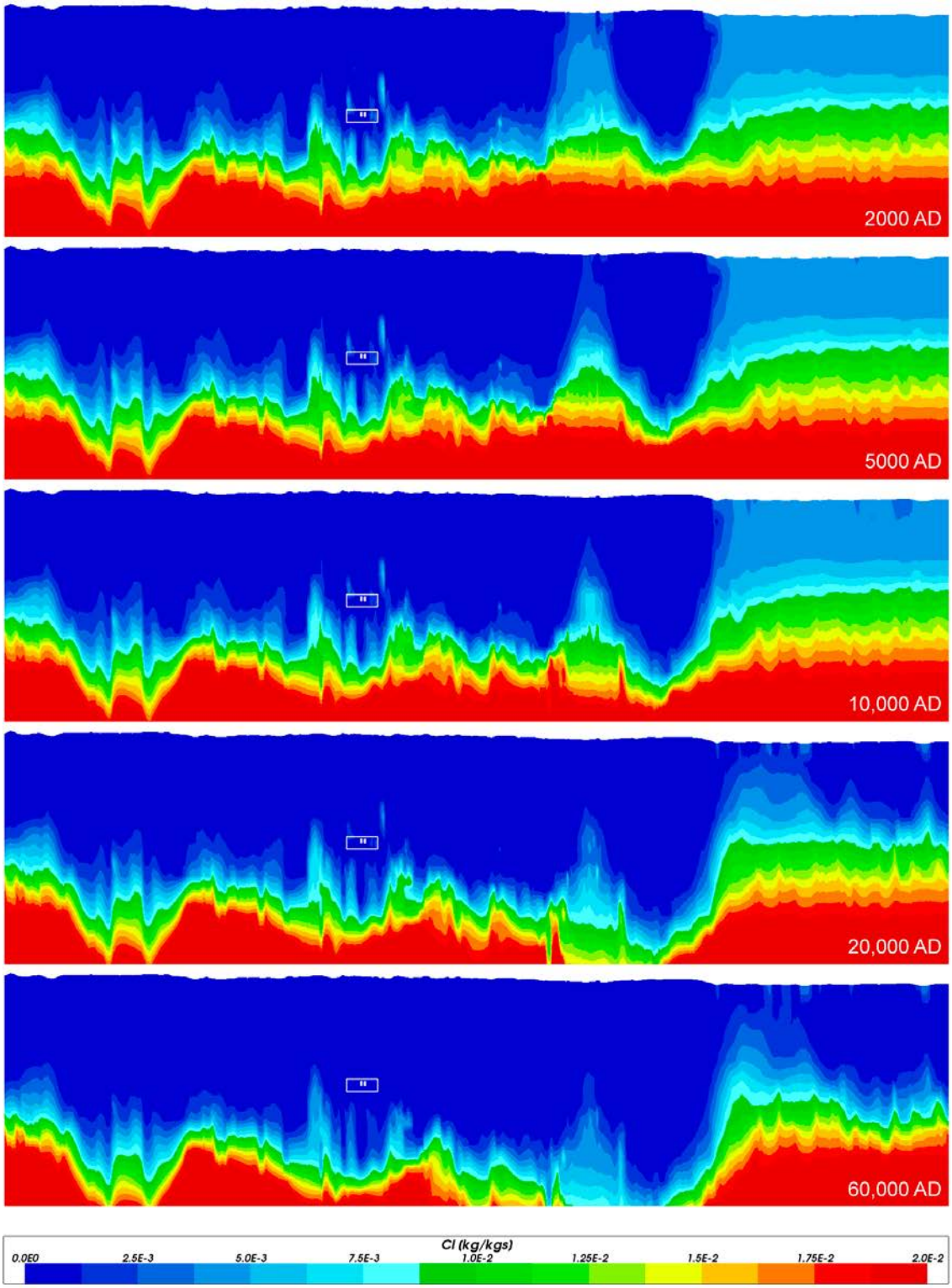

Figure 4-41. *Total chloride mass fractions on vertical W-E catchment scale slices through the repository volume for Case 2, for dates (from top to bottom) 2000 AD, 5000 AD, 10 000 AD, 20 000 AD and 60 000 AD. The refined volume and repository vaults are shown in white. Model shown down to an elevation of −1 100 m. Vertical scale has been magnified by a factor of 4.*

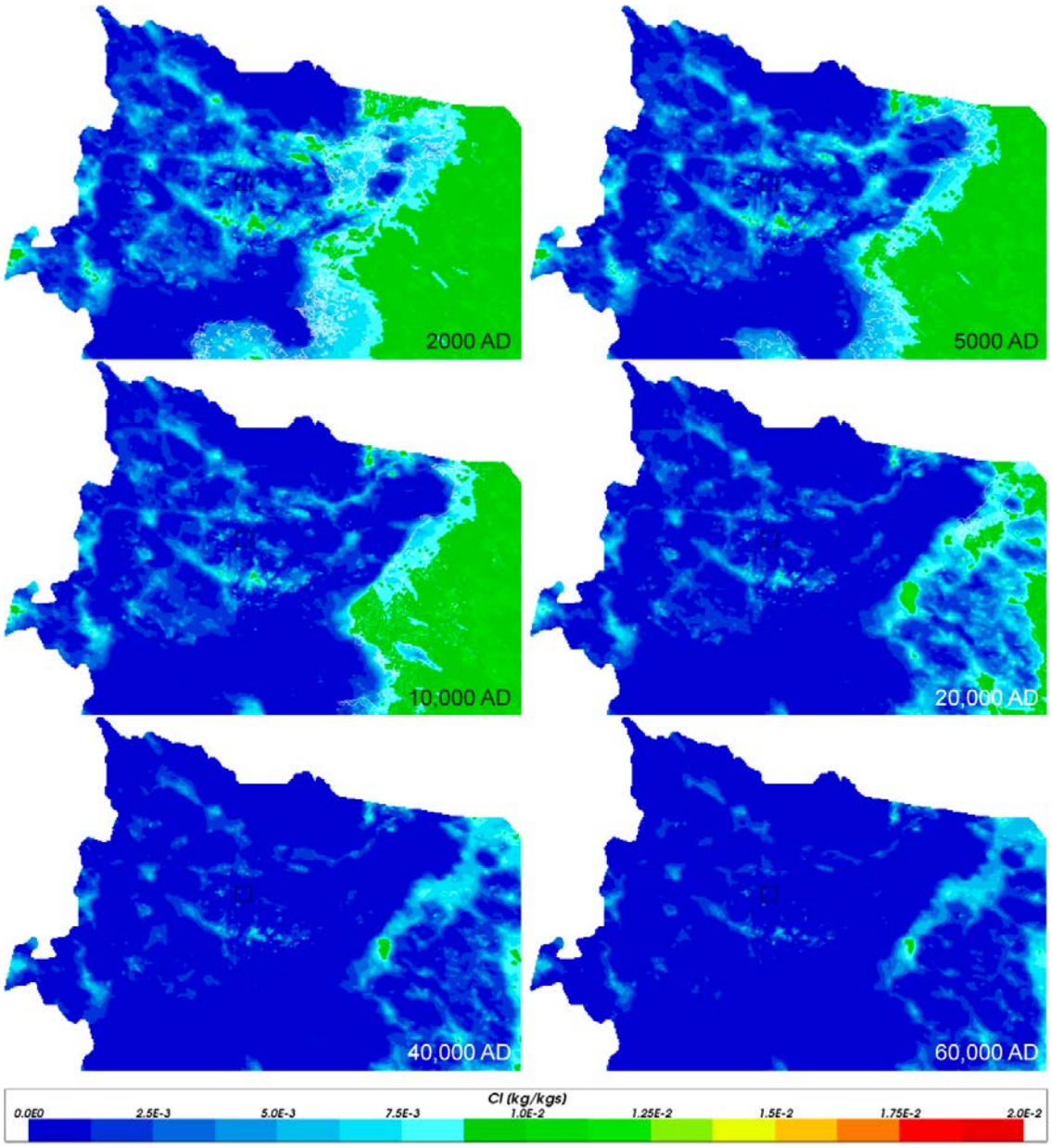

Figure 4-42. *Total chloride mass fractions on horizontal catchment scale slices at an elevation of −500 m through the repository volume for Case 2, for dates (from left to right, top to bottom) 2000 AD, 5000 AD, 10 000 AD, 20 000 AD, 40 000 AD and 60 000 AD. The refined volume is shown in black and the shoreline is shown in white up to 20 000 AD.*

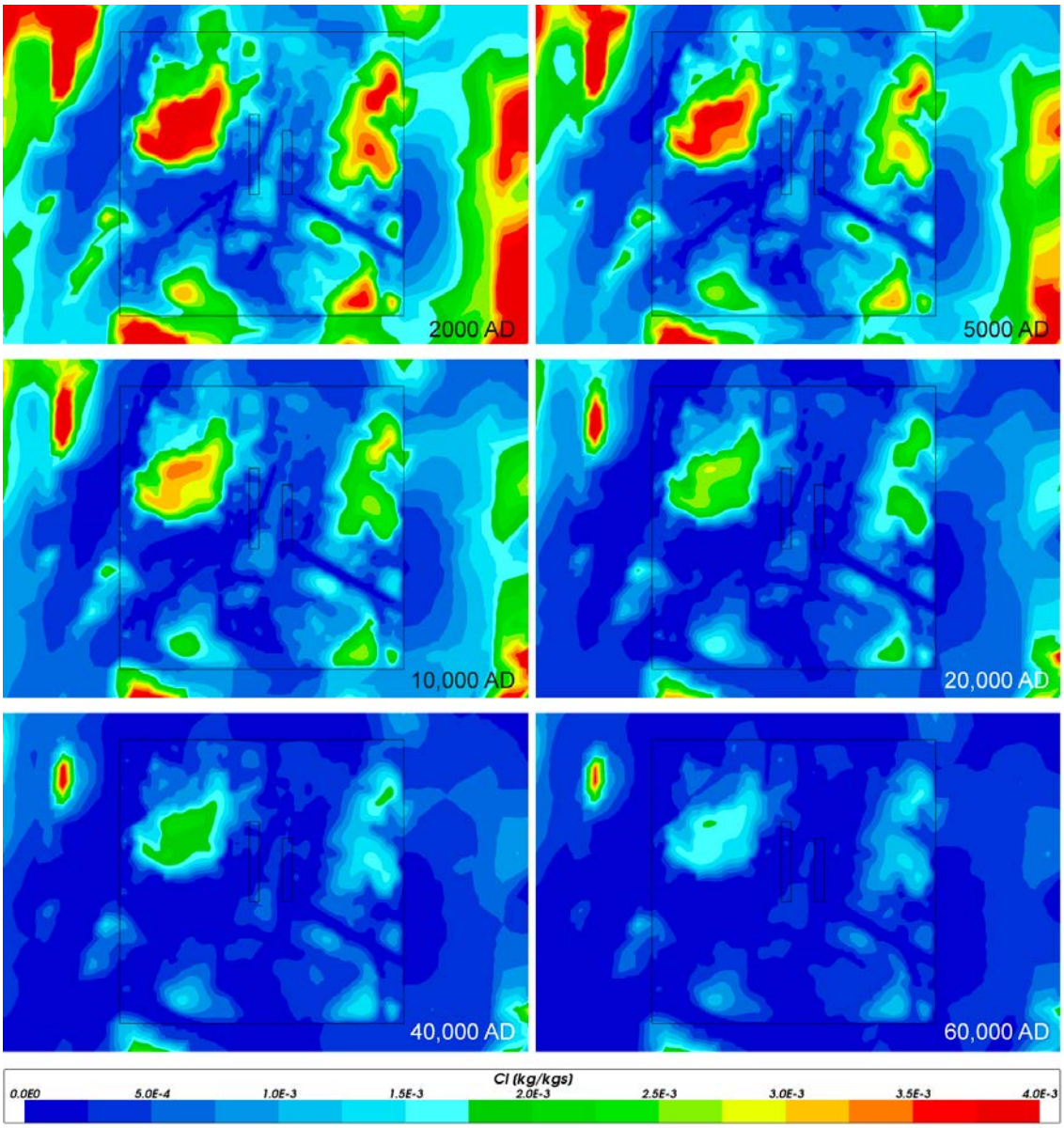

Figure 4-43. *Close-up view of total chloride mass fractions on horizontal slices at an elevation of −500 m through the repository volume for Case 2, for dates (from left to right, top to bottom) 2000 AD, 5000 AD, 10 000 AD, 20 000 AD, 40 000 AD and 60 000 AD. The refined volume and repository vaults are shown in black.*

4.3.4 Magnesium

Figure 4-44 shows a comparison of statistical distributions of total magnesium concentrations for the three modelled cases. The results for magnesium are visually identical for all three cases confirming that chemical reactions have no influence on the magnesium content in the groundwater. This is as expected, as none of the mineral reactions included in Cases 2 and 3 involve magnesium. The general trend of magnesium concentrations in the repository volume increasing with time is due to the Altered Meteoric water infiltrating from the ground surface. The Altered Meteoric water has a higher magnesium concentration than the water present in the repository volume at 2000 AD. Figure 4-45 through Figure 4-50 show magnesium mass fractions in the groundwater on a catchment scale for Cases 1 and 2. The catchment scale slices show no difference between Cases 2 and 3. East of the repository volume residual Littorina water with higher Mg concentrations is seen at the early times. As the shoreline is displaced outside the model domain after 20 000 AD, this water is gradually diluted with the infiltrating Altered Meteoric water.

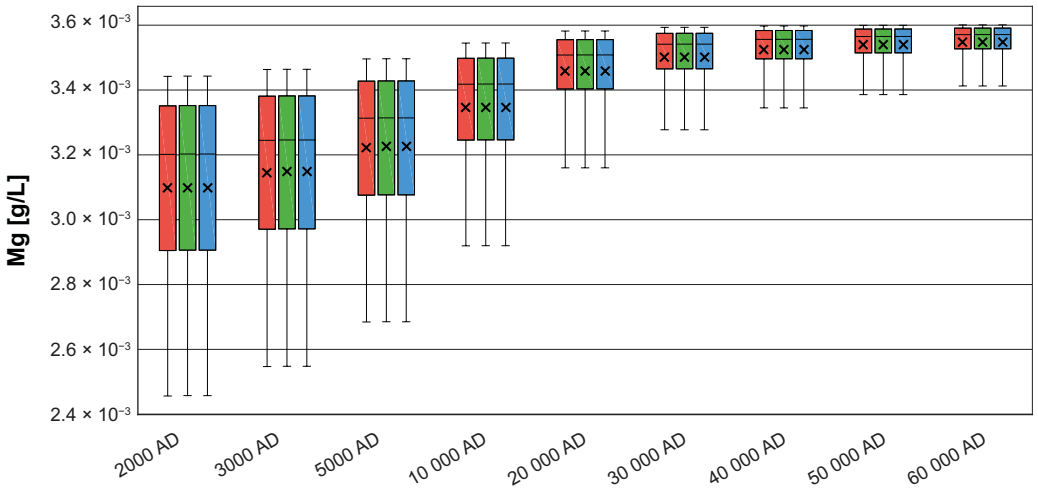

Figure 4-44. *Box and whisker plot showing a comparison of statistical distributions of total magnesium concentrations for the three cases (Case 1 – red, Case 2 – green, Case 3 – blue) on a regular grid of points within the repository volume between elevations −530 m and −470 m. The statistical measures are the median, the 25th and 75th percentiles (box), the mean (cross) and the 5th and 95th percentiles (whiskers).*

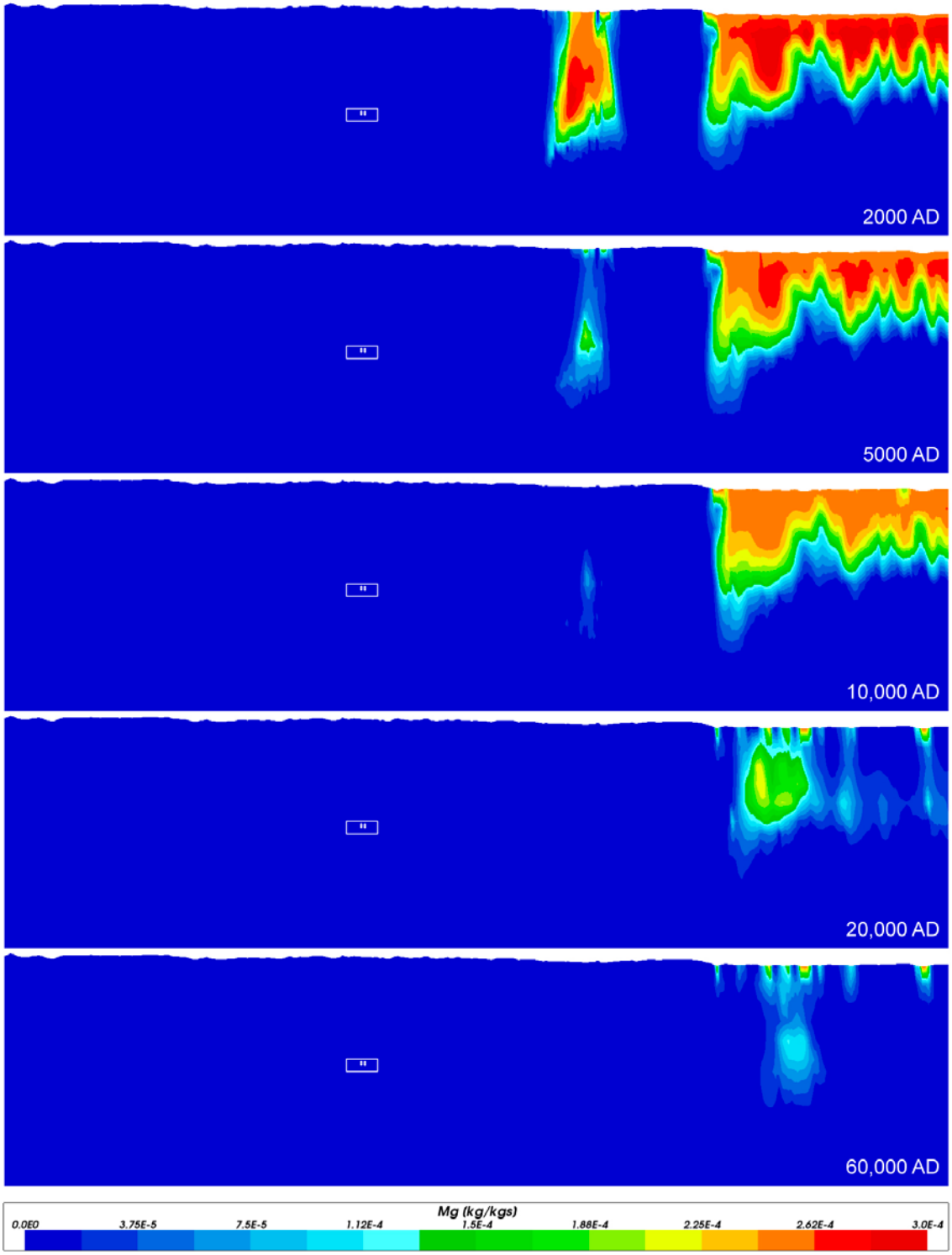

Figure 4-45. *Total magnesium mass fractions on vertical W-E catchment scale slices through the repository volume for Case 1, for dates (from top to bottom) 2000 AD, 5000 AD, 10 000 AD, 20 000 AD and 60 000 AD. The refined volume and repository vaults are shown in white. Model shown down to an elevation of −1 100 m. Vertical scale has been magnified by a factor of 4.*

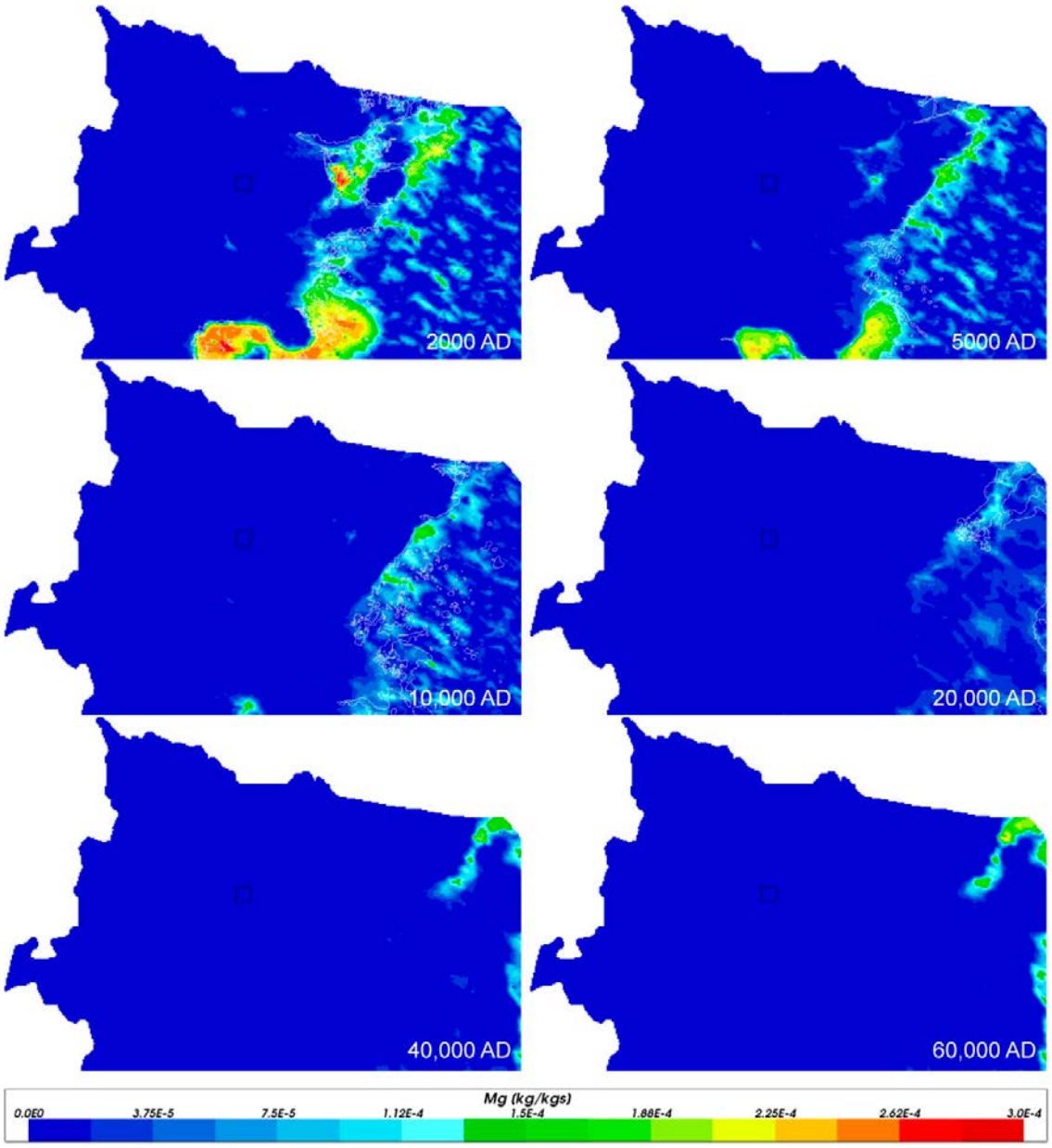

Figure 4-46. *Total magnesium mass fractions on horizontal catchment scale slices at an elevation of −500 m through the repository volume for Case 1, for dates (from left to right, top to bottom) 2000 AD, 5000 AD, 10 000 AD, 20 000 AD, 40 000 AD and 60 000 AD. The refined volume is shown in black and the shoreline is shown in white up to 20 000 AD.*

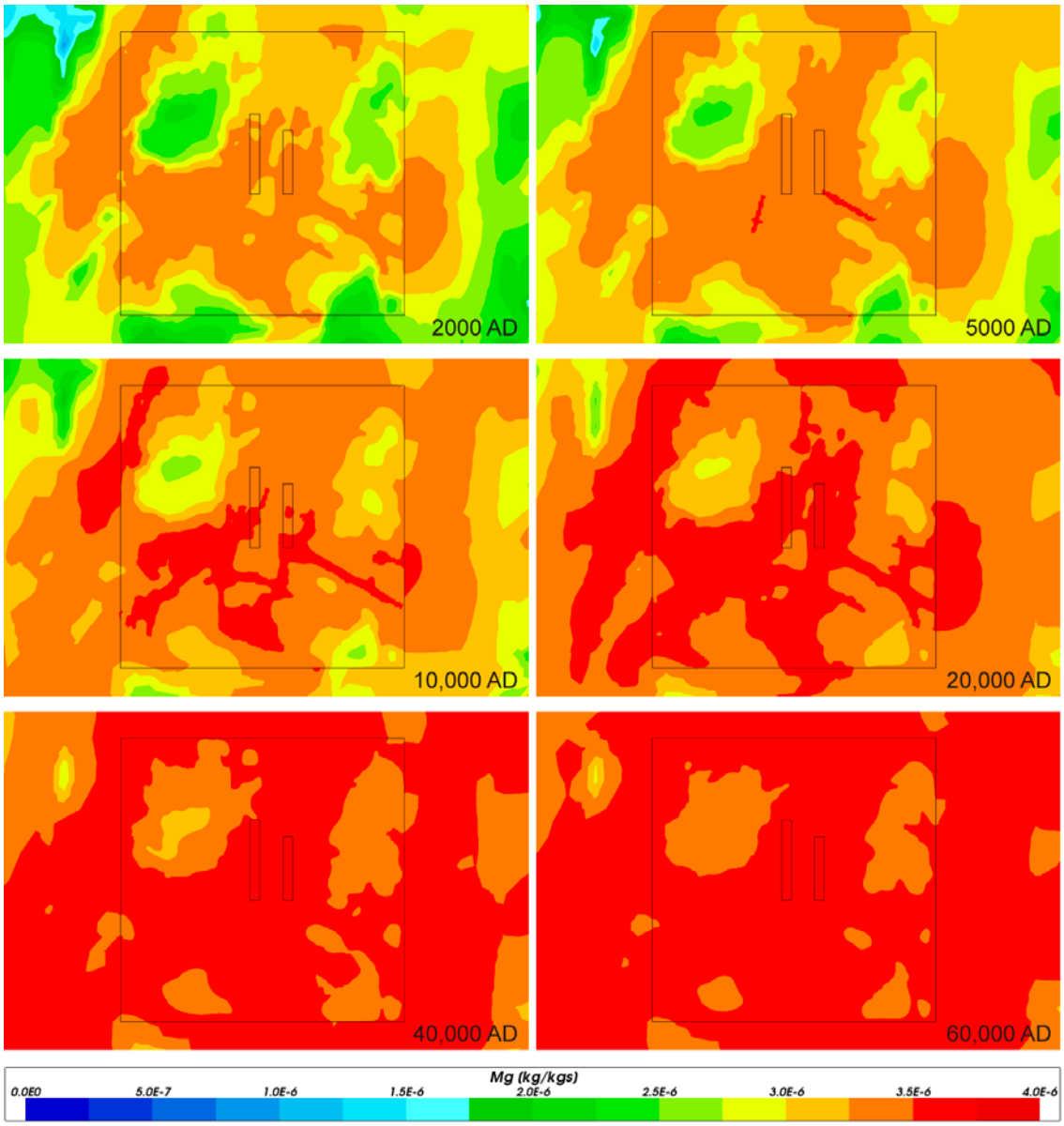

Figure 4-47. *Close-up view of total magnesium mass fractions on horizontal slices at an elevation of −500 m through the repository volume for Case 1, for dates (from left to right, top to bottom) 2000 AD, 5000 AD, 10 000 AD, 20 000 AD, 40 000 AD and 60 000 AD. The refined volume and repository vaults are shown in black. Note that the range of concentrations is much lower than that shown in Figure 4-46.*

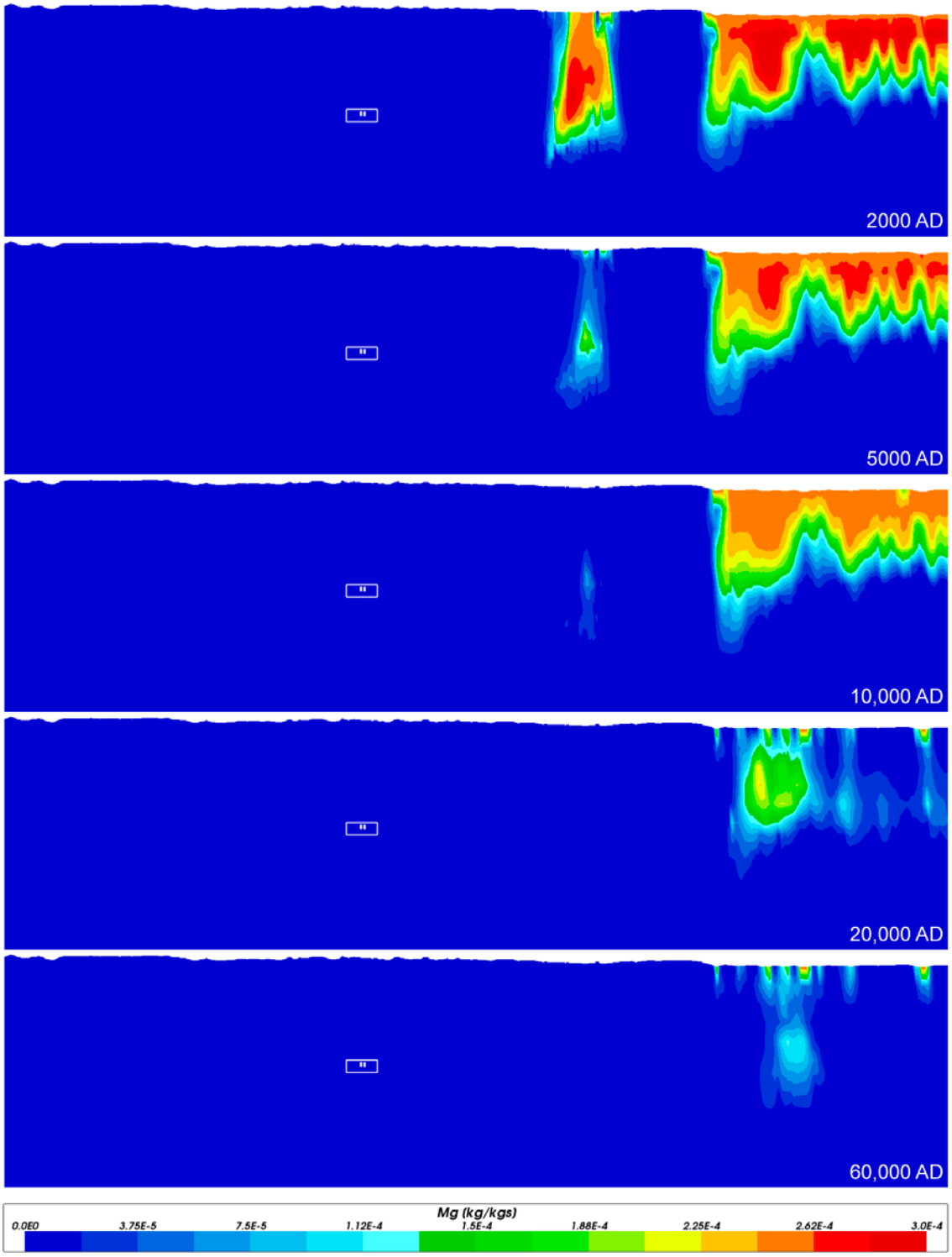

Figure 4-48. *Total magnesium mass fractions on vertical W-E catchment scale slices through the repository volume for Case 2, for dates (from top to bottom) 2000 AD, 5000 AD, 10 000 AD, 20 000 AD and 60 000 AD. The refined volume and repository vaults are shown in white. Model shown down to an elevation of −1 100 m. Vertical scale has been magnified by a factor of 4.*

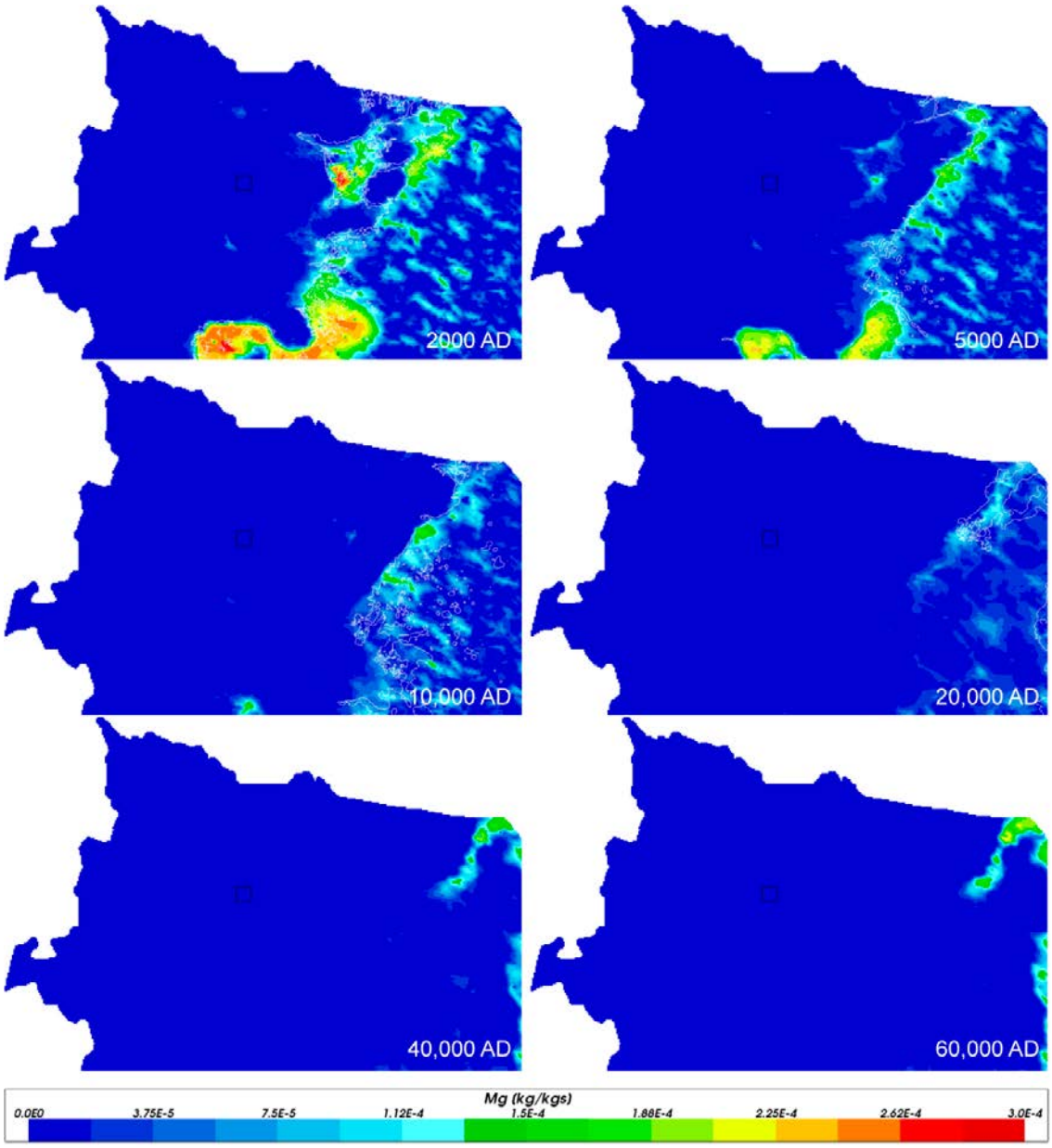

Figure 4-49. *Total magnesium mass fractions on horizontal catchment scale slices at an elevation of −500 m through the repository volume for Case 2, for dates (from left to right, top to bottom) 2000 AD, 5000 AD, 10 000 AD, 20 000 AD, 40 000 AD and 60 000 AD. The refined volume is shown in black and the shoreline is shown in white up to 20 000 AD.*

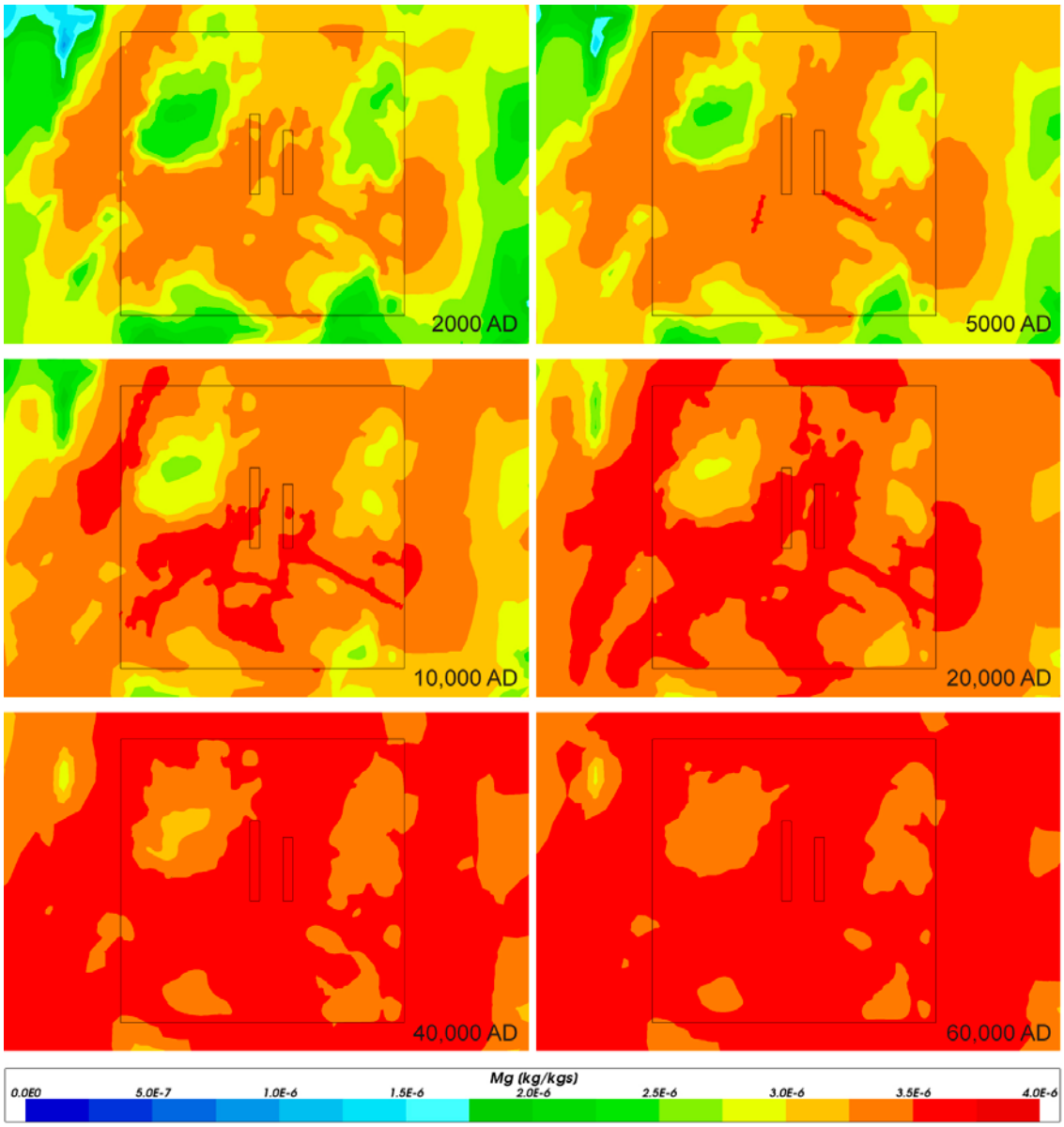

Figure 4-50. *Close-up view of total magnesium mass fractions on horizontal slices at an elevation of −500 m through the repository volume for Case 2, for dates (from left to right, top to bottom) 2000 AD, 5000 AD, 10 000 AD, 20 000 AD, 40 000 AD and 60 000 AD. The refined volume and repository vaults are shown in black. Note that the range of concentrations is much lower than that shown in Figure 4-49.*

4.3.5 Sodium

Figure 4-51 shows a comparison of statistical distributions of total sodium concentrations for the three cases. The results for sodium are visually identical for all three cases confirming that chemical reactions have no influence on the sodium content in the groundwater. This is as expected, as none of the mineral reactions considered in Cases 2 and 3 involve sodium. The general trend of sodium concentrations in the repository volume decreasing with time is due to the Altered Meteoric water infiltrating from the ground surface diluting the water present in the repository volume at 2000 AD.

Figure 4-52 through Figure 4-57 show sodium mass fractions in the groundwater on a catchment scale for Cases 1 and 2.

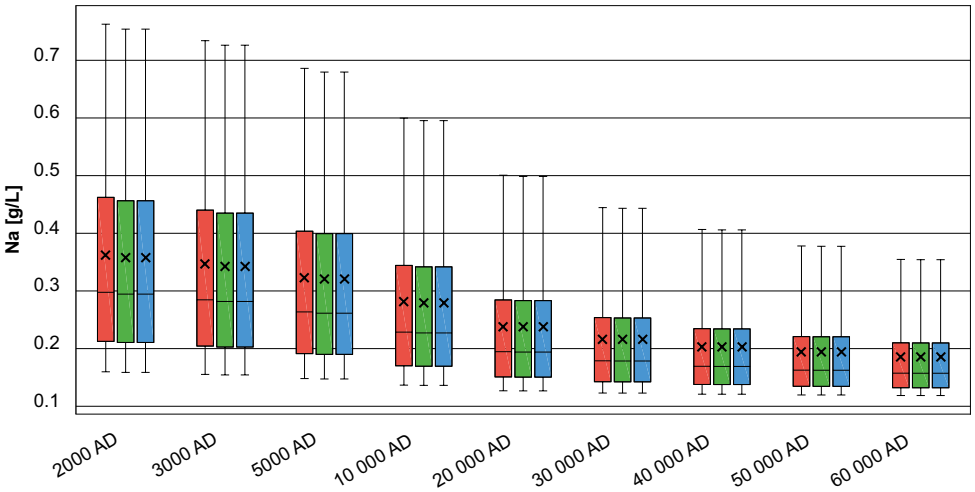

Figure 4-51. *Box and whisker plot showing a comparison of statistical distributions of total sodium concentrations for the three cases (Case 1 – red, Case 2 – green, Case 3 – blue) on a regular grid of points within the repository volume between elevations −530 m and −470 m. The statistical measures are the median, the 25th and 75th percentiles (box), the mean (cross) and the 5th and 95th percentiles (whiskers).*

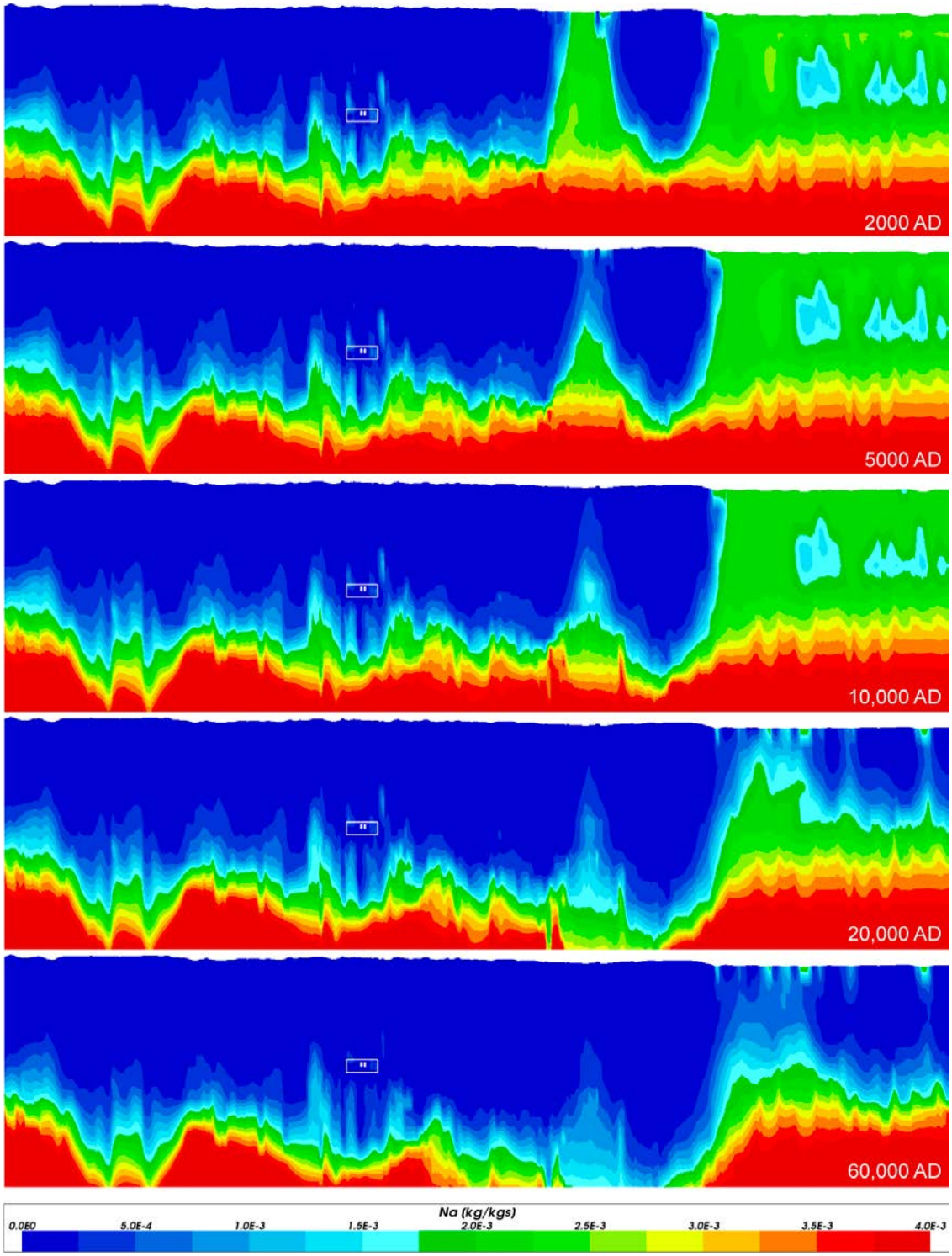

Figure 4-52. *Total sodium mass fractions on vertical W-E catchment scale slices through the repository volume for Case 1, for dates (from top to bottom) 2000 AD, 5000 AD, 10 000 AD, 20 000 AD and 60 000 AD. The refined volume and repository vaults are shown in white. Model shown down to an elevation of -1100 m. Vertical scale has been magnified by a factor of 4.*

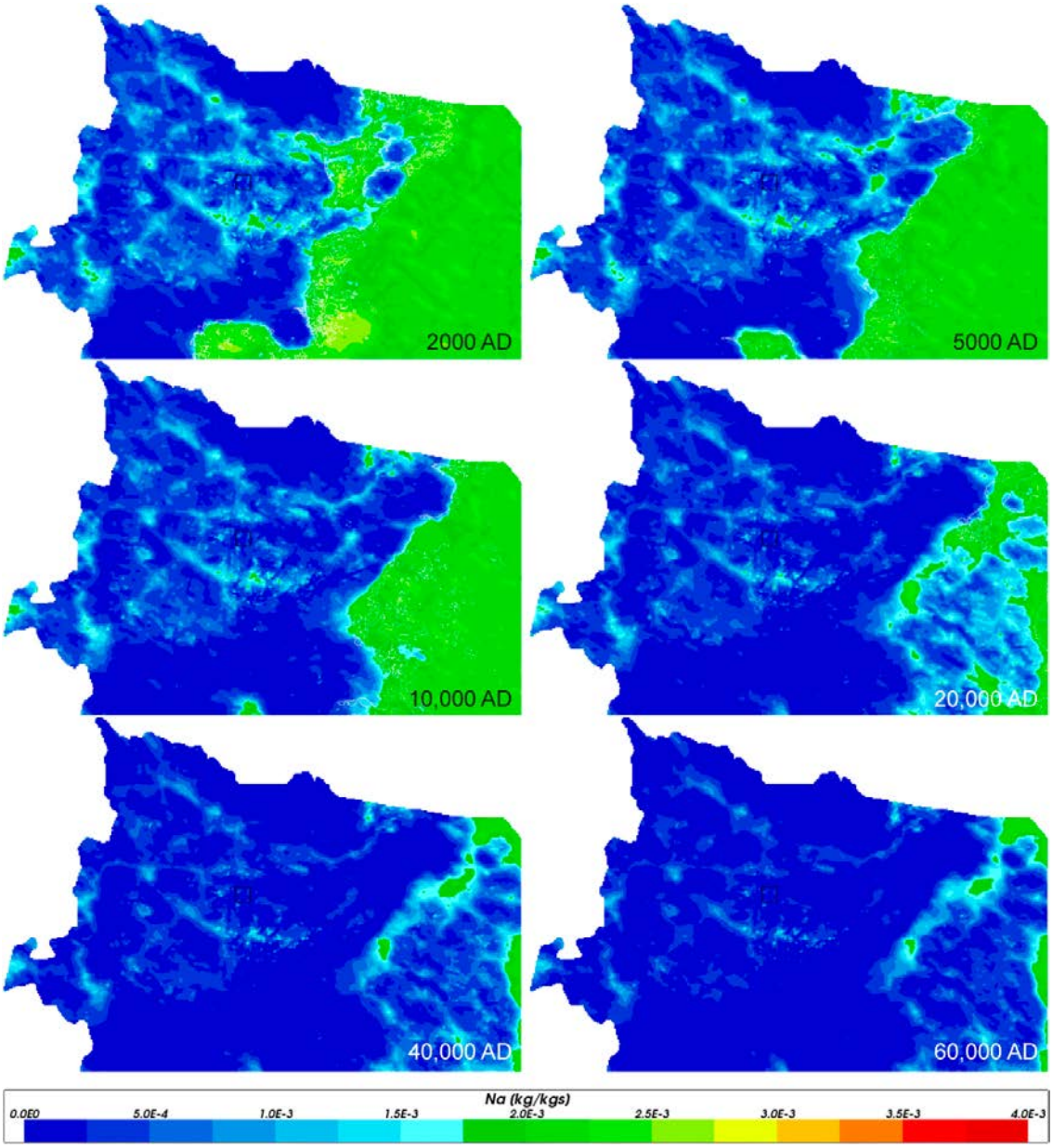

Figure 4-53. *Total sodium mass fractions on horizontal catchment scale slices at an elevation of −500 m through the repository volume for Case 1, for dates (from left to right, top to bottom) 2000 AD, 5000 AD, 10 000 AD, 20 000 AD, 40 000 AD and 60 000 AD. The refined volume is shown in black and the shoreline is shown in white up to 20 000 AD.*

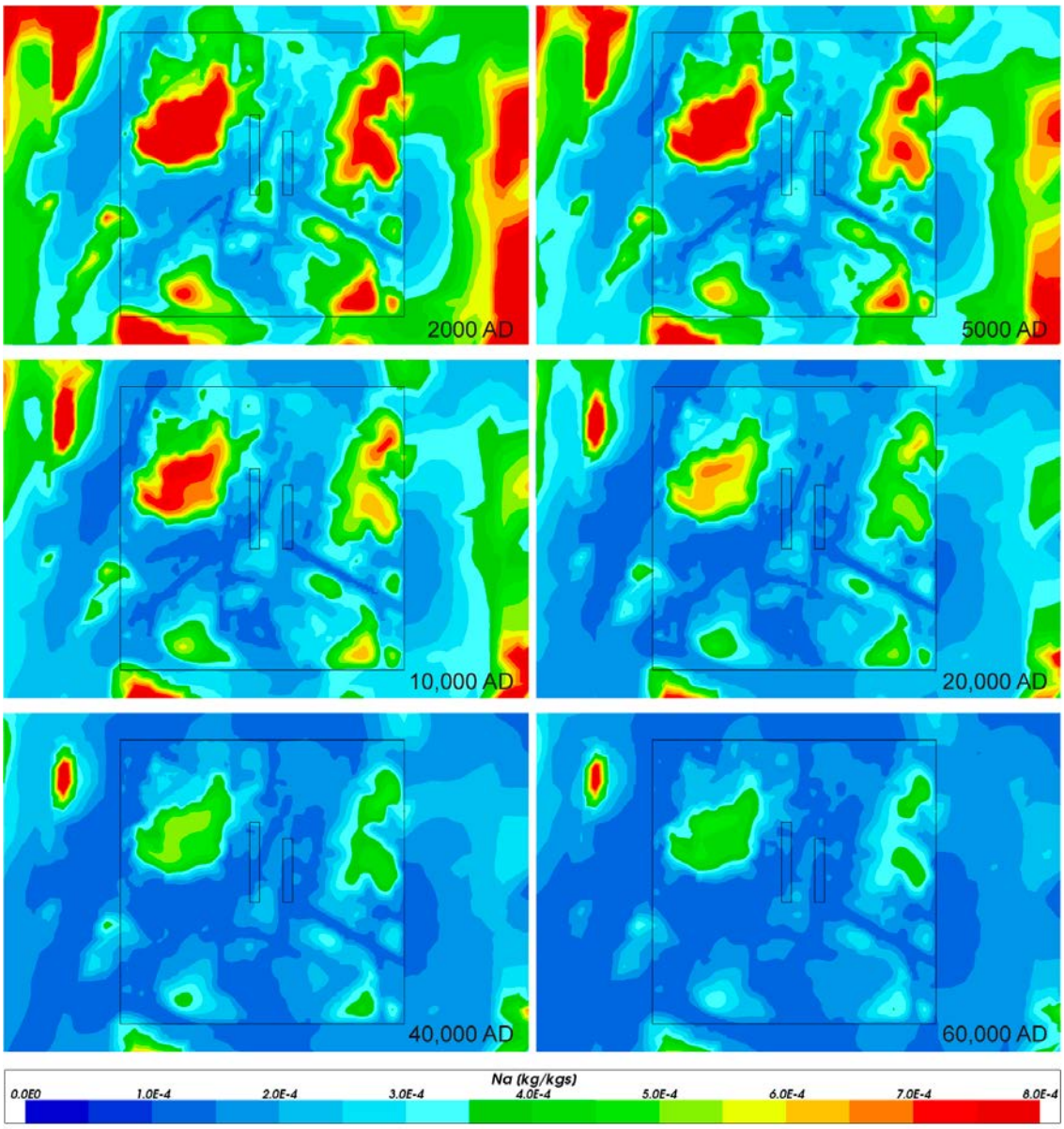

Figure 4-54. *Close-up view of total sodium mass fractions on horizontal slices at an elevation of −500 m through the repository volume for Case 1, for dates (from left to right, top to bottom) 2000 AD, 5000 AD, 10 000 AD, 20 000 AD, 40 000 AD and 60 000 AD. The refined volume and repository vaults are shown in black. Note that the range of concentrations is lower than that shown in Figure 4-53.*

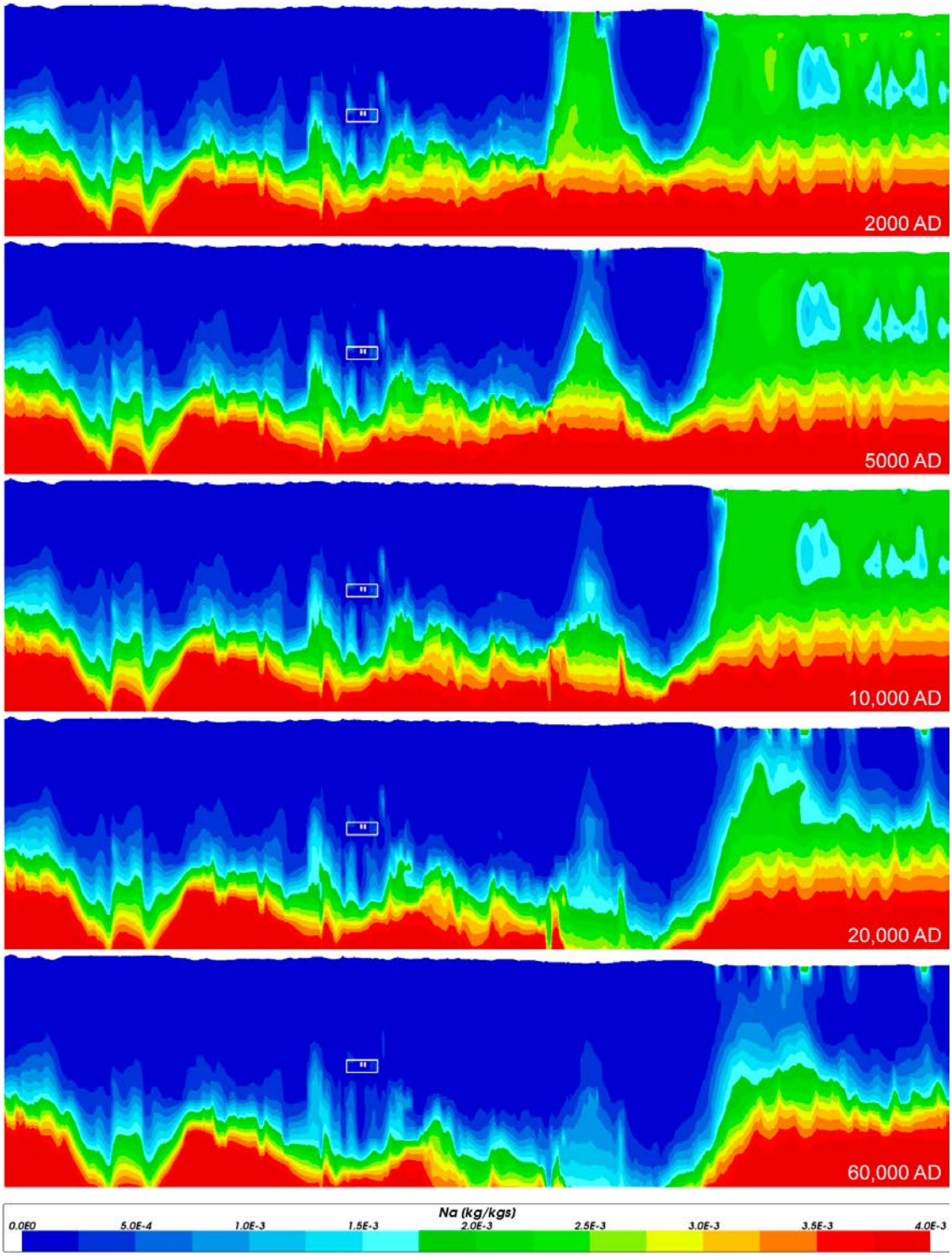

Figure 4-55. *Total sodium mass fractions on vertical W-E catchment scale slices through the repository volume for Case 2, for dates (from top to bottom) 2000 AD, 5000 AD, 10 000 AD, 20 000 AD and 60 000 AD. The refined volume and repository vaults are shown in white. Model shown down to an elevation of −1 100 m. Vertical scale has been magnified by a factor of 4.*

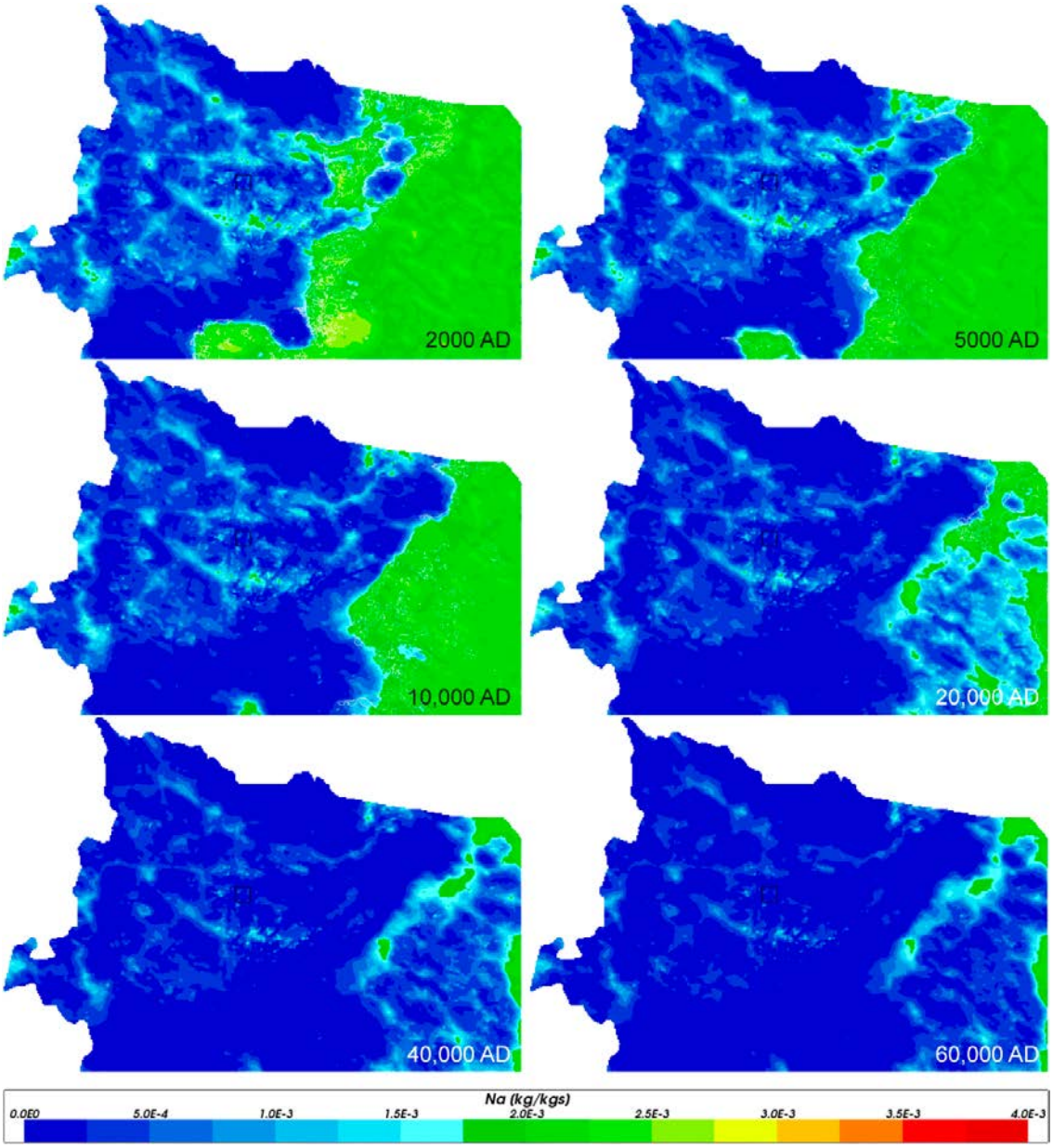

Figure 4-56. *Total sodium mass fractions on horizontal catchment scale slices at an elevation of −500 m through the repository volume for Case 2, for dates (from left to right, top to bottom) 2000 AD, 5000 AD, 10 000 AD, 20 000 AD, 40 000 AD and 60 000 AD. The refined volume is shown in black and the shoreline is shown in white up to 20 000 AD.*

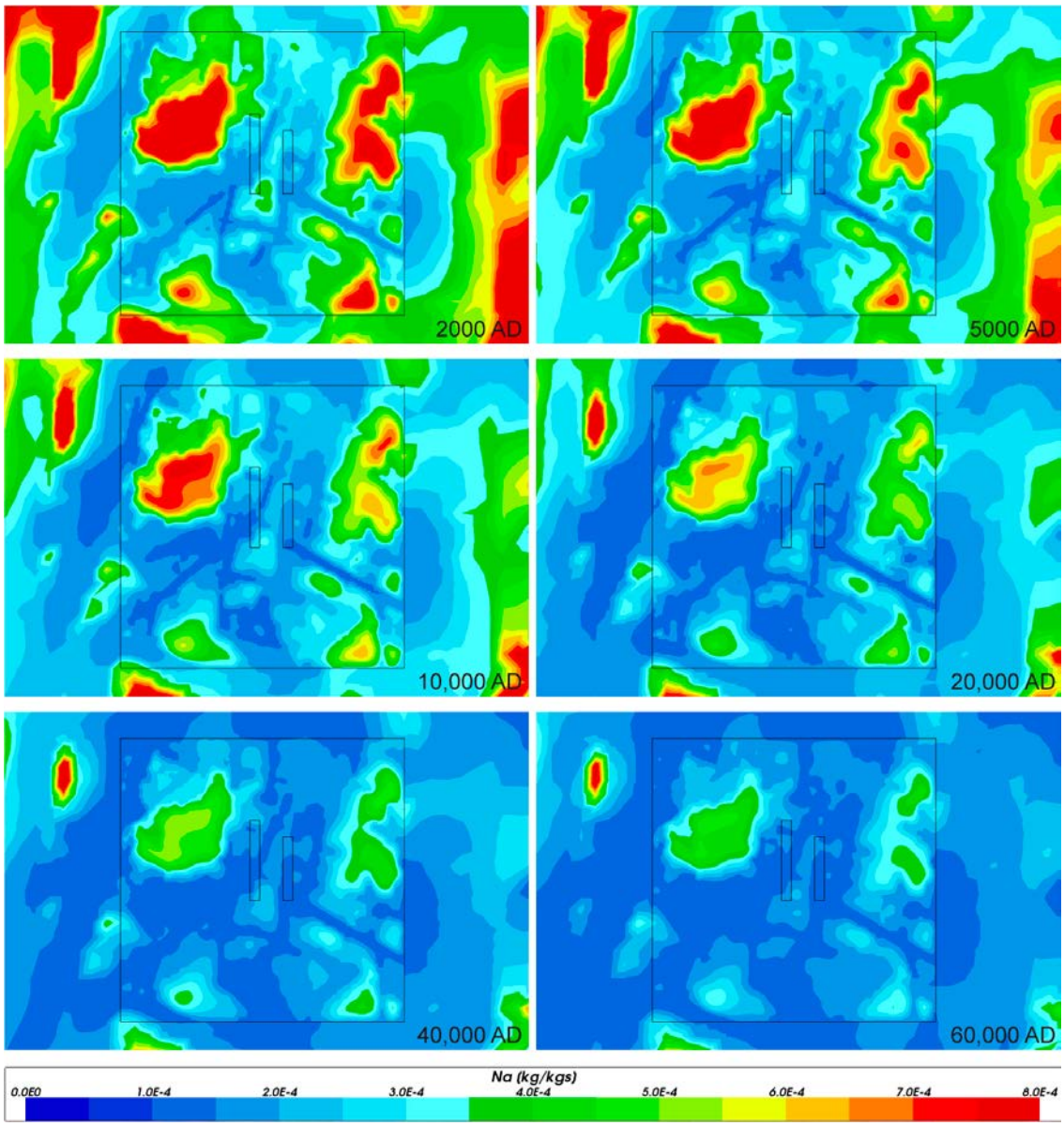

Figure 4-57. *Close-up view of total sodium mass fractions on horizontal slices at an elevation of -500 m through the repository volume for Case 2, for dates (from left to right, top to bottom) 2000 AD, 5000 AD, 10 000 AD, 20 000 AD, 40 000 AD and 60 000 AD. The refined volume and repository vaults are shown in black. Note that the range of concentrations is lower than that shown in Figure 4-56.*

4.3.6 pH

Figure 4-58 shows a comparison of statistical distributions of pH in the repository volume for the two cases with chemical reactions. The pH is not calculated for Case 1. There is a general trend of a slight increase in pH with time. It can also be noted that the spatial variability within the repository volume increases with time. The pH evolution is virtually identical for Cases 2 and 3. This suggests that the redox pathways described in Table 3-1 for the two cases do not differ in their effect on the spatial or temporal pH variability to any significant degree within the repository volume. Also on a catchment scale, no significant differences between the cases were observed, and the catchment focussed results are therefore shown for Case 2 only. The spatial and temporal variability is illustrated for the catchment scale on a vertical slice in Figure 4-59 and on a horizontal slice at 500 metres depth in Figure 4-60 and zoomed in to the repository volume in Figure 4-61. A band of low pH at intermediate depths is noted across the entire time span. This band is likely due to continuous in-mixing of residual glacial and inter-glacial matrix water and calcite precipitation at these depths (cf. Figure 4-30 and Figure 4-31). Spots with high pH (8.5 up to 10.5) can be seen in Figure 4-59 and Figure 4-60, in particular to the east of the repository volume in the area below the sea (right in the figure) and most prominently at early times. These spots are likely numerical artefacts occurring when residual Littorina water is continuously intermixed with upconing deep saline water, and the interface between the waters is resolved by a relatively coarse grid at this distance from the repository volume. Consistent with the repository volume results, Figure 4-59 and Figure 4-60 show a general increase in pH on a catchment scale at repository depth (except for the discharge area below the sea). This results from the gradual penetration of Altered Meteoric water from the ground surface, with a gradual slight dilution of the groundwater initially present at repository depth. The influence of hydraulically conductive fractures is evident from Figure 4-61, and in particular for later times where bands of high pH (~8) coincide with hydraulic zones in the model (cf. Section 4.4). It should be noted that the fractures in the repository volume are generated stochastically in the DFN realisation (no deterministic deformation zones intersect the repository volume).

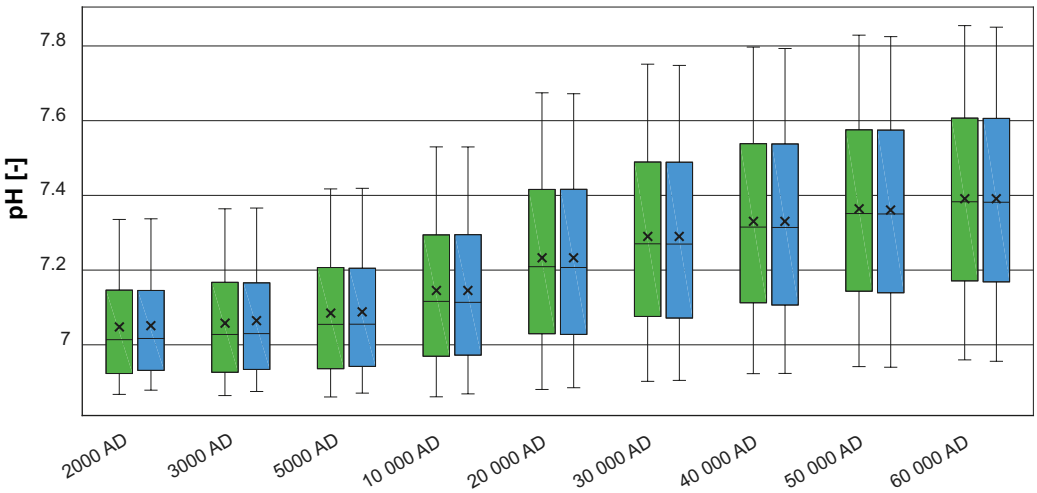

Figure 4-58. *Box and whisker plot showing a comparison of statistical distributions of pH for the two cases with chemical reactions (Case 2 – green, Case 3 – blue) on a regular grid of points within the repository volume between elevations −530 m and −470 m. The statistical measures are the median, the 25th and 75th percentiles (box), the mean (cross) and the 5th and 95th percentiles (whiskers).*

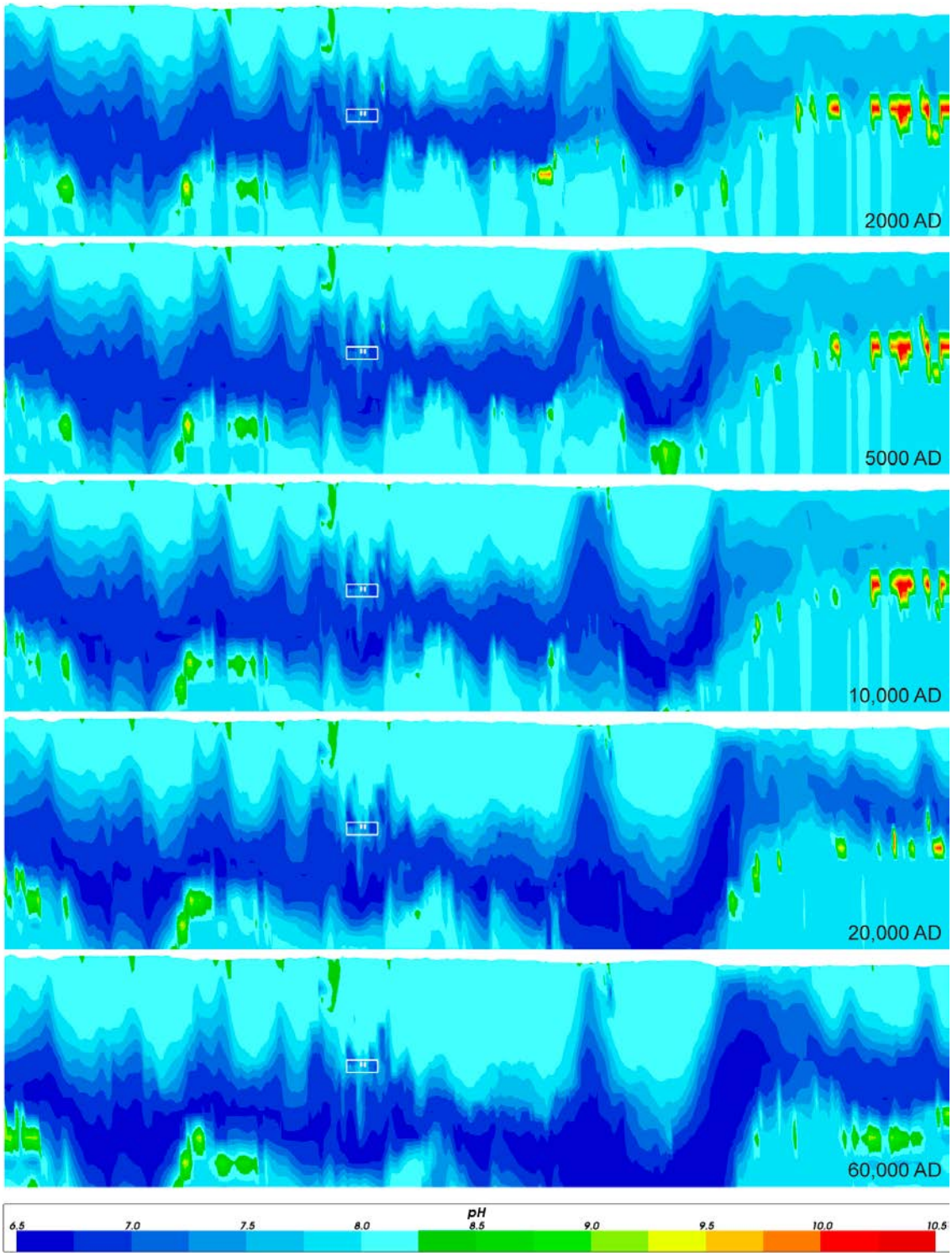

Figure 4-59. *Values of pH on vertical W-E catchment scale slices through the repository volume for Case 2, for dates (from top to bottom) 2000 AD, 5000 AD, 10 000 AD, 20 000 AD and 60 000 AD. The refined volume and repository vaults are shown in white. Model shown down to an elevation of -1100 m. Vertical scale has been magnified by a factor of 4.*

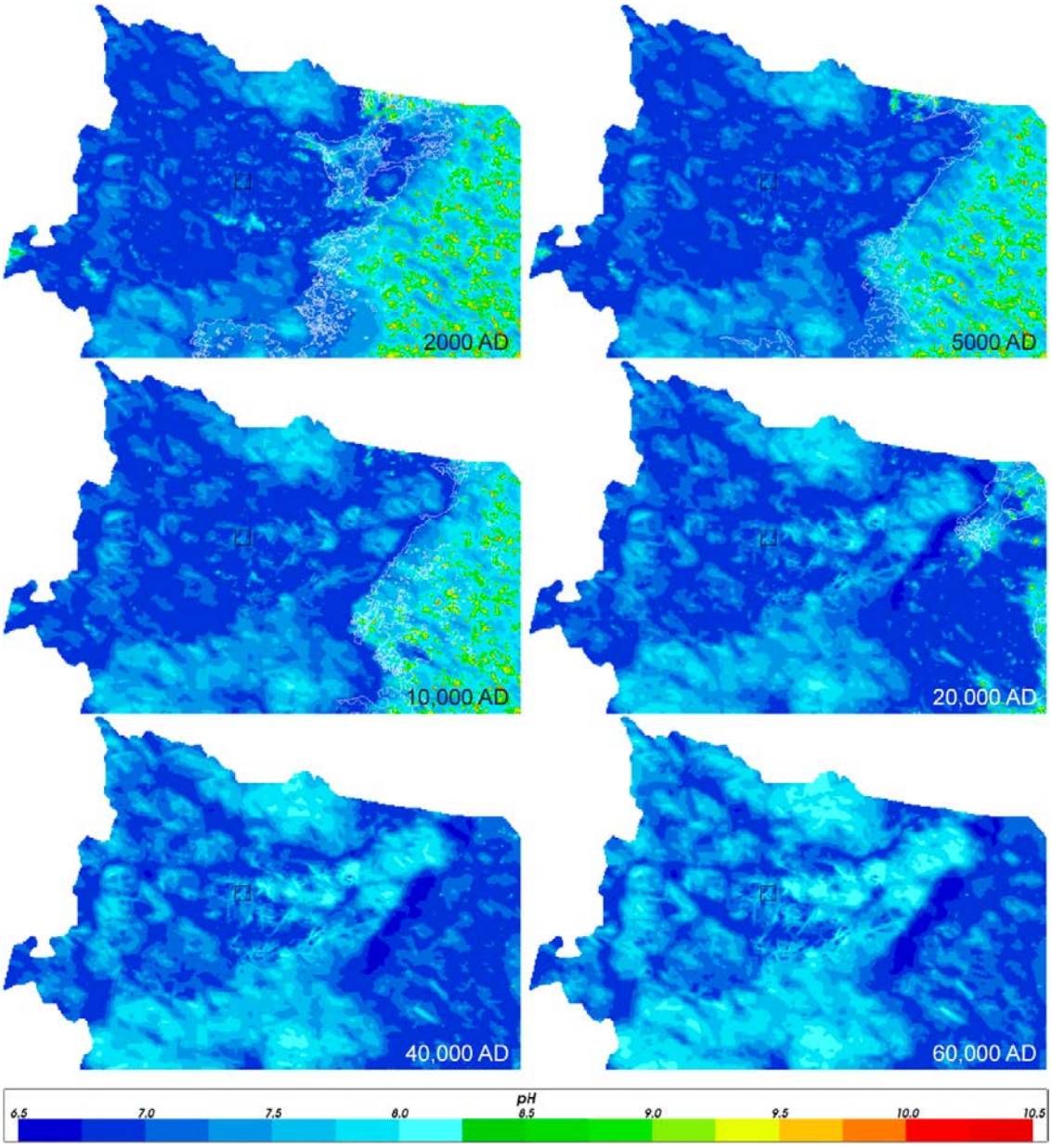

Figure 4-60. *Values of pH on horizontal catchment scale slices at an elevation of −500 m through the repository volume for Case 2, for dates (from left to right, top to bottom) 2000 AD, 5000 AD, 10 000 AD, 20 000 AD, 40 000 AD and 60 000 AD. The refined volume is shown in black and the shoreline is shown in white up to 20 000 AD.*

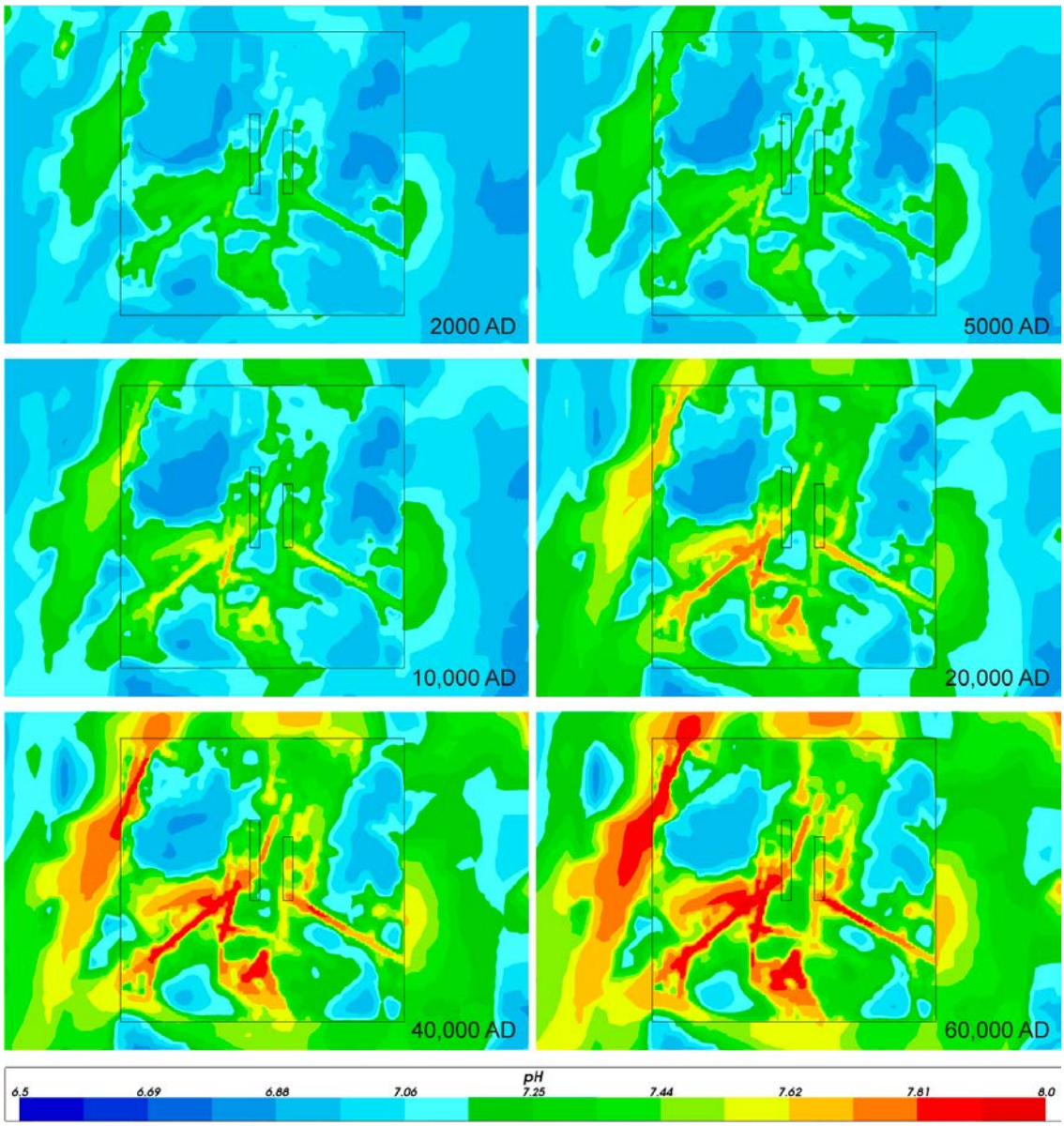

Figure 4-61. *Close-up view of values of pH on horizontal slices at an elevation of −500 m through the repository volume for Case 2, for dates (from left to right, top to bottom) 2000 AD, 5000 AD, 10 000 AD, 20 000 AD, 40 000 AD and 60 000 AD. The refined volume and repository vaults are shown in black. Note the limited pH range compared with Figure 4-60.*

4.3.7 Calcium

Figure 4-62 shows a comparison of statistical distributions of total calcium concentrations for the three modelled cases.

The calcium concentration gradually decreases over time, as the more dilute Altered Meteoric water infiltrates from the top, gradually diluting the slightly more calcium-rich water composition at repository depth at 2000 AD. Temporal changes are most prominent during the first 20 000 years after which the average concentration in the repository volume levels out with a slightly decreasing spatial variability with time. After 20 000 years, the shore-line is displaced outside the catchment scale domain, resulting in a continuous infiltration of Altered Meteoric water at the entire top boundary.

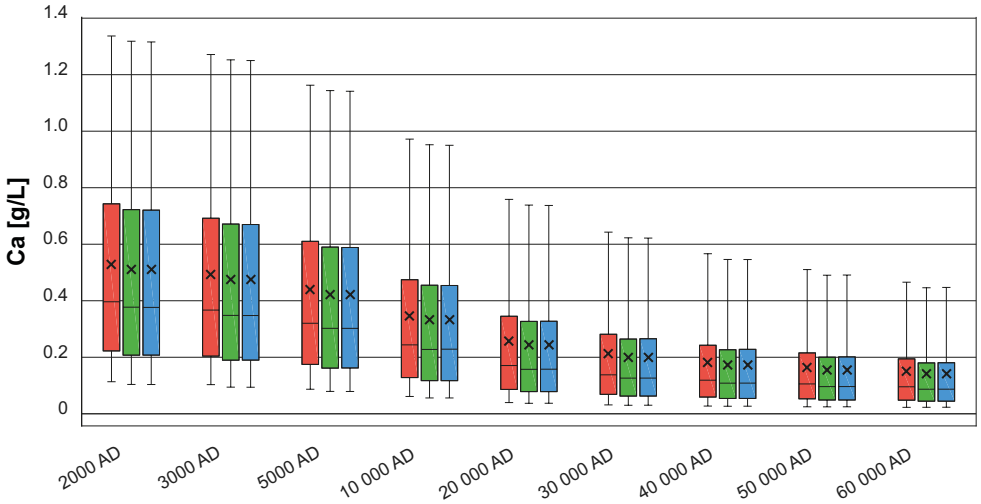

Figure 4-62. *Box and whisker plot showing a comparison of statistical distribution of total calcium concentrations for the three cases (Case 1 – red, Case 2 – green, Case 3 – blue) on a regular grid of points within the repository volume between elevations −530 m and −470 m. The statistical measures are the median, the 25th and 75th percentiles (box), the mean (cross) and the 5th and 95th percentiles (whiskers).*

There is a small difference in calcium concentrations between Case 1 (transport and mixing of components only) and Cases 2 and 3, which also represent chemical reactions. A slightly lower calcium concentration in Cases 2 and 3, as compared with Case 1, suggests a minor super-saturation in Case 1 that results in calcite precipitation in Cases 2 and 3. The small influence of chemical reactions is not discernible, both for the repository volume and on a catchment scale, in Figure 4-63 through Figure 4-65 for Case 1 and Figure 4-66 to Figure 4-68 for Case 2, where the results are essentially identical. The results therefore suggest that the spatial and temporal evolution of calcium in both the repository volume and on a catchment scale is controlled primarily by transport and mixing of groundwater constituents, with a small influence of chemical reactions (calcite precipitation). This behaviour is fairly typical in systems of this type when the reactive solute has a relatively high concentration (Gimeno et al. 2010). Furthermore, no differences between Cases 2 and 3 could be seen which indicates that the calcium evolution is not affected by the assumed redox pathway differing in the two cases (cf. Section 3.1).

4.3.8 Inorganic carbon

Figure 4-69 shows a comparison of statistical distributions of total inorganic carbon concentrations for the three modelled cases. The total carbon concentration gradually increases over time, as the more carbon-rich Altered Meteoric water infiltrates from the top, gradually mixing with the water composition at repository depth at 2000 AD. Temporal changes are most prominent during the first 20 000 years after which the average concentration in the repository volume levels-out with a slightly decreasing spatial variability with time. After 20 000 years, the shore-line is displaced outside the catchment scale domain, resulting in a continuous infiltration of Altered Meteoric water at the entire top boundary.

As also indicated by the evolution of calcium, the carbon concentrations are less in Case 2 and 3 as compared with Case 1 where no chemical reactions are included. The lower concentrations in Cases 2 and 3 suggest a disequilibrium with calcite in Case 1 that results in calcite precipitation in Cases 2 and 3. This is consistent with the change in calcium concentrations between the cases described in Subsection 4.3.7. Only a very minor difference between Cases 2 and 3 can be seen in Figure 4-69, which indicate that the difference in assumed redox pathway between the two cases has little influence on the carbon concentrations in the repository volume.

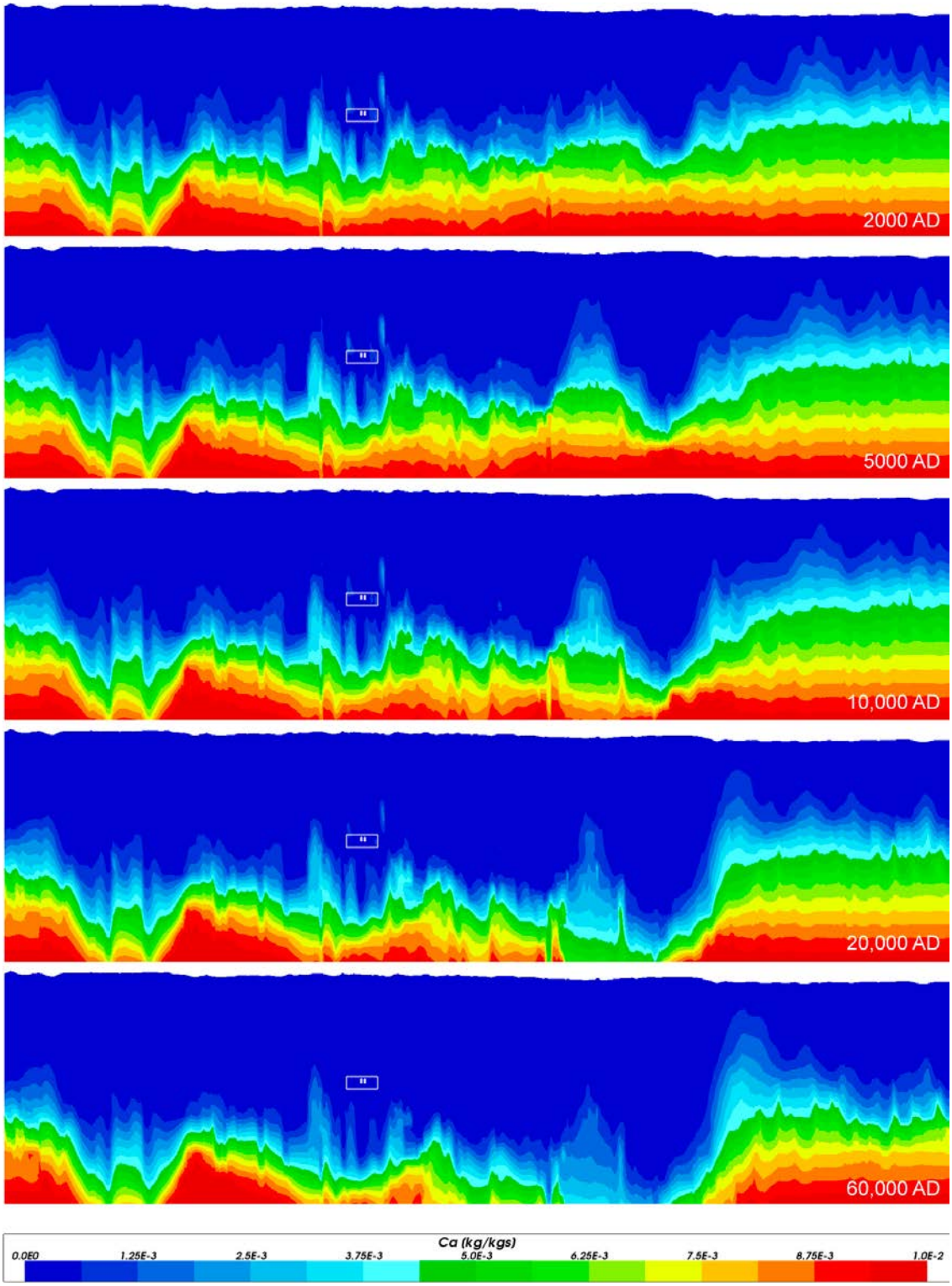

Figure 4-63. *Total calcium mass fractions on vertical W-E catchment scale slices through the repository volume for Case 1, for dates (from top to bottom) 2000 AD, 5000 AD, 10 000 AD, 20 000 AD and 60 000 AD. The refined volume and repository vaults are shown in white. Model shown down to an elevation of −1 100 m. Vertical scale has been magnified by a factor of 4.*

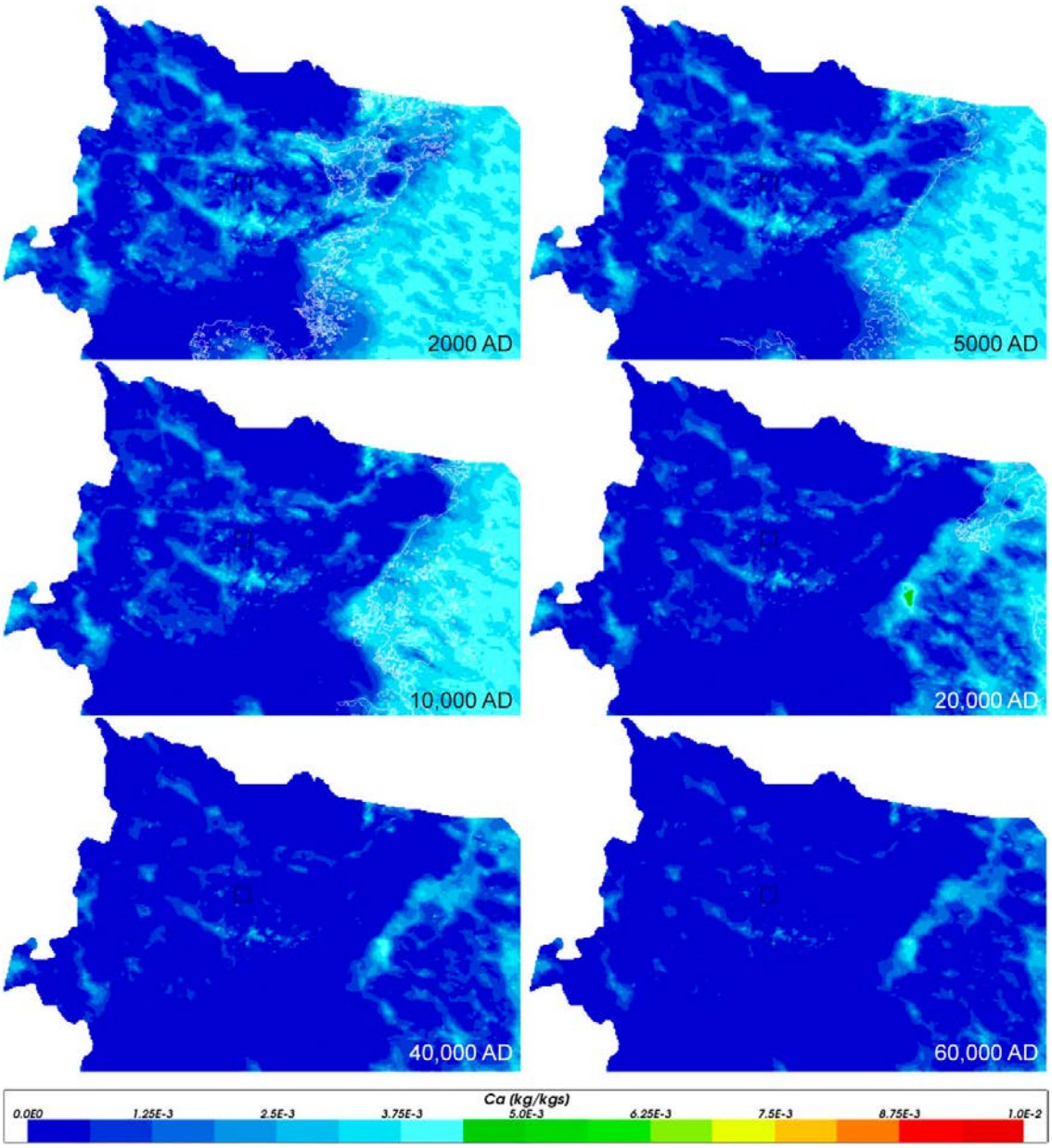

Figure 4-64. *Total calcium mass fractions on horizontal catchment scale slices at an elevation of −500 m through the repository volume for Case 1, for dates (from left to right, top to bottom) 2000 AD, 5000 AD, 10 000 AD, 20 000 AD, 40 000 AD and 60 000 AD. The refined volume is shown in black and the shoreline is shown in white up to 20 000 AD.*

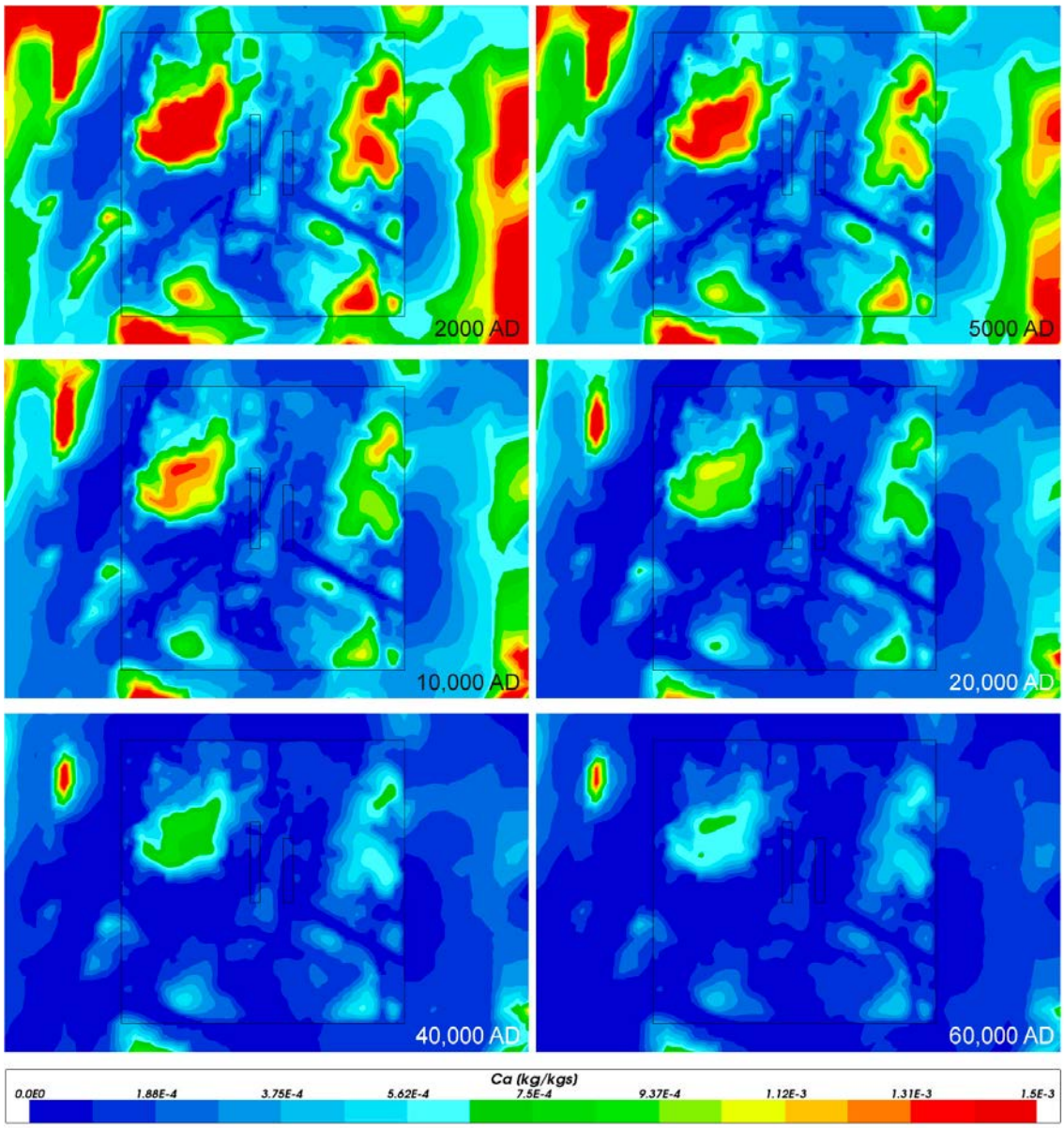

Figure 4-65. *Close-up view of total calcium mass fractions on horizontal slices at an elevation of −500 m through the repository volume for Case 1, for dates (from left to right, top to bottom) 2000 AD, 5000 AD, 10 000 AD, 20 000 AD, 40 000 AD and 60 000 AD. The refined volume and repository vaults are shown in black. Note that the scale in this figure has a lower maximum value than in Figure 4-64.*

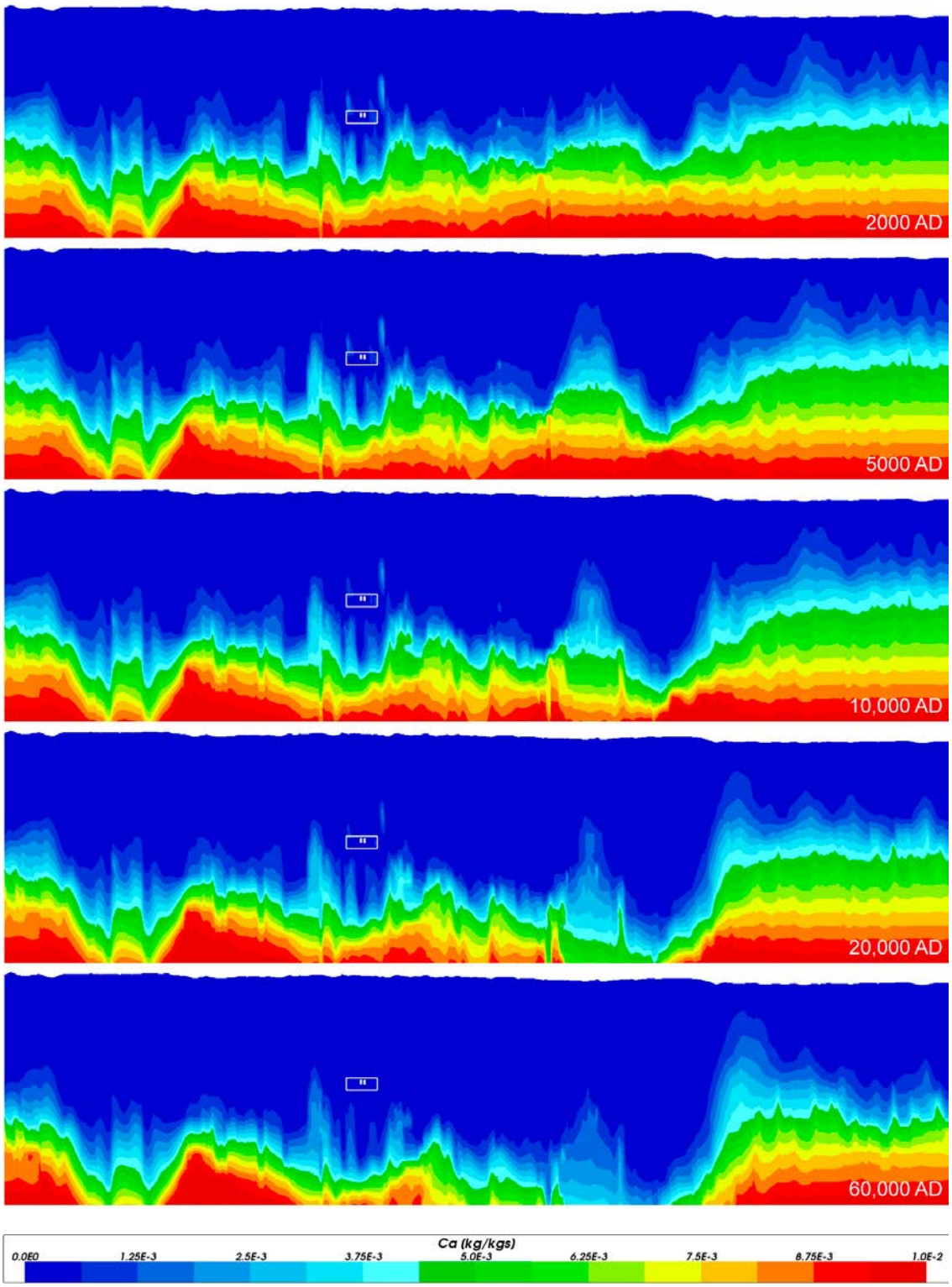

Figure 4-66. *Total calcium mass fractions on vertical W-E catchment scale slices through the repository volume for Case 2, for dates (from top to bottom) 2000 AD, 5000 AD, 10 000 AD, 20 000 AD and 60 000 AD. The refined volume and repository vaults are shown in white. Model shown down to an elevation of −1 100 m. Vertical scale has been magnified by a factor of 4.*

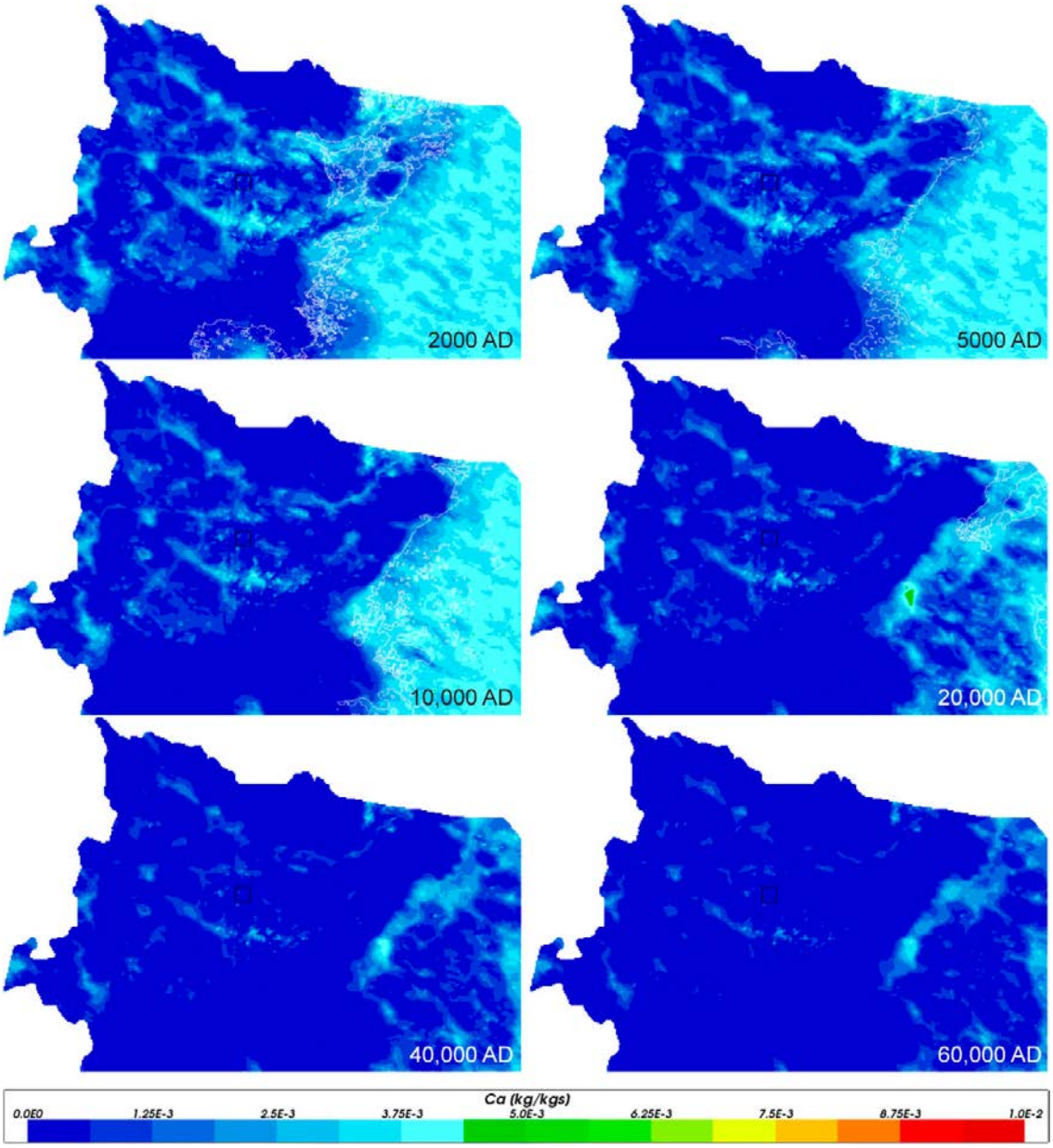

Figure 4-67. *Total calcium mass fractions on horizontal catchment scale slices at an elevation of −500 m through the repository volume for Case 2, for dates (from left to right, top to bottom) 2000 AD, 5000 AD, 10 000 AD, 20 000 AD, 40 000 AD and 60 000 AD. The refined volume is shown in black and the shoreline is shown in white up to 20 000 AD.*

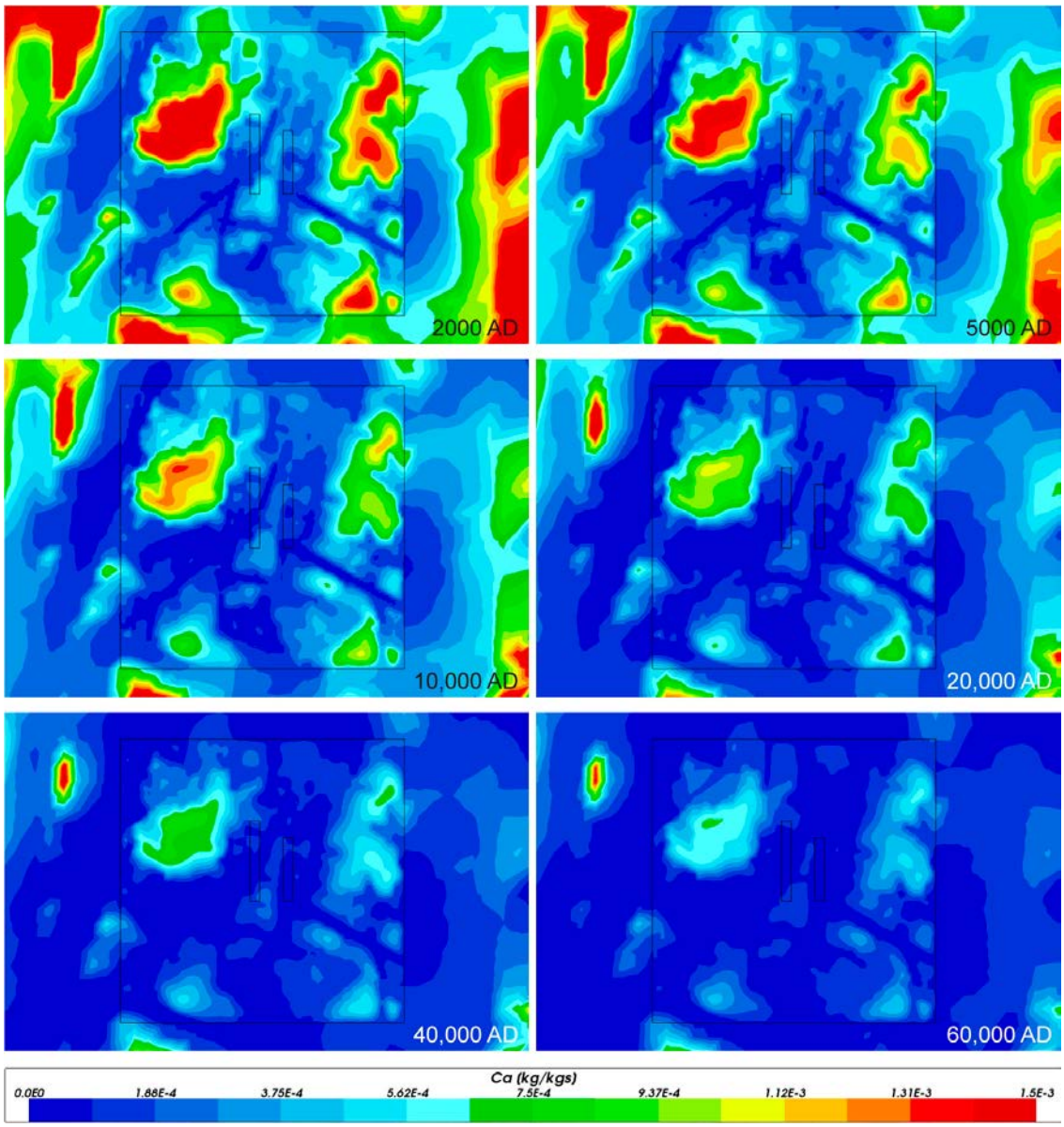

Figure 4-68. *Close-up view of total calcium mass fractions on horizontal slices at an elevation of −500 m through the repository volume for Case 2, for dates (from left to right, top to bottom) 2000 AD, 5000 AD, 10 000 AD, 20 000 AD, 40 000 AD and 60 000 AD. The refined volume and repository vaults are shown in black. Note that the scale in this figure has a lower maximum value than in Figure 4-67.*

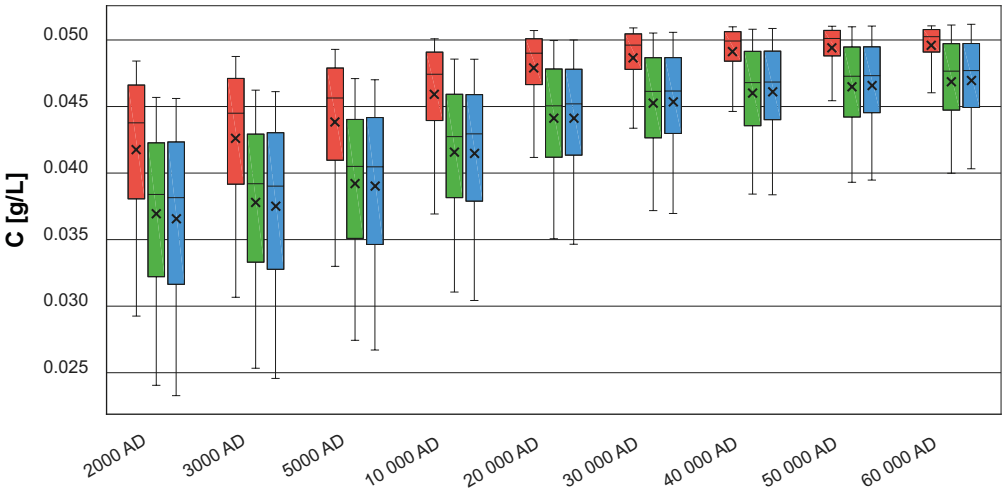

Figure 4-69. *Box and whisker plot showing a comparison of statistical distributions of total inorganic carbon concentrations for the three cases (Case 1 – red, Case 2 – green, Case 3 – blue) on a regular grid of points within the repository volume between elevations −530 m and −470 m. The statistical measures are the median, the 25th and 75th percentiles (box), the mean (cross) and the 5th and 95th percentiles (whiskers).*

Figure 4-70 through Figure 4-75 show the total inorganic carbon mass fractions on catchment scale slice plots. These figures show that the differences between Cases 1 and 2 are also present on a catchment scale. Altered Meteoric water infiltrating from the top boundary along conductive zones is seen as “fingers” of carbonate-rich zones in Case 2 (Figure 4-73).

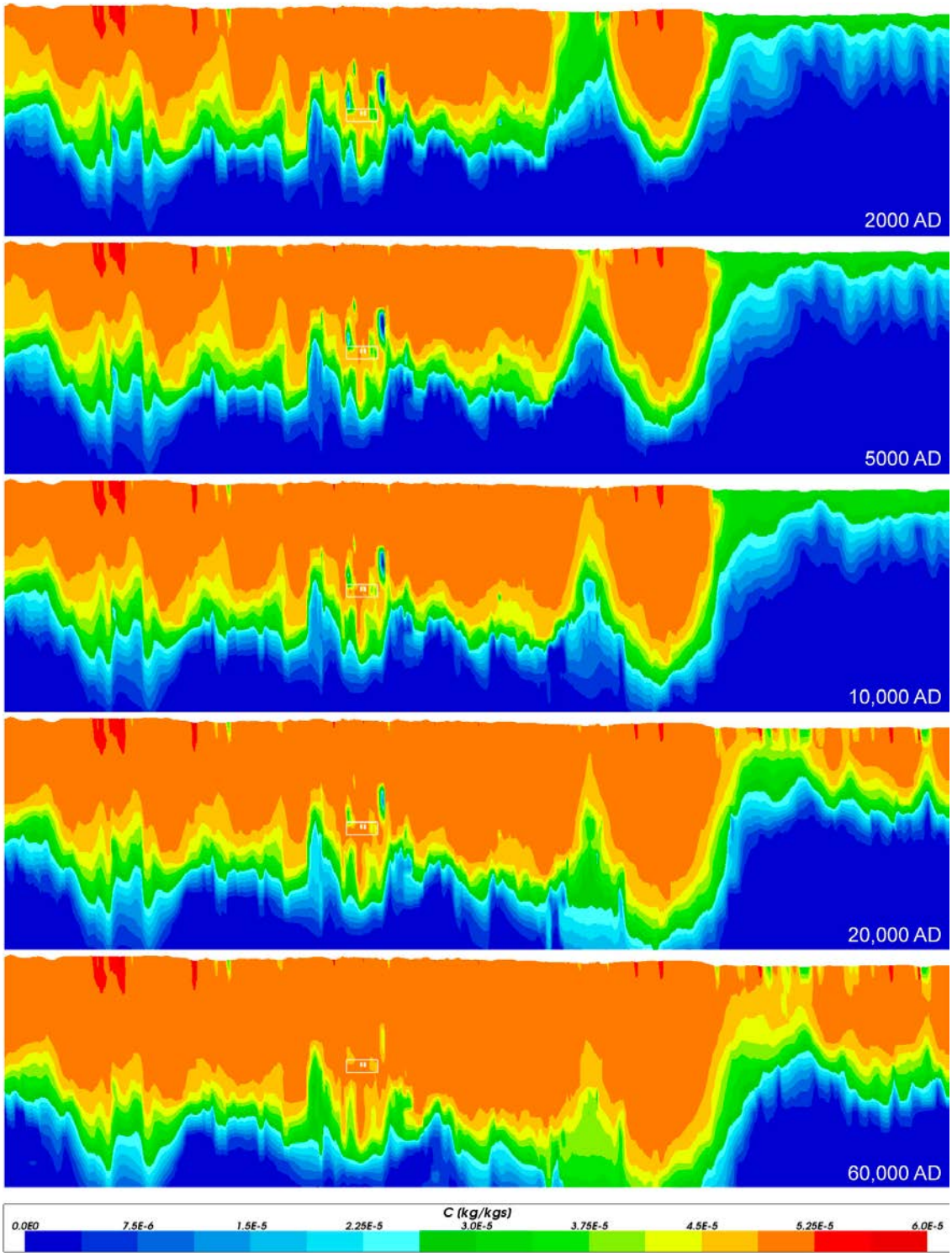

Figure 4-70. *Total inorganic carbon mass fractions on vertical W-E catchment scale slices through the repository volume for Case 1, for dates (from top to bottom) 2000 AD, 5000 AD, 10 000 AD, 20 000 AD and 60 000 AD. The refined volume and repository vaults are shown in white. Model shown down to an elevation of -1100 m. Vertical scale has been magnified by a factor of 4.*

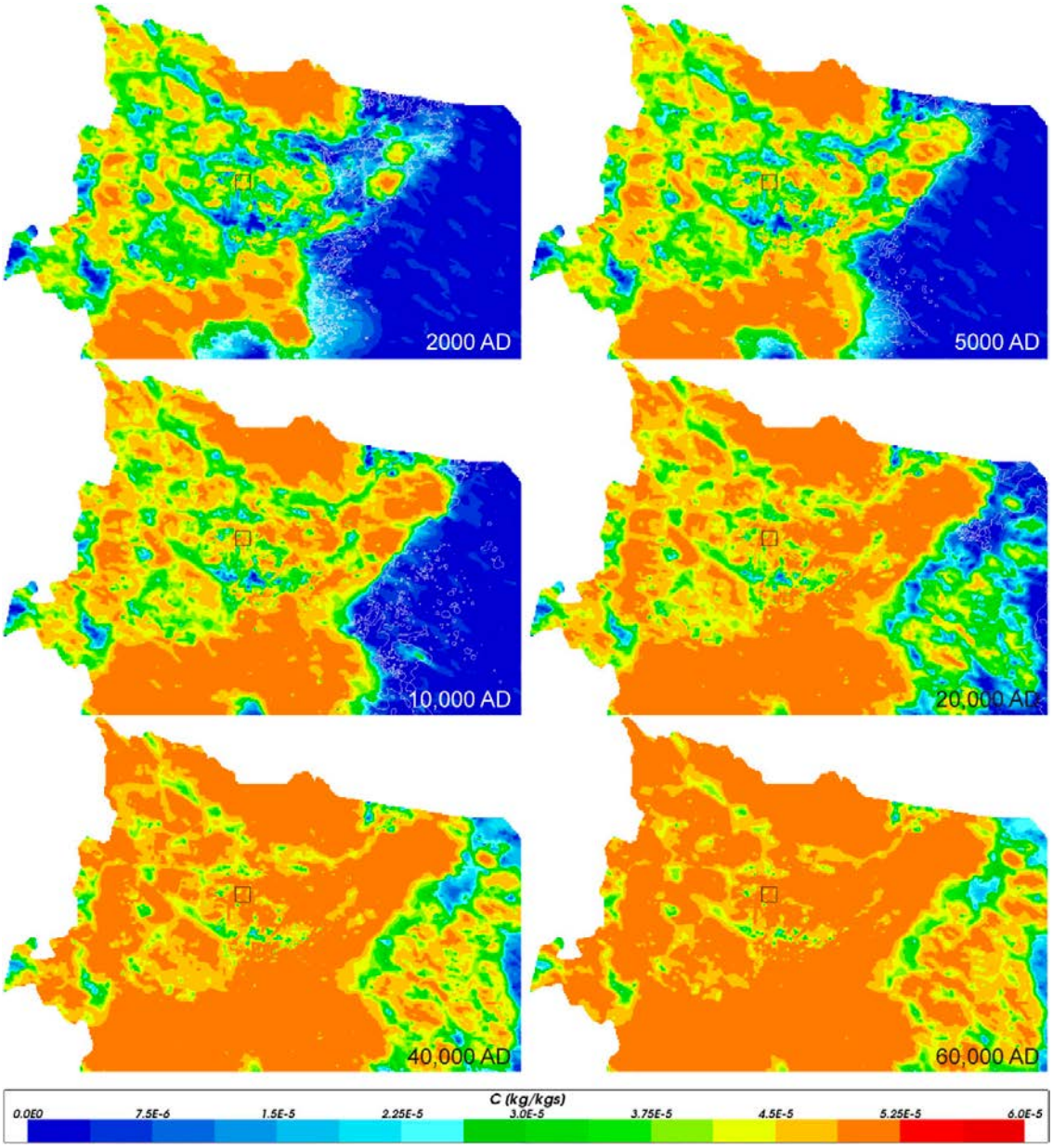

Figure 4-71. *Total inorganic carbon mass fractions on horizontal catchment scale slices at an elevation of −500 m through the repository volume for Case 1, for dates (from left to right, top to bottom) 2000 AD, 5000 AD, 10 000 AD, 20 000 AD, 40 000 AD and 60 000 AD. The refined volume is shown in black and the shoreline is shown in white up to 20 000 AD.*

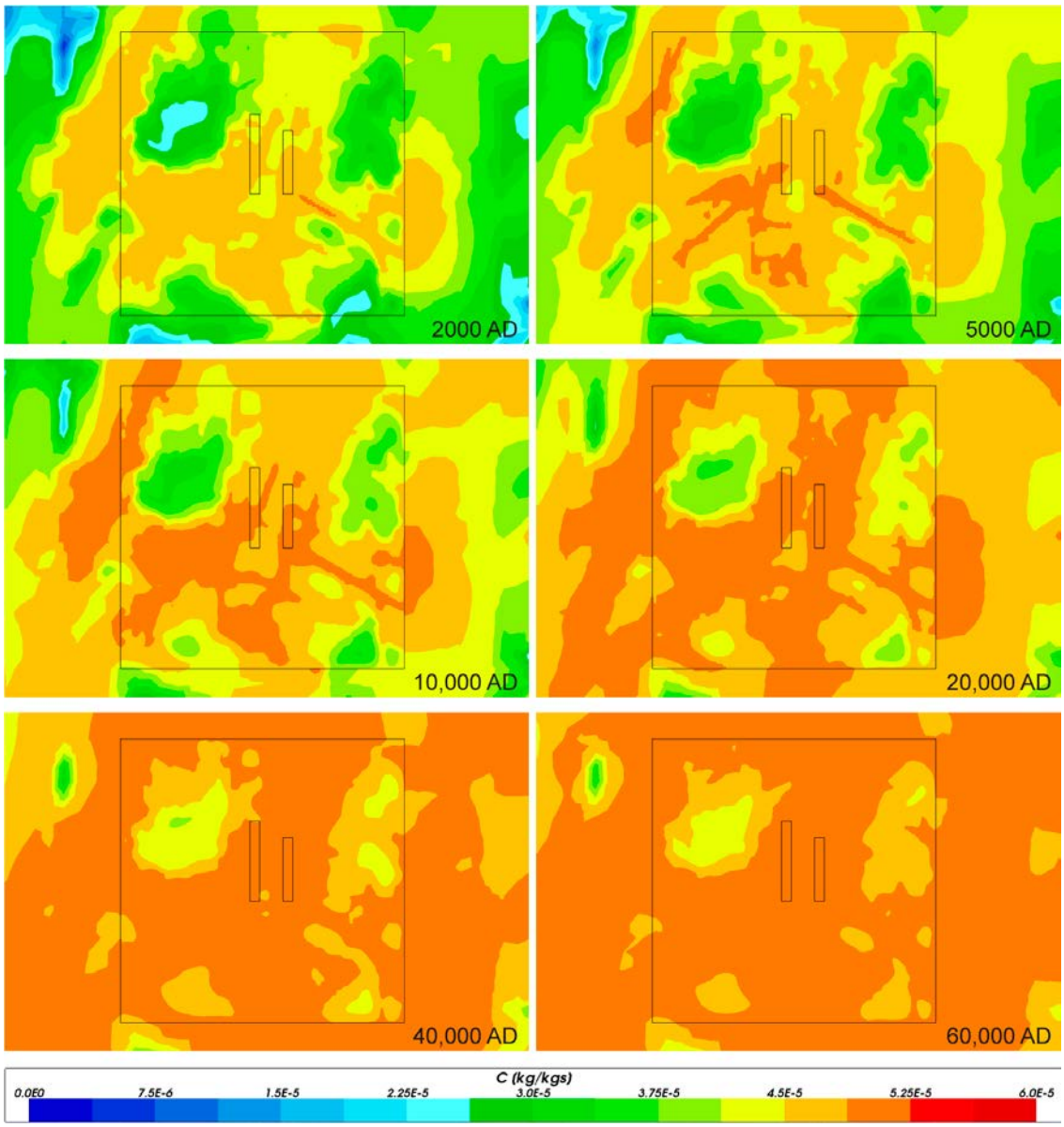

Figure 4-72. *Close-up view of total inorganic carbon mass fractions on horizontal slices at an elevation of −500 m through the repository volume for Case 1, for dates (from left to right, top to bottom) 2000 AD, 5000 AD, 10 000 AD, 20 000 AD, 40 000 AD and 60 000 AD. The refined volume and repository vaults are shown in black.*

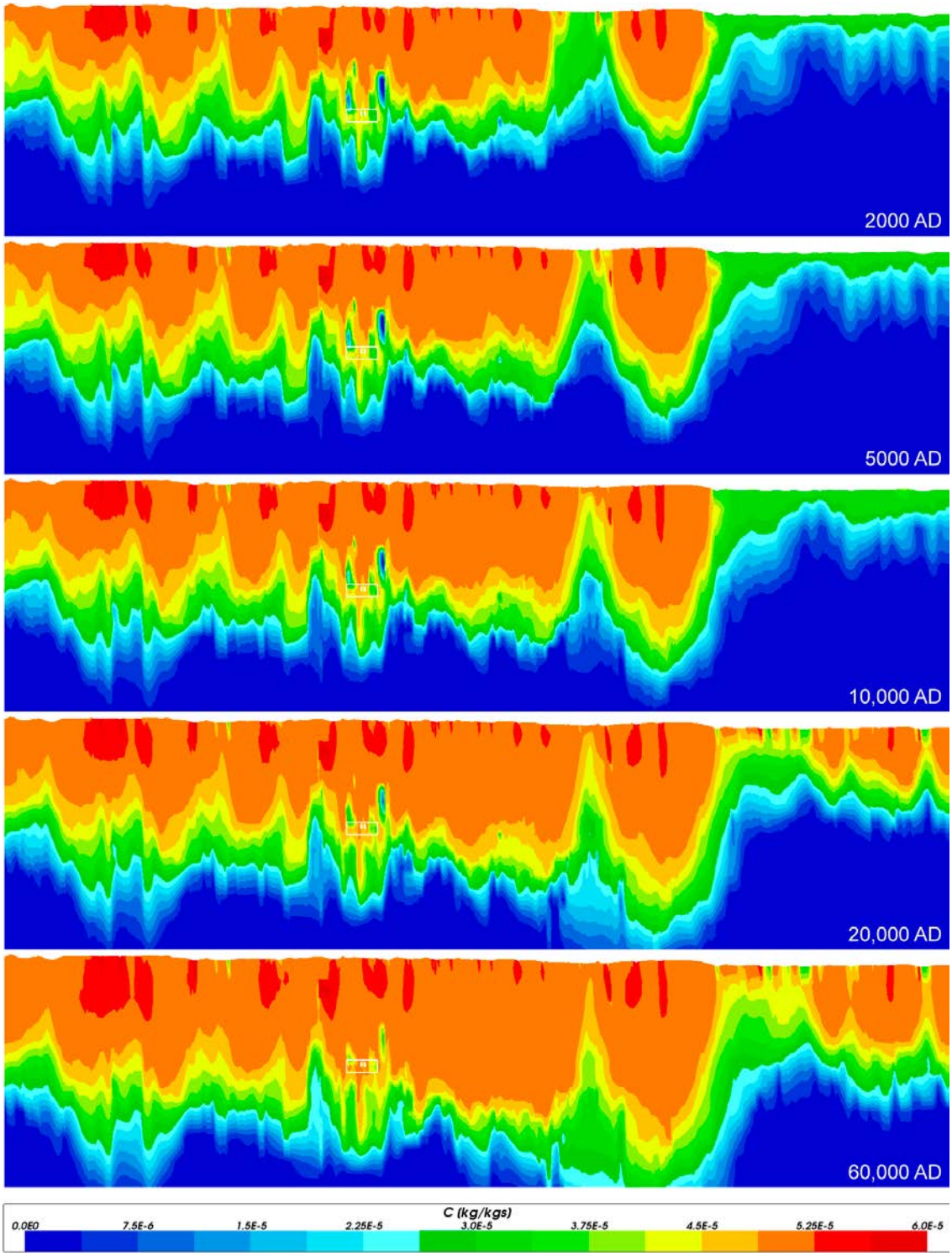

Figure 4-73. *Total inorganic carbon mass fractions on vertical W-E catchment scale slices through the repository volume for Case 2, for dates (from top to bottom) 2000 AD, 5000 AD, 10 000 AD, 20 000 AD and 60 000 AD. The refined volume and repository vaults are shown in white. Model shown down to an elevation of −1 100 m. Vertical scale has been magnified by a factor of 4.*

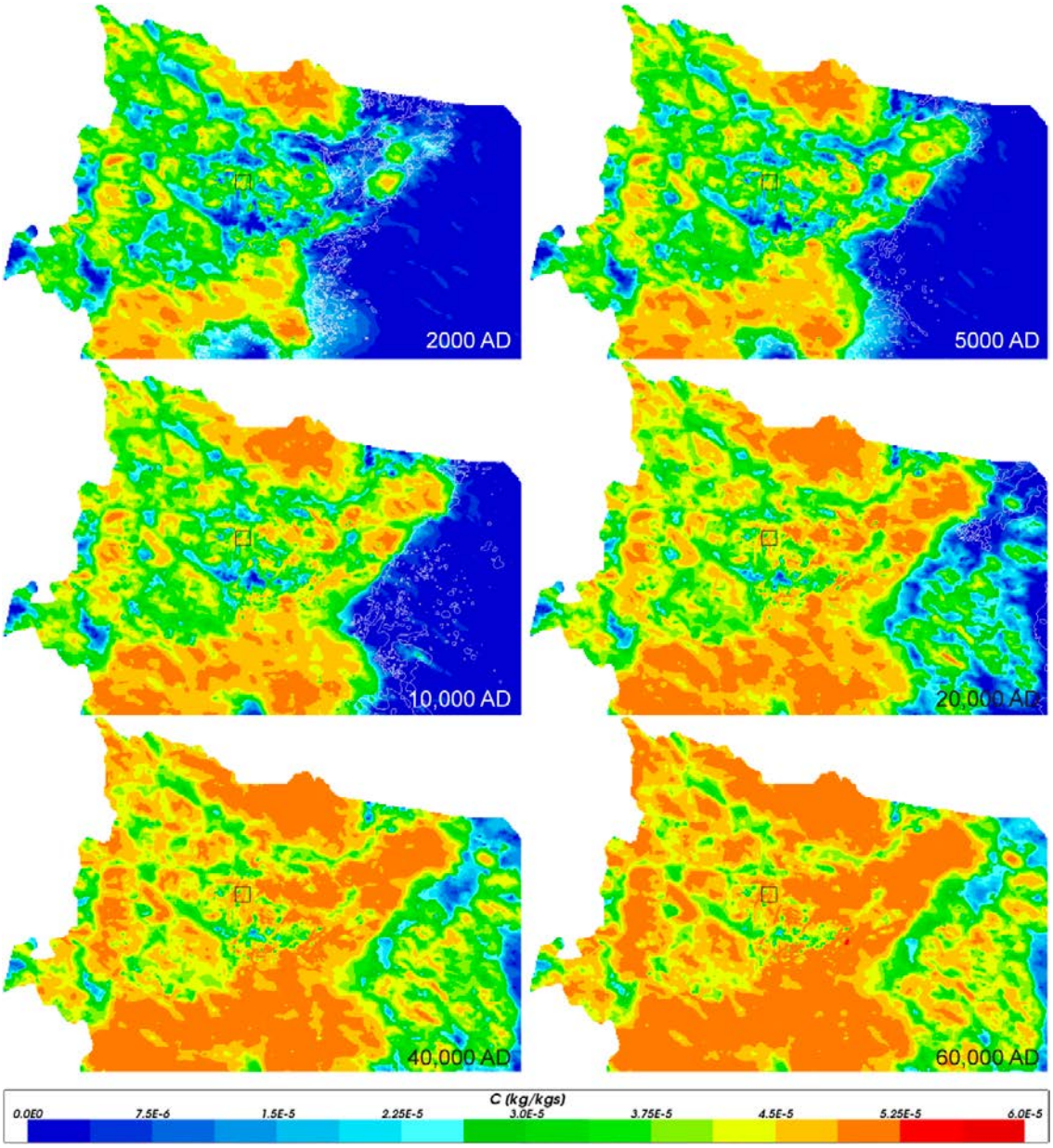

Figure 4-74. *Total inorganic carbon mass fractions on horizontal catchment scale slices at an elevation of −500 m through the repository volume for Case 2, for dates (from left to right, top to bottom) 2000 AD, 5000 AD, 10 000 AD, 20 000 AD, 40 000 AD and 60 000 AD. The refined volume is shown in black and the shoreline is shown in white up to 20 000 AD.*

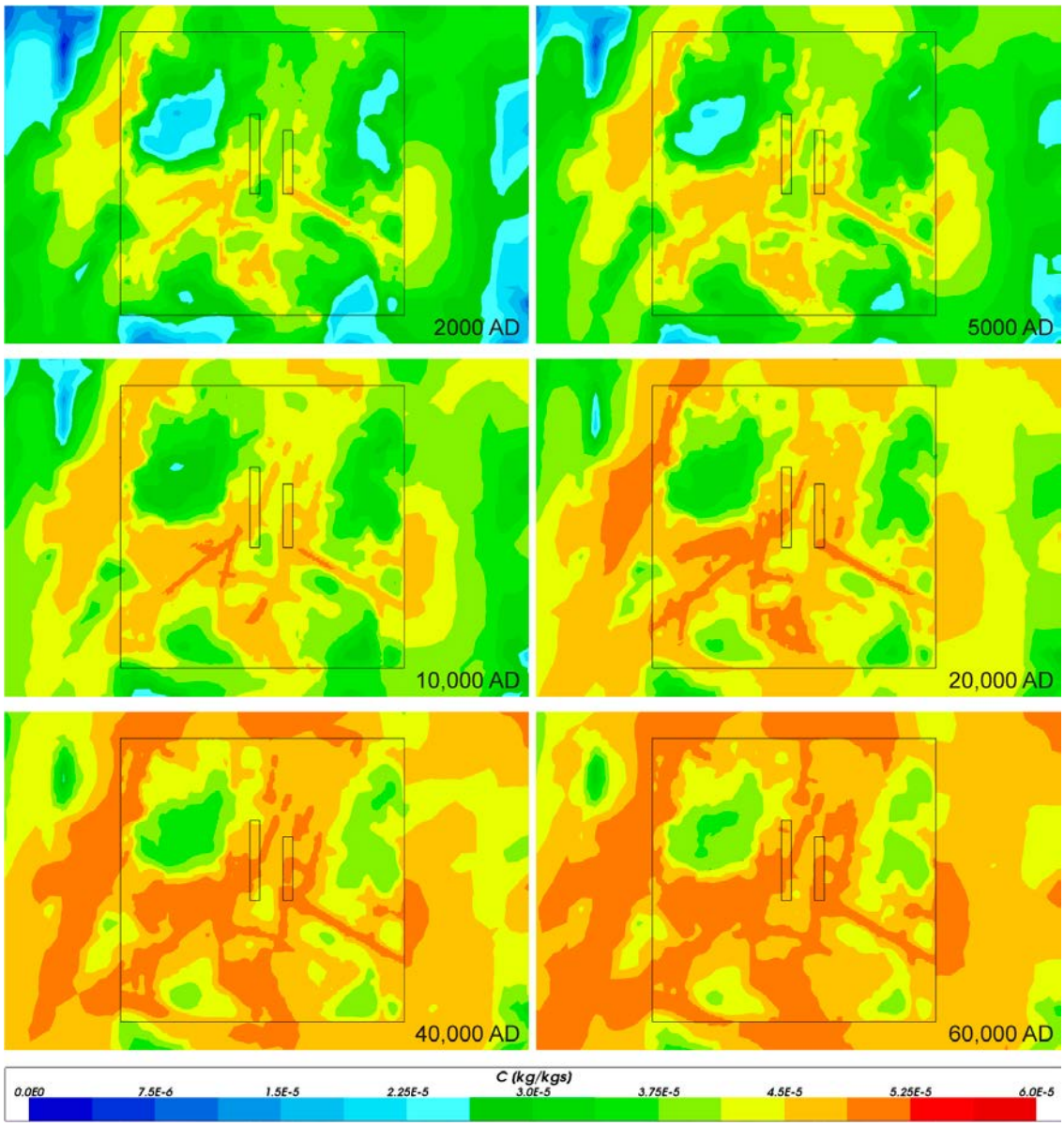

Figure 4-75. *Close-up view of total inorganic carbon mass fractions on horizontal slices at an elevation of −500 m through the repository volume for Case 2, for dates (from left to right, top to bottom) 2000 AD, 5000 AD, 10 000 AD, 20 000 AD, 40 000 AD and 60 000 AD. The refined volume and repository vaults are shown in black.*

4.3.9 pE

Figure 4-76 shows a comparison of statistical distributions of pE in the repository volume for the two cases with chemical reactions. A general trend of decreasing pE (gradually more reducing) conditions with time is observed. Based on the pE values given in Table 3-7 one might expect pE to increase with increasing fractions of Altered Meteoric water present. The initial water compositions in Table 3-7 are the result of equilibrium with microcrystalline $Fe(OH)_3$ (described and discussed in Auqué et al. 2006), whereas in the ConnectFlow calculations, the Grenthe calibration for the $Fe(OH)_3$ equilibrium reaction has been assumed (Grenthe et al. 1992). This implies an adjustment downwards for both the pE and Fe concentration of this groundwater boundary condition directly upon initialisation which has consequences for the pE in mixed groundwaters. As for the pH evolution, the spatial variability within the repository volume increases with time as the more dilute Altered Meteoric water penetrates from the ground surface, and primarily through a few hydraulically conductive deformation zones. From the vertical slices in Figure 4-77 (Case 2) and Figure 4-80 (Case 3) this is seen as the band of less-reducing conditions (in red) is gradually pushed deeper with time by the infiltrating water. This conclusion is further supported by the horizontal slices at repository depth shown in Figure 4-78 and Figure 4-79 for Case 2, and Figure 4-81 and Figure 4-82 for Case 3, with slightly more reducing features, particularly at later times, that coincide with conductive deformation zones (cf. Section 4.4) generated stochastically in the DFN representation.

As may be expected, the redox evolution differs to some extent between Cases 2 and 3, since they are based on two different redox pathways (cf. Section 3.1). A slightly steeper decrease in pE with time in the repository volume is observed for Case 2 as compared with Case 3. The difference is however small.

Note the wedge-shaped area with high pE (red colour) above the repository volume in Figure 4-80 extending downwards from the ground surface and another similarly shaped area to the right of the repository volume. It is concluded that these are numerical artefacts arising due to the changed discretisation between the facility scale and catchment scale model domains (cf. Subsection 3.3.1). Specifically, the reaction front is not well resolved at the coarsest grid scale and so there is a disconnect in hydrogeochemical state at the boundary with the finer scale grid. Although not shown in the figure, this artefact is present along the entire facility scale/catchment scale interface (see illustration of the computational grid in Figure 3-3). The effect appears to be local along the interface with negligible influence on the chemical evolution in the repository volume. Similarly, as for the pH evolution, numerical artefacts occur at the interface between residual Littorina water and upconing Deep Saline water to the east of the repository volume in the area below the sea (right side of the slices figures). This is seen as spots with low pE values at repository depth, and particularly at the early times.

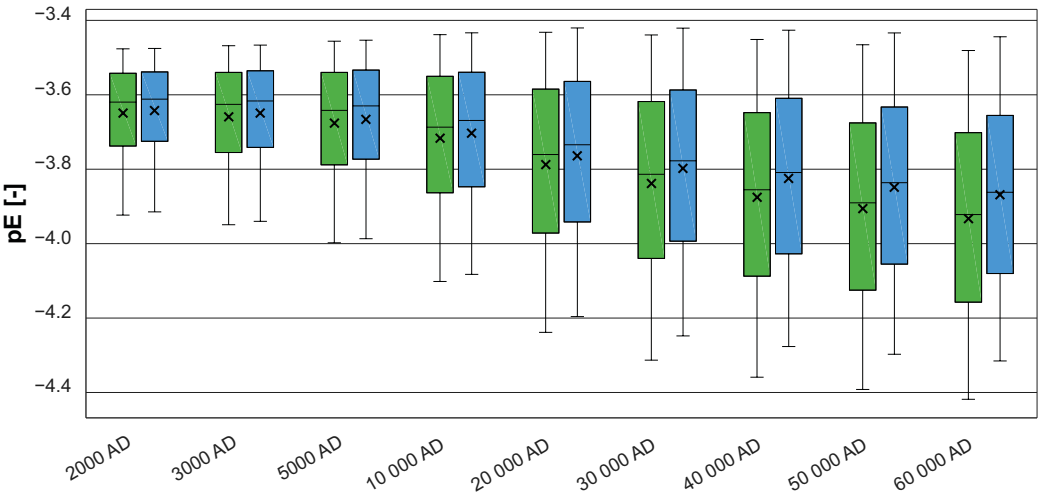

Figure 4-76. *Box and whisker plot showing a comparison of statistical distributions of pE for the two cases with chemical reactions (Case 2 – green, Case 3 – blue) on a regular grid of points within the repository volume between elevations −530 m and −470 m. The statistical measures are the median, the 25th and 75th percentiles (box), the mean (cross) and the 5th and 95th percentiles (whiskers).*

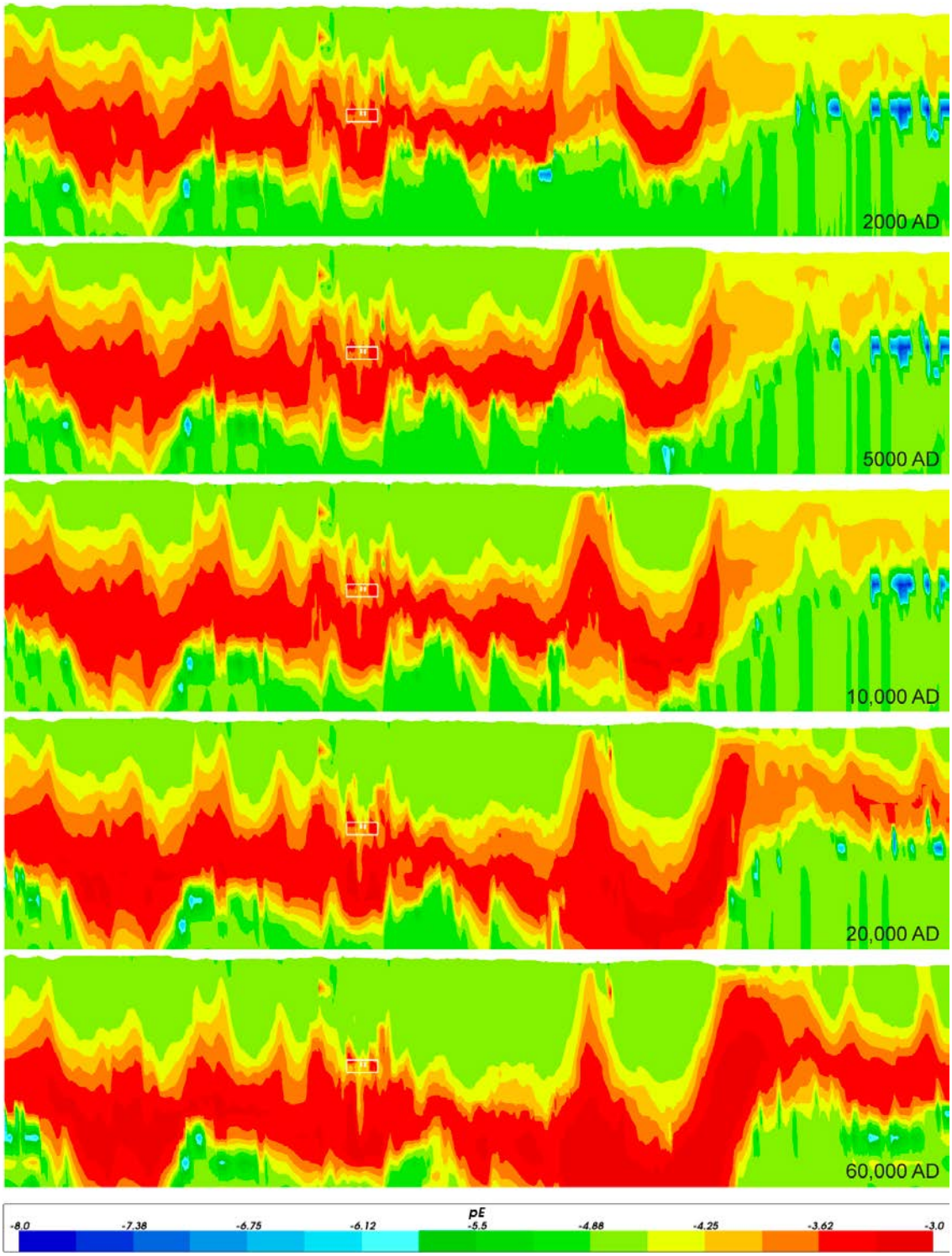

Figure 4-77. *Values of pE on vertical W-E catchment scale slices through the repository volume for Case 2, for dates (from top to bottom) 2000 AD, 5000 AD, 10 000 AD, 20 000 AD and 60 000 AD. The refined volume and repository vaults are shown in white. Model shown down to an elevation of −1 100 m. Vertical scale has been magnified a factor 4.*

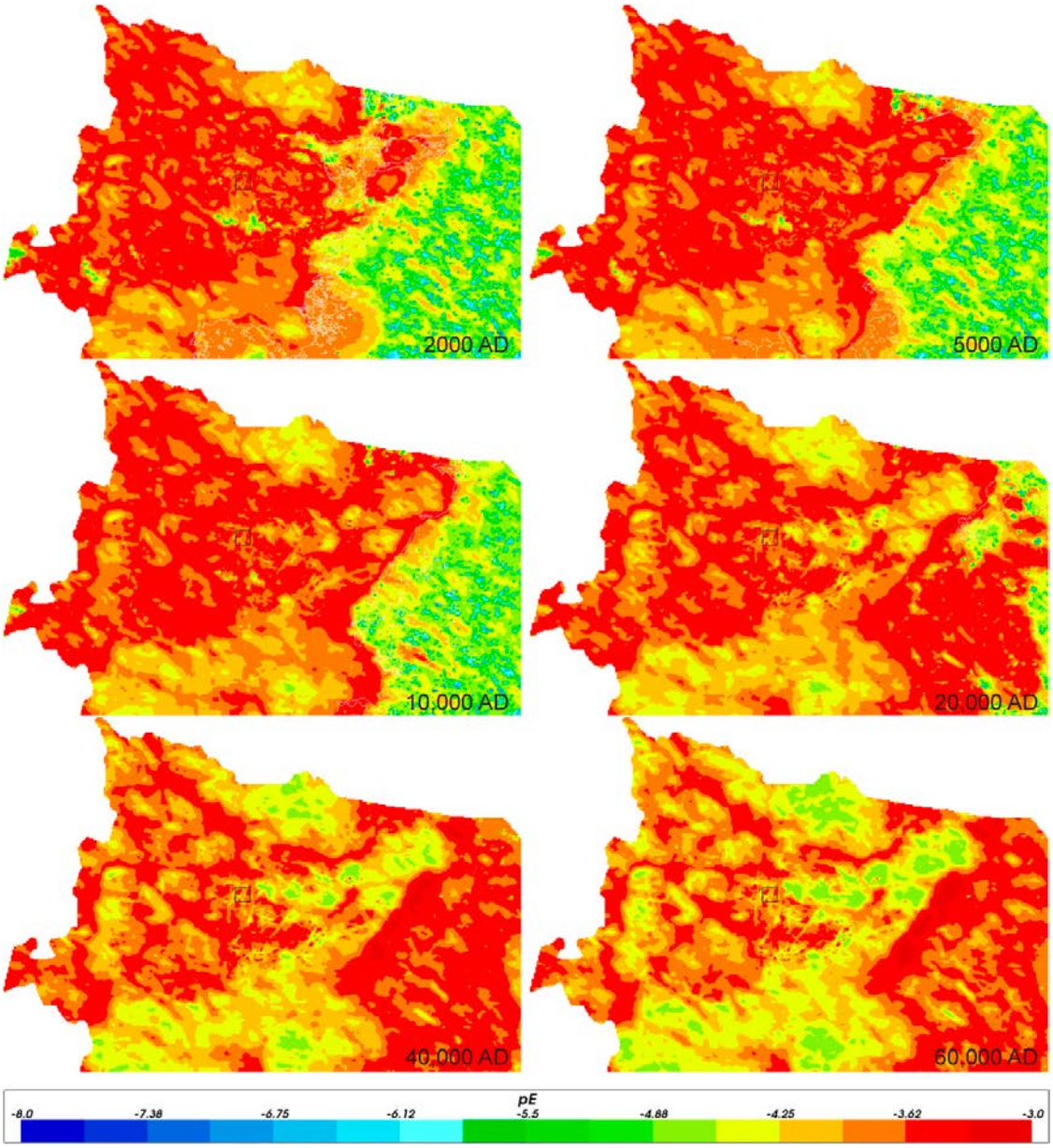

Figure 4-78. *Values of pE on horizontal catchment scale slices at an elevation of -500 m through the repository volume for Case 2, for dates (from left to right, top to bottom) 2000 AD, 5000 AD, 10 000 AD, 20 000 AD, 40 000 AD and 60 000 AD. The refined volume is shown in black and the shoreline is shown in white up to 20 000 AD.*

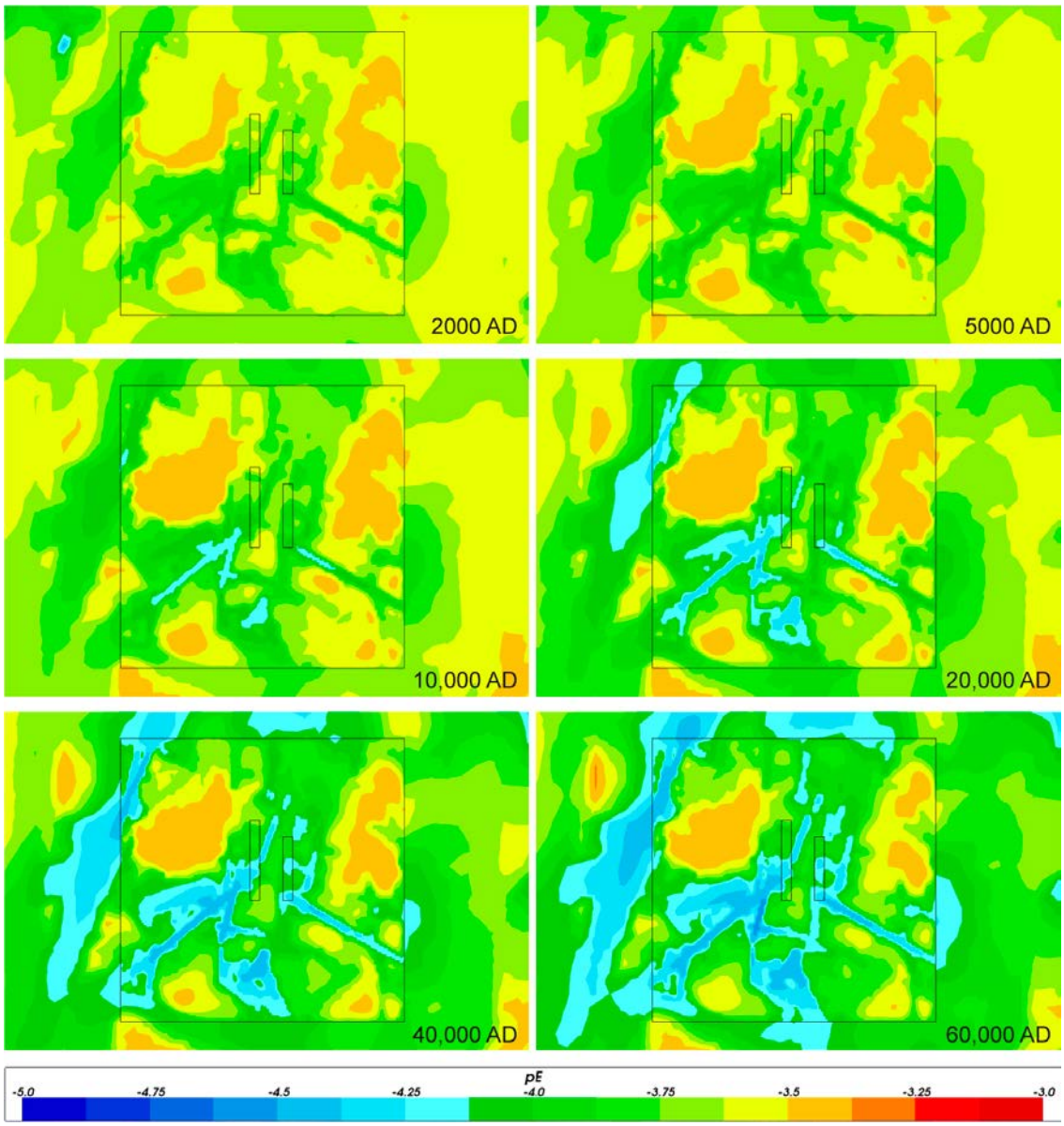

Figure 4-79. *Close-up view of values of pE on horizontal slices at an elevation of -500 m through the repository volume for Case 2, for dates (from left to right, top to bottom) 2000 AD, 5000 AD, 10 000 AD, 20 000 AD, 40 000 AD and 60 000 AD. The refined volume and repository vaults are shown in black.*

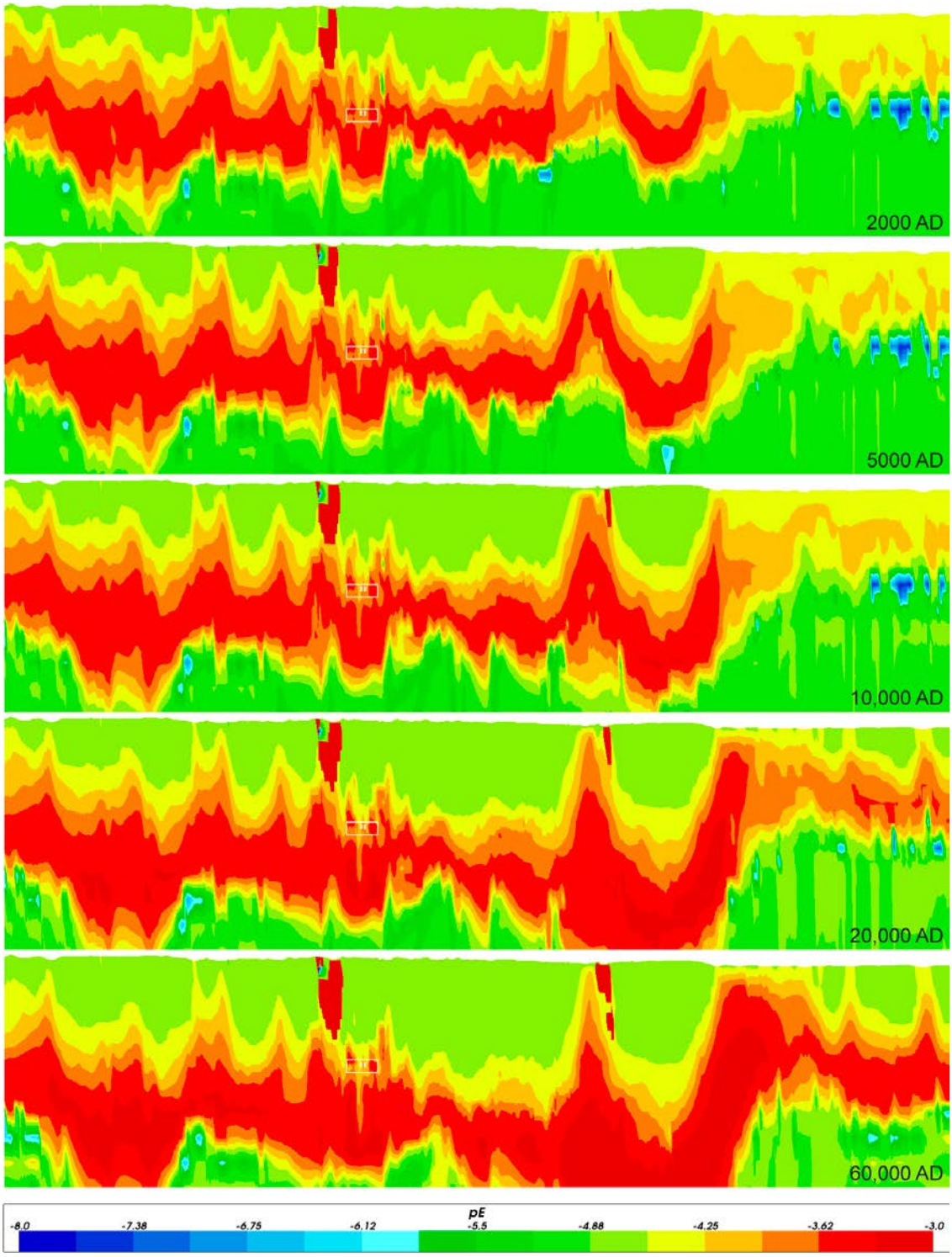

Figure 4-80. *Values of pE on vertical W-E catchment scale slices through the repository volume for Case 3, for dates (from top to bottom) 2000 AD, 5000 AD, 10 000 AD, 20 000 AD and 60 000 AD. The refined volume and repository vaults are shown in white. Model shown down to an elevation of −1 100 m. Vertical scale has been magnified by a factor of 4.*

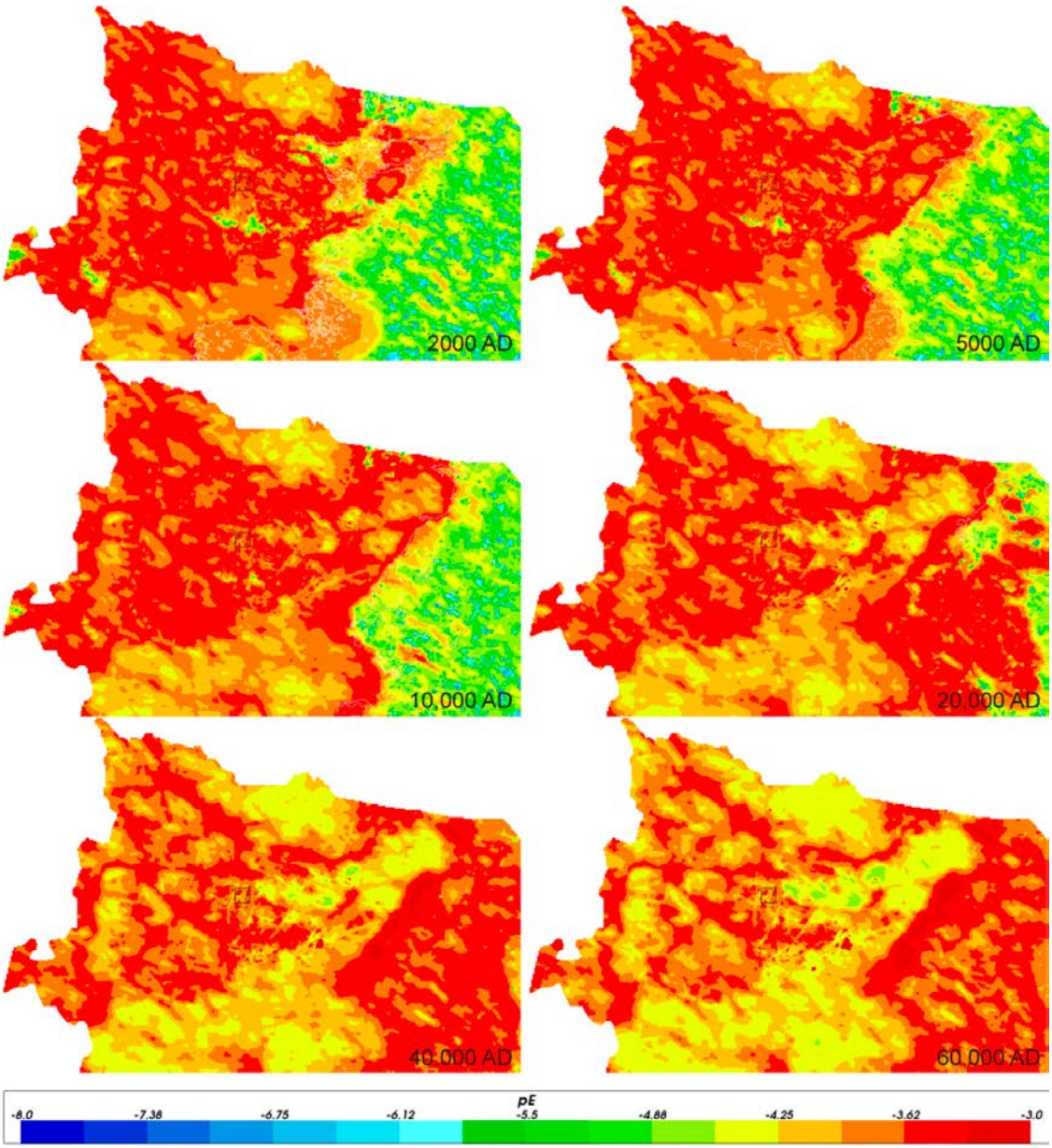

Figure 4-81. *Values of pE on horizontal catchment scale slices at an elevation of -500 m through the repository volume for Case 3, for dates (from left to right, top to bottom) 2000 AD, 5000 AD, 10 000 AD, 20 000 AD, 40 000 AD and 60 000 AD. The refined volume is shown in black and the shoreline is shown in white up to 20 000 AD.*

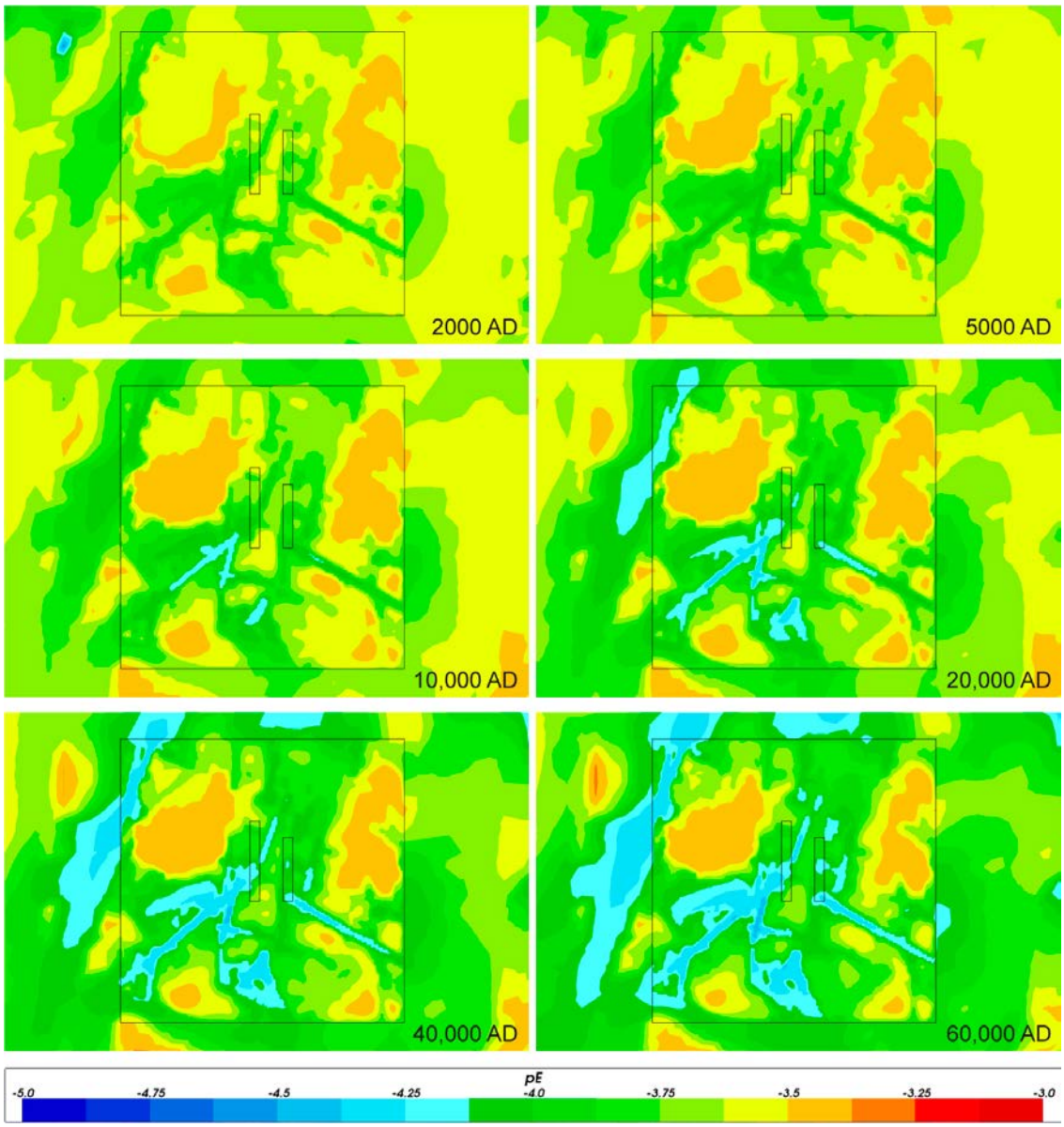

Figure 4-82. *Close-up view of values of pE on horizontal slices at an elevation of -500 m through the repository volume for Case 3, for dates (from left to right, top to bottom) 2000 AD, 5000 AD, 10 000 AD, 20 000 AD, 40 000 AD and 60 000 AD. The refined volume and repository vaults are shown in black.*

4.3.10 Sulphur and sulphide

Figure 4-83 shows a comparison of statistical distributions of total sulphur concentrations for the three modelled cases. A general trend of decreasing total sulphur with time is consistent with the results for chemical species discussed previously, as dilute Altered Meteoric water infiltrates from the top boundary, diluting the groundwater present at repository depth. The total sulphur concentrations are similar for all cases, with a slightly higher concentration in Case 2. This may indicate a slight dissolution of amorphous FeS in this case. In Case 3, a different redox pathway is assumed involving ferric oxyhydroxide which does not contribute to sulphur concentrations.

Figure 4-84 shows a comparison of statistical distributions of free hydrogen sulphide (HS^-) for the two cases with chemical reactions. The increased HS^- concentration in Case 2 may also indicate that dissolution of FeS occurs.

Total sulphur mass fractions on a catchment scale are shown for Case 1 (Figure 4-85 through Figure 4-87), Case 2 (Figure 4-88 through Figure 4-90), and Case 3 (Figure 4-91 through Figure 4-93). On all slice plots, the differences are hardly detectable between the cases. The results suggest that the sulphur content is controlled by transport and mixing processes and only to a very minor extent affected by chemical reactions in Case 2.

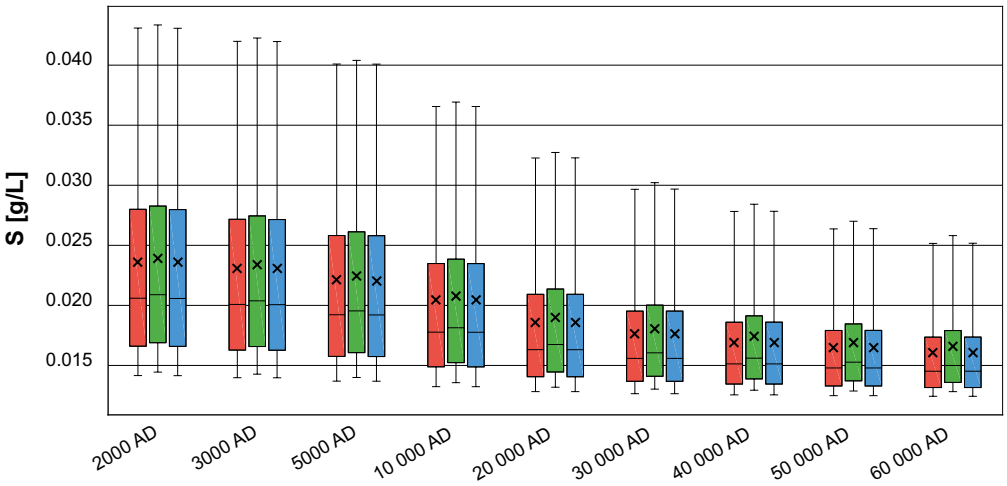

Figure 4-83. *Box and whisker plot showing a comparison of statistical distributions of total sulphur concentrations for the three cases (Case 1 – red, Case 2 – green, Case 3 – blue) on a regular grid of points within the repository volume between elevations −530 m and −470 m. The statistical measures are the median, the 25th and 75th percentiles (box), the mean (cross) and the 5th and 95th percentiles (whiskers).*

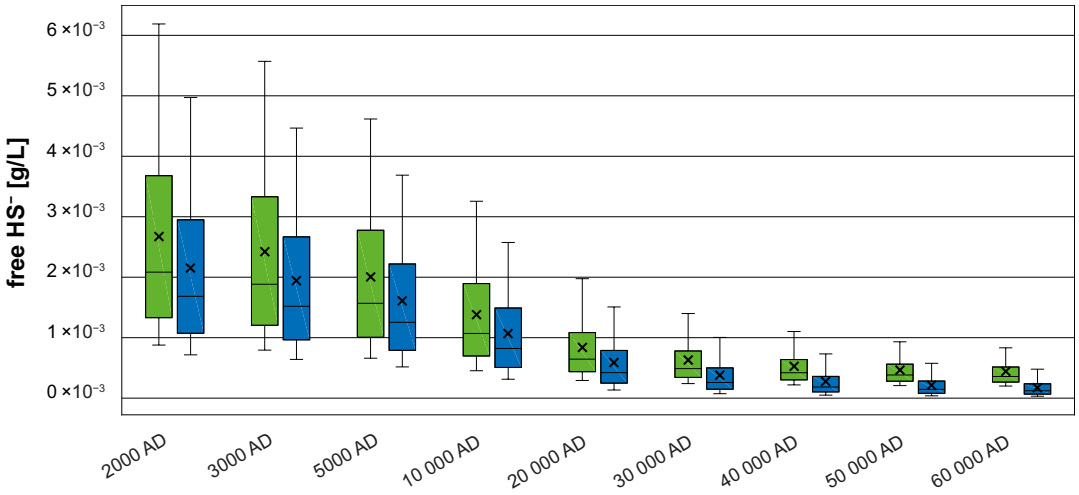

Figure 4-84. *Box and whisker plot showing a comparison of statistical distributions of free hydrogen sulphide (HS^-) concentrations for the two cases with chemical reactions (Case 2 – green, Case 3 – blue) on a regular grid of points within the repository volume between elevations −530 m and −470 m. The statistical measures are the median, the 25th and 75th percentiles (box), the mean (cross) and the 5th and 95th percentiles (whiskers).*

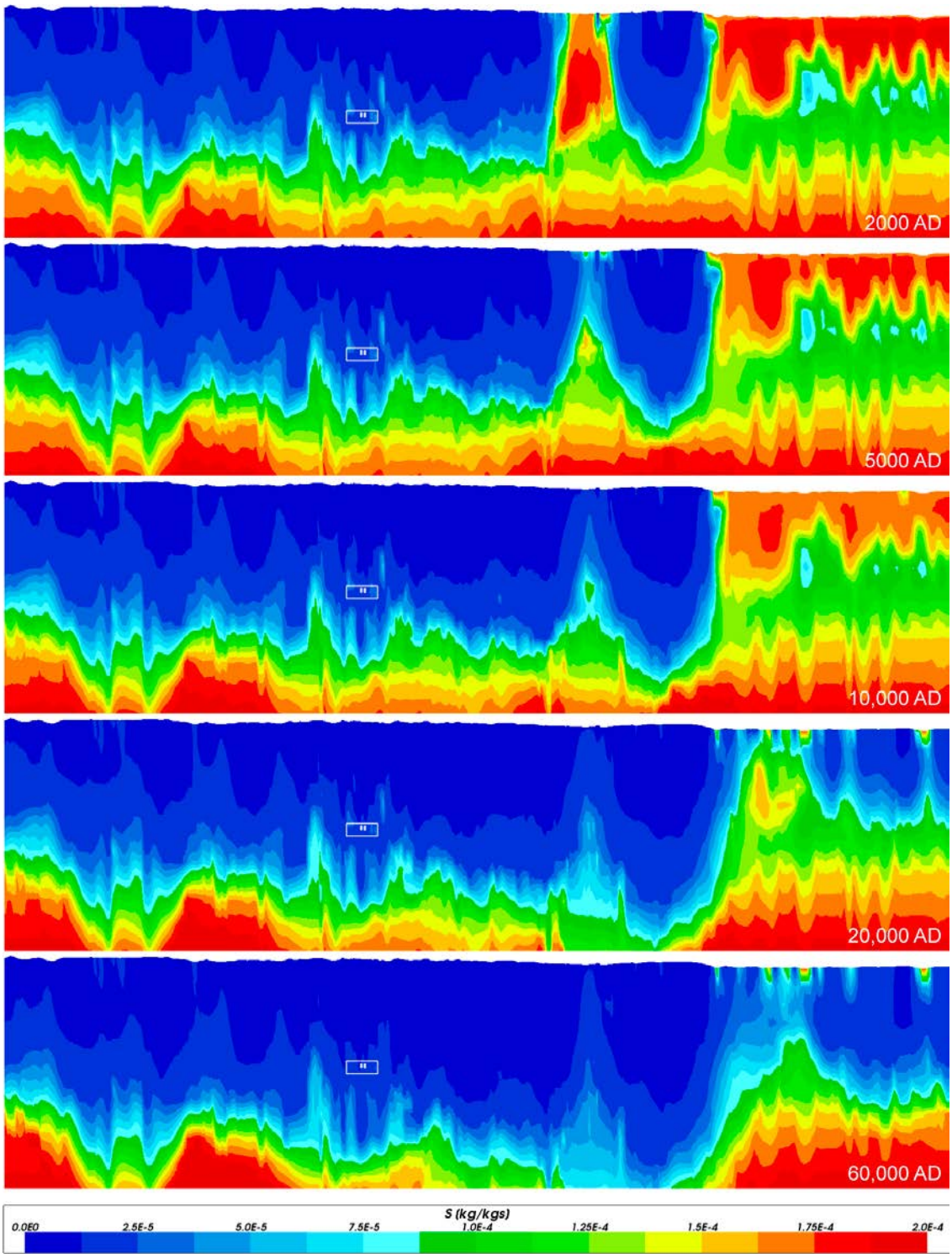

Figure 4-85. *Total sulphur mass fractions on vertical W-E catchment scale slices through the repository volume for Case 1, for dates (from top to bottom) 2000 AD, 5000 AD, 10 000 AD, 20 000 AD and 60 000 AD. The refined volume and repository vaults are shown in white. Model shown down to an elevation of −1 100 m. Vertical scale has been magnified by a factor of 4.*

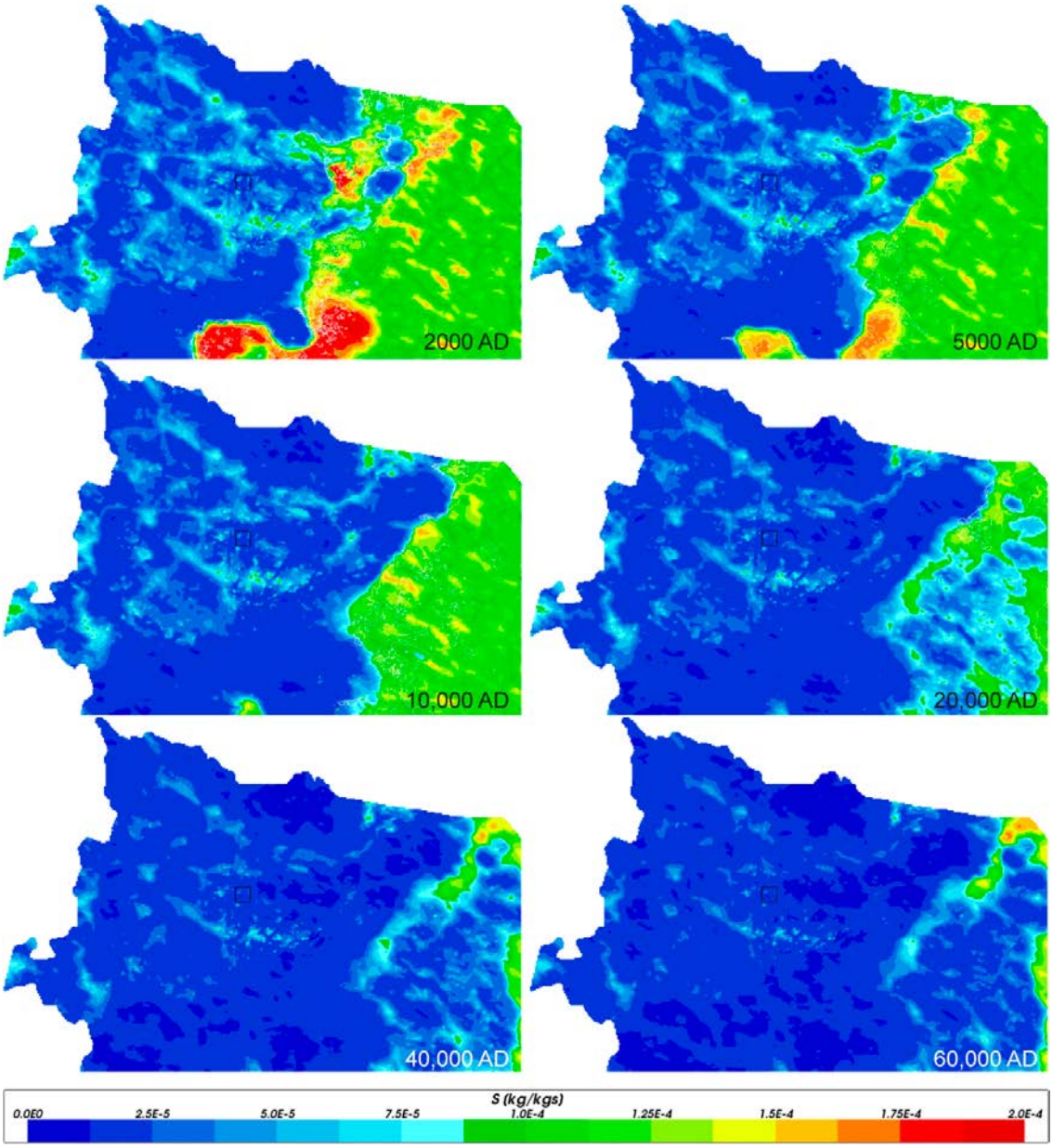

Figure 4-86. *Total sulphur mass fractions on horizontal catchment scale slices at an elevation of −500 m through the repository volume for Case 1, for dates (from left to right, top to bottom) 2000 AD, 5000 AD, 10 000 AD, 20 000 AD, 40 000 AD and 60 000 AD. The refined volume is shown in black and the shoreline is shown in white up to 20 000 AD.*

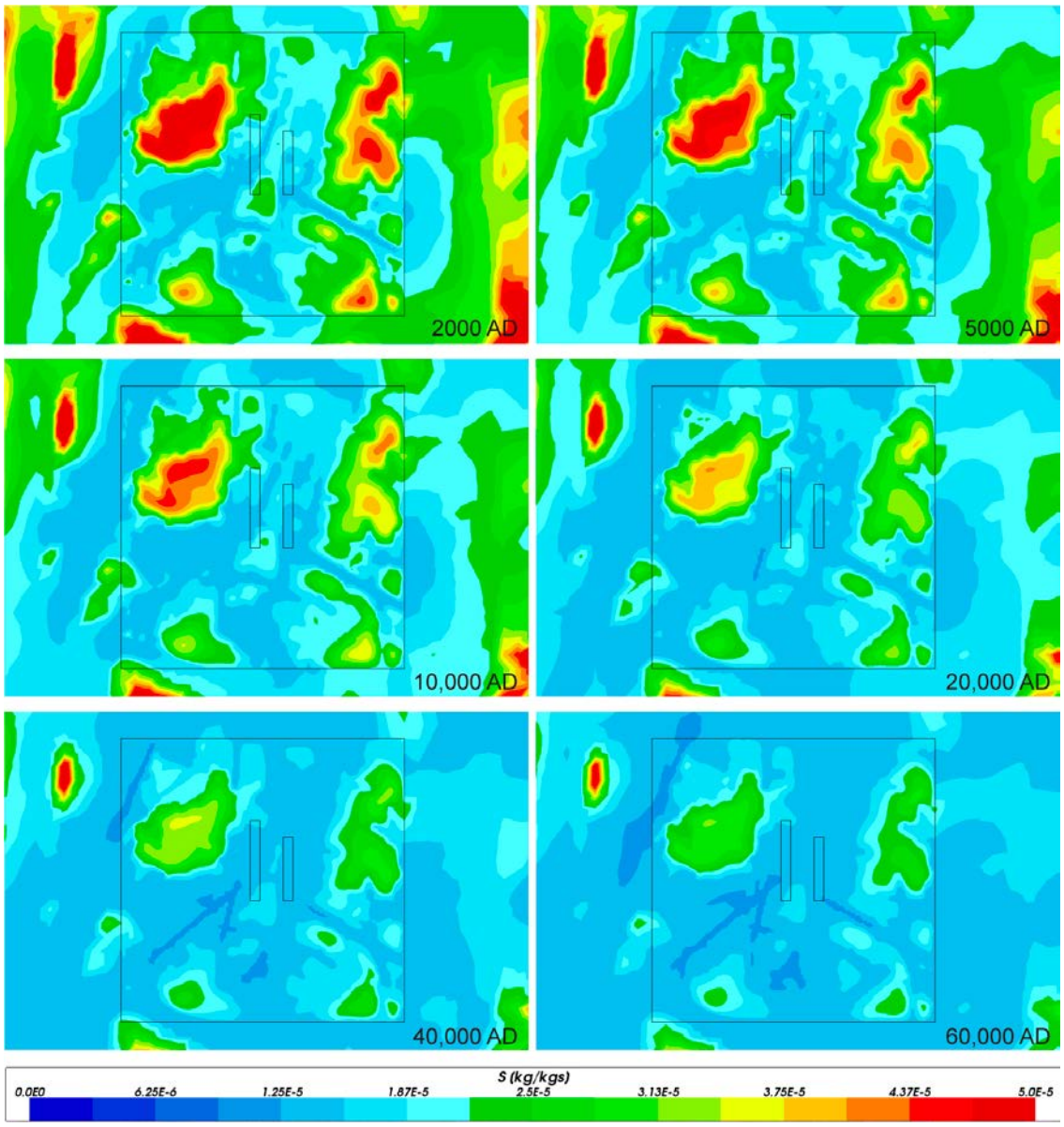

Figure 4-87. *Close-up view of total sulphur mass fractions on horizontal slices at an elevation of −500 m through the repository volume for Case 1, for dates (from left to right, top to bottom) 2000 AD, 5000 AD, 10 000 AD, 20 000 AD, 40 000 AD and 60 000 AD. The refined volume and repository vaults are shown in black. Note that the maximum of the range is lower than in Figure 4-86.*

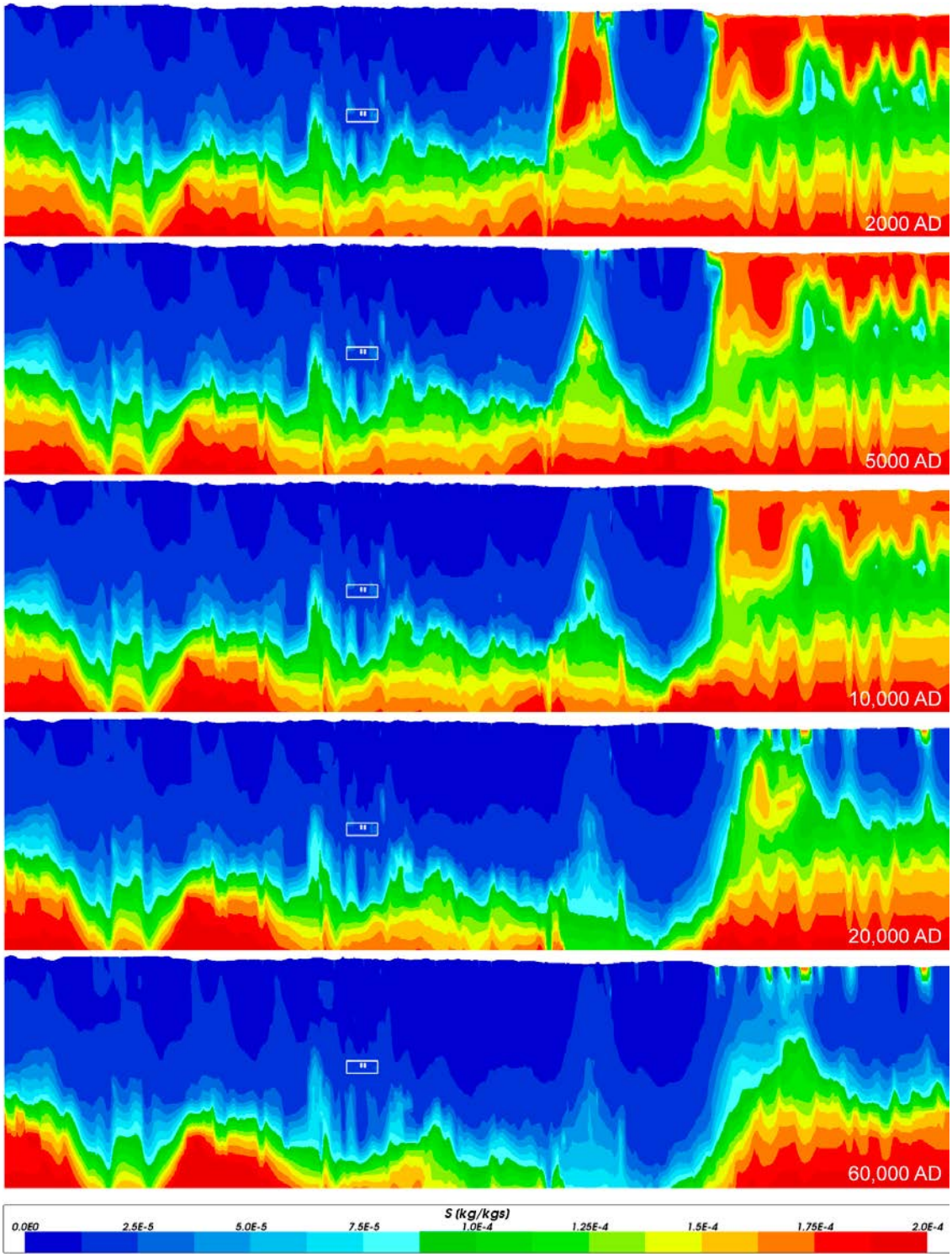

Figure 4-88. *Total sulphur mass fractions on vertical W-E catchment scale slices through the repository volume for Case 2, for dates (from top to bottom) 2000 AD, 5000 AD, 10 000 AD, 20 000 AD and 60 000 AD. The refined volume and repository vaults are shown in white. Model shown down to an elevation of −1 100 m. Vertical scale has been magnified by a factor of 4.*

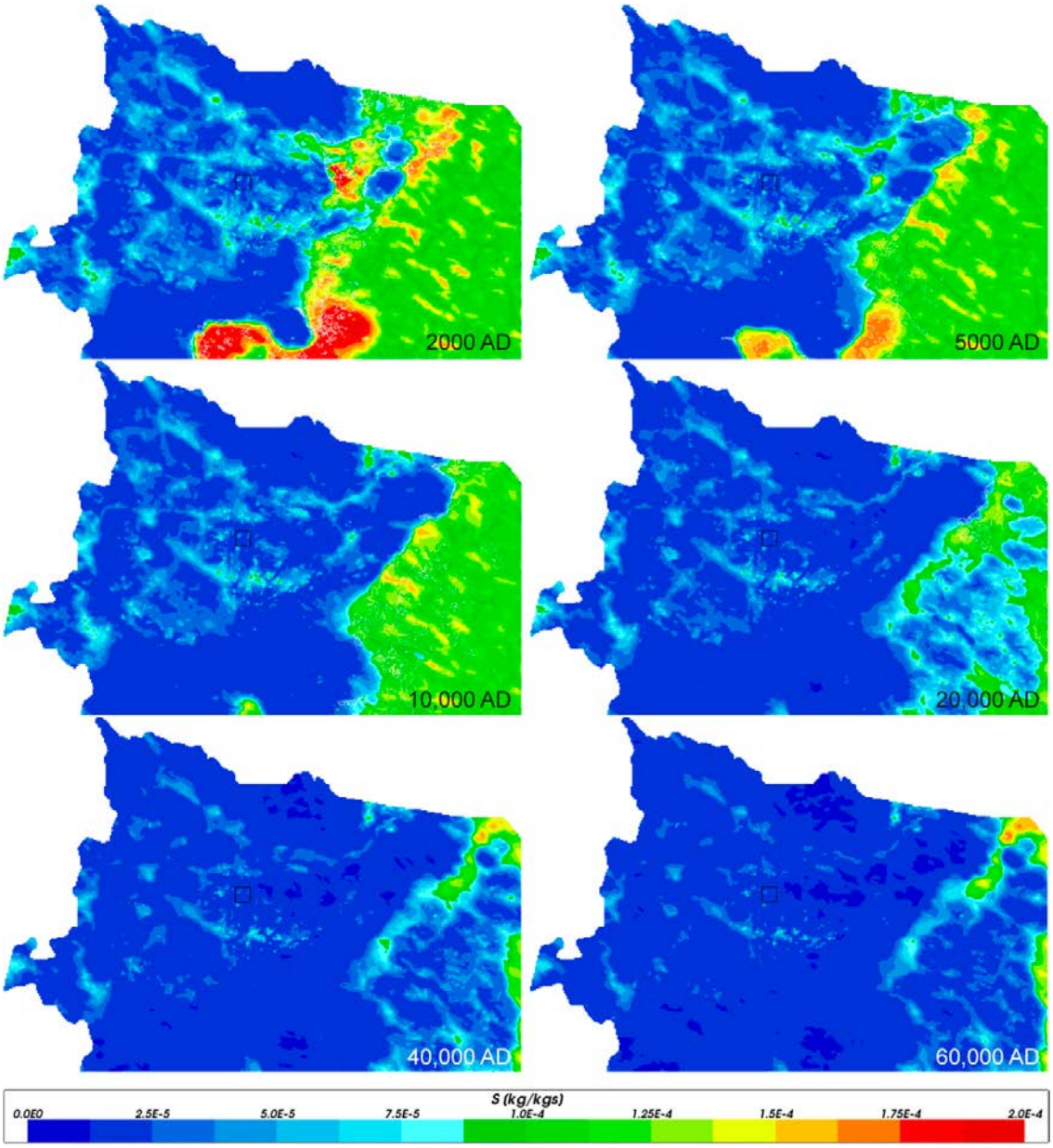

Figure 4-89. *Total sulphur mass fractions on horizontal catchment scale slices at an elevation of −500 m through the repository volume for Case 2, for dates (from left to right, top to bottom) 2000 AD, 5000 AD, 10 000 AD, 20 000 AD, 40 000 AD and 60 000 AD. The refined volume is shown in black and the shoreline is shown in white up to 20 000 AD.*

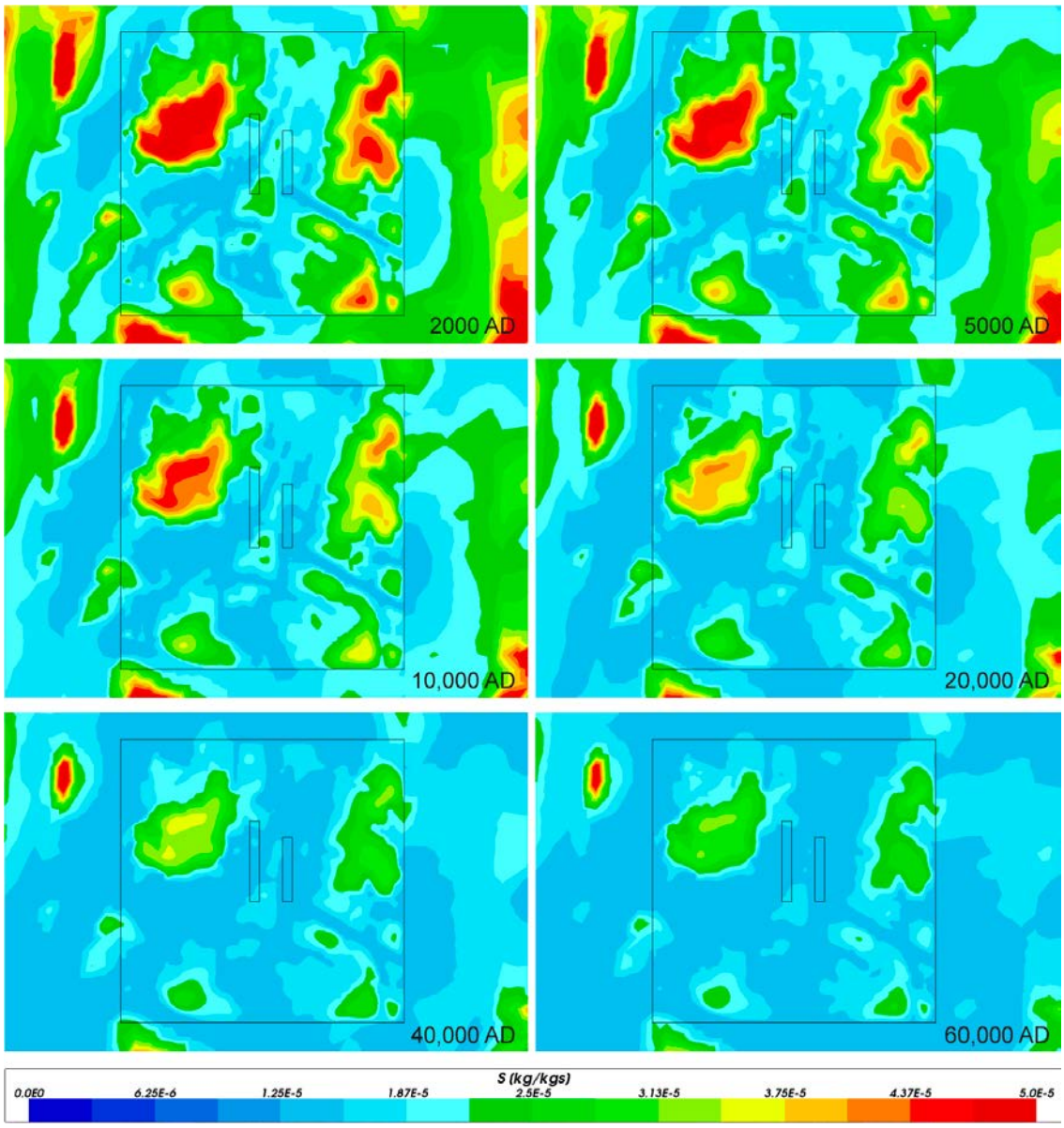

Figure 4-90. *Close-up view of total sulphur mass fractions on horizontal slices at an elevation of −500 m through the repository volume for Case 2, for dates (from left to right, top to bottom) 2000 AD, 5000 AD, 10 000 AD, 20 000 AD, 40 000 AD and 60 000 AD. The refined volume and repository vaults are shown in black. Note that the maximum of the range is lower than in Figure 4-89.*

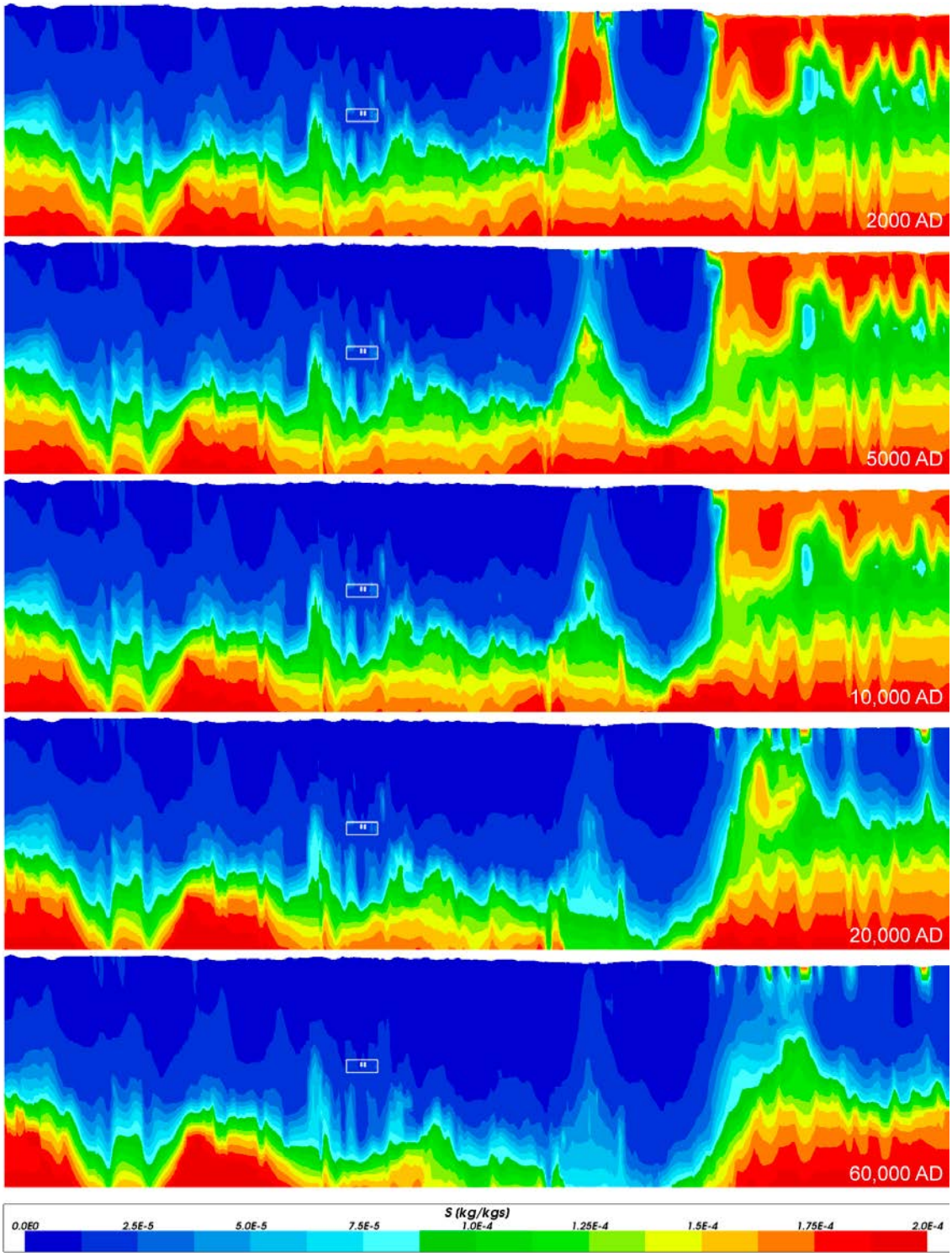

Figure 4-91. *Total sulphur mass fractions on vertical W-E catchment scale slices through the repository volume for Case 3, for dates (from top to bottom) 2000 AD, 5000 AD, 10 000 AD, 20 000 AD and 60 000 AD. The refined volume and repository vaults are shown in white. Model shown down to an elevation of −1 100 m. Vertical scale has been magnified a factor 4.*

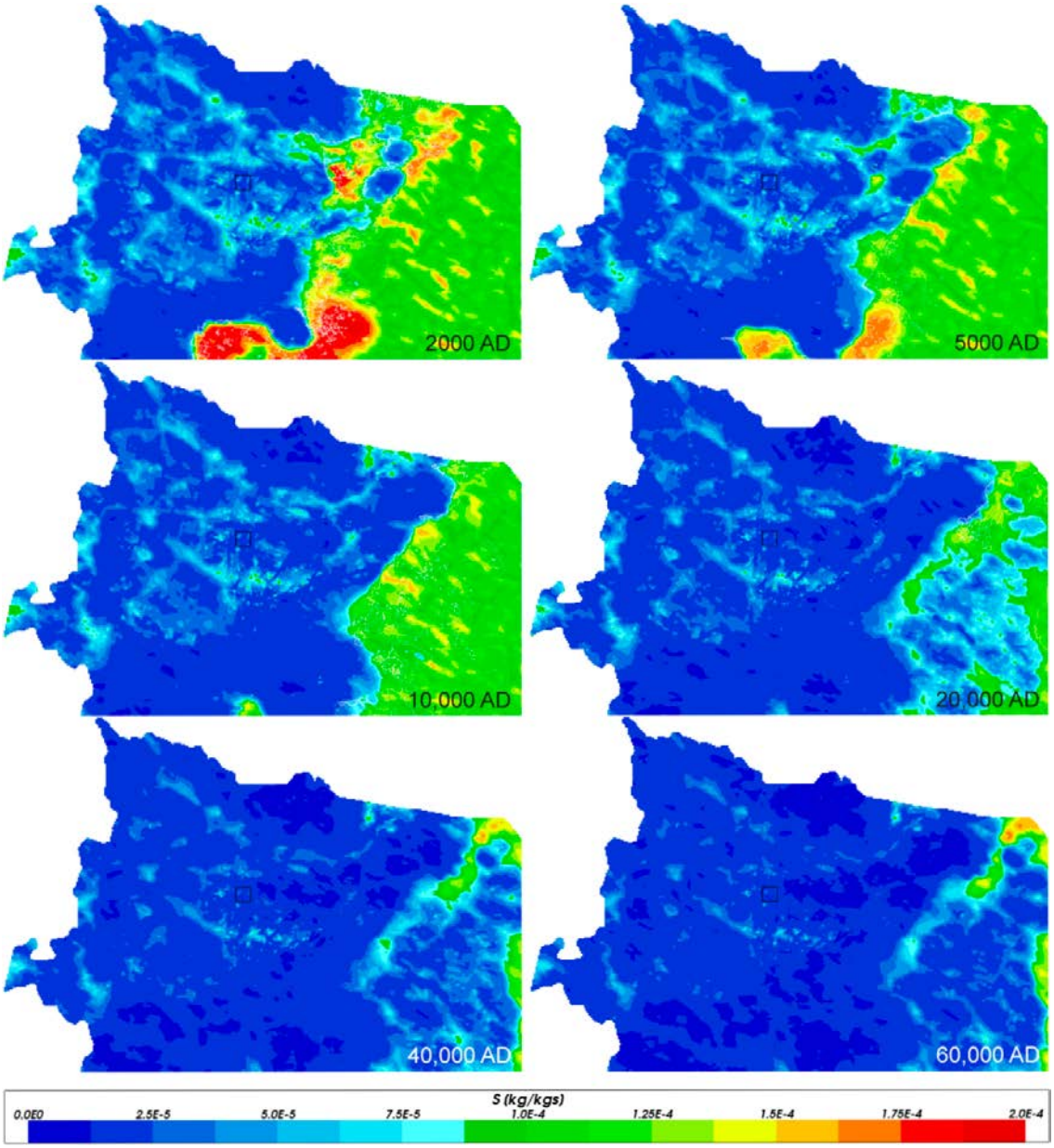

Figure 4-92. *Total sulphur mass fractions on horizontal catchment scale slices at an elevation of −500 m through the repository volume for Case 3, for dates (from left to right, top to bottom) 2000 AD, 5000 AD, 10 000 AD, 20 000 AD, 40 000 AD and 60 000 AD. The refined volume is shown in black and the shoreline is shown in white up to 20 000 AD.*

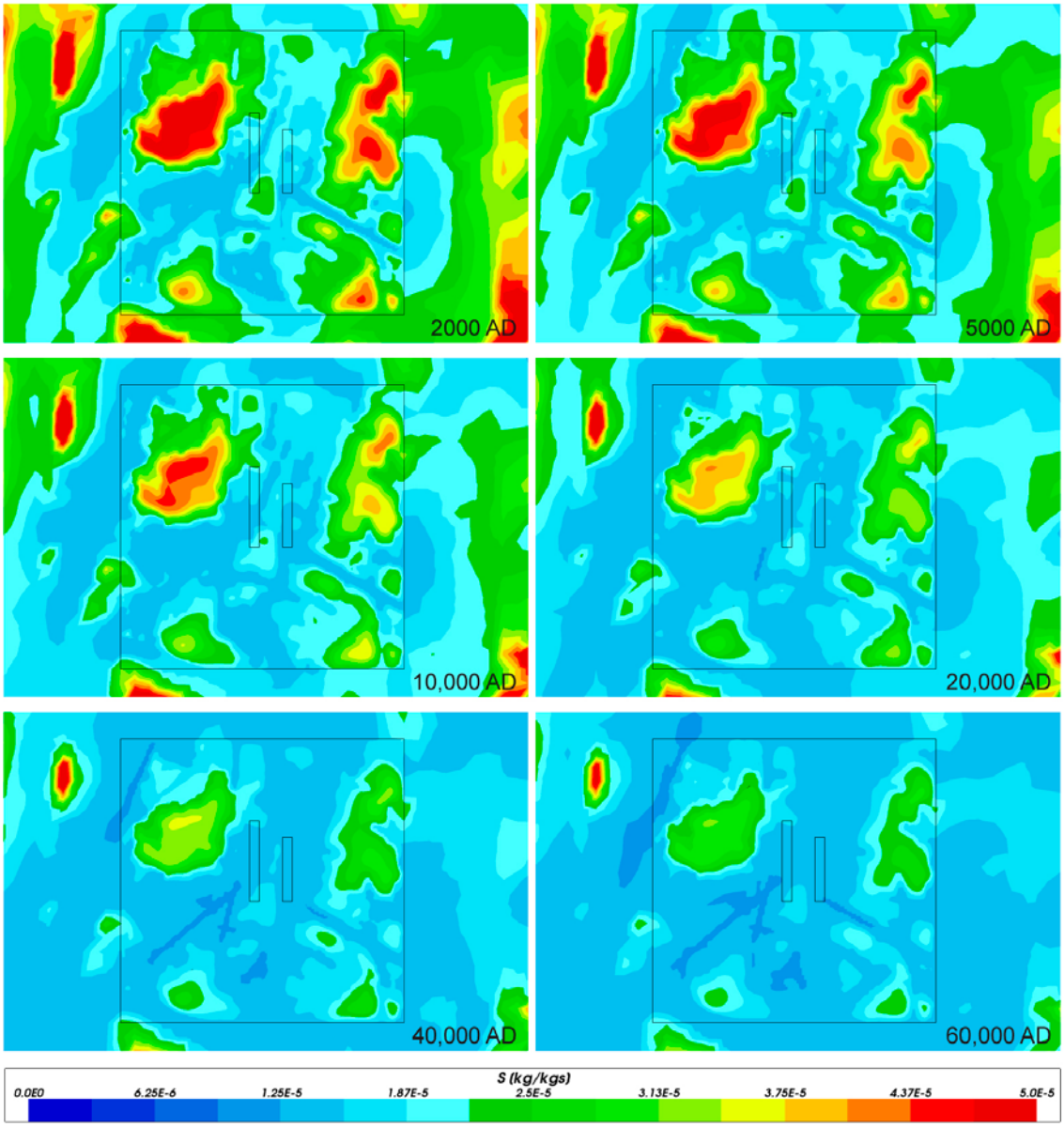

Figure 4-93. *Close-up view of total sulphur mass fractions on horizontal slices at an elevation of −500 m through the repository volume for Case 3, for dates (from left to right, top to bottom) 2000 AD, 5000 AD, 10 000 AD, 20 000 AD, 40 000 AD and 60 000 AD. The refined volume and repository vaults are shown in black. Note that the maximum of the range is lower than in Figure 4-92.*

4.3.11 Iron

Figure 4-94 shows a comparison of statistical distributions of total iron concentrations for the two cases with chemical reactions. Cases 2 and 3 differ in the assumed redox pathway (see Section 3.1). Local equilibrium with FeS is assumed in Case 2, whereas local equilibrium with $Fe(OH)_3$ is assumed in Case 3. For Case 1, the iron concentration in the repository volume is much lower than for Cases 2 and 3, which is why it is omitted in the following figures.

The difference in iron concentrations between Cases 2 and 3 reflects the difference in the chosen redox pathway. In Case 2, FeS is dissolved to reach equilibrium with the groundwater. A slight increase in total dissolved iron with time is seen for this case, which is consistent with the decreasing concentration of free hydrogen sulphide with time described in Section 4.3.10. This also explains the slightly increasing total sulphur in Case 2 relative to Cases 1 and 3. In Case 3, there is an opposite trend with decreasing iron concentrations with time. This reflects the dissolution of ferric oxyhydroxide which decreases as the pH increases in the repository volume with time.

Total iron mass fractions on a catchment scale are shown for Case 2 (Figure 4-95 to Figure 4-97) and Case 3 (Figure 4-98 to Figure 4-100). As discussed for pE in Subsection 4.3.9, numerical artefacts are seen at the interface between the facility scale and catchment scale model domains (cf. Subsection 3.3.1). For the iron concentrations this is seen as wedge-shaped areas with alternating high and low concentrations above the repository volume and to the right of the repository volume in Figure 4-95 that extend downwards from the ground surface. Although not shown in the figure, this artefact is present along the entire facility scale/catchment scale interface (see wireframe illustration of the computational grid in Figure 3-3). The effect appears to be local along the interface with negligible influence on the chemical evolution in the repository volume. Redox reactions are particularly sensitive to numerical effects and the consequences are readily seen for iron due to its low concentration.

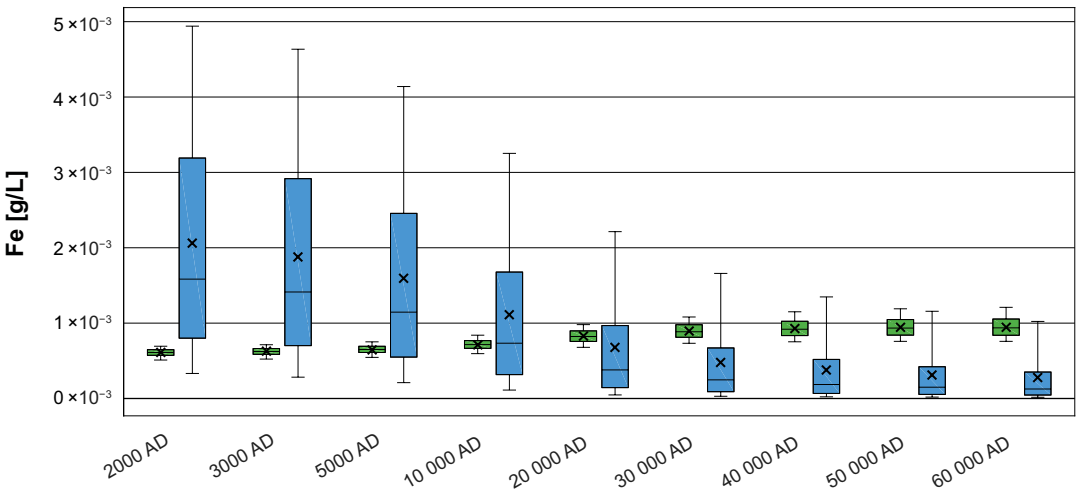

Figure 4-94. *Box and whisker plot showing a comparison of statistical distributions of total iron concentrations for the two cases with chemical reactions (Case 2 – green, Case 3 – blue) on a regular grid of points within the repository volume between elevations −530 m and −470 m. The statistical measures are the median, the 25th and 75th percentiles (box), the mean (cross) and the 5th and 95th percentiles (whiskers).*

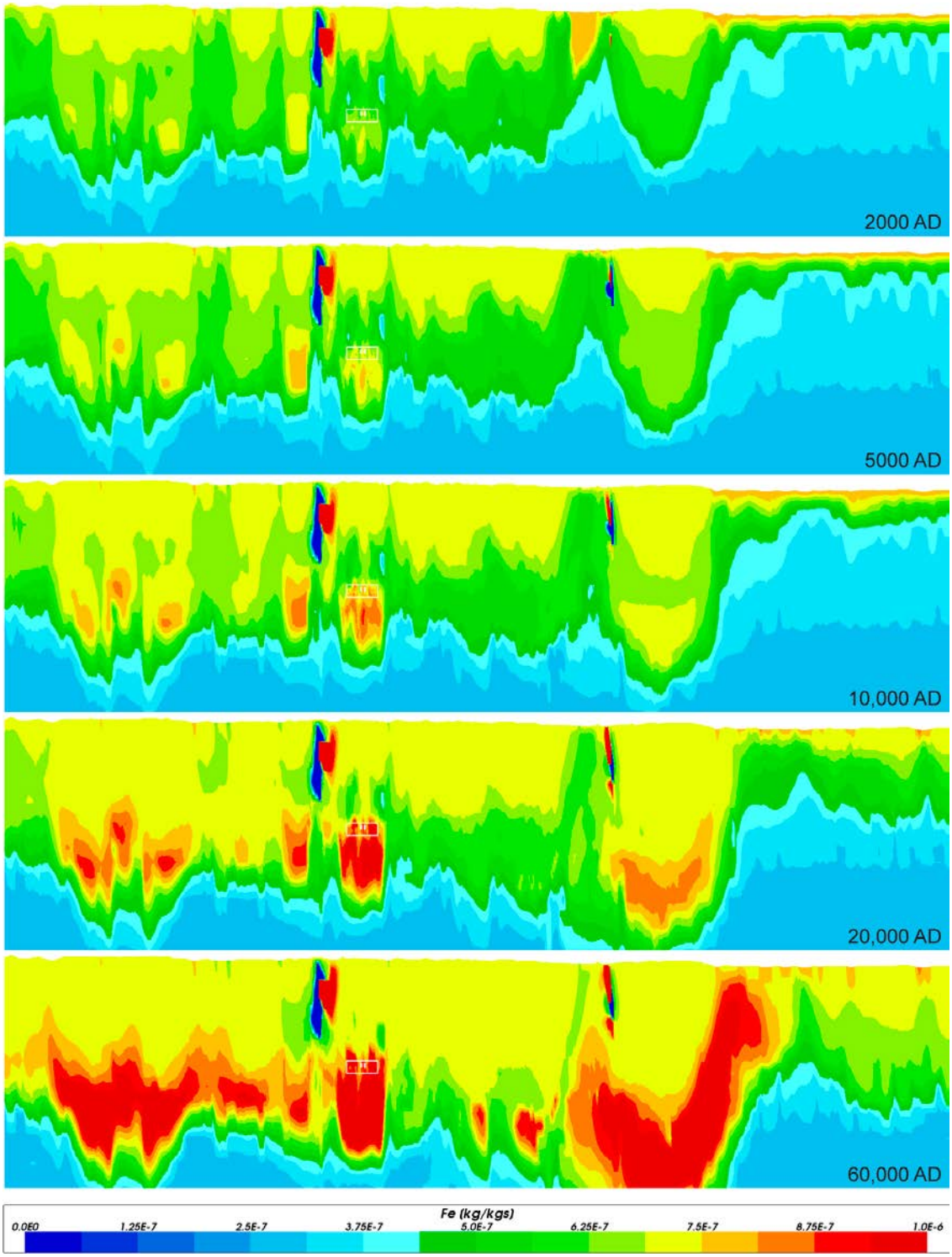

Figure 4-95. *Total iron mass fractions on vertical W-E catchment scale slices through the repository volume for Case 2, for dates (from top to bottom) 2000 AD, 5000 AD, 10 000 AD, 20 000 AD and 60 000 AD. The refined volume and repository vaults are shown in white. Model shown down to an elevation of −1 100 m. Vertical scale has been magnified by a factor of 4.*

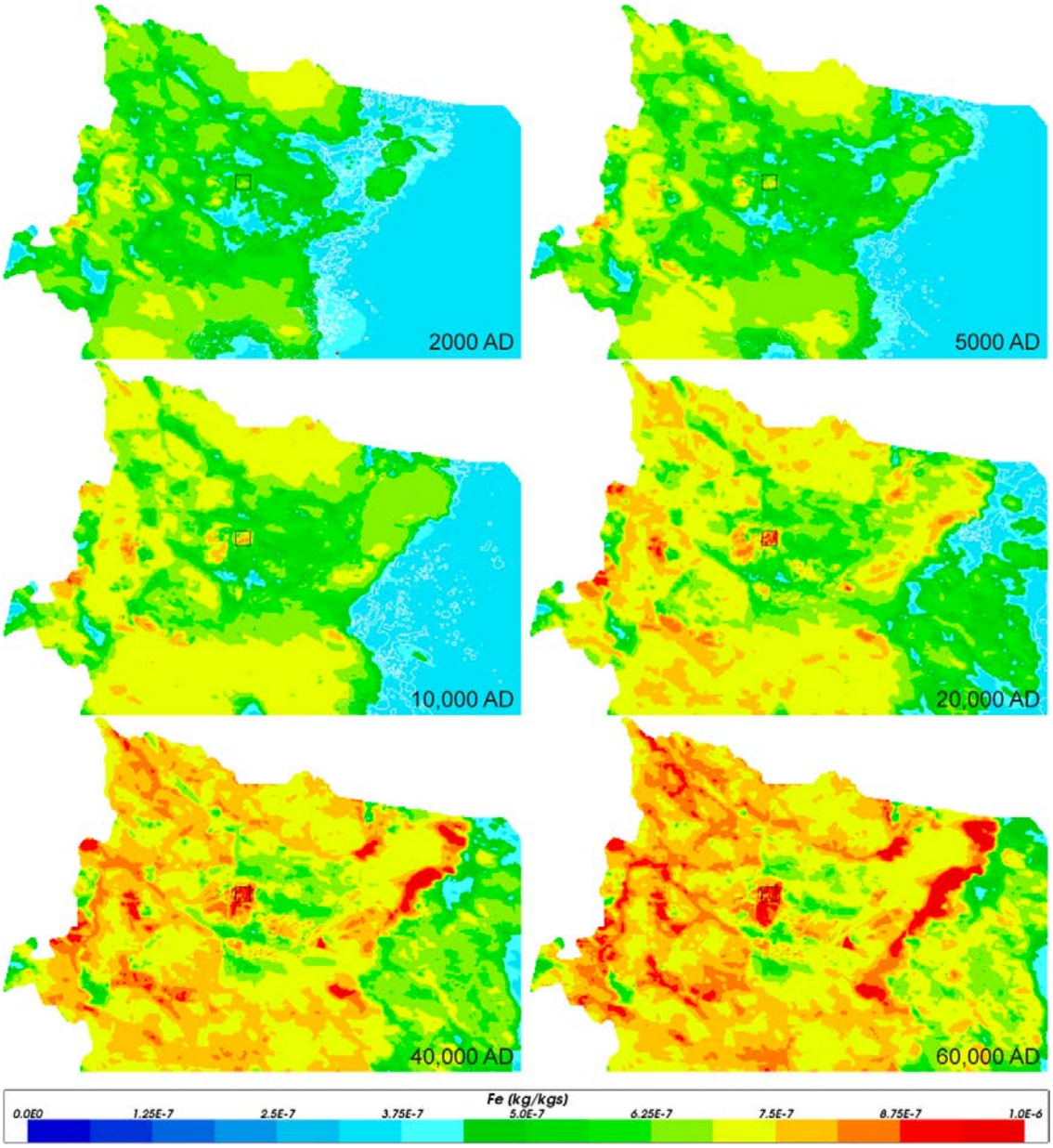

Figure 4-96. *Total iron mass fractions on horizontal catchment scale slices at an elevation of −500 m through the repository volume for Case 2, for dates (from left to right, top to bottom) 2000 AD, 5000 AD, 10 000 AD, 20 000 AD, 40 000 AD and 60 000 AD. The refined volume is shown in black and the shoreline is shown in white up to 20 000 AD.*

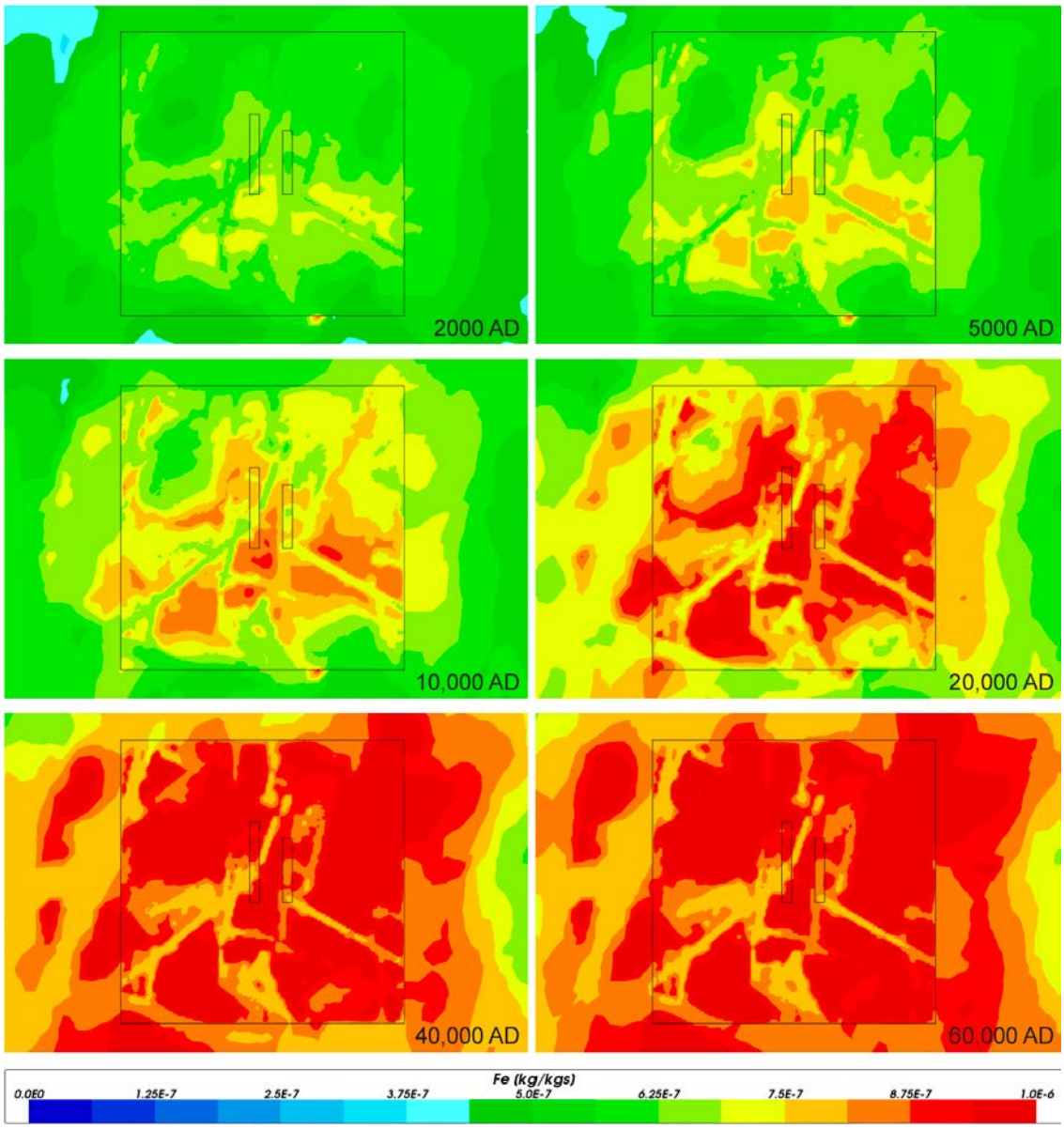

Figure 4-97. *Close-up view of total iron mass fractions on horizontal slices at an elevation of −500 m through the repository volume for Case 2, for dates (from left to right, top to bottom) 2000 AD, 5000 AD, 10 000 AD, 20 000 AD, 40 000 AD and 60 000 AD. The refined volume and repository vaults are shown in black.*

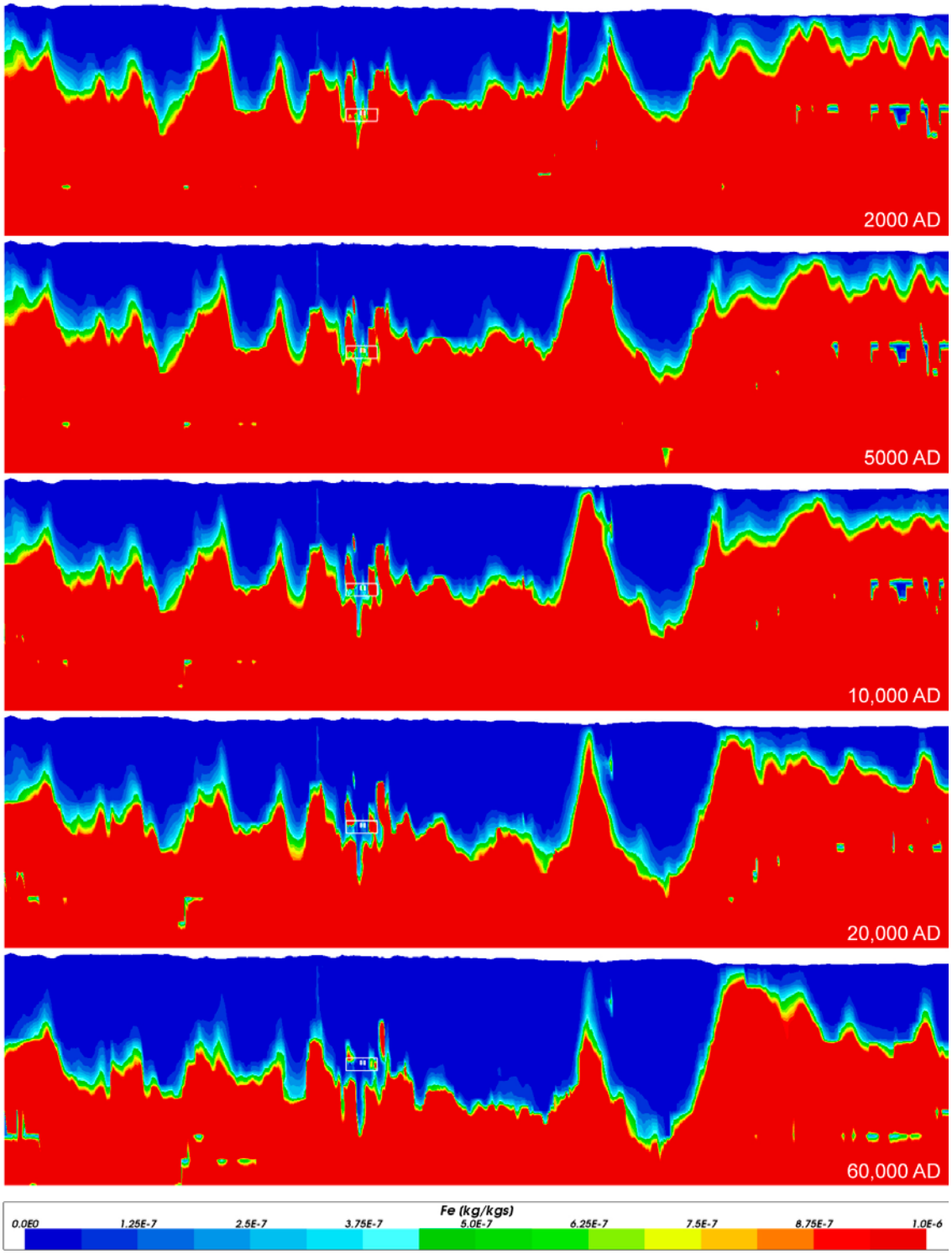

Figure 4-98. *Total iron mass fractions on vertical W-E catchment scale slices through the repository volume for Case 3, for dates (from top to bottom) 2000 AD, 5000 AD, 10 000 AD, 20 000 AD and 60 000 AD. The refined volume and repository vaults are shown in white. Model shown down to an elevation of −1 100 m. Vertical scale has been magnified by a factor of 4.*

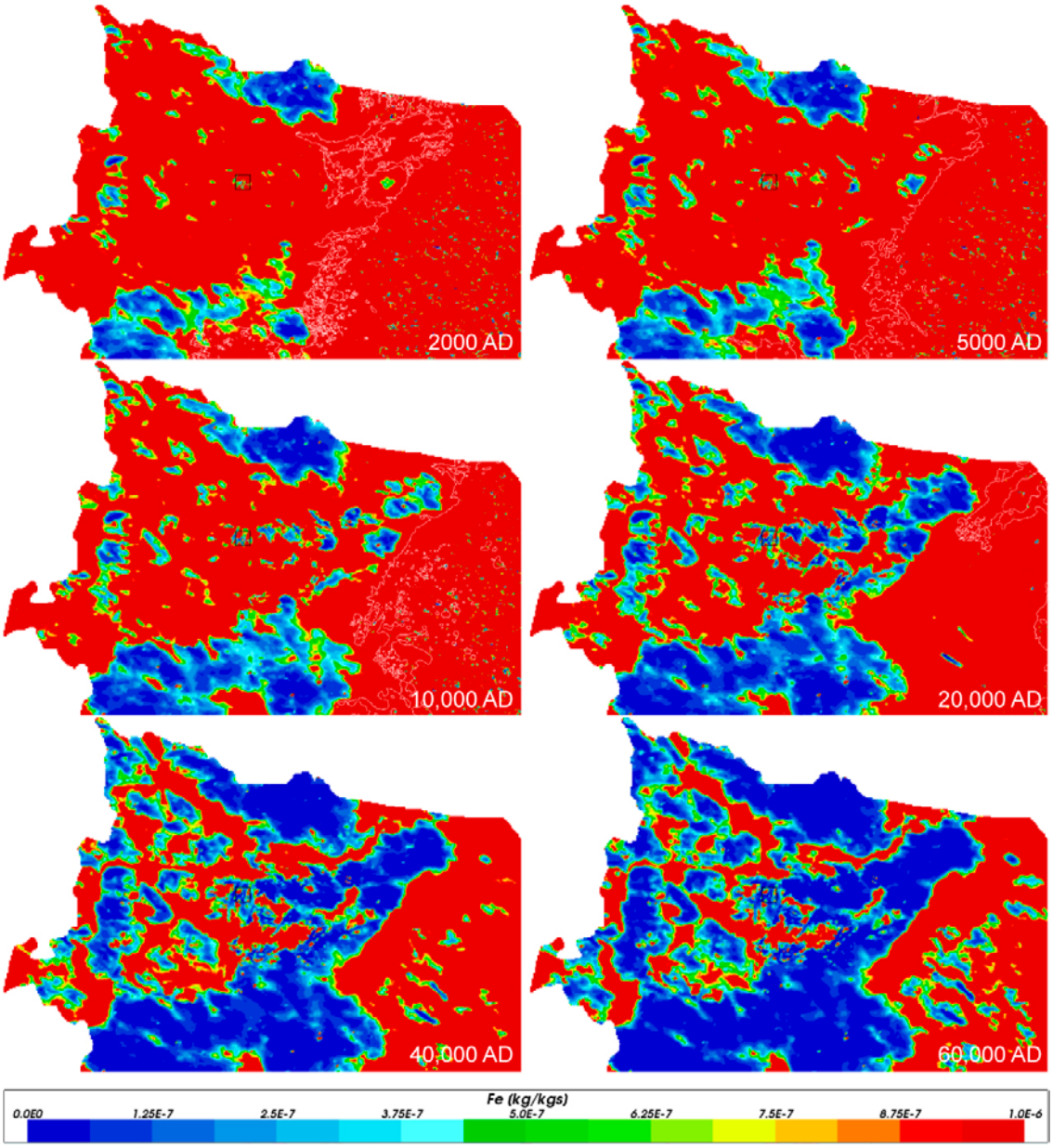

Figure 4-99. *Total iron mass fractions on horizontal catchment scale slices at an elevation of −500 m through the repository volume for Case 3, for dates (from left to right, top to bottom) 2000 AD, 5000 AD, 10 000 AD, 20 000 AD, 40 000 AD and 60 000 AD. The refined volume is shown in black and the shoreline is shown in white up to 20 000 AD.*

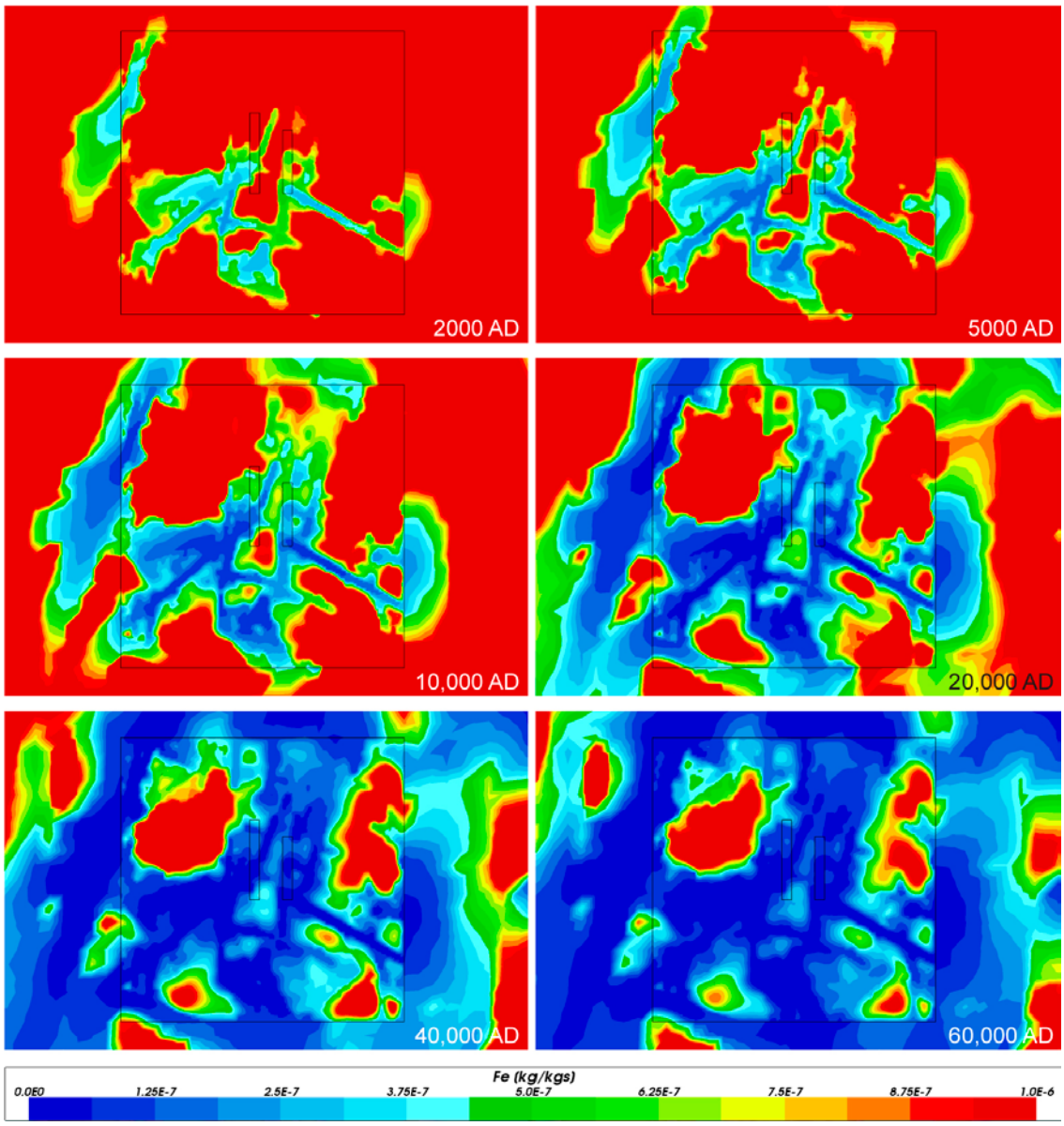

Figure 4-100. *Close-up view of total iron mass fractions on horizontal slices at an elevation of −500 m through the repository volume for Case 3, for dates (from left to right, top to bottom) 2000 AD, 5000 AD, 10 000 AD, 20 000 AD, 40 000 AD and 60 000 AD. The refined volume and repository vaults are shown in black.*

4.4 Sensitivity to HRD realisation

4.4.1 Permeability distribution

To investigate the sensitivity of the catchment scale groundwater flow and hydrogeochemical evolution to the spatial distribution of hydraulic properties in the HRD, a set of five DFN realisations were used to derive the spatially varying properties of the HRD for Case 1, which is the variant without chemical reactions. In this section, the distribution of upscaled permeability is compared between realisations. The statistical analysis in the following sections examines the effects of the different realisations in more detail.

Figure 4-101 shows vertical slices at different scales through the facility volume with the deformation zones (purple) superimposed on the permeability (K_{xx}) distribution for HRD realisation 1. The refined volume and repository vaults are shown in white for orientation.

Figure 4-102 shows horizontal slices at different scales at an elevation of −500 m through the facility volume with the deformation zones (purple) superimposed on the permeability (K_{xx}) distribution for HRD realisation 1. The refined volume and repository vaults are shown in white for orientation.

The effective permeability is a combined result of the underlying stochastic DFN upscaled to block permeability and the deterministic deformation zones weighted together, as described in Sections 2.2.3 and 2.2.5. In the close-up views, the effects of discretisation are seen when fractures cross the interface between the coarser and the finer resolved parts of the grid. Also, on the catchment scale, the different fracture intensities and upscaled permeabilities in the various fracture domains are visible.

In Figure 4-103 through Figure 4-105, the principal hydraulic permeability distributions for the five HRD realisations of Case 1 are shown on various vertical and horizontal slices. In each figure, K_{xx} (horizontal permeability in X-direction) is shown in the left column and K_{zz} (vertical permeability) in the right. In all pictures, the refined volume and repository vaults are shown in white for context.

It is clear from the figures that the fractures crossing the interface between different refinements in the model grid, are continued properly even though the changes in upscaled permeability due to the fractures are resolved differently at the different grid scales. The length of one single cell side (30 m) in the coarser grid surrounding the refined repository volume corresponds to six cells (each 5 m) in the finer grid within the volume. When a fracture with high permeability passes from the finer discretised repository volume out into the coarse grid surrounding it, the permeability is spread over a larger cell volume and therefore decreases at the same time as the fracture seemingly widens. If the fracture also happens to intersect more than one grid cell in width, it might appear to be a very large structure. These are all scale effects arising from the geometry of the fractures and the ECPM grid.

The figures show that there are some differences between the horizontal (X-component, K_{xx}) and vertical (K_{zz}) permeabilities, generally within one order of magnitude. It is also clear from the figures that there are significant local differences in properties between the five HRD realisations. Even though the underlying DFN's are based on the same fracture statistics, the stochastic nature of the generated fracture networks results in locally different permeabilities. For example, it can be seen in realisations 1 and 3 that there are more features with higher permeabilities present around and crossing the repository volume. Conversely, realisations 2, 4 and 5, show less connecting features in and around the repository volume. It should be noted though that the fracture network is three-dimensional, making it difficult to visualise the overall situation within the volume of interest. Also, the groundwater flow rate is a function of the entire connected fracture system, so changes in flows locally within the repository volume are a result of differences in the entire permeability field in the model and not only the closest fractures. This makes it difficult to predict which one of the realisations will give the highest flows or most flushing of saline waters, etc. Note that a transmissivity trend with depth is applied to deformation zones, so that their contribution to the permeability of the ECPM model diminishes below an elevation of around −500 m.

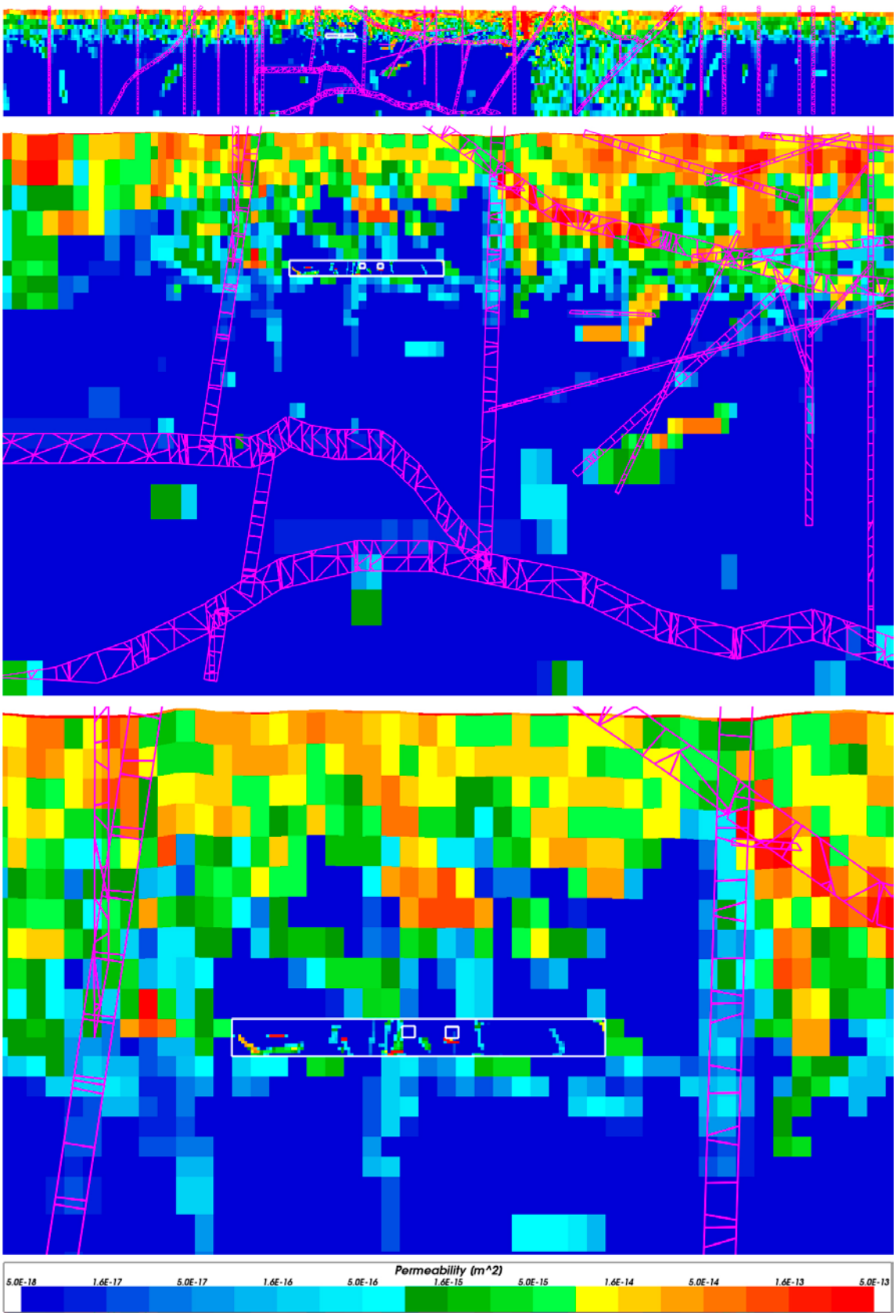

Figure 4-101. *Vertical slices at different scales through the repository volume showing the deformation zones (purple) superimposed on the permeability (K_{xx}) distribution for HRD realisation 1. The refined volume and repository vaults are shown in white. Model shown from the top down to an elevation of −2 075 m for the top two sections and −850 m for the bottom section.*

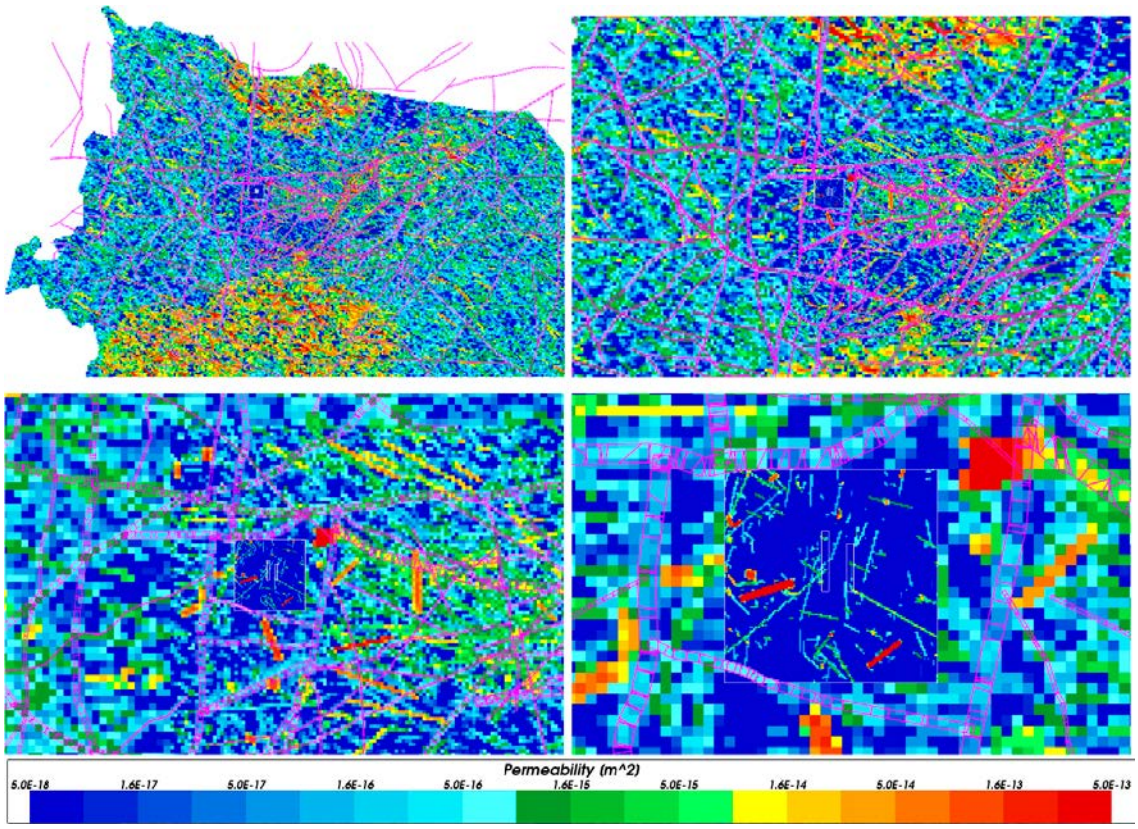

Figure 4-102. *Horizontal slices at different scales at an elevation of -500 m through the repository volume showing the deformation zones (purple) superimposed on the permeability (K_{xx}) distribution for HRD realisation 1. The refined volume and repository vaults are shown in white.*

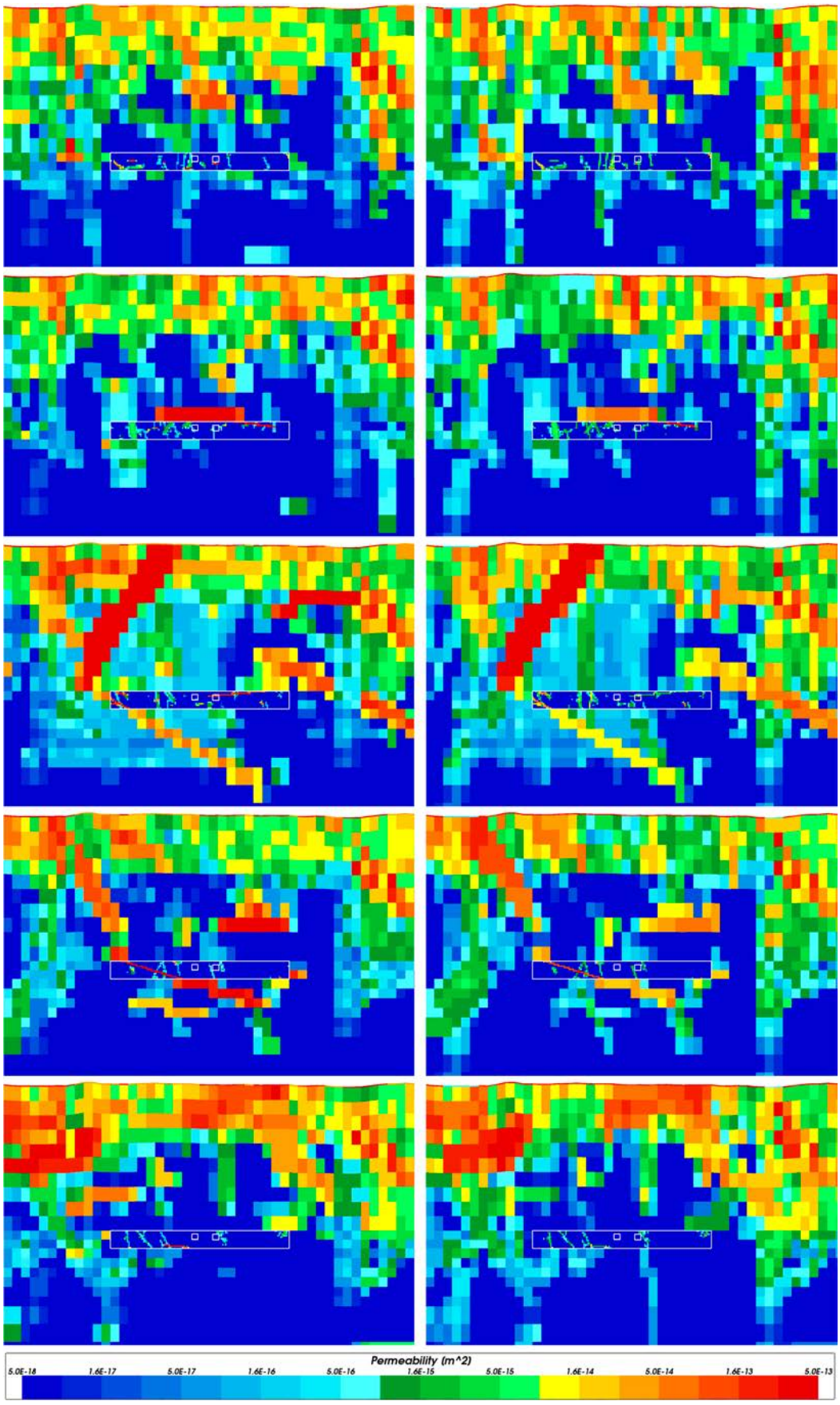

Figure 4-103. *Permeability (K_{xx} – left, K_{zz} – right) distribution on vertical W-E slices through the repository volume for Case 1, HRD realisations 1–5 (from top to bottom). The refined volume and repository vaults are shown in white. Model shown from the top down to an elevation of −850 m.*

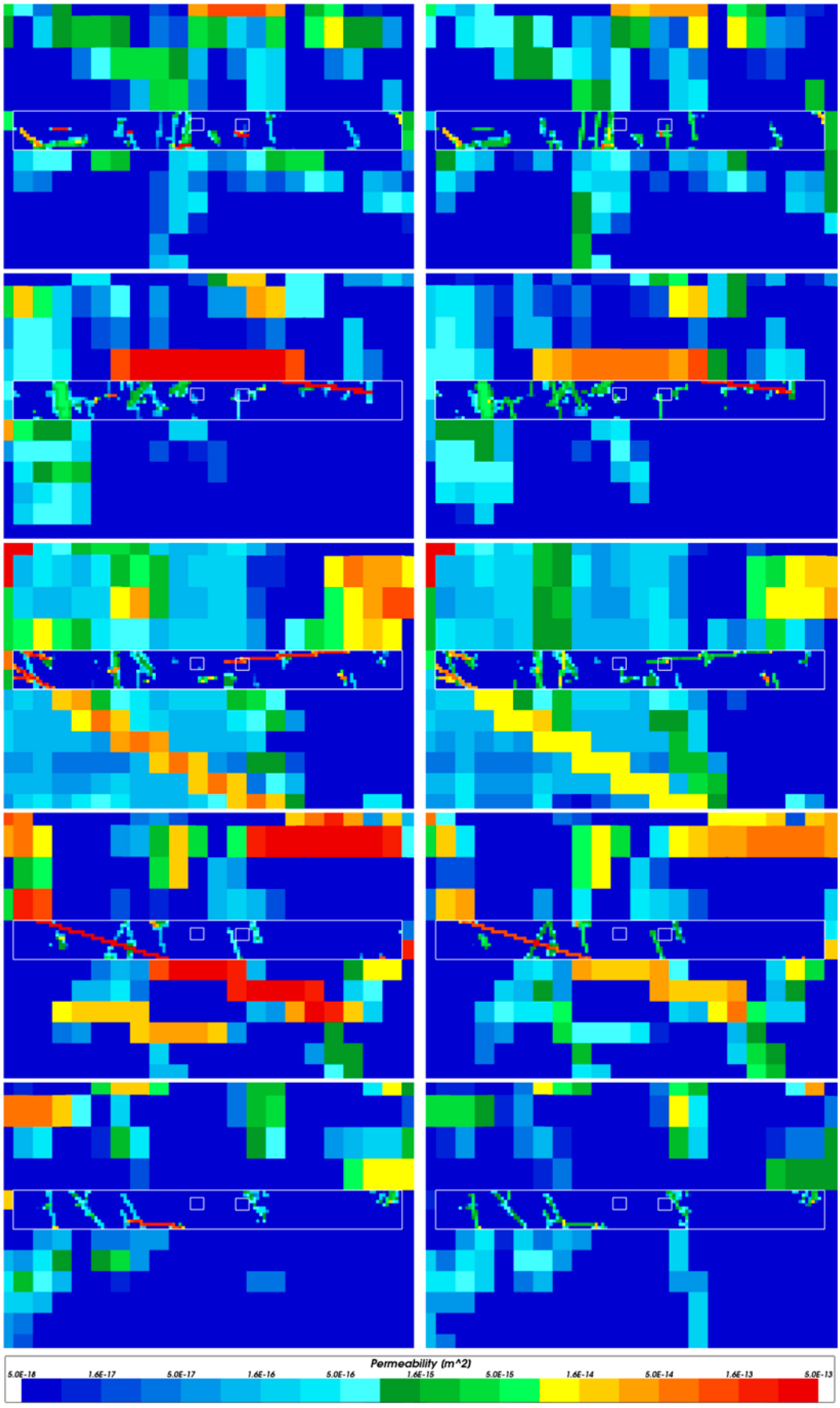

Figure 4-104. *Close-up view of the permeability (K_{xx} – left, K_{zz} – right) distribution on vertical W-E slices through the repository volume for Case 1, HRD realisations 1–5 (from top to bottom). The refined volume and repository vaults are shown in white.*

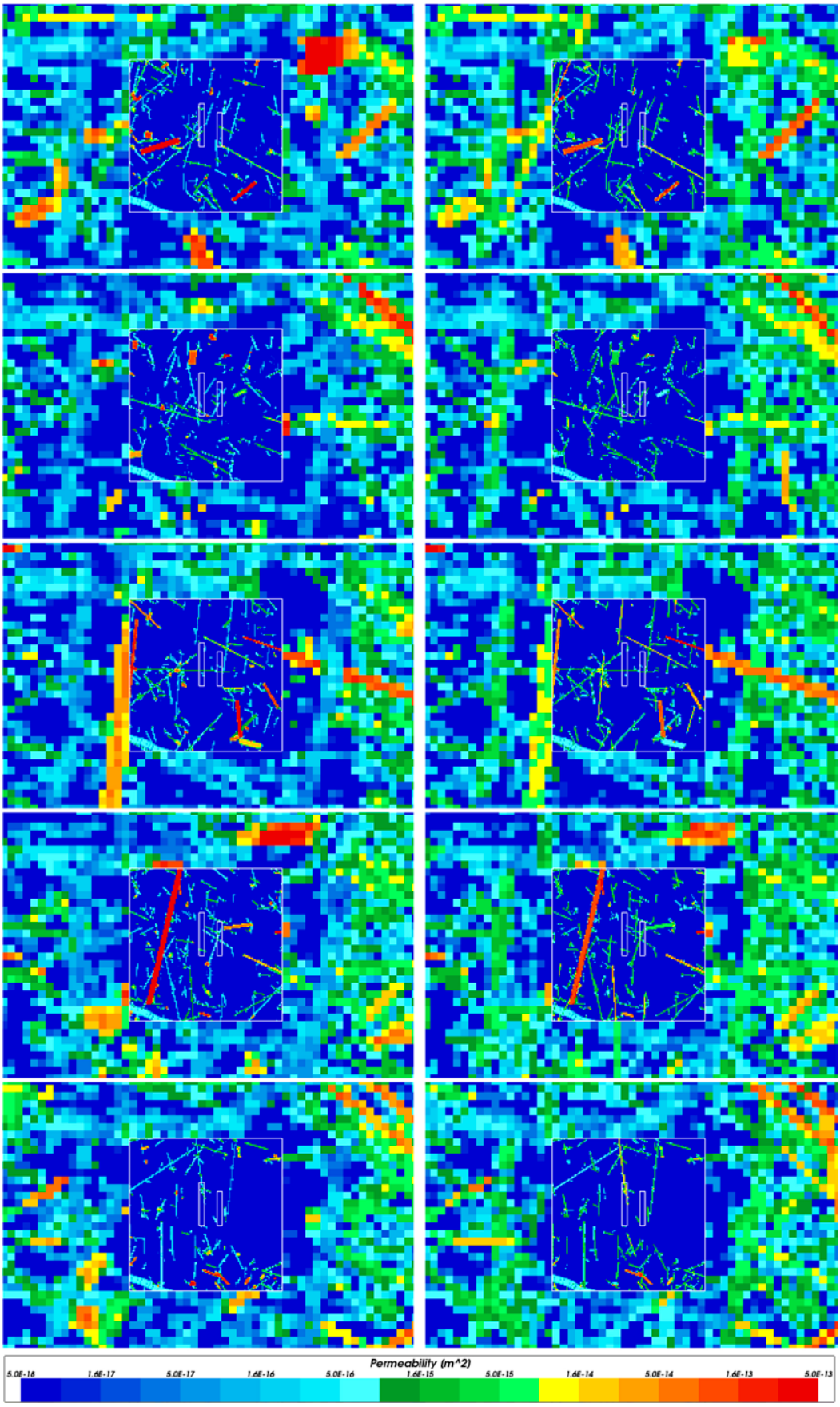

Figure 4-105. *Close-up view of the permeability (K_{xx} – left, K_{zz} – right) distribution on horizontal slices at an elevation of −500 m for Case 1, HRD realisations 1–5 (from top to bottom). The refined volume and repository vaults are shown in white.*

4.4.2 Chemistry

Figure 4-106 through Figure 4-112 show box and whisker plots of selected chemical components as a function of time ranging from 2000 AD to 60 000 AD, for the five HRD realisations of Case 1. The data has been exported on a regular grid of points within the refined part of the model corresponding to the repository volume between elevations −530 m and −470 m. The points correspond to the corner nodes of the elements within the refined volume. The element size is 5 m cubed, which makes a total of 190 333 points used in the analysis.

In general, the figures show that the five realisations form two distinct groups in terms of results, with HRD realisations 1 and 3 on one side of the range and realisations 2, 4 and 5 on the other. The different HRD realisations show a correlation between the generated permeabilities and the modelled chemical results. Higher permeabilities in and around the repository volume, lead to more and deeper flushing of saline waters, with fresher water entering from the top of the model.

The results are discussed for each chemical component separately in the following sections.

4.4.3 TDS

Figure 4-106 shows a comparison of statistical distributions of total dissolved solids (TDS) for the five realisations of Case 1. Realisations 1 and 3 show lower salinities and therefore indicate the presence of one or more large stochastic fractures. These fractures will tend to be well connected and have a higher transmissivity (due to the transmissivity-size relationship) and hence have a strong influence on flow, resulting in locally higher permeability close to the repository volume (see also Subsection 4.6.4). This leads to increased flushing of the initially more saline groundwater around the repository.

4.4.4 Chloride

Figure 4-107 shows a comparison of statistical distributions of total chloride concentrations for the five realisations of Case 1. The distribution of chloride shows the same behaviour as described above for salinity. In the repository volume, the Deep Saline water, partially present in the initial water composition, has been flushed by Altered Meteoric water to a higher degree in realisations 1 and 3. This is demonstrated by the lower chloride concentration in these realisations.

4.4.5 Calcium

Figure 4-108 shows a comparison of statistical distributions of total calcium concentrations for the five realisations of Case 1. Higher concentrations of calcium are found in Deep Saline water, but also in Inter-glacial water. Although not present in the repository volume, calcium is also found, to some extent, in Littorina water. The distribution of calcium shows the same behaviour as described above for chloride and confirms the reasoning for the lower concentrations of calcium in realisations 1 and 3 as being due to more extensive flushing of the older waters in the repository volume.

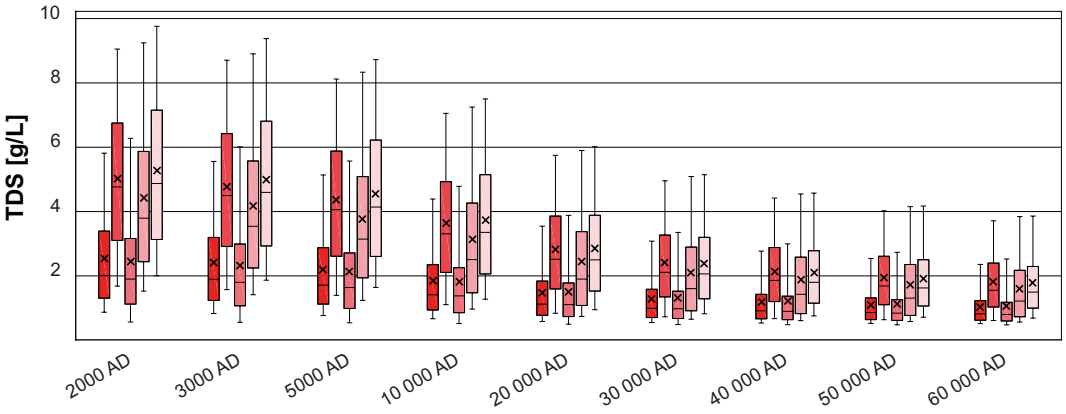

Figure 4-106. *Box and whisker plot showing a comparison of statistical distributions of TDS for the five realisations of Case 1 (r1 – dark red to r5 – light red) on a regular grid of points within the repository volume between elevations −530 m and −470 m. The statistical measures are the median, the 25th and 75th percentiles (box), the mean (cross) and the 5th and 95th percentiles (whiskers).*

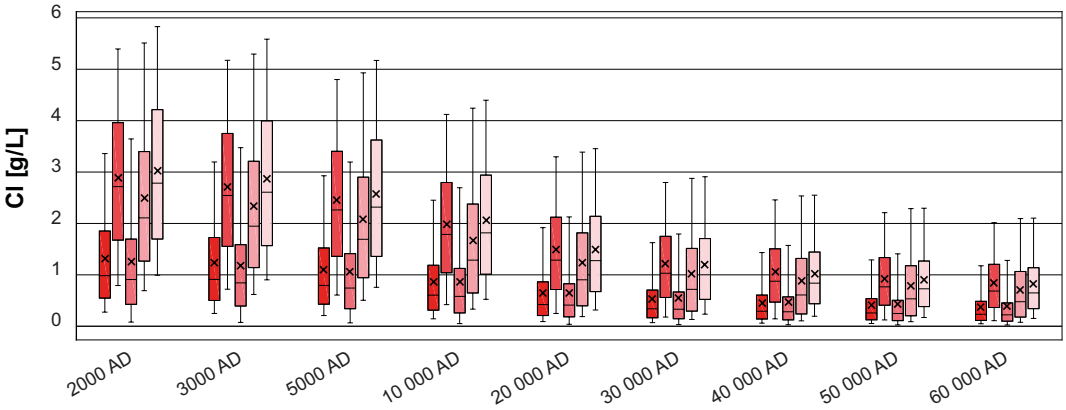

Figure 4-107. *Box and whisker plot showing a comparison of statistical distributions of total chloride concentrations for the five realisations of Case 1 (r1 – dark red to r5 – light red) on a regular grid of points within the repository volume between elevations −530 m and −470 m. The statistical measures are the median, the 25th and 75th percentiles (box), the mean (cross) and the 5th and 95th percentiles (whiskers).*

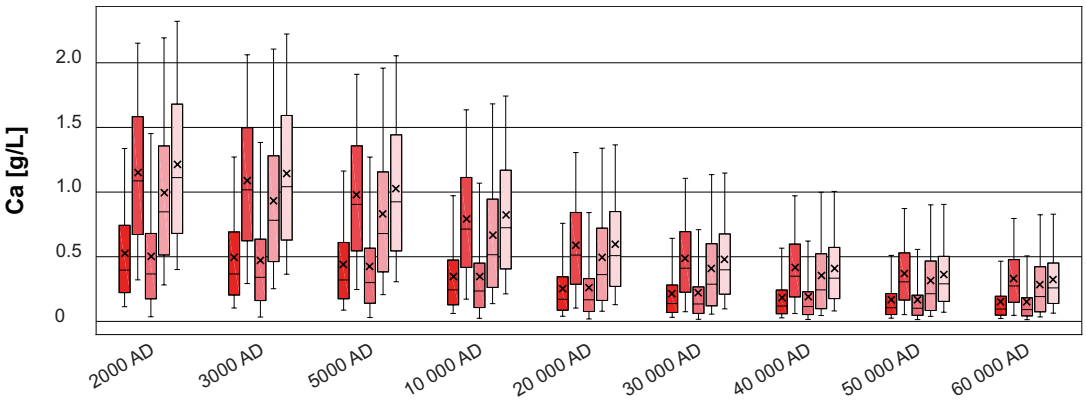

Figure 4-108. *Box and whisker plot showing a comparison of statistical distributions of total calcium concentrations for the five realisations of Case 1 (r1 – dark red to r5 – light red) on a regular grid of points within the repository volume between elevations −530 m and −470 m. The statistical measures are the median, the 25th and 75th percentiles (box), the mean (cross) and the 5th and 95th percentiles (whiskers).*

4.4.6 Inorganic carbon

Figure 4-109 shows a comparison of statistical distributions of total inorganic carbon concentrations for the five realisations of Case 1. Inorganic carbon is found in higher concentrations in Altered Meteoric water and to some extent in Littorina water (not present in the repository volume). Altered Meteoric water enters the system through the top surface and successively flushes the more saline water, increasing the proportion of inorganic carbon. Consequently the distribution of inorganic carbon shows the opposite behaviour to the previously discussed chemical components chloride and calcium, hence realisations 1 and 3 now show the highest concentrations.

4.4.7 Sulphur

Figure 4-110 shows a comparison of statistical distributions of total sulphur concentrations for the five realisations of Case 1. Sulphur is present predominantly in Deep Saline and Inter-glacial waters. Littorina water containing sulphur is not present in the repository volume. The distribution of sulphur shows the same behaviour as described above for chloride and calcium and the same discussion regarding the results applies.

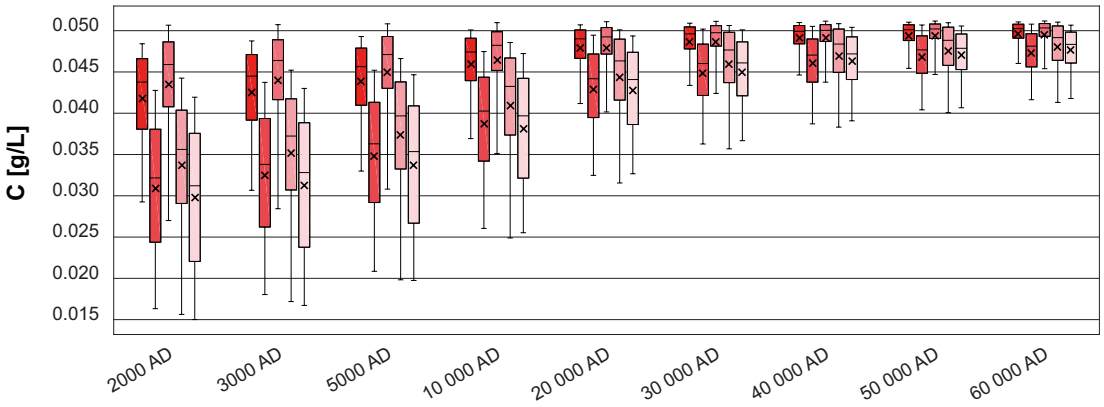

Figure 4-109. *Box and whisker plot showing a comparison of statistical distributions of total inorganic carbon concentrations for the five realisations of Case 1 (r1 – dark red to r5 – light red) on a regular grid of points within the repository volume between elevations −530 m and −470 m. The statistical measures are the median, the 25th and 75th percentiles (box), the mean (cross) and the 5th and 95th percentiles (whiskers).*

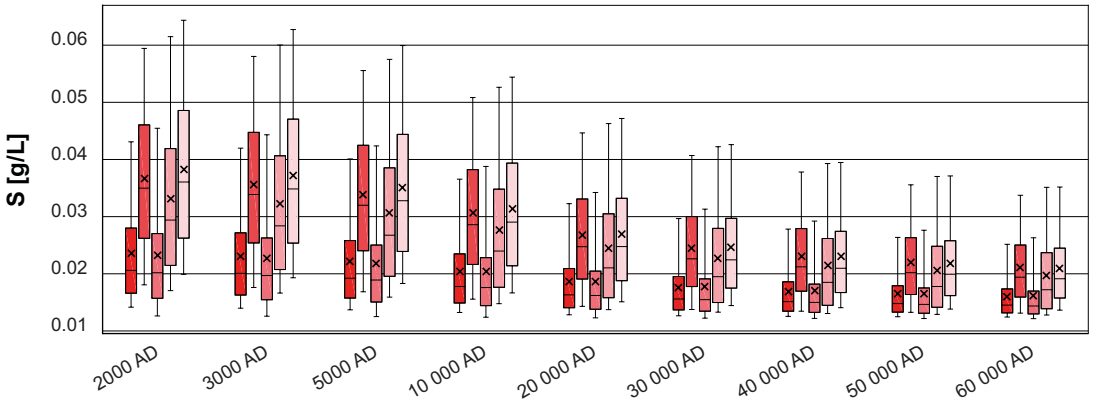

Figure 4-110. *Box and whisker plot showing a comparison of statistical distributions of total sulphur concentrations for the five realisations of Case 1 (r1 – dark red to r5 – light red) on a regular grid of points within the repository volume between elevations −530 m and −470 m. The statistical measures are the median, the 25th and 75th percentiles (box), the mean (cross) and the 5th and 95th percentiles (whiskers).*

4.4.8 Magnesium

Figure 4-111 shows a comparison of statistical distributions of total magnesium concentrations for the five realisations of Case 1. The distribution of magnesium shows the same behaviour as described above for inorganic carbon. Magnesium is found in higher concentrations in Altered Meteoric water and to some extent in Littorina water (not present in the repository volume). Altered Meteoric water enters the system through the top surface and successively flushes the more saline water, thus introducing higher concentrations of magnesium. These results indicate a greater intensity of transmissive stochastic fractures in realisation 1 and 3 close to the repository volume, resulting in a locally higher permeability.

4.4.9 Sodium

Figure 4-112 shows a comparison of statistical distributions of total sodium concentrations for the five realisations of Case 1. Higher concentrations of sodium are found in Deep Saline and Interglacial waters and, although not present in the repository volume, in Littorina water. The distribution of sodium shows the same behaviour as described above for chloride, calcium and sulphur, and again confirms that flushing is more extensive in realisations 1 and 3.

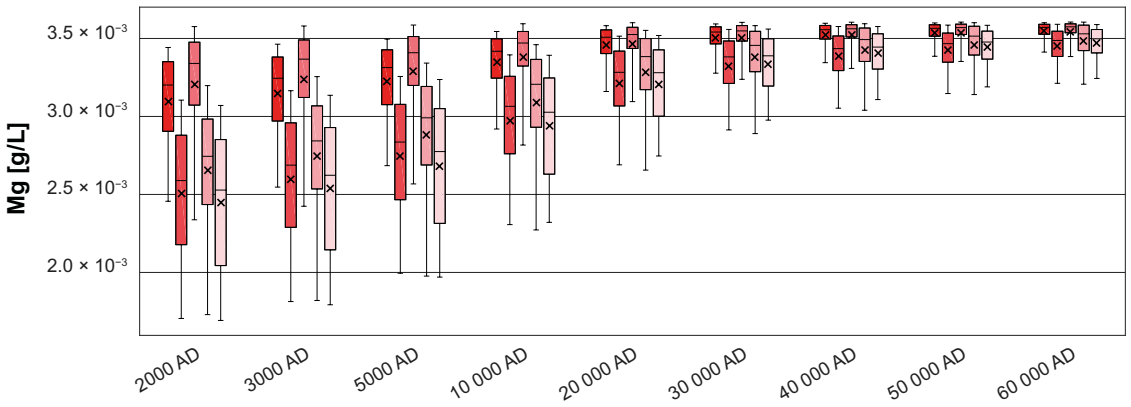

Figure 4-111. *Box and whisker plot showing a comparison of statistical distributions of total magnesium concentrations for the five realisations of Case 1 (r1 – dark red to r5 – light red) on a regular grid of points within the repository volume between elevations −530 m and −470 m. The statistical measures are the median, the 25th and 75th percentiles (box), the mean (cross) and the 5th and 95th percentiles (whiskers).*

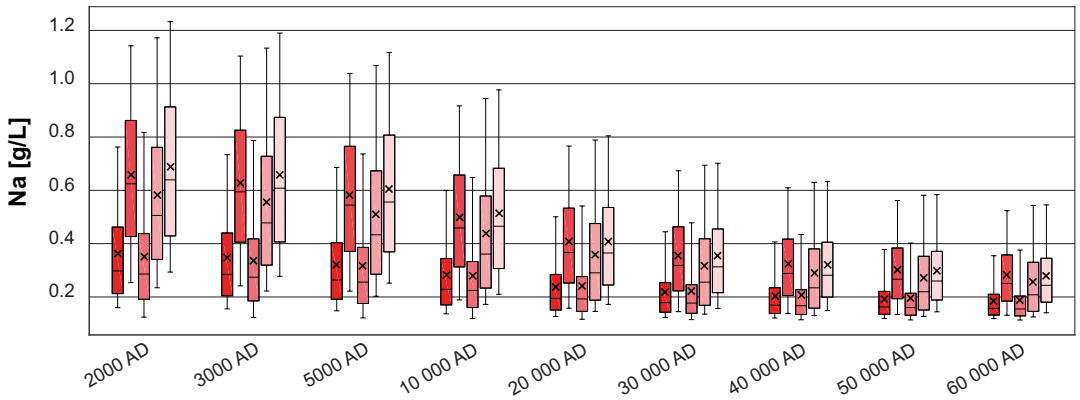

Figure 4-112. *Box and whisker plot showing a comparison of statistical distributions of total sodium concentrations for the five realisations of Case 1 (r1 – dark red to r5 – light red) on a regular grid of points within the repository volume between elevations −530 m and −470 m. The statistical measures are the median, the 25th and 75th percentiles (box), the mean (cross) and the 5th and 95th percentiles (whiskers).*

4.5 Borehole chemistry at 2000 AD

The hydrogeological model used in the present SFL study uses the same HRD parameterisation, HCD, boundary conditions and domain as the SR-Site Elaborated Hydro-DFN model for Laxemar (Section E.4, Joyce et al. 2010). However, the models are not identical with respect to, for example, the realisation of the HRD and the grid resolution.

In order to check to what extent the results have changed, the calculated groundwater composition from the three modelled SFL cases at 2000 AD was compared with the results from the SR-Site Elaborated Hydro-DFN model. The calibration of the model was also tested against the present-day measured groundwater composition. No attempt was made to re-calibrate the SR-Site Elaborated Hydro-DFN model.

A detailed illustration of the comparison is shown in Figure 4-113 through Figure 4-122. Simulated profiles of selected chemical constituents are shown for boreholes in HRD_C and HRD_EW007. In each figure, a comparison between the SR-Site Elaborated Hydro-DFN and the three modelled SFL cases, is shown together with measured data for the selected chemical constituent. All three SFL cases are based on realisation 1 of the HRD. However, because the fracture-generation code in ConnectFlow has changed since the SR-Site study, realisation 1 of the DFN used in the SFL model will be different from realisation 1 used in the SR-Site Elaborated Hydro-DFN model. Changes in results are therefore to be expected when comparing between SFL and SR-Site.

There is very little difference between the three SFL cases for the various chemical constituents. When comparing the SR-Site Elaborated Hydro-DFN model and SFL Case 1 (both without chemical reactions, so representing only component transport), some differences can be seen, even though the results are broadly in the same range. These differences are attributed to the differences in HRD realisations used. The effects of different HRD realisations are presented in Subsection 4.5.1.

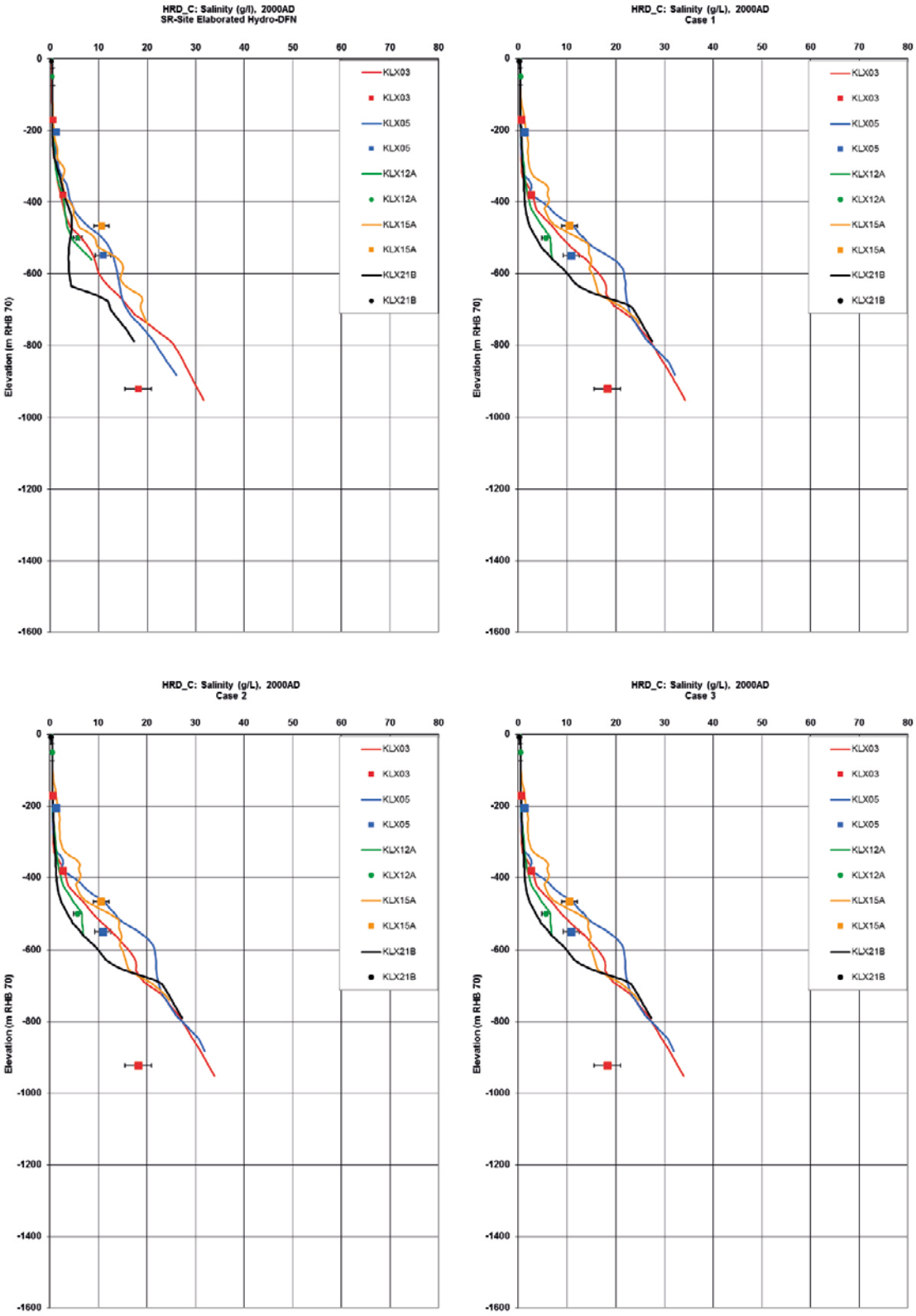

Figure 4-113. *A comparison of the modelled and measured salinity distributions in the fracture system for boreholes in HRD_C for the SR-Site Elaborated Hydro-DFN case (top left), Case 1 (top right), Case 2 (bottom left), and Case 3 (bottom right). Square symbols are used for category 1–3 data, circles are used for the pore water data, and filled circles are used for category 4 data. The error bars on the data indicate the laboratory analytical error.*

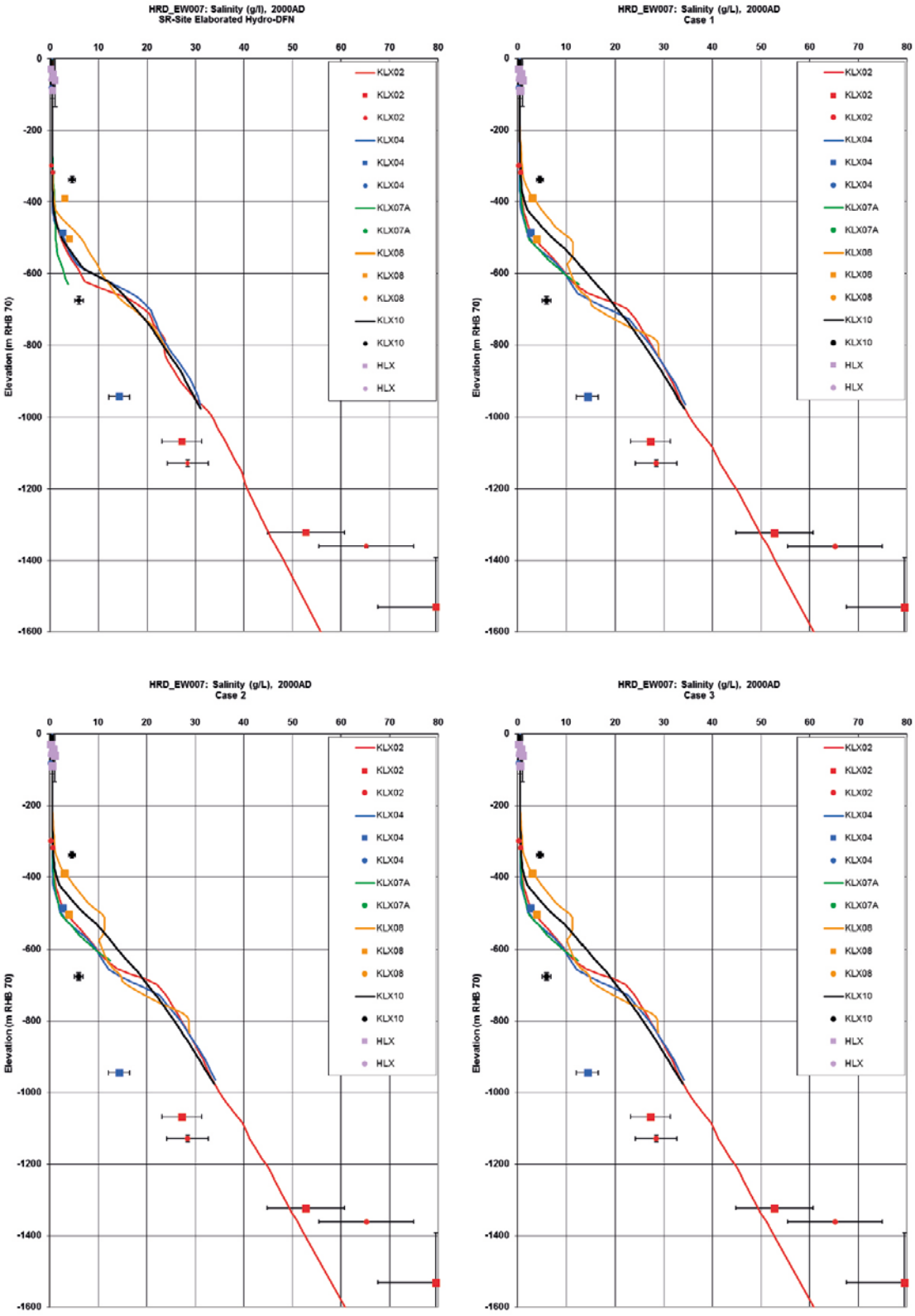

Figure 4-114. *A comparison of the modelled and measured salinity distributions in the fracture system for boreholes in HRD_EW007 for the SR-Site Elaborated Hydro-DFN case (top left), Case 1 (top right), Case 2 (bottom left), and Case 3 (bottom right). Square symbols are used for category 1–3 data, circles are used for the pore water data, and filled circles are used for category 4 data. The error bars on the data indicate the laboratory analytical error.*

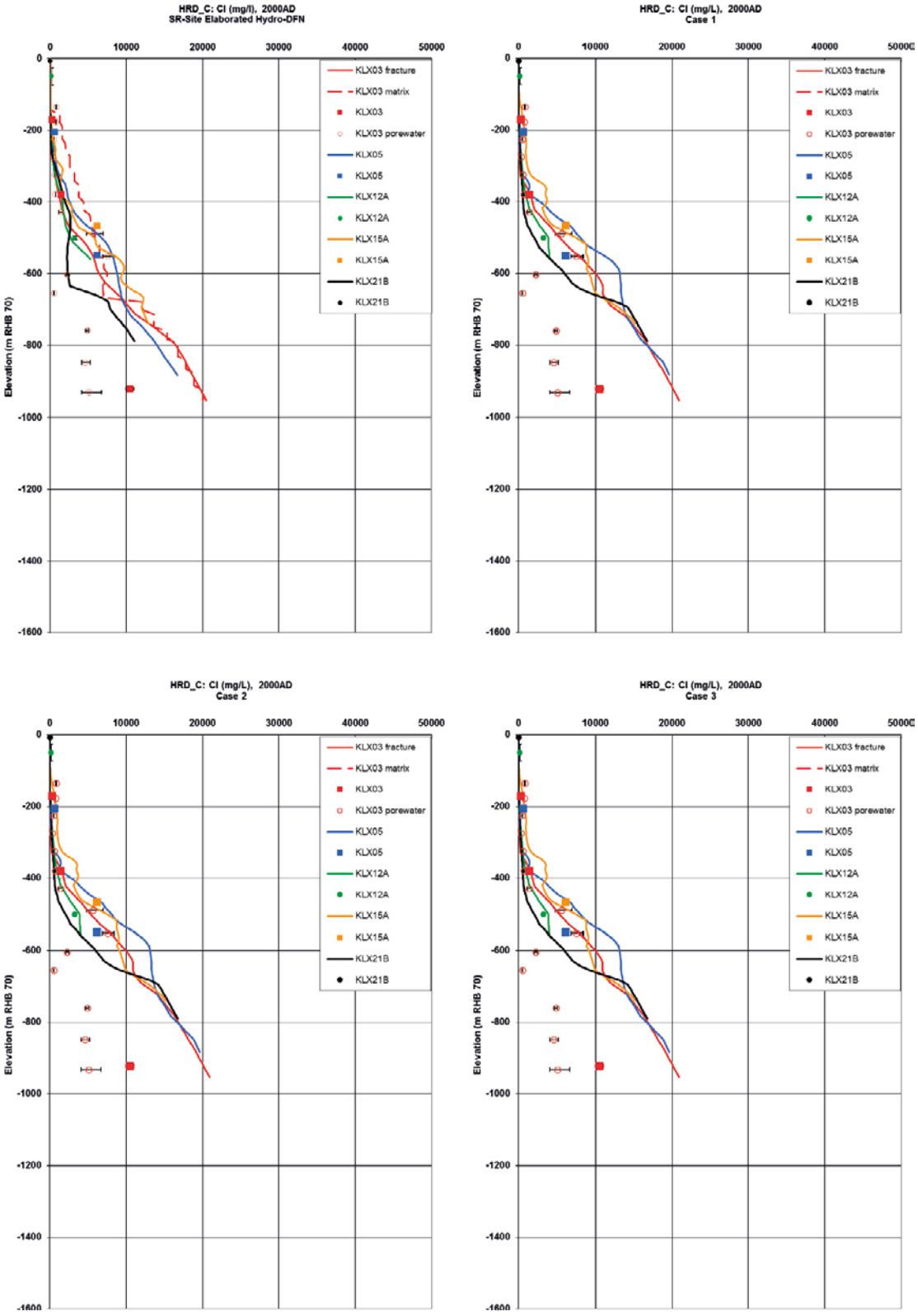

Figure 4-115. *A comparison of the modelled and measured chloride concentrations in the fracture system for boreholes in HRD_C for the SR-Site Elaborated Hydro-DFN case (top left), Case 1 (top right), Case 2 (bottom left), and Case 3 (bottom right). Square symbols are used for category 1–3 data, circles are used for the pore water data, and filled circles are used for category 4 data. The error bars on the data indicate the laboratory analytical error.*

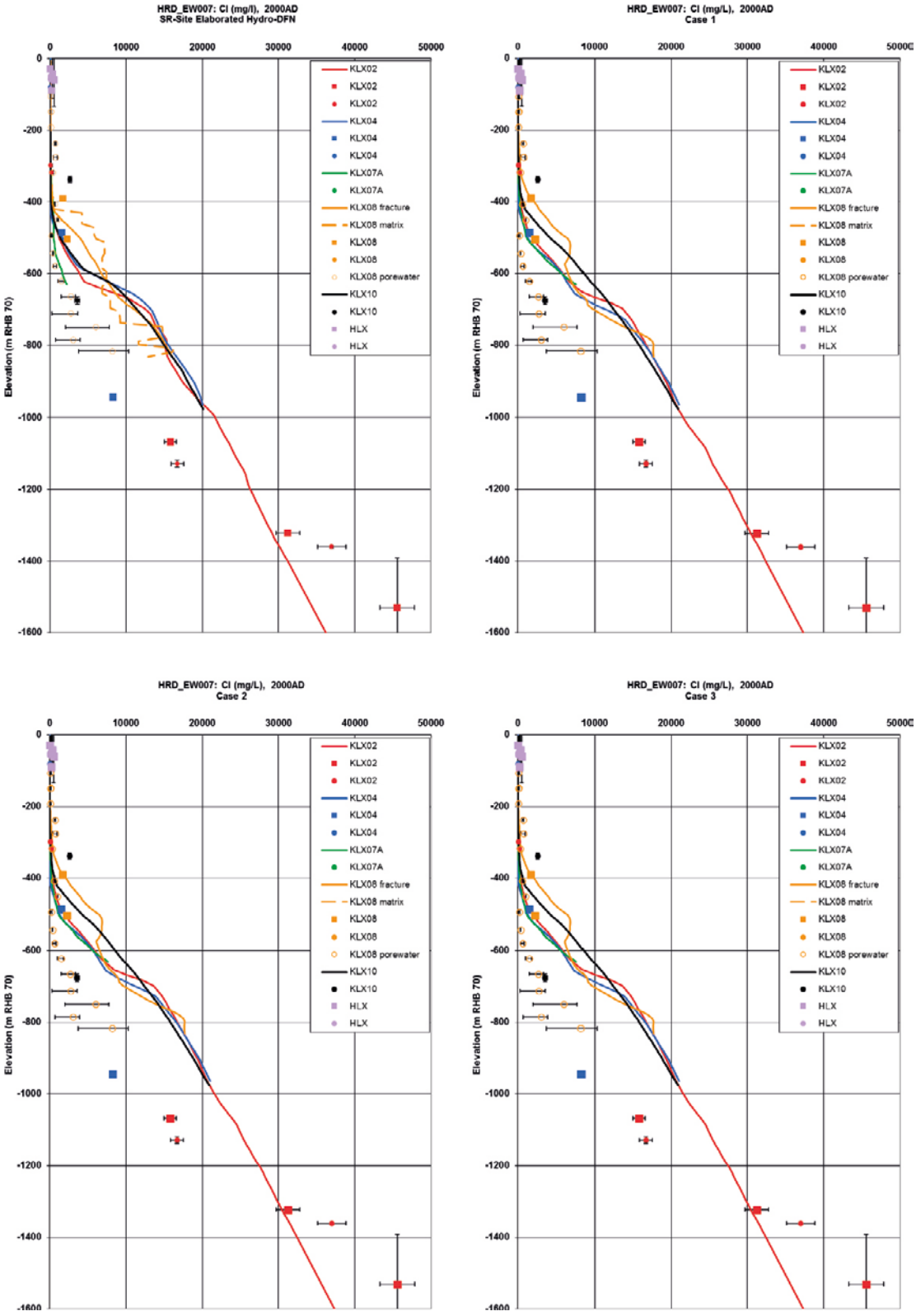

Figure 4-116. *A comparison of the modelled and measured chloride concentrations in the fracture system for boreholes in HRD_EW007 for the SR-Site Elaborated Hydro-DFN case (top left), Case 1 (top right), Case 2 (bottom left), and Case 3 (bottom right). Square symbols are used for category 1–3 data, circles are used for the pore water data, and filled circles are used for category 4 data. The error bars on the data indicate the laboratory analytical error.*

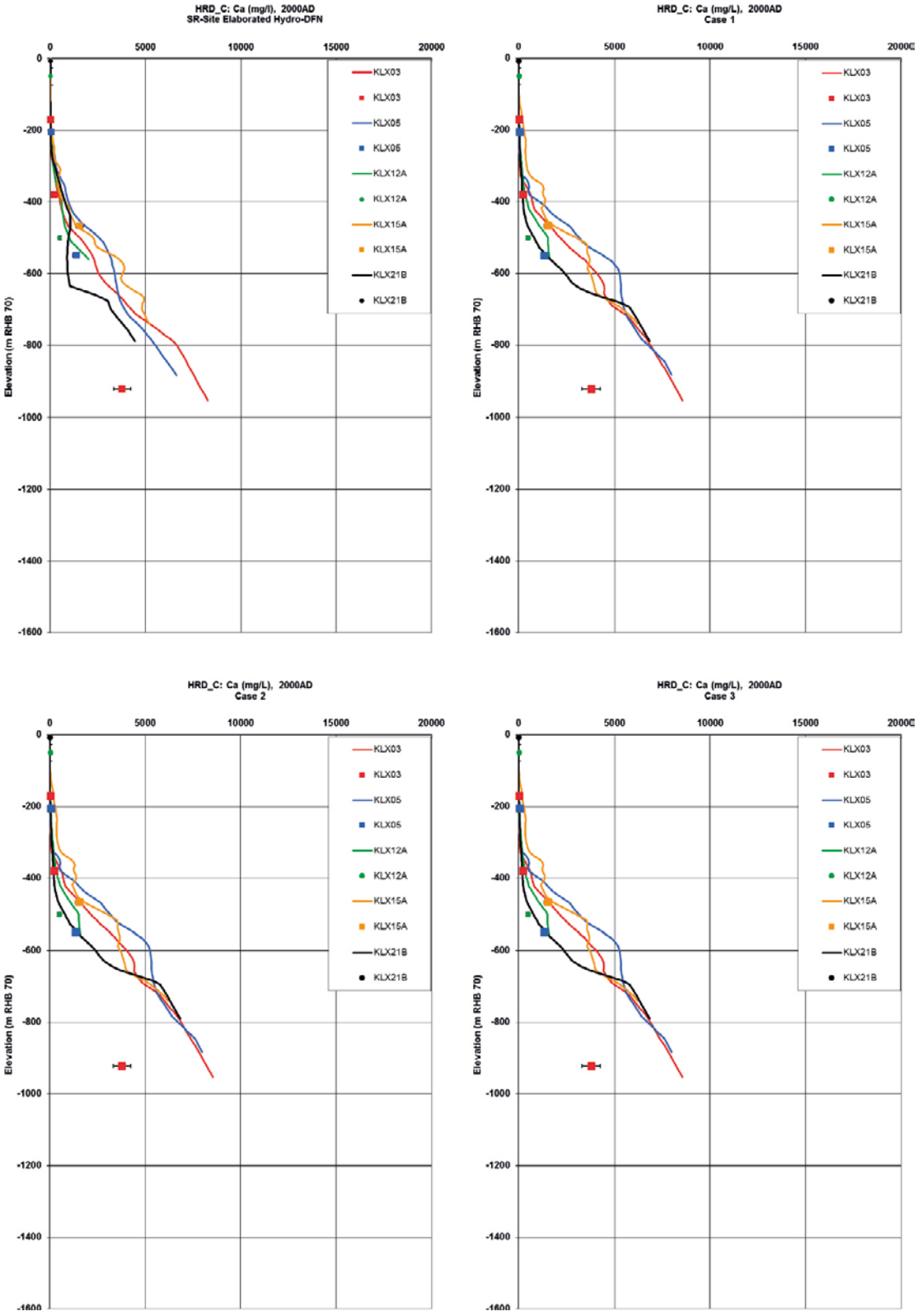

Figure 4-117. *A comparison of the modelled and measured calcium concentrations in the fracture system for boreholes in HRD_C for the SR-Site Elaborated Hydro-DFN case (top left), Case 1 (top right), Case 2 (bottom left), and Case 3 (bottom right). Square symbols are used for category 1–3 data, circles are used for the pore water data, and filled circles are used for category 4 data. The error bars on the data indicate the laboratory analytical error.*

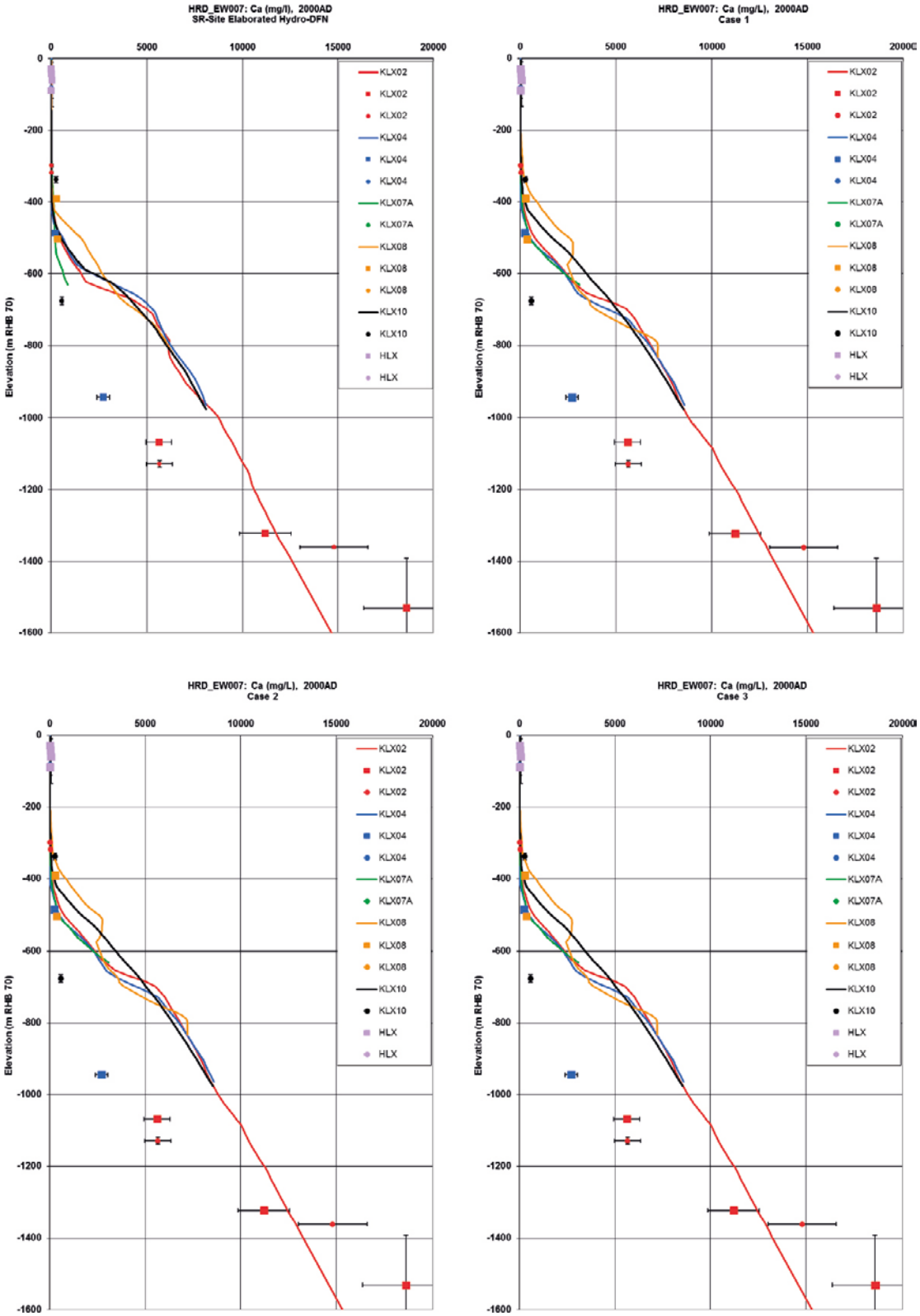

Figure 4-118. *A comparison of the modelled and measured calcium concentrations in the fracture system for boreholes in HRD_EW007 for the SR-Site Elaborated Hydro-DFN case (top left), Case 1 (top right), Case 2 (bottom left), and Case 3 (bottom right). Square symbols are used for category 1–3 data, circles are used for the pore water data, and filled circles are used for category 4 data. The error bars on the data indicate the laboratory analytical error.*

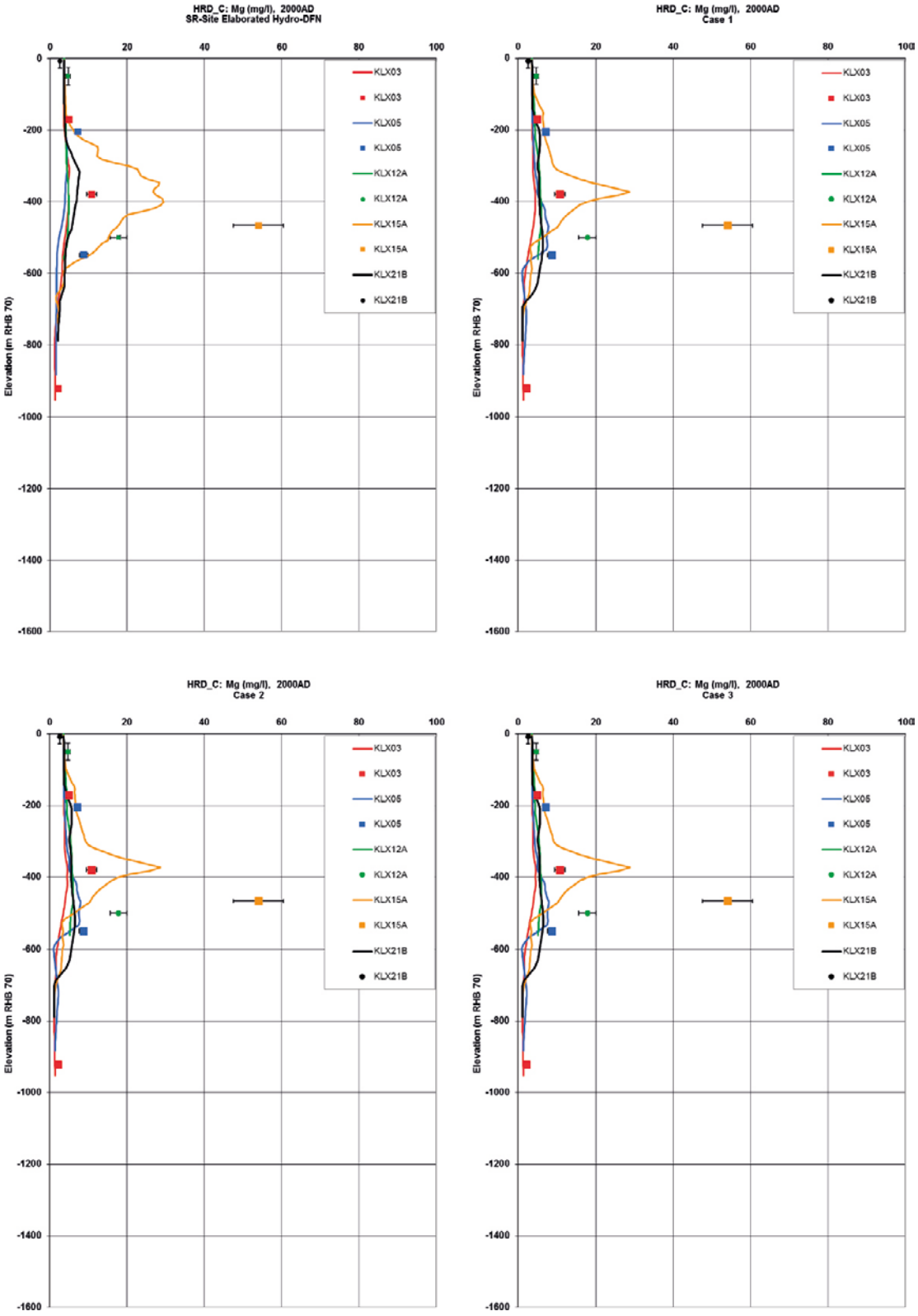

Figure 4-119. *A comparison of the modelled and measured magnesium concentrations in the fracture system for boreholes in HRD_C for the SR-Site Elaborated Hydro-DFN case (top left), Case 1 (top right), Case 2 (bottom left), and Case 3 (bottom right). Square symbols are used for category 1–3 data, circles are used for the pore water data, and filled circles are used for category 4 data. The error bars on the data indicate the laboratory analytical error.*

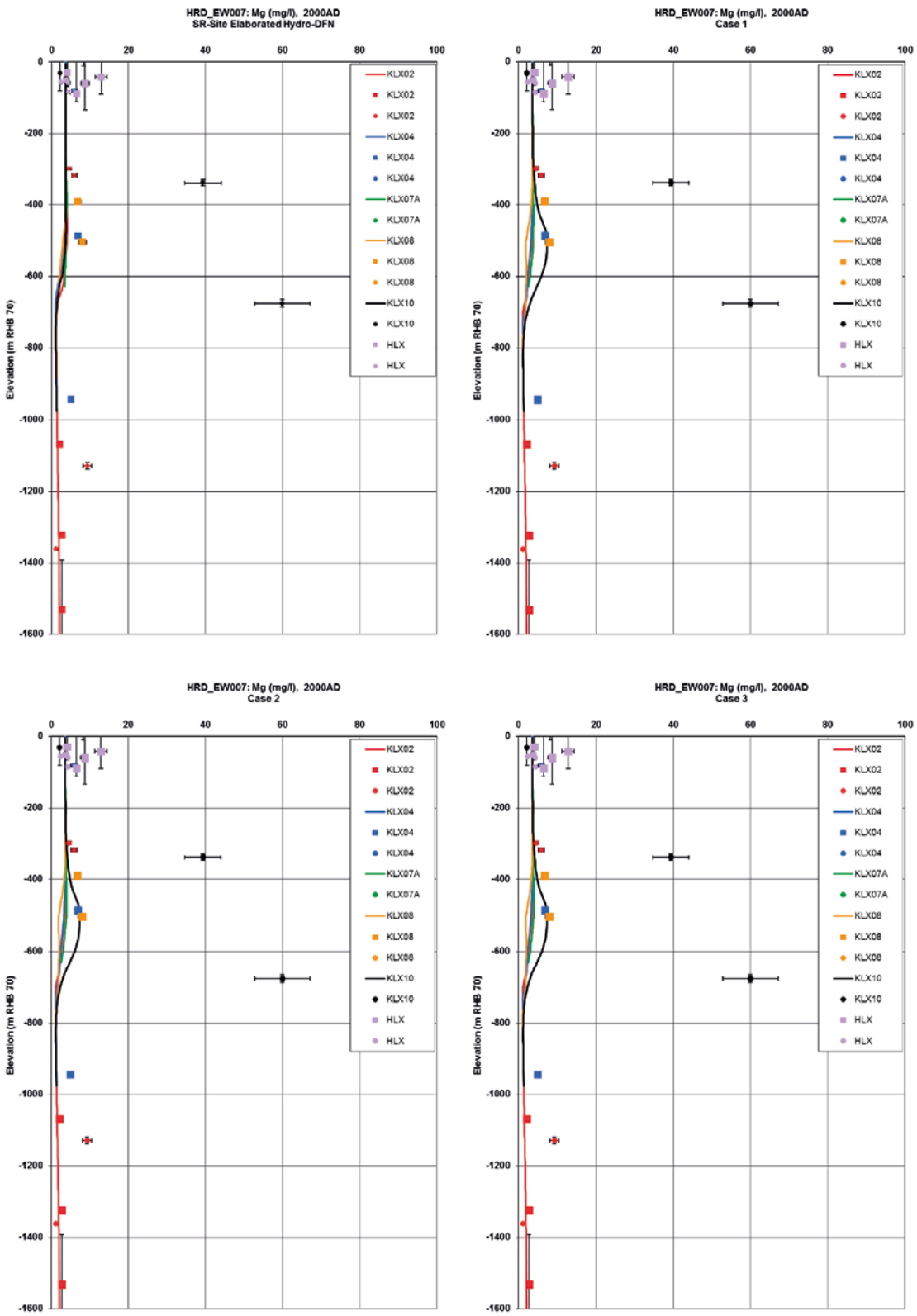

Figure 4-120. *A comparison of the modelled and measured magnesium concentrations in the fracture system for boreholes in HRD_EW007 for the SR-Site Elaborated Hydro-DFN case (top left), Case 1 (top right), Case 2 (bottom left), and Case 3 (bottom right). Square symbols are used for category 1–3 data, circles are used for the pore water data, and filled circles are used for category 4 data. The error bars on the data indicate the laboratory analytical error.*

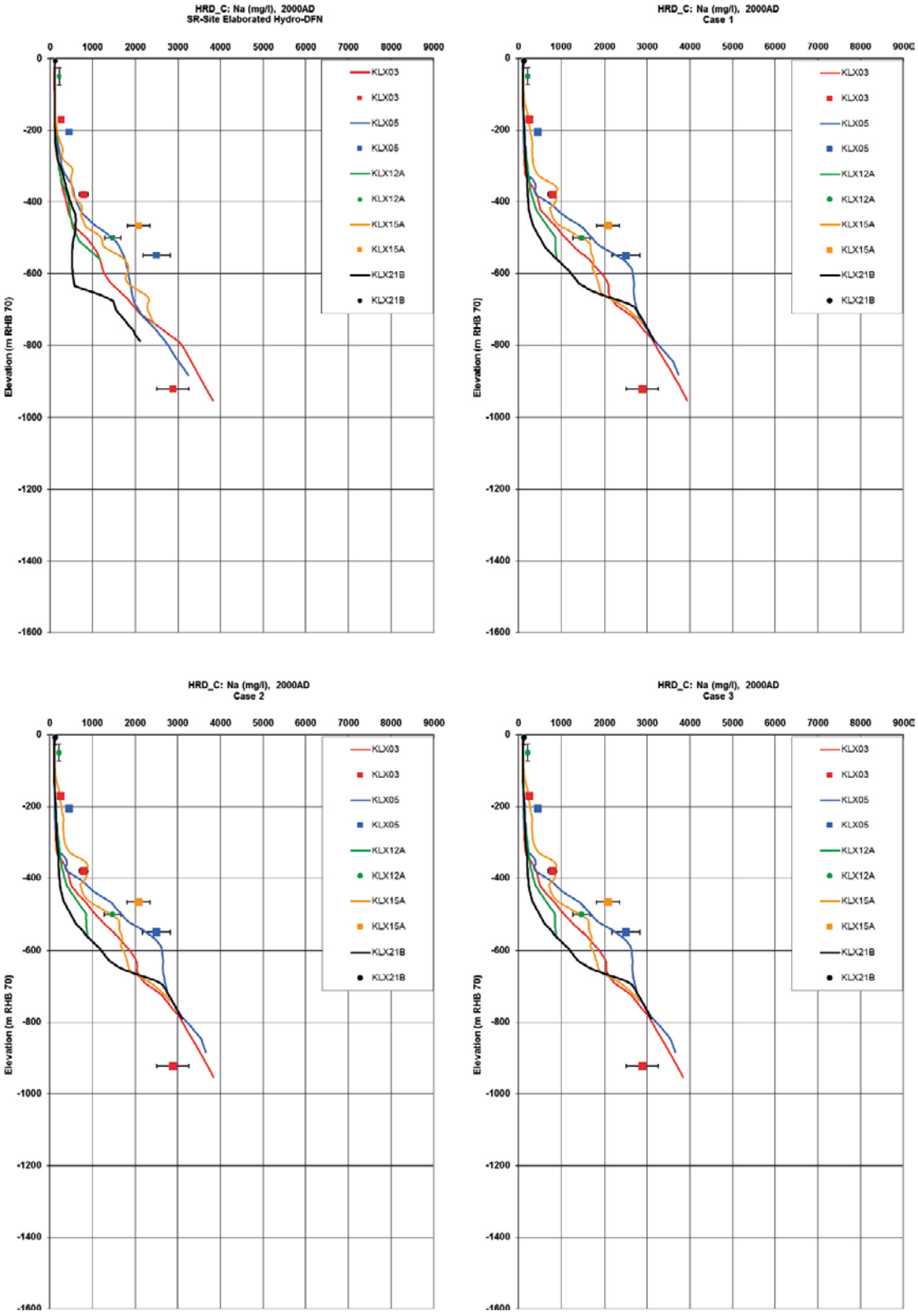

Figure 4-121. *A comparison of the modelled and measured sodium concentrations in the fracture system for boreholes in HRD_C for the SR-Site Elaborated Hydro-DFN case (top left), Case 1 (top right), Case 2 (bottom left), and Case 3 (bottom right). Square symbols are used for category 1–3 data, circles are used for the pore water data, and filled circles are used for category 4 data. The error bars on the data indicate the laboratory analytical error.*

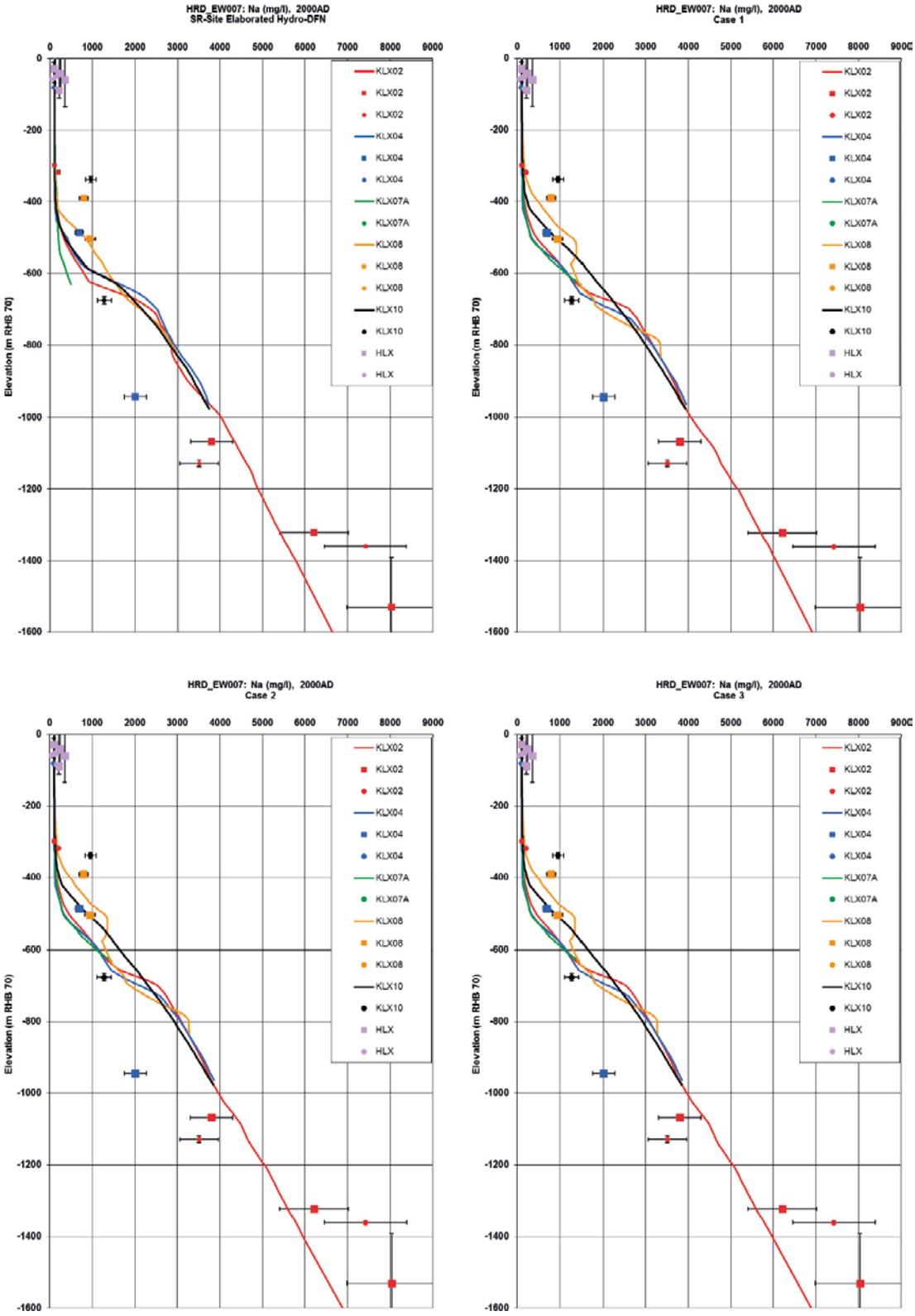

Figure 4-122. *A comparison of the modelled and measured sodium concentrations in the fracture system for boreholes in HRD_EW007 for the SR-Site Elaborated Hydro-DFN case (top left), Case 1 (top right), Case 2 (bottom left), and Case 3 (bottom right). Square symbols are used for category 1–3 data, circles are used for the pore water data, and filled circles are used for category 4 data. The error bars on the data indicate the laboratory analytical error.*

4.5.1 Sensitivity to HRD realisation

To address the sensitivity of the hydrogeochemical calibration to the stochastic variability of the HRD, a set of five realisations of the HRD DFN were used to derive the upscaled spatially varying properties of the HRD for Case 1, i.e. the case without chemical reactions. The calibration of the model was tested against the present-day measured groundwater composition in the same way as in the SR-Site Elaborated Hydro-DFN model for Laxemar (Section E.4, Joyce et al. 2010).

A detailed illustration of the effects of HRD spatial heterogeneity is shown in Figure 4-123 through Figure 4-125. Simulated profiles of selected chemical constituents are shown for boreholes KLX03 (in HRD_C) and KLX08 (in HRD_EW007). In each plot, a comparison between one realisation of the SR-Site Elaborated Hydro-DFN and the five realisations of Case 1 is shown, together with measured data for the selected chemical constituent.

The results for the five realisations of Case 1 show that there is variation in the concentrations of the chemical constituents due to variations in upscaled properties between the different realisations of the HRD DFN. Down to 400 m depth, the results for Case 1 show less variation and are in the same range as for the SR-Site Elaborated Hydro-DFN model. Below 400 m depth, the variation increases for the Case 1 realisations and values are generally higher than in the SR-Site Elaborated Hydro-DFN model, indicating less penetration of meteoric water and therefore less flushing of saline waters. However, there has been no attempt made to calibrate the current model, and the small number of data points at depth mean there is considerable uncertainty in the true values.

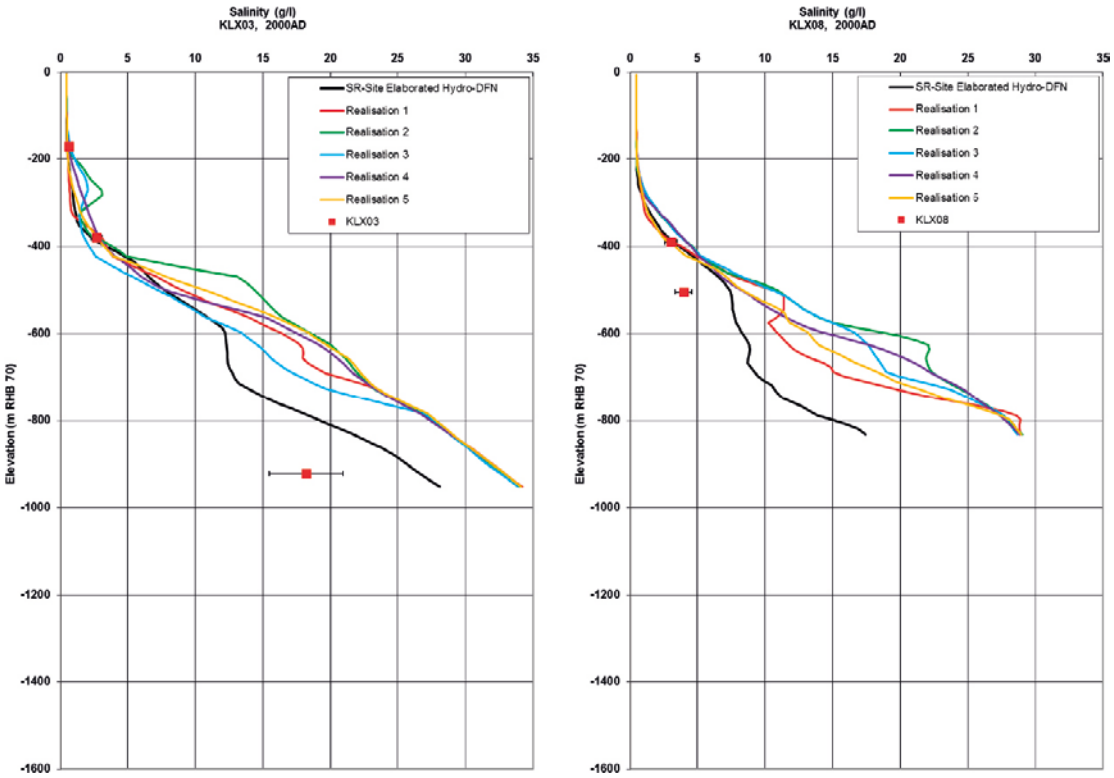

Figure 4-123. *A comparison of the modelled salinity distributions in the fracture system for boreholes KLX03 (left) and KLX08 (right) for the SR-Site Elaborated Hydro-DFN case (black line) and the five realisations of Case 1. The measured salinities are shown as square symbols (category 1–3 data). The error bars on the data indicate the laboratory analytical error.*

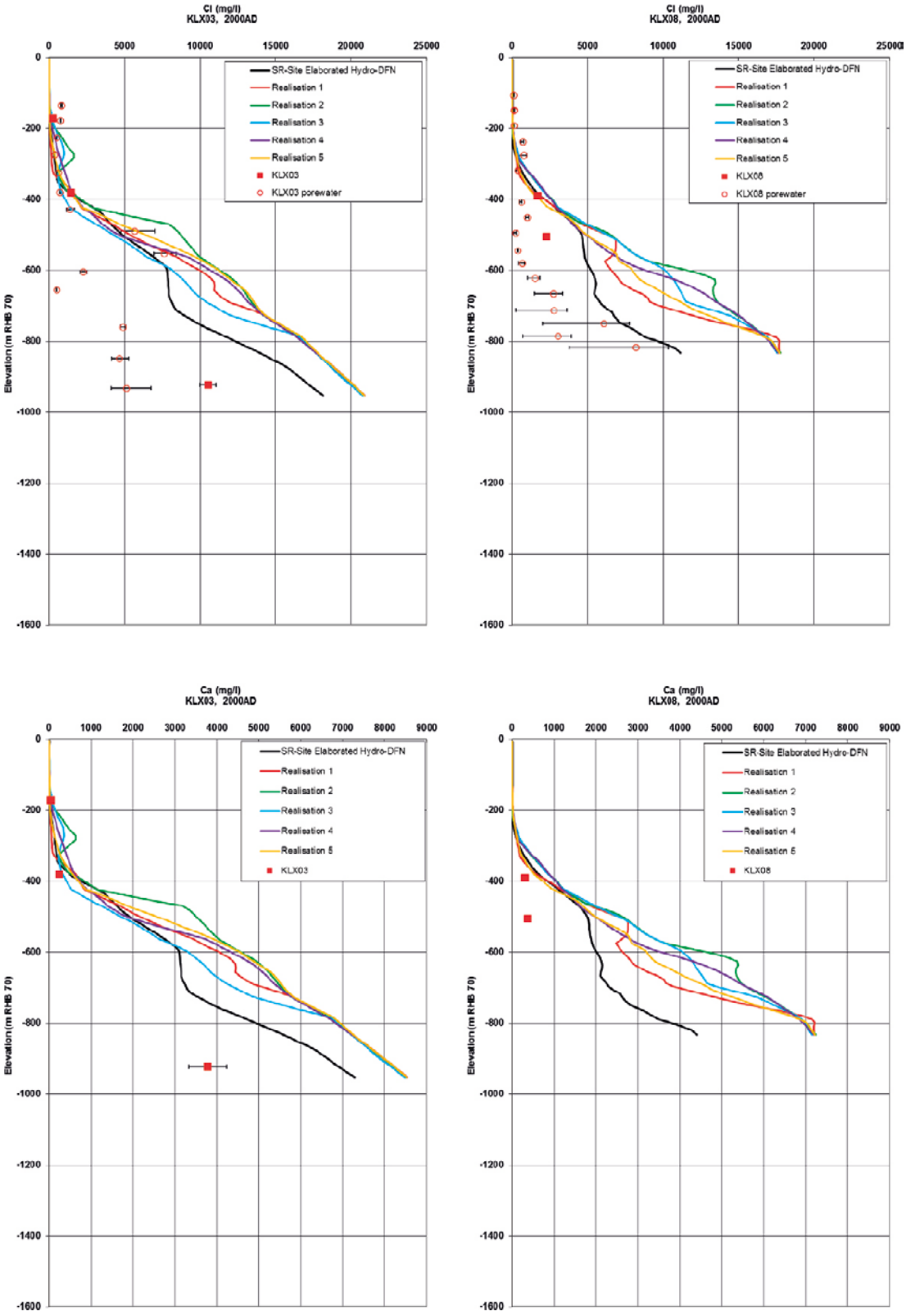

Figure 4-124. *A comparison of the modelled chloride (top) and calcium (bottom) concentrations in the fracture system for boreholes KLX03 (left) and KLX08 (right) for the SR-Site Elaborated Hydro-DFN case (black line) and the five realisations of Case 1. The measured concentrations are shown as square symbols (category 1–3 data), and circles (pore water data). The error bars on the data indicate the laboratory analytical error.*

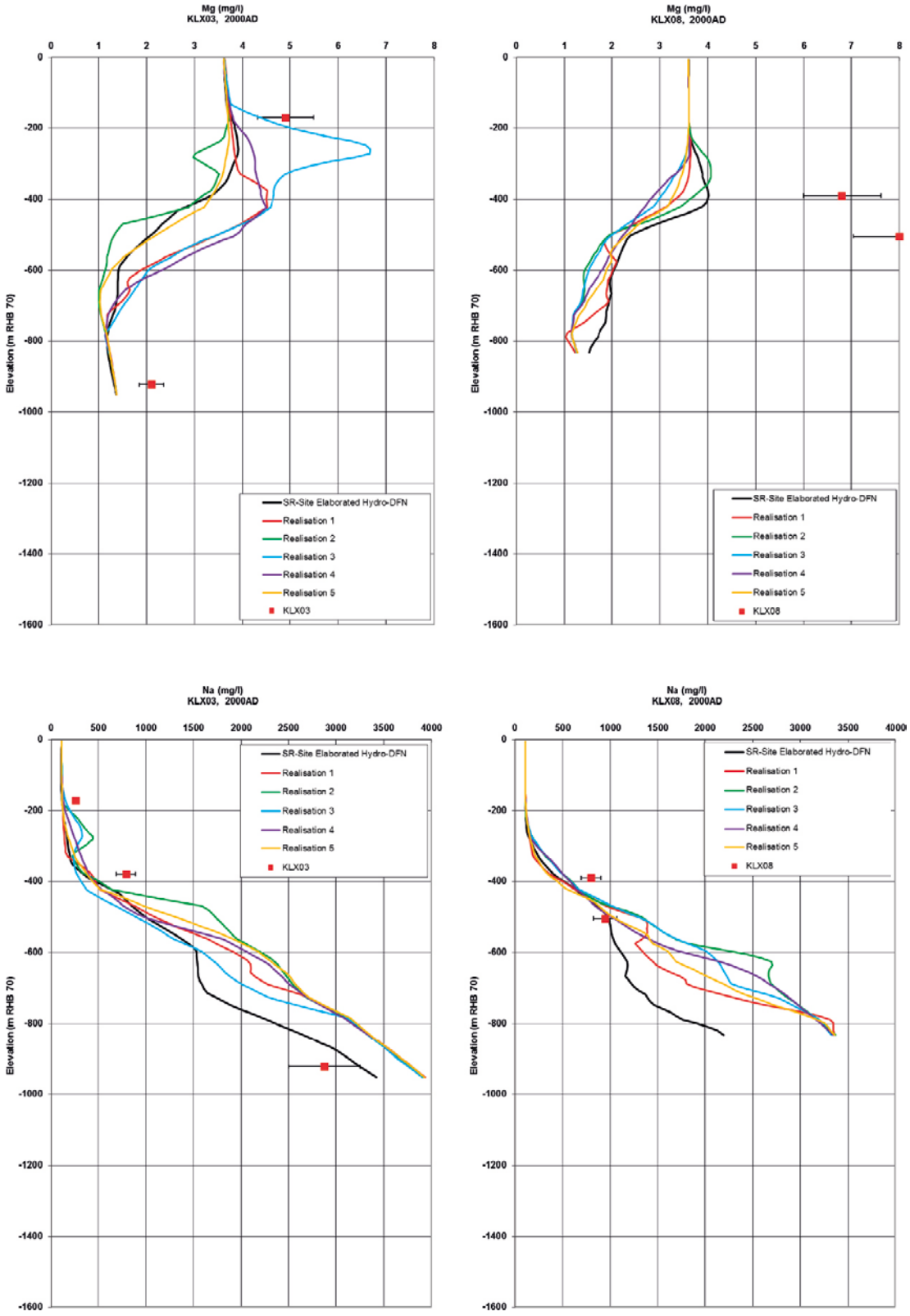

Figure 4-125. *A comparison of the modelled magnesium (top) sodium (bottom) concentrations in the fracture system for boreholes KLX03 (left) and KLX08 (right) for the SR-Site Elaborated Hydro-DFN case (black line) and the five realisations of Case 1. The measured concentrations are shown as square symbols (category 1–3 data). The error bars on the data indicate the laboratory analytical error.*

4.6 Facility focussed groundwater flow and particle tracking

4.6.1 Presentation of results

The results presented in this section relate to the particle-tracking calculations carried out for the facility focussed model. The results are presented and compared for each case, realisation and time slice considered.

The particle-exit locations and performance measures (described in Subsection 2.2.11) are the main results of this work. As stated in Subsection 2.2.11, performance measures are only calculated for path segments that are within the DFN parts (i.e. within the facility scale volume) of the facility focussed model, not including repository structures (i.e. the ramp and shaft).

Particle-exit locations (recharge and discharge locations) are displayed as points overlain on the top surface of the domain. Only particles that have successfully reached the top surface of the model are included. The particles are coloured by type (recharge or discharge). The top surface of the model is coloured by elevation to indicate the topography. Sea is coloured by a constant blue colour regardless of depth. The magnitude of both topography and bathymetry is indicated using contour lines with a equidistance of 5 m. In order to provide context, the top surface is also overlain (for 2000 AD) by surface features (rivers and present shoreline) and model features (deformation zones and the SFL repository location). Elevations are relative to sea level at 2000 AD.

Cumulative distribution plots (CDF) are used to show the cumulative fraction of particles as a function of performance measure value. The plots exclude particles that do not start (because of the flow direction) or fail to reach the top surface of the model and then the fractions are re-normalised to the range zero to one. The percentage of successful particles is included in the plot captions. The ranges of the horizontal axes of the plots do not indicate the minimum or maximum values of the performance measures but were chosen to be consistent between plots of different sets of results to ease comparison.

4.6.2 Evolution of exit locations with time

Figure 4-126 to Figure 4-133 show the variation of particle recharge locations and exit locations with time for Case 1. At 7980 BC, the repository location is below the sea, but because of land rise due to post-glacial rebound, the land emerges from the sea over time and the shoreline retreats to the east. At all times, the recharge locations are above and slightly west of the repository location, so recharge to the vaults is from above. Discharge locations are towards the sea or low-lying land (except at 7980 BC when the site is below sea level), but are affected by the location of deformation zones. Most particles exit the model to the north along deformation zones ZSMNS001, ZSMEW002 and ZSMNW119, to the southeast along deformation zones ZSMEW007 and ZSMNE006 and a few to the south along deformation zone ZSMNW042. In some cases, there is some horizontal travel in the regolith, particularly where the flow is directed around lower permeability layers, such as Z3 (post-glacial clay) or Z5 (glacial clay). As the shoreline recedes with time, the particle-exit locations tend to become more distant from the repository location due to the change in groundwater flow patterns (flow is generally towards the coast).

Figure 4-134 to Figure 4-136 show the pathways for particles released from the vaults at 7980 BC, 2000 AD and 60 000 AD respectively. For all three release times, the particles travel downwards and then predominantly to the north and southeast. The paths at 7980 BC are more disperse than those at 2000 AD and 60 000 AD. There is little difference in the paths between 2000 AD and 60 000 AD for particles discharging close to the repository, but there is a greater proportion of longer, more horizontal paths discharging further from the repository at 60 000 AD. In all cases, the maximum depth reached by particles is around 1100 m. The particle paths in the DFN are stochastic, so the ten particles released at each starting location follow different pathways and so represent dispersion at the scale of the fracture network.

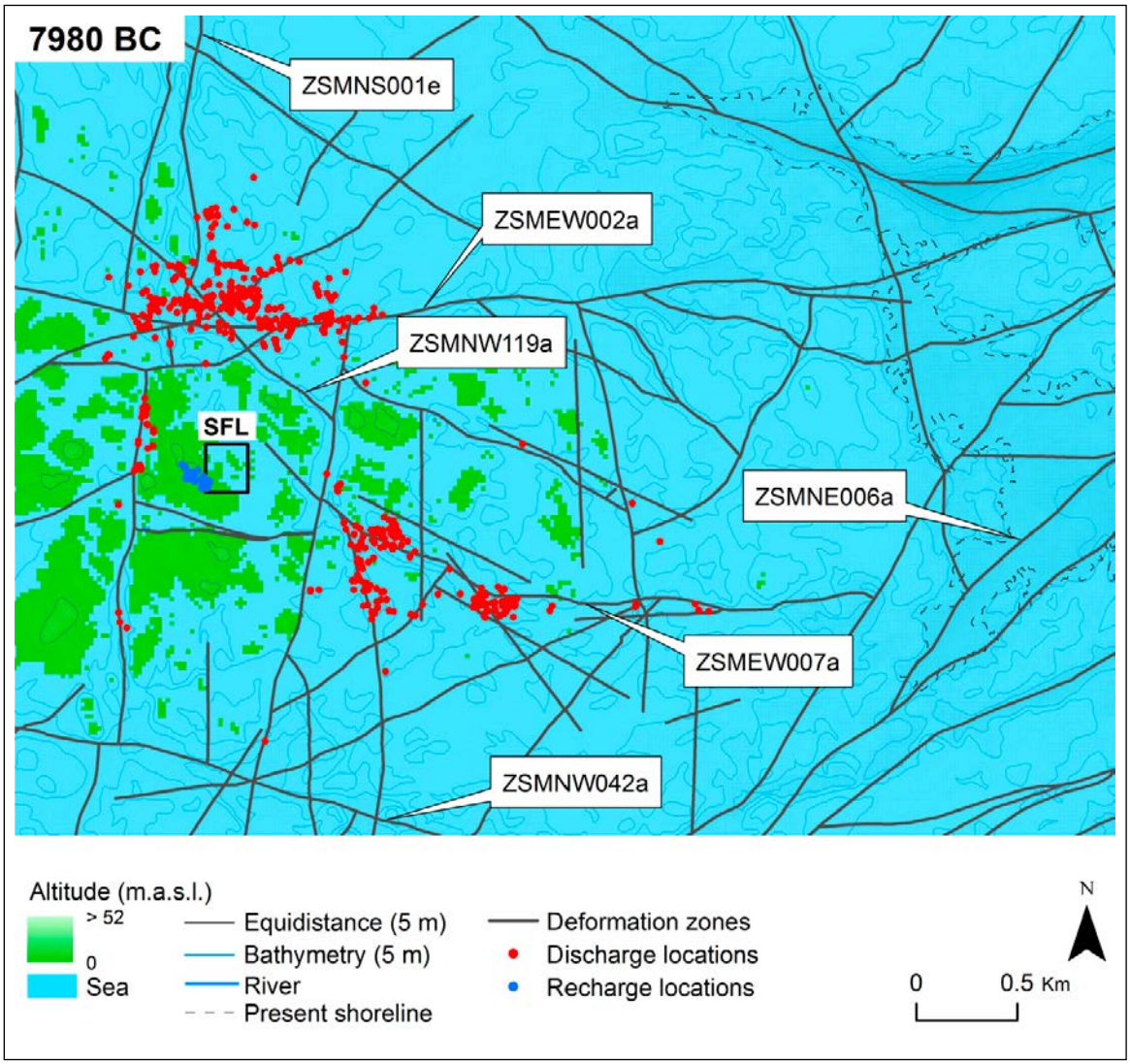

Figure 4-126. *Particle recharge (blue) and discharge (red) locations at the ground surface for Case 1 of the facility focussed model at 7980 BC. The model surface is coloured by elevation (land in green, sea in blue). Present shoreline (dashed grey), deformation zones at −20 m elevation (dark grey) and the SFL repository location (black) are added for context.*

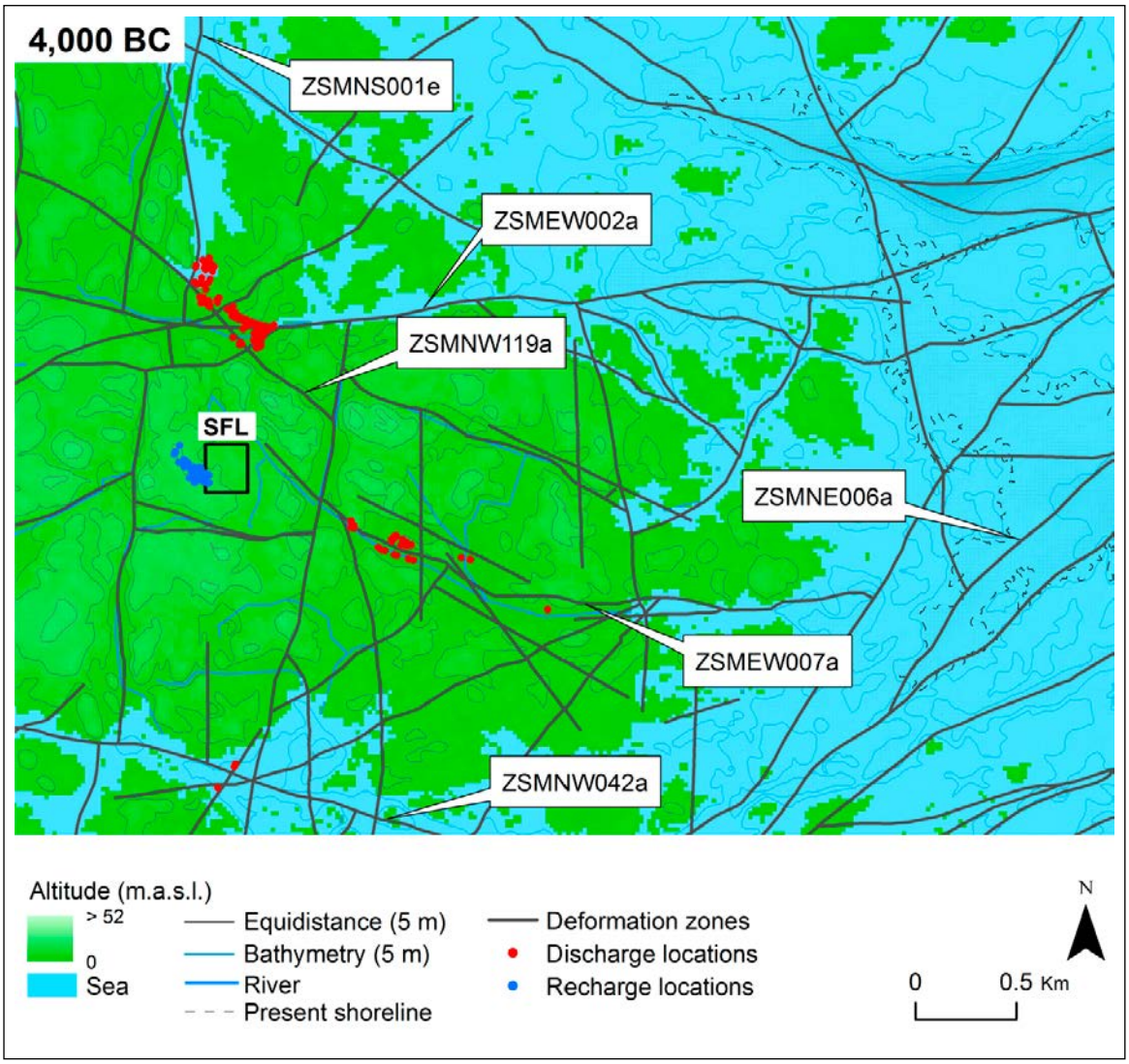

Figure 4-127. *Particle recharge (blue) and discharge (red) locations at the ground surface for Case 1 of the facility focussed model at 4000 BC. The model surface is coloured by elevation (land in green, sea in blue). Rivers (blue), present shoreline (dashed grey), deformation zones at −20 m elevation (dark grey) and the SFL repository location (black) are added for context.*

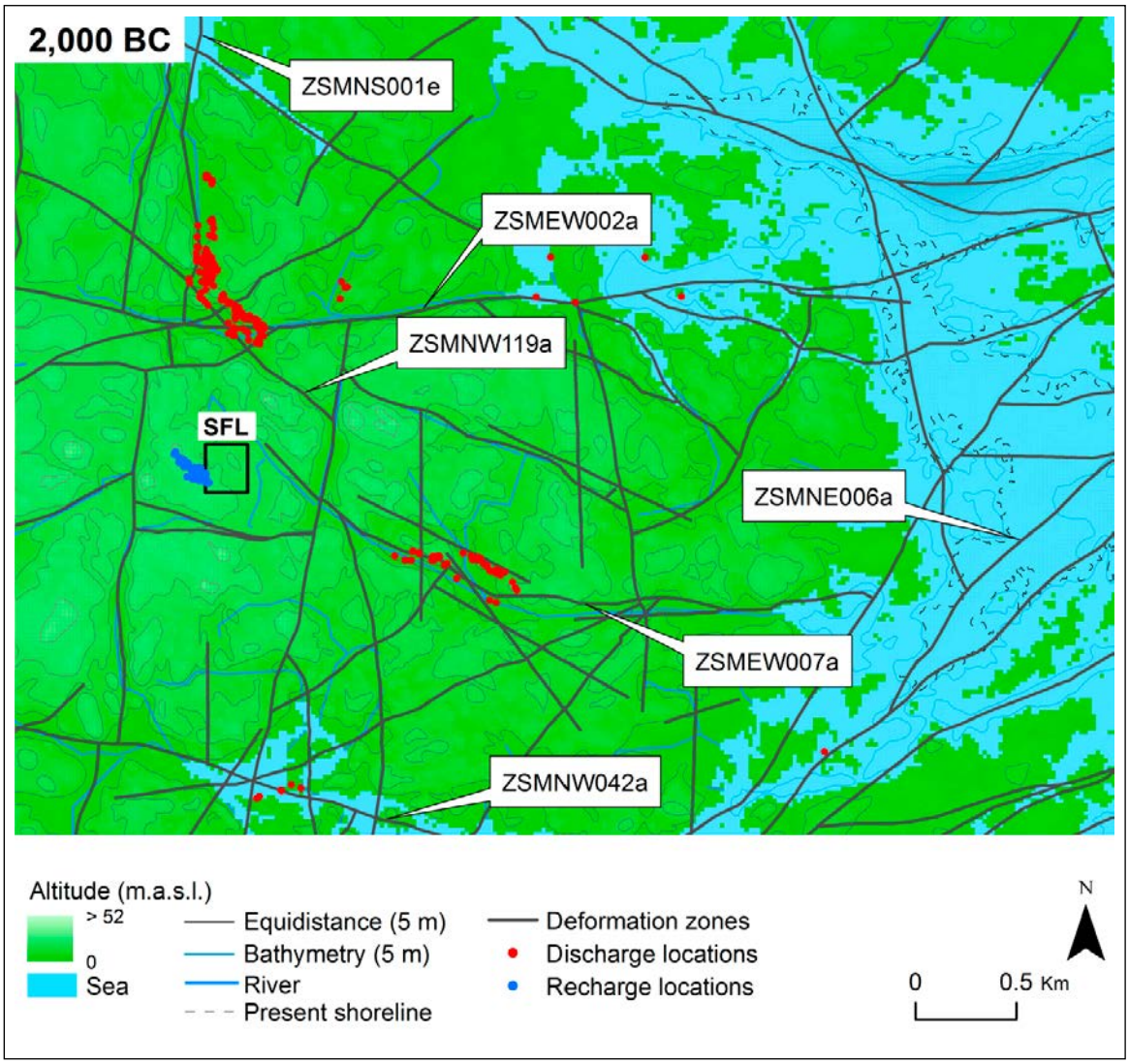

Figure 4-128. *Particle recharge (blue) and discharge (red) locations at the ground surface for Case 1 of the facility focussed model at 2000 BC. The model surface is coloured by elevation (land in green, sea in blue). Rivers (blue), present shoreline (dashed grey), deformation zones at −20 m elevation (dark grey) and the SFL repository location (black) are added for context.*

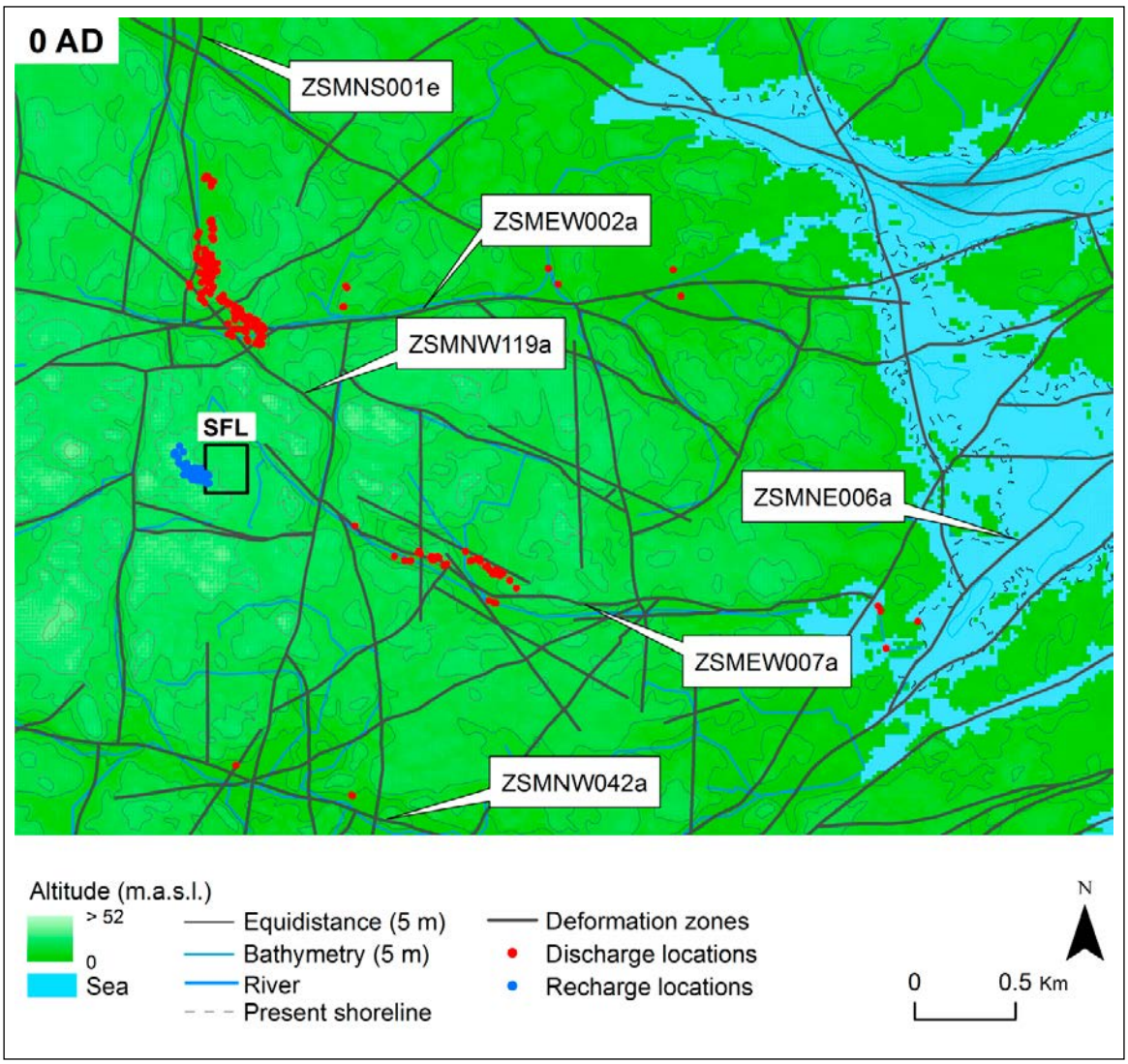

Figure 4-129. *Particle recharge (blue) and discharge (red) locations at the ground surface for Case 1 of the facility focussed model at 0 AD. The model surface is coloured by elevation (land in green, sea in blue). Rivers (blue), present shoreline (dashed grey), deformation zones at −20 m elevation (dark grey) and the SFL repository location (black) are added for context.*

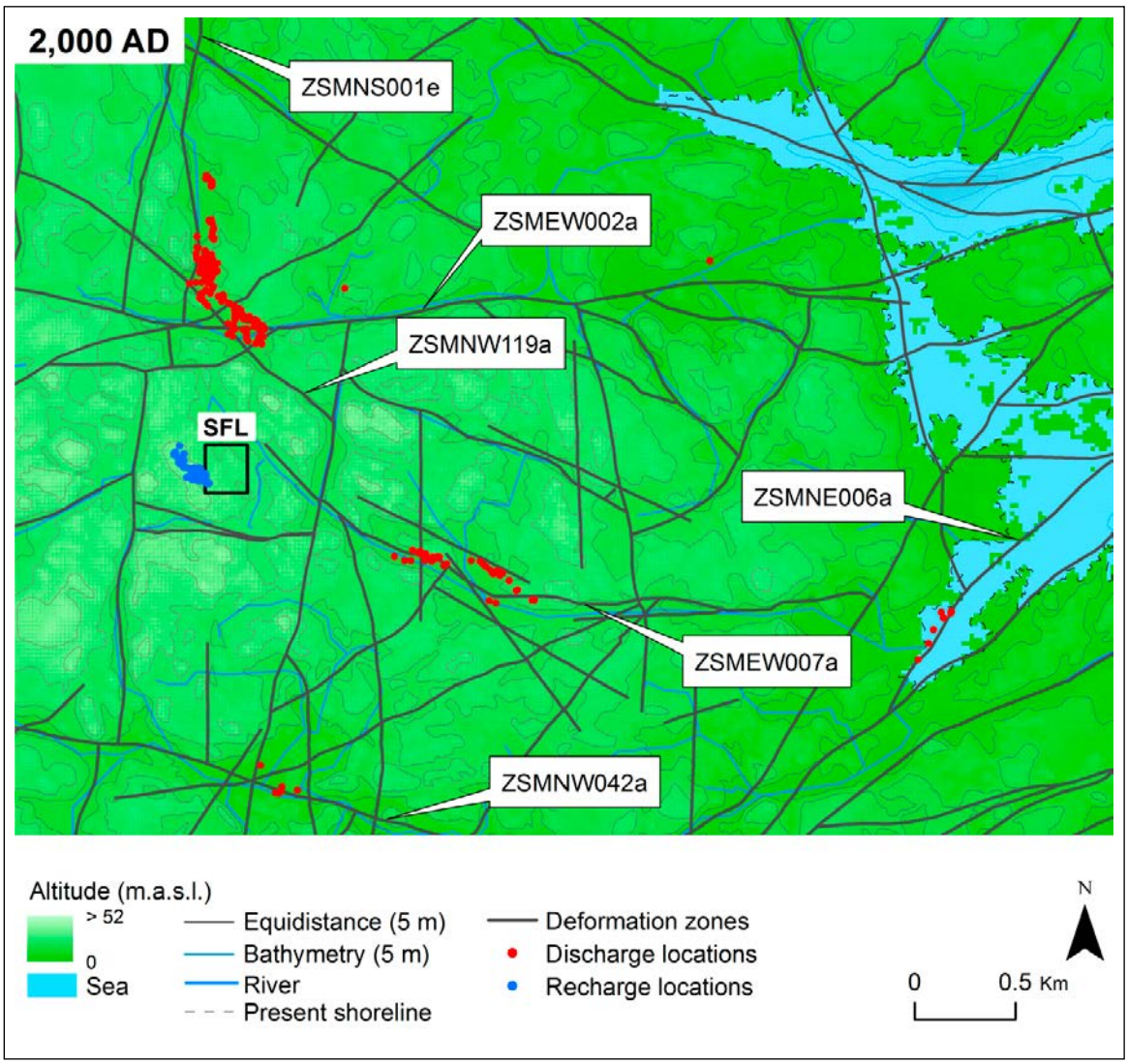

Figure 4-130. *Particle recharge (blue) and discharge (red) locations at the ground surface for Case 1 of the facility focussed model at 2000 AD. The model surface is coloured by elevation (land in green, sea in blue). Rivers (blue), present shoreline (dashed grey), deformation zones at −20 m elevation (dark grey) and the SFL repository location (black) are added for context.*

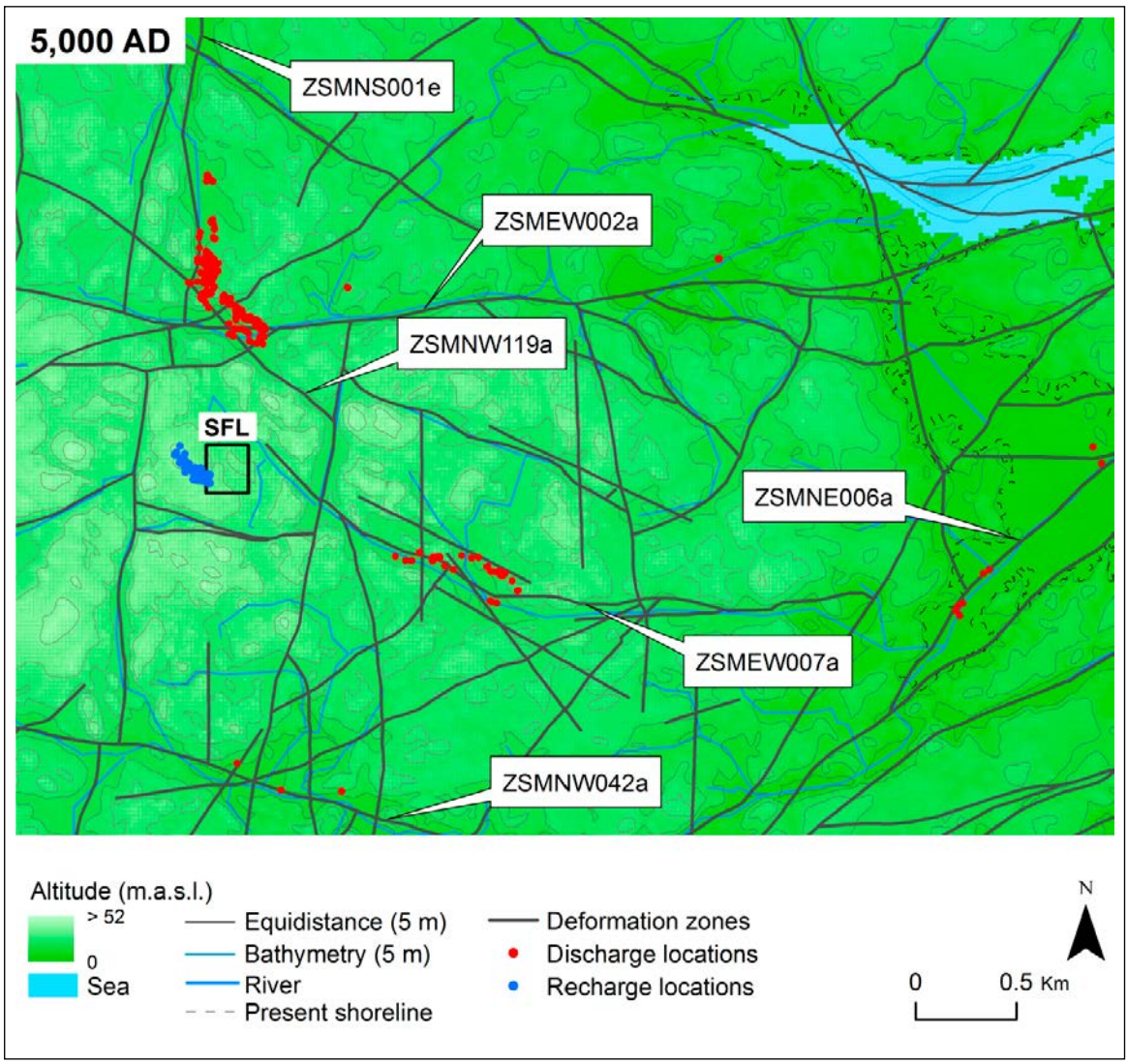

Figure 4-131. *Particle recharge (blue) and discharge (red) locations at the ground surface for Case 1 of the facility focussed model at 5000 AD. The model surface is coloured by elevation (land in green, sea in blue). Rivers (blue), present shoreline (dashed grey), deformation zones at −20 m elevation (dark grey) and the SFL repository location (black) are added for context.*

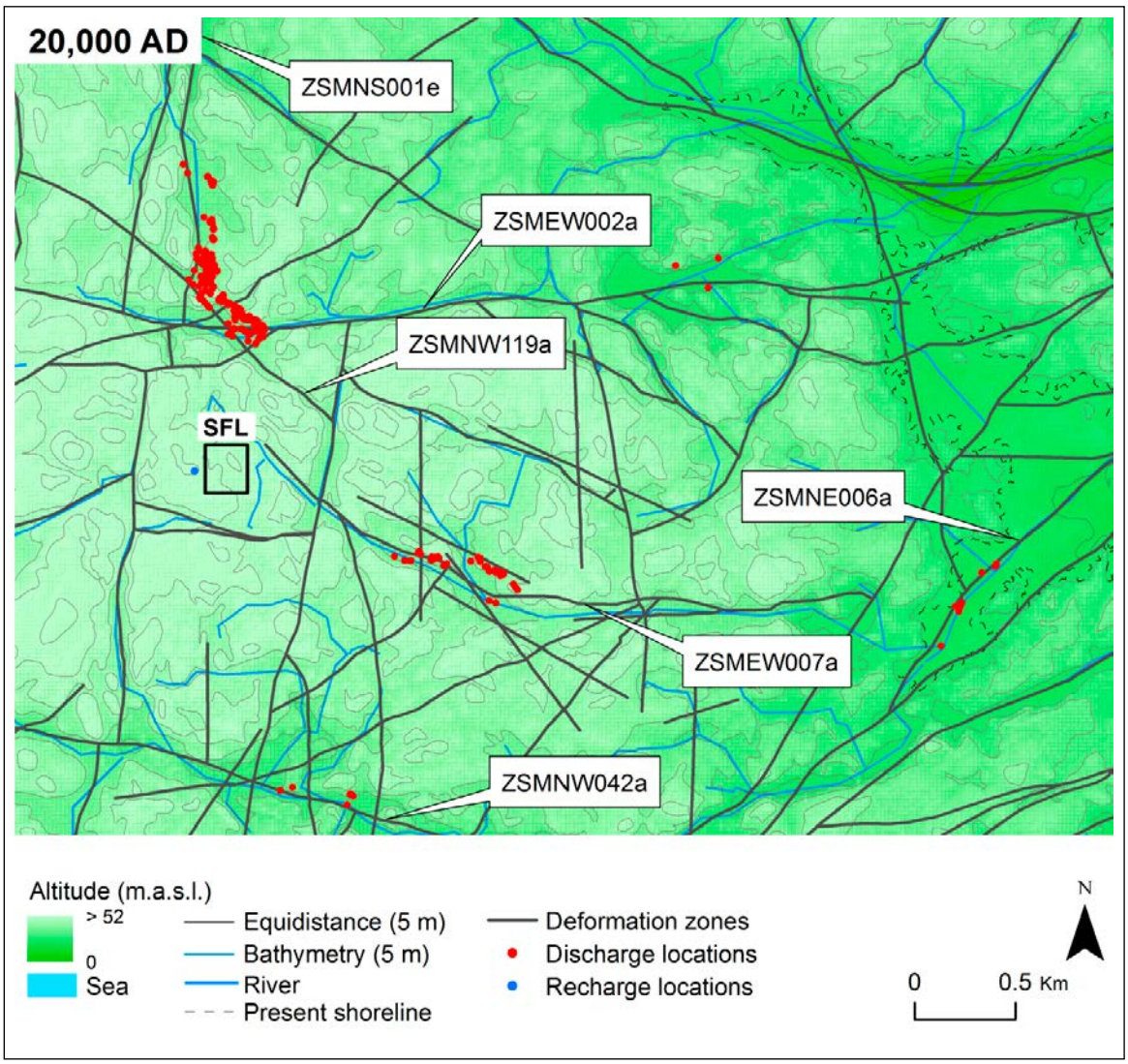

Figure 4-132. *Particle recharge (blue) and discharge (red) locations at the ground surface for the facility focussed model at 20 000 AD. The model surface is coloured by elevation (land in green, sea in blue). Rivers (blue), present shoreline (dashed grey), deformation zones at −20 m elevation (dark grey) and the SFL repository location (black) are added for context.*

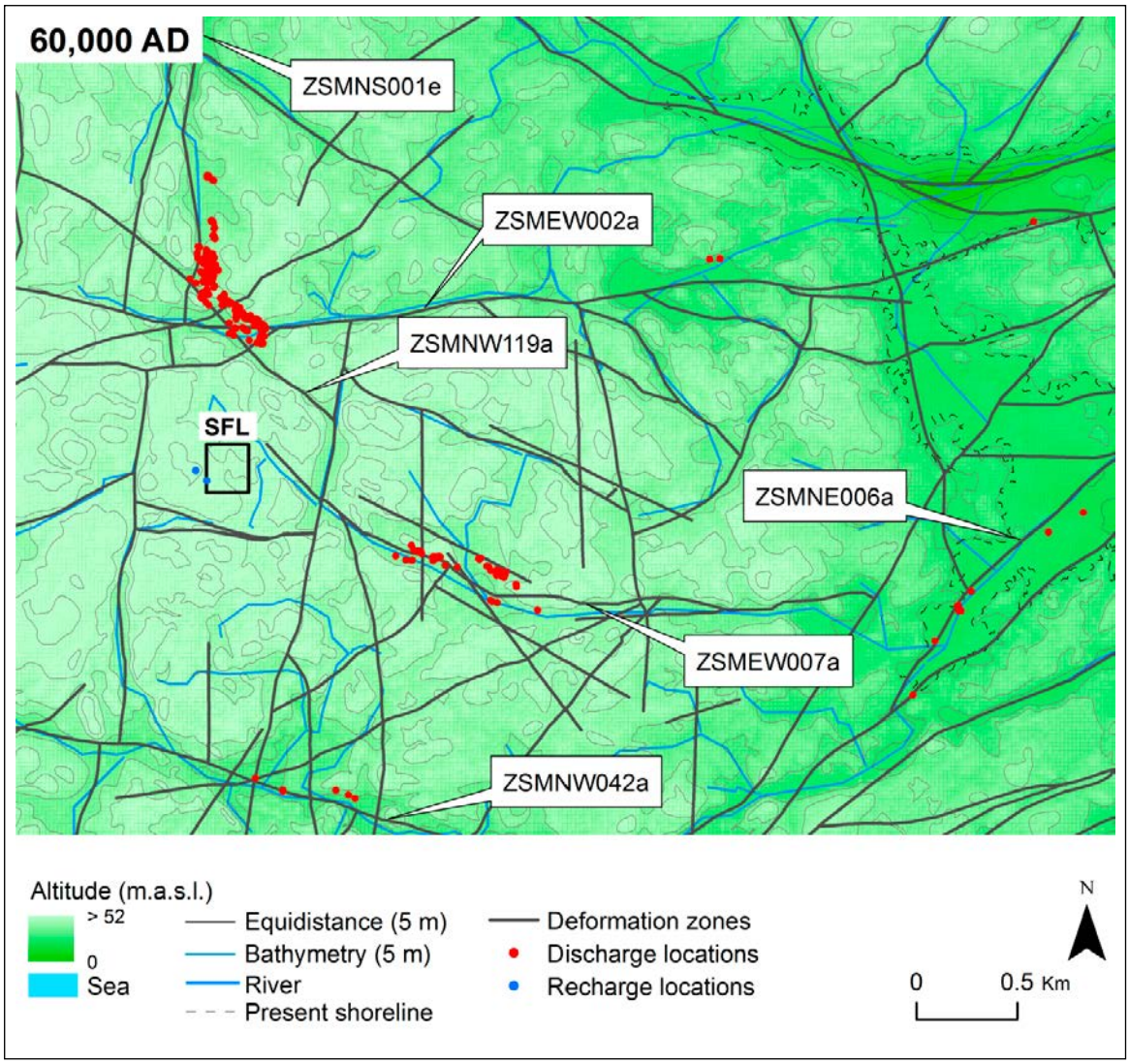

Figure 4-133. *Particle recharge (blue) and discharge (red) locations at the ground surface for Case 1 of the facility focussed model at 60 000 AD. The model surface is coloured by elevation (land in green, sea in blue). Rivers (blue), present shoreline (dashed grey), deformation zones at −20 m elevation (dark grey) and the SFL repository location (black) are added for context.*

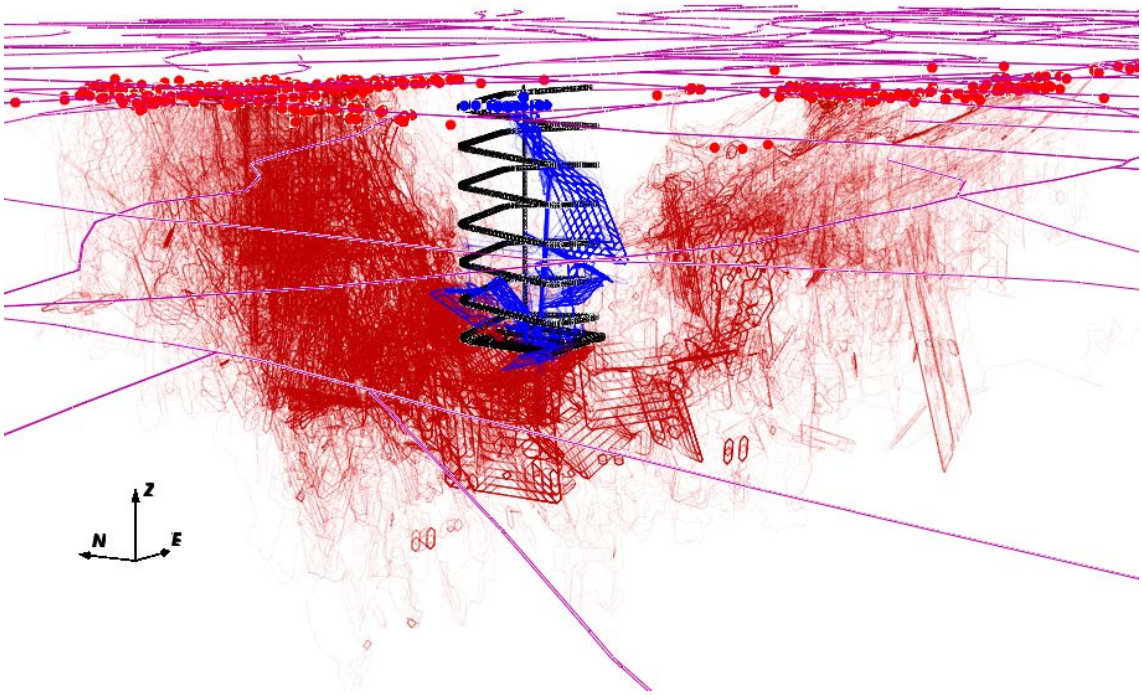

Figure 4-134. *Particle recharge (blue) and discharge (dark red) pathways for Case 1 of the facility focussed model at 7980 BC looking towards the northeast. Deformation zones at −20 m elevation (purple) and repository structures (black) are added for context.*

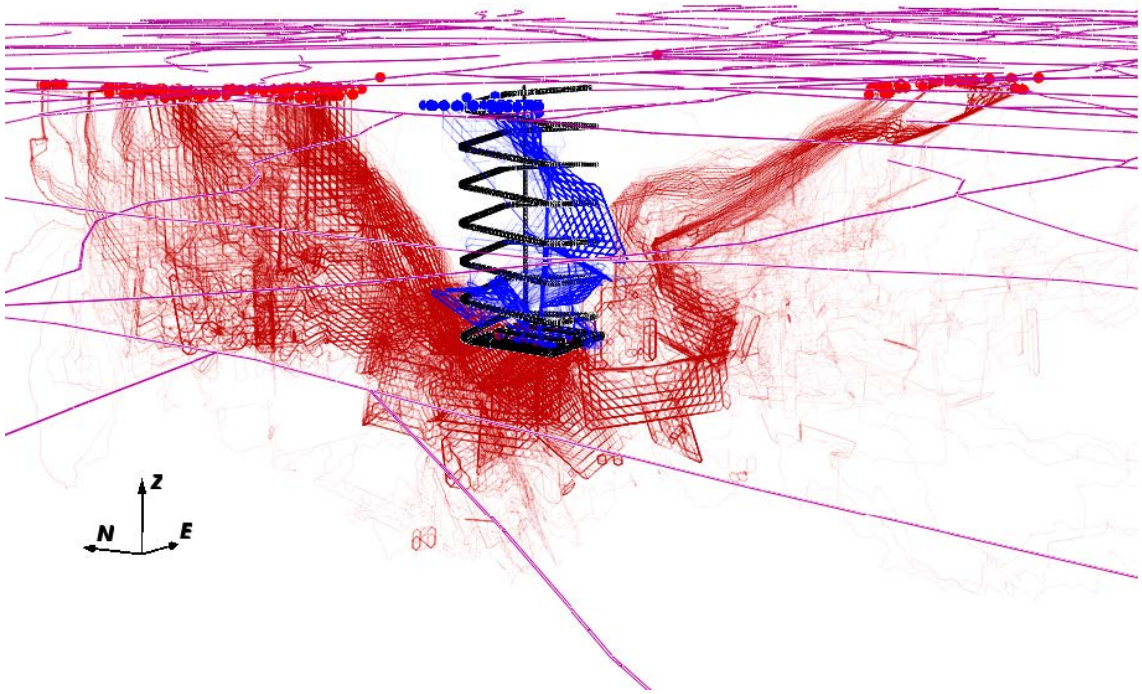

Figure 4-135. *Particle recharge (blue) and discharge (dark red) pathways for Case 1 of the facility focussed model at 2000 AD looking towards the northeast. Deformation zones at −20 m elevation (purple) and repository structures (black) are added for context.*

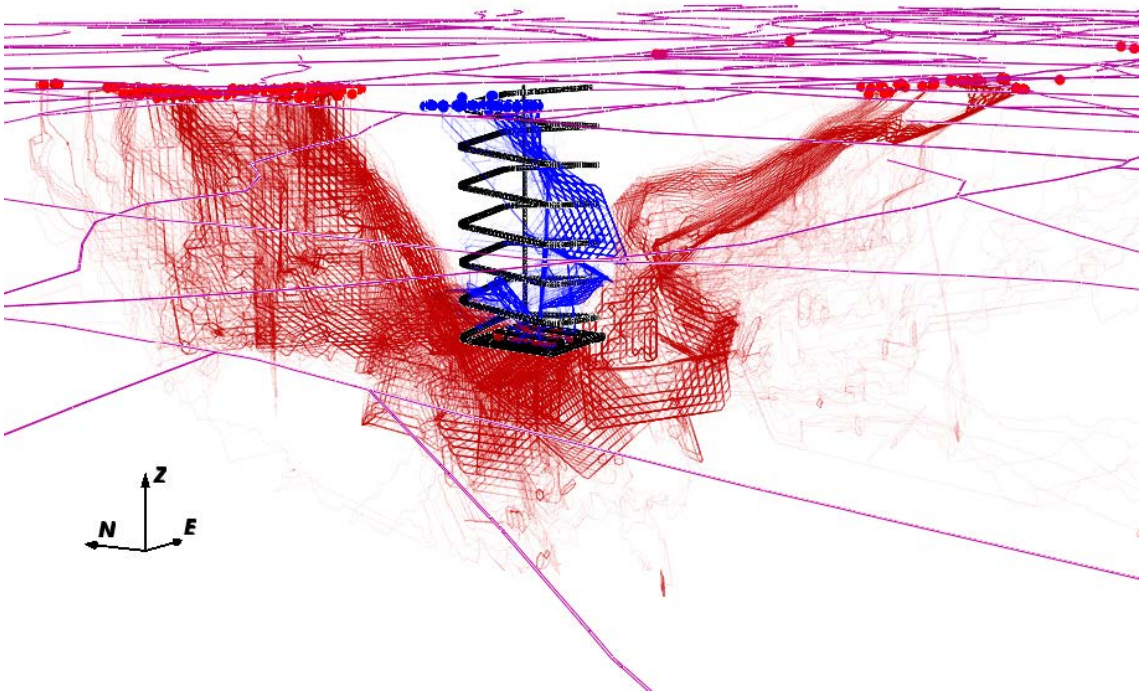

Figure 4-136. *Particle recharge (blue) and discharge (dark red) pathways for Case 1 of the facility focussed model at 60 000 AD looking towards the northeast. Deformation zones at −20 m elevation (purple) and repository structures (black) are added for context.*

4.6.3 Evolution of performance measures with time

Figure 4-137 to Figure 4-141 show the cumulative distribution function (CDF) plots of each performance measure (see Section 2.2.11) at each time slice for Case 1. Only one realisation of the HRD was used and an HCD with deterministic depth-dependent properties. The percentage of particles successfully reaching the top surface of the model is repeated below each plot. Note that only particles that are released at fracture intersections where there is flow out of a vault are continued and so the percentage of successful particles is not expected to exceed around 50 % (assuming an even distribution of flows into and out of the vaults). The CDF's are quite similar for the different particle release times, apart from at 7980 BC and, to a lesser extent, at 4000 BC. The earlier times have lower U and Q_{eq} values and larger F, t and L values. This is consistent with the lower pressure gradients associated with the site being fully or partially below sea level. In general, the far-field performance measures (F, t and L) vary more with time than the near-field performance measures (U and Q_{eq}) as they are more affected by the distance to the shoreline. However, as the shoreline becomes more distant at later times, its influence wanes and so the performance measures at later times are very similar to each other.

Table 4-4 shows the statistics of the performance measures (10^{th}, 50^{th} and 90^{th} percentiles) for each particle release time. Again, these show that the earlier times, particularly 7980 BC, have quite different performance measure statistics than the later times, due to the site being completely or partially below sea level. There is relatively little difference in performance measure statistics between the later times due to the declining influence of shoreline location as it moves further from the site.

Table 4-4. Performance measure statistics for Case 1, r1, of the facility focussed model, for particles successfully reaching the model top boundary (34–47 %), released at the specified times.

Performance measure	7980 BC	4000 BC	2000 BC	0 AD	2000 AD	5000 AD	20 000 AD	60 000 AD
$\log_{10}$(U) [m^2/y]								
10th-percentile	−3.940	−3.769	−3.646	−3.651	−3.592	−3.626	−3.612	−3.611
Median	−2.951	−2.612	−2.535	−2.517	−2.514	−2.512	−2.499	−2.496
90th-percentile	−2.014	−1.673	−1.597	−1.588	−1.604	−1.614	−1.566	−1.585
$\log_{10}(Q_{eq})$ [m^3/y]								
10th-percentile	−4.303	−4.229	−4.144	−4.131	−4.124	−4.137	−4.131	−4.140
Median	−3.563	−3.442	−3.411	−3.402	−3.399	−3.402	−3.388	−3.388
90th-percentile	−2.949	−2.744	−2.708	−2.701	−2.720	−2.722	−2.714	−2.716
$\log_{10}$(F) [y/m]								
10th-percentile	5.289	4.478	4.403	4.389	4.385	4.393	4.381	4.389
Median	5.585	4.893	4.799	4.776	4.782	4.755	4.769	4.751
90th-percentile	5.890	5.659	5.323	5.297	5.505	5.236	5.357	5.193
$\log_{10}$(t) [y]								
10th-percentile	2.894	1.884	1.917	1.907	1.903	1.900	1.902	1.892
Median	3.271	2.342	2.248	2.226	2.249	2.210	2.224	2.186
90th-percentile	3.732	3.125	2.998	2.921	2.944	3.012	2.987	2.953
$\log_{10}$(L) [m]								
10th-percentile	3.489	3.238	3.227	3.225	3.222	3.224	3.224	3.224
Median	3.699	3.349	3.343	3.333	3.328	3.330	3.321	3.324
90th-percentile	3.971	3.586	3.538	3.521	3.500	3.510	3.489	3.492

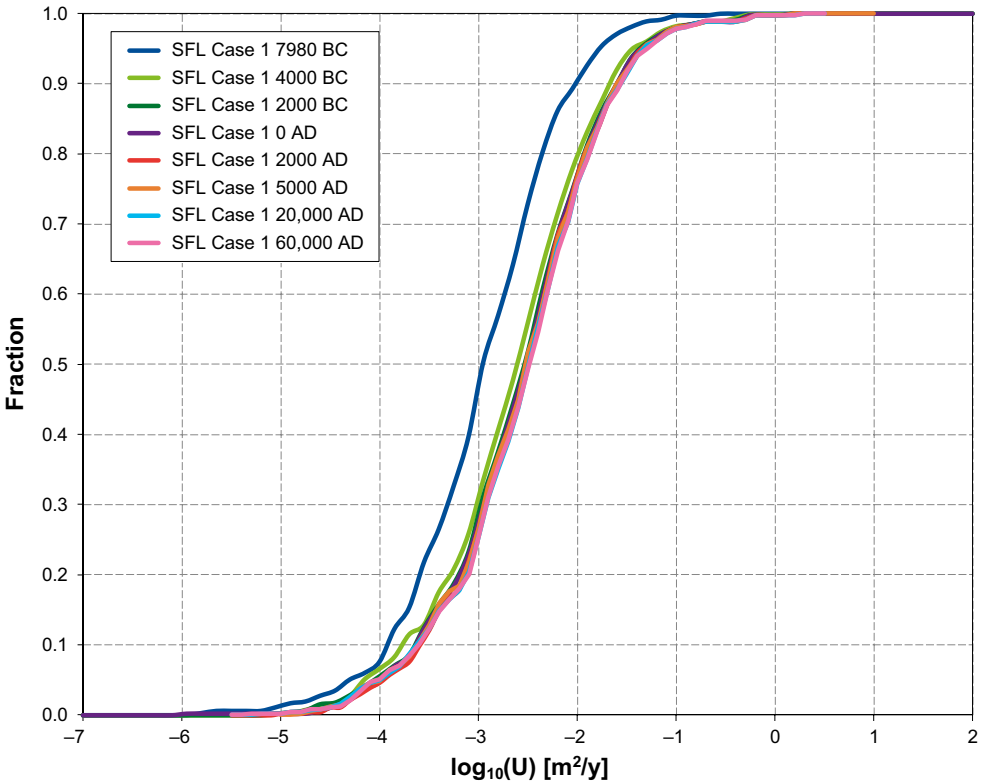

Figure 4-137. *Normalised CDF plots of equivalent flux (U) for Case 1 of the facility focussed model for particles successfully reaching the model top boundary (34–47 %), released at the specified times.*

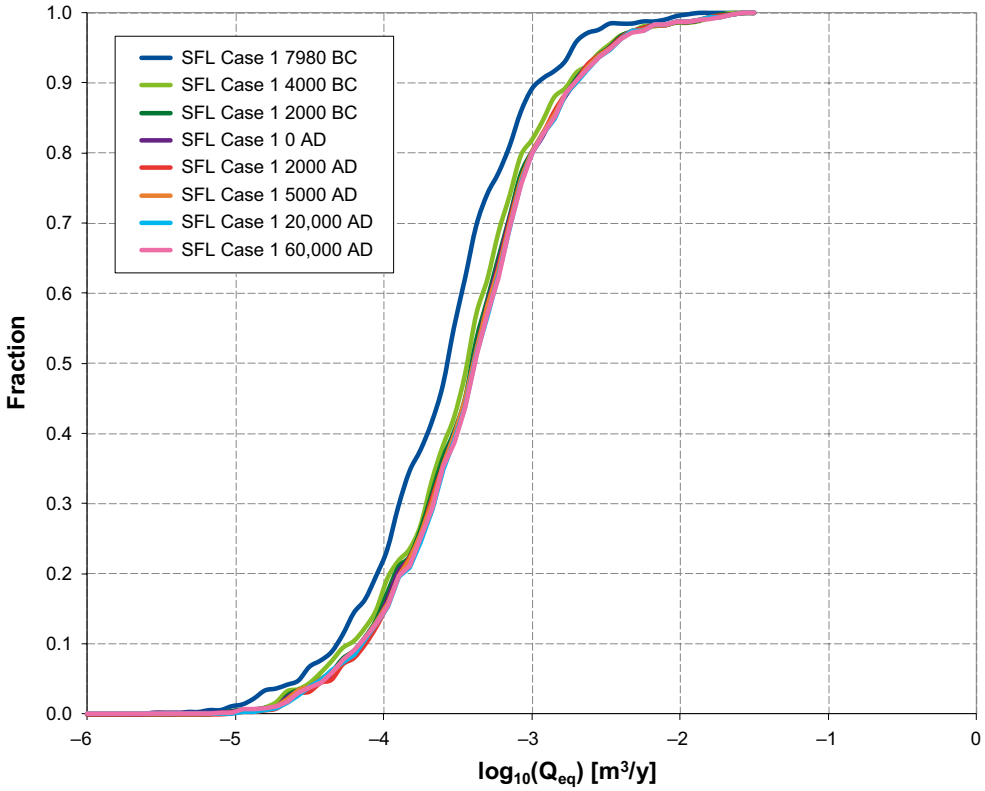

Figure 4-138. *Normalised CDF plots of equivalent flow rate (Q_{eq}) for Case 1 of the facility focussed model for particles successfully reaching the model top boundary (34–47 %), released at the specified times.*

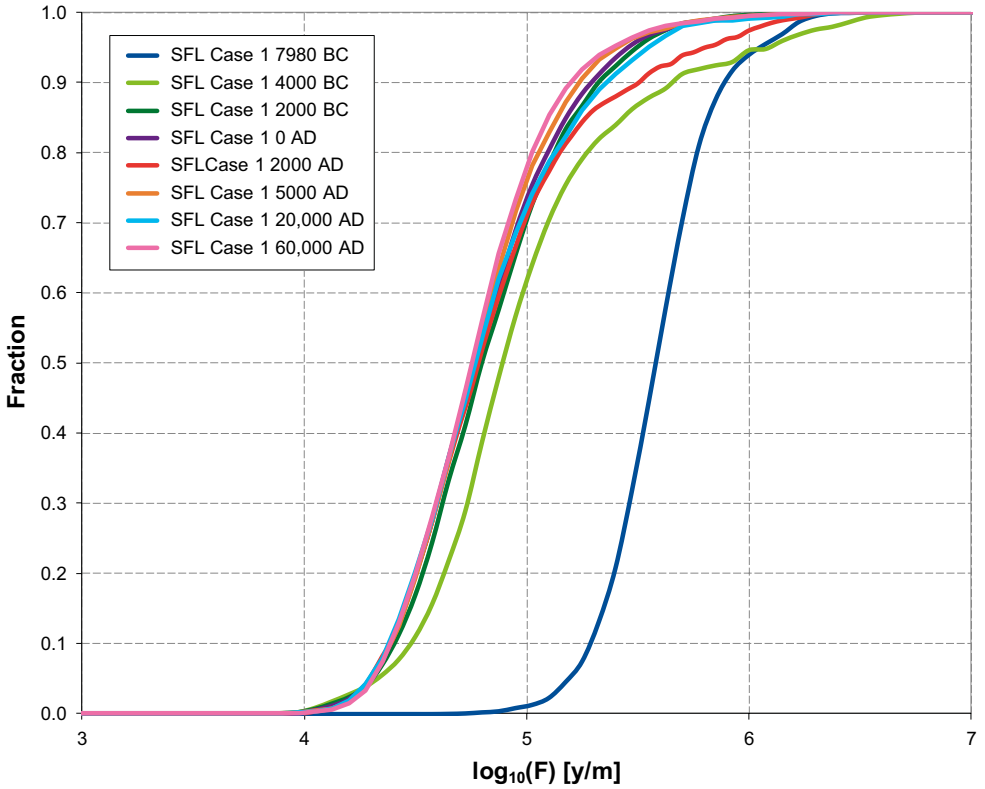

Figure 4-139. *Normalised CDF plots of flow-related transport resistance (F) for Case 1 of the facility focussed model for particles successfully reaching the model top boundary (34–47 %), released at the specified times.*

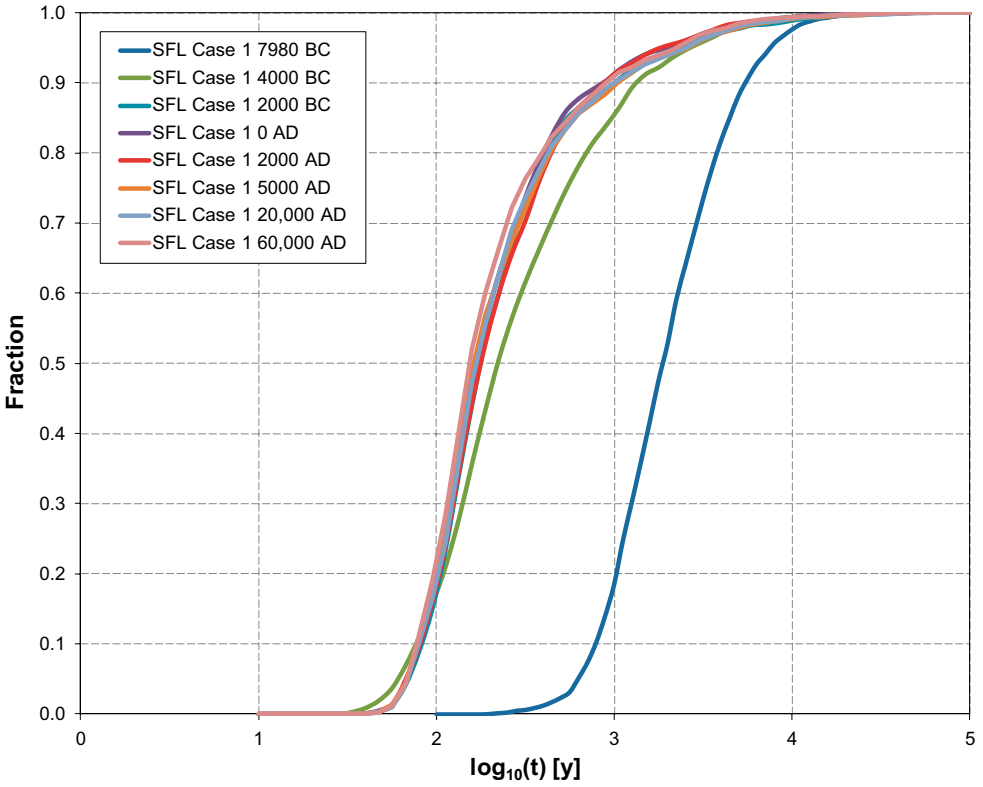

Figure 4-140. *Normalised CDF plots of travel time (t) for Case 1 of the facility focussed model for particles successfully reaching the model top boundary (34–47 %), released at the specified times.*

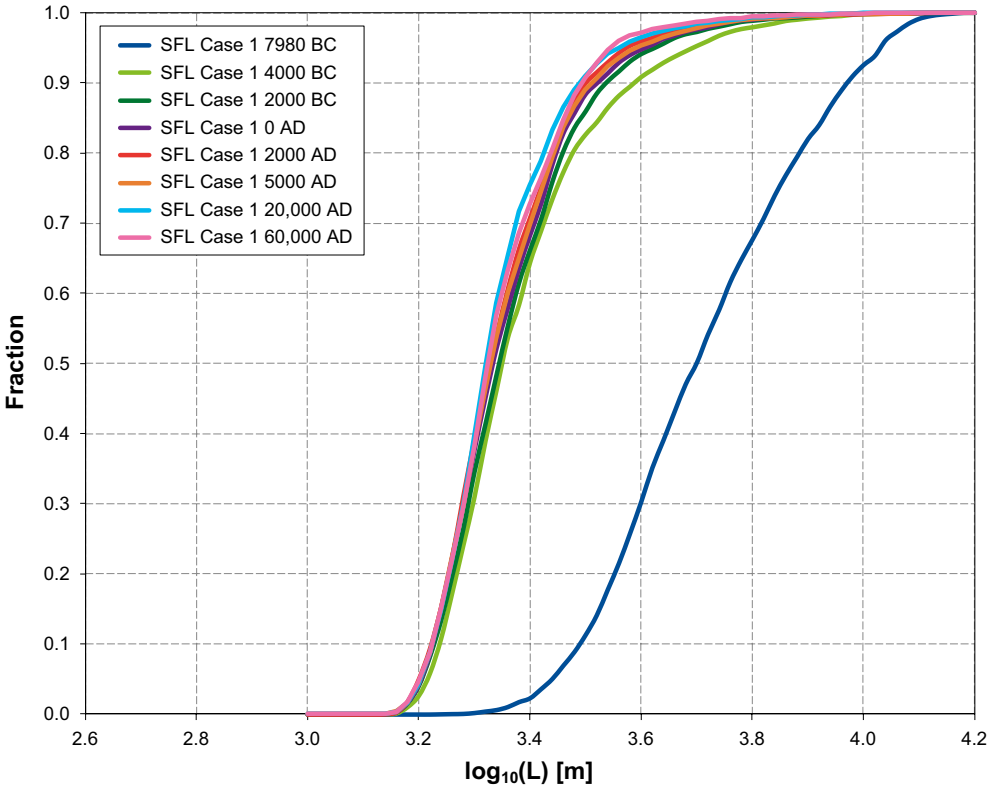

Figure 4-141. *Normalised CDF plots of path length (L) for Case 1 of the facility focussed model for particles successfully reaching the model top boundary (34–47 %), released at the specified times.*

4.6.4 Multiple realisations

The effect of stochastic variability of the DFN was explored for Case 1 of the facility focussed model at 2000 AD using five realisations of the HRD. The first realisation, denoted r1, used an HCD with deterministic depth-dependent properties. The other four realisations, denoted r2 to r5, each used a different realisation of an HCD with stochastic, depth-dependent properties. Although there are insufficient realisations to fully assess the variability, this analysis should give an indication of the likely spread of performance measure statistics between realisations.

Table 4-5 and Figure 4-142 to Figure 4-146 show the performance statistics and cumulative distribution functions (CDF's) for the five realisations. The variability between realisations is greater than the variability between time slices. In particular, realisations r1 and r3 have significantly higher U and Qeq values and significantly lower F, t and L values than the other realisations, although realisation r4 also has relatively low L values. The differences for realisations r1 and r3 are due to the occurrence of large sub-vertical factures that intersect the vaults (see also Subsection 4.4.1). These large fractures can deliver more flow from the recharge area above the repository directly to the vaults and also provide connectivity from the vaults to other large flow-carrying fractures and deformation zones. They also provide direct pathways to the surface with relatively low transport resistance. An example of a large fracture found in realisation 3 is shown in Figure 4-147. This is an important finding, as it suggests that the intersection of the vaults with large sub-vertical fractures would have significant detriments for performance measures, and hence it a key uncertainty to be addressed in the site characterisation and conceptualisation of the DFN model.

Figure 4-148 shows the particle recharge locations for each realisation. In addition to the recharge locations shown for realisation r1 in Figure 4-130, other realisations also show recharge locations a little to the south of the repository area. Figure 4-149 shows the particle discharge locations for each realisation. In general, the realisations have discharge locations in the same areas, but not all realisations discharge to all of the areas. In particular, only realisation r1 has particles exiting at the southernmost discharge area and only realisations r1 and r3 have particles exiting at the most south-eastern discharge area. This shows that there is some variability of recharge and discharge areas between realisations, but the same general areas are used over the ensemble of realisations in most cases.

Table 4-5. Performance measure statistics for five realisations of Case 1, of the facility focussed model, for particles successfully reaching the model top boundary (26–46 %), released at 2000 AD.

Performance measure	r1	r2	r3	r4	r5
$\log_{10}(U)$ [m^2/y]					
10th-percentile	−3.592	−4.628	−3.606	−4.431	−4.080
Median	−2.514	−3.389	−2.527	−3.251	−3.053
90th-percentile	−1.604	−2.574	−1.661	−2.360	−2.032
$\log_{10}(Q_{eq})$ [m^3/y]					
10th-percentile	−4.124	−4.703	−4.183	−4.631	−4.376
Median	−3.399	−3.832	−3.420	−3.839	−3.722
90th-percentile	−2.720	−3.150	−2.744	−2.994	−2.984
$\log_{10}(F)$ [y/m]					
10th-percentile	4.385	5.091	3.726	4.768	4.640
Median	4.782	5.615	4.356	5.434	5.077
90th-percentile	5.505	6.315	5.269	6.584	5.567
$\log_{10}(t)$ [y]					
10th-percentile	1.903	2.378	1.042	2.010	2.121
Median	2.249	2.784	1.516	2.525	2.614
90th-percentile	2.944	3.212	2.231	3.246	3.256
$\log_{10}(L)$ [m]					
10th-percentile	3.222	3.420	3.191	3.264	3.386
Median	3.328	3.606	3.280	3.377	3.676
90th-percentile	3.500	3.855	3.433	3.559	3.945

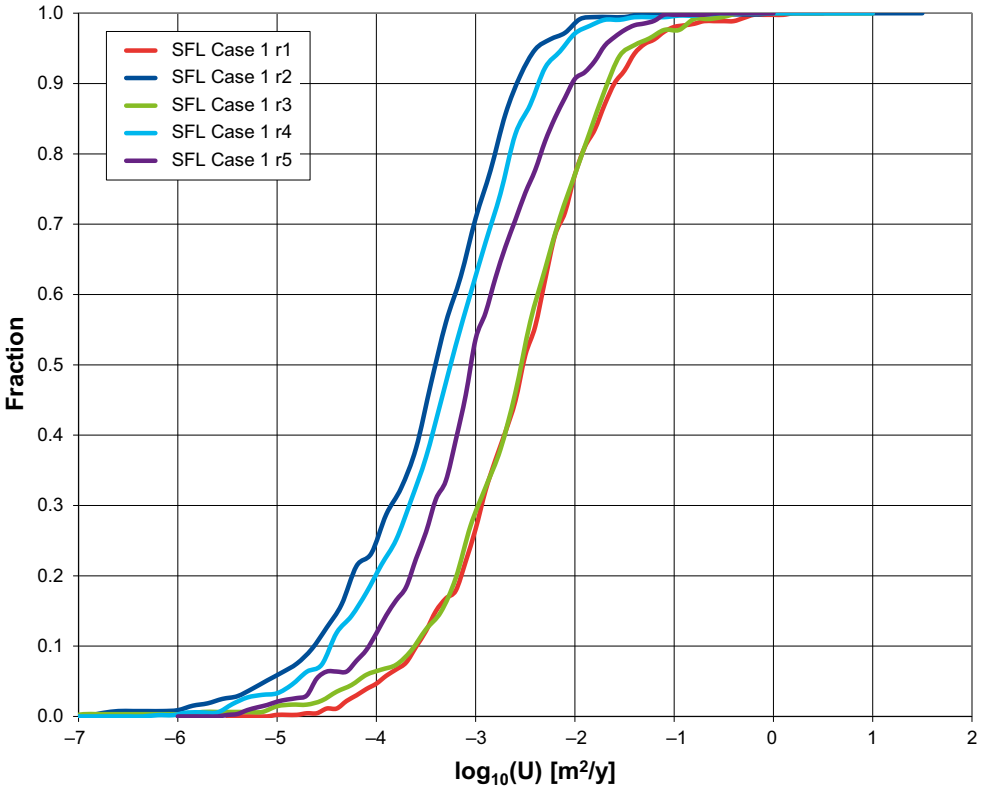

Figure 4-142. *Normalised CDF plots of equivalent flux (U) for five realisations of Case 1 of the facility focussed model for particles successfully reaching the model top boundary (26–46 %), released at 2000 AD.*

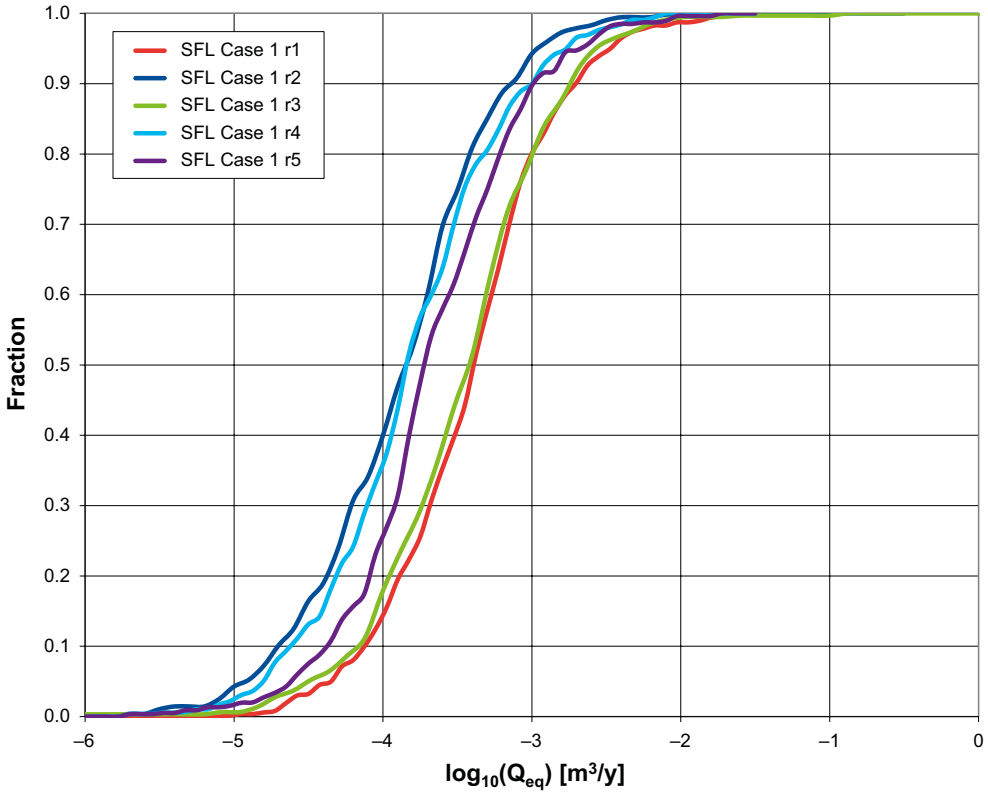

Figure 4-143. *Normalised CDF plots of equivalent flow rate (Q_{eq}) for five realisations of Case 1 of the facility focussed model for particles successfully reaching the model top boundary (26–46 %), released at 2000 AD.*

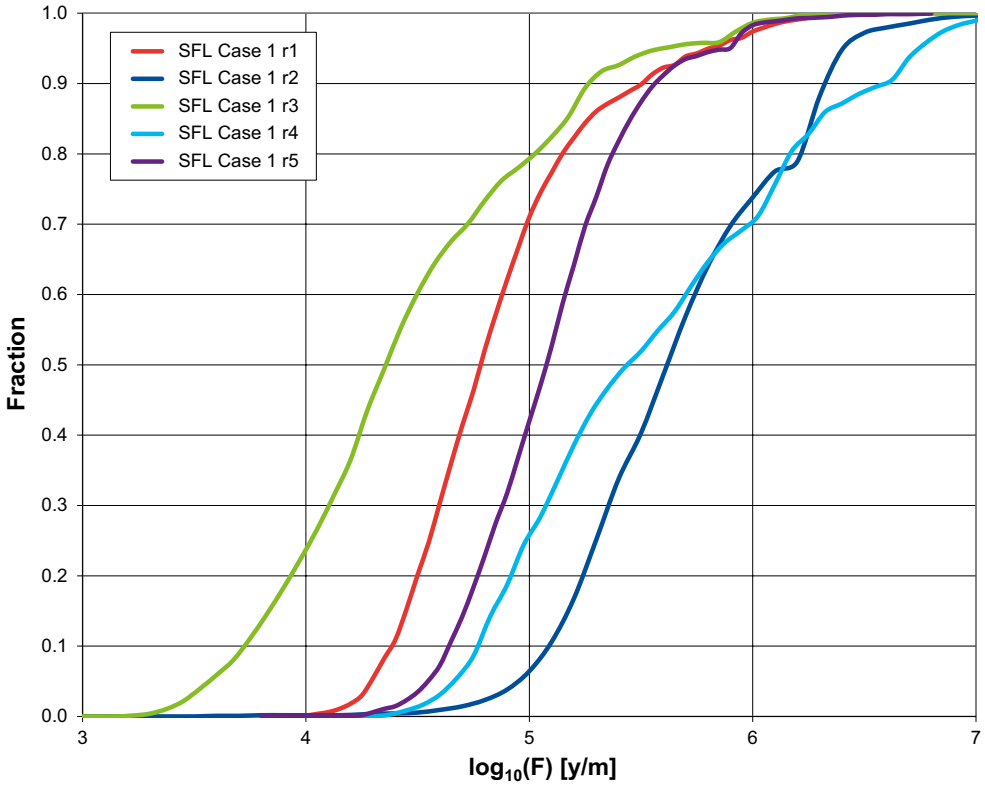

Figure 4-144. *Normalised CDF plots of flow-related transport resistance (F) for five realisations of Case 1 of the facility focussed model for particles successfully reaching the model top boundary (26–46 %), released at 2000 AD.*

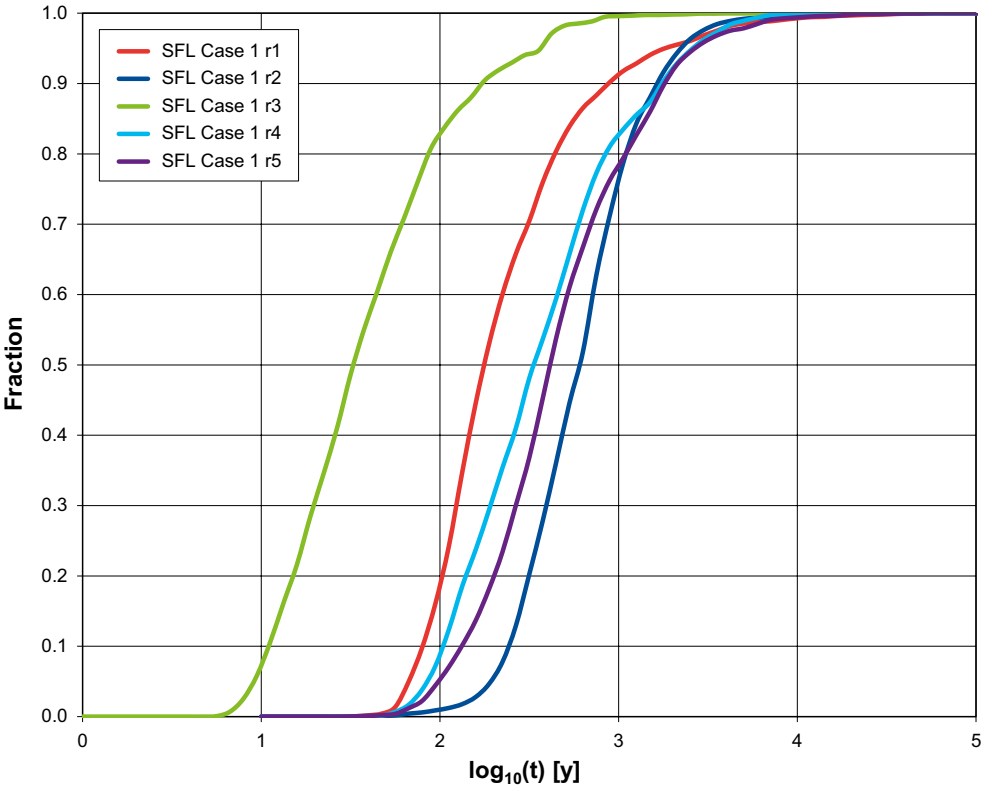

Figure 4-145. *Normalised CDF plots of travel time (t) for five realisations of Case 1 of the facility focussed model for particles successfully reaching the model top boundary (26–46 %), released at 2000 AD.*

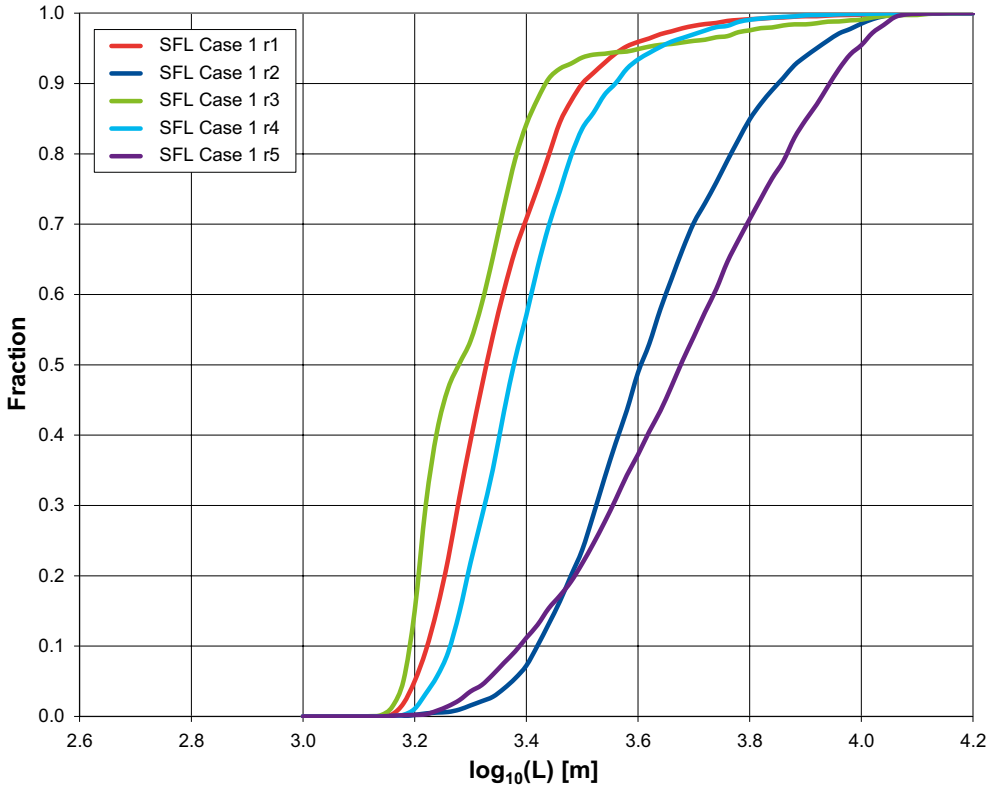

Figure 4-146. *Normalised CDF plots of path length (L) for five realisations of Case 1 of the facility focussed model for particles successfully reaching the model top boundary (26–46 %), released at 2000 AD.*

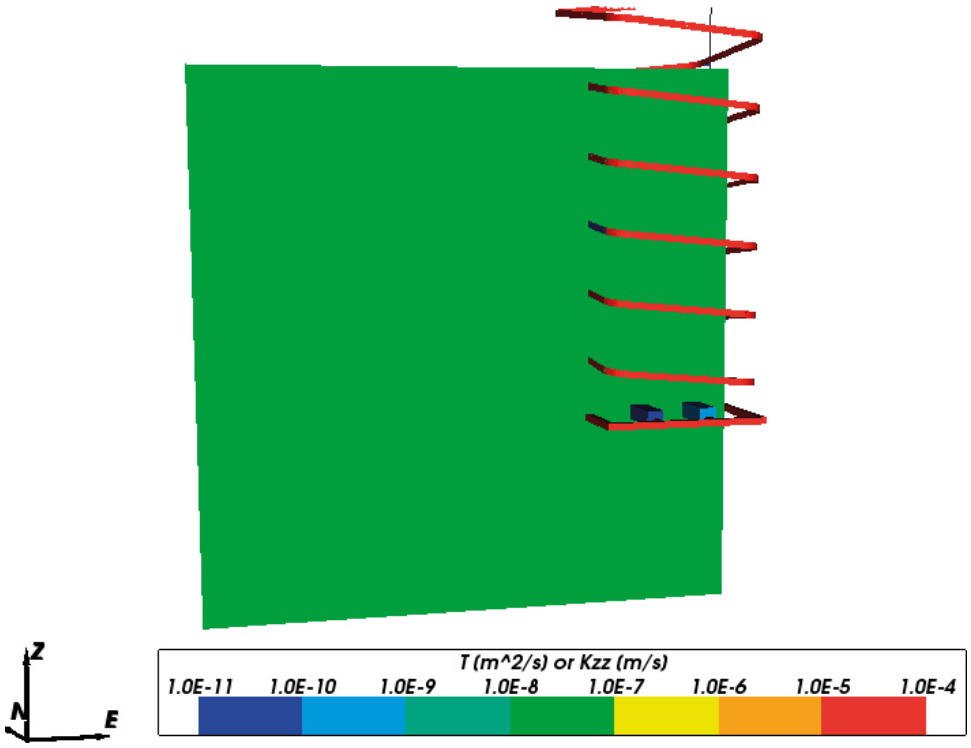

Figure 4-147. *A large fracture intersecting the vaults for realisation 3 of Case 1 of the facility focussed model, coloured by transmissivity [m^2/s]. The repository structures are coloured by the vertical component of hydraulic conductivity [m/s].*

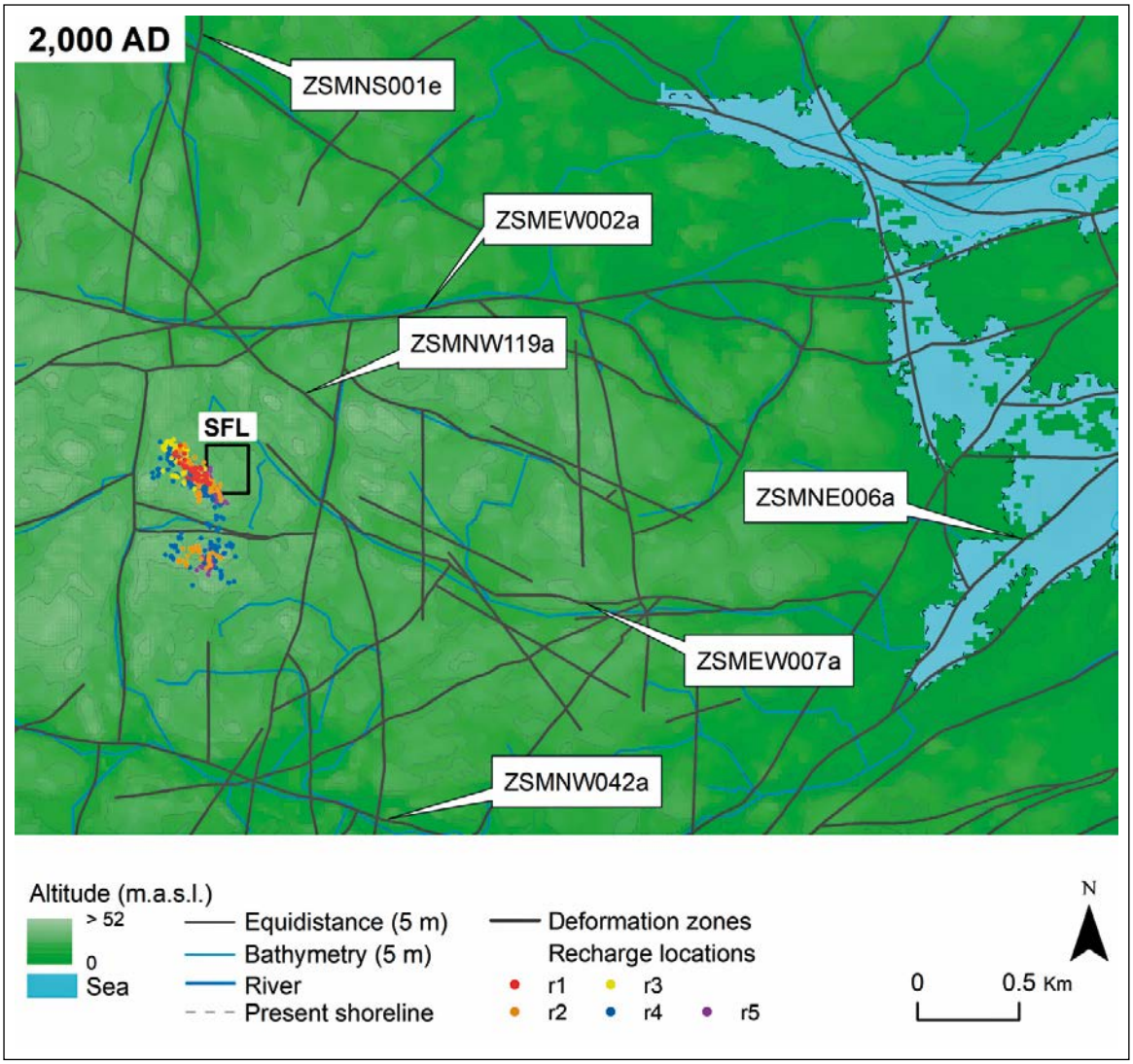

Figure 4-148. *Particle recharge locations at the ground surface for each realisation of Case 1 of the facility focussed model at 2000 AD (r1=red, r2=orange, r3=yellow, r4=blue, r5=purple). The model surface is coloured by elevation (land in green, sea in blue). Rivers (blue), present shoreline (dashed grey), deformation zones at −20 m elevation (dark grey) and the SFL repository location (black) are added for context.*

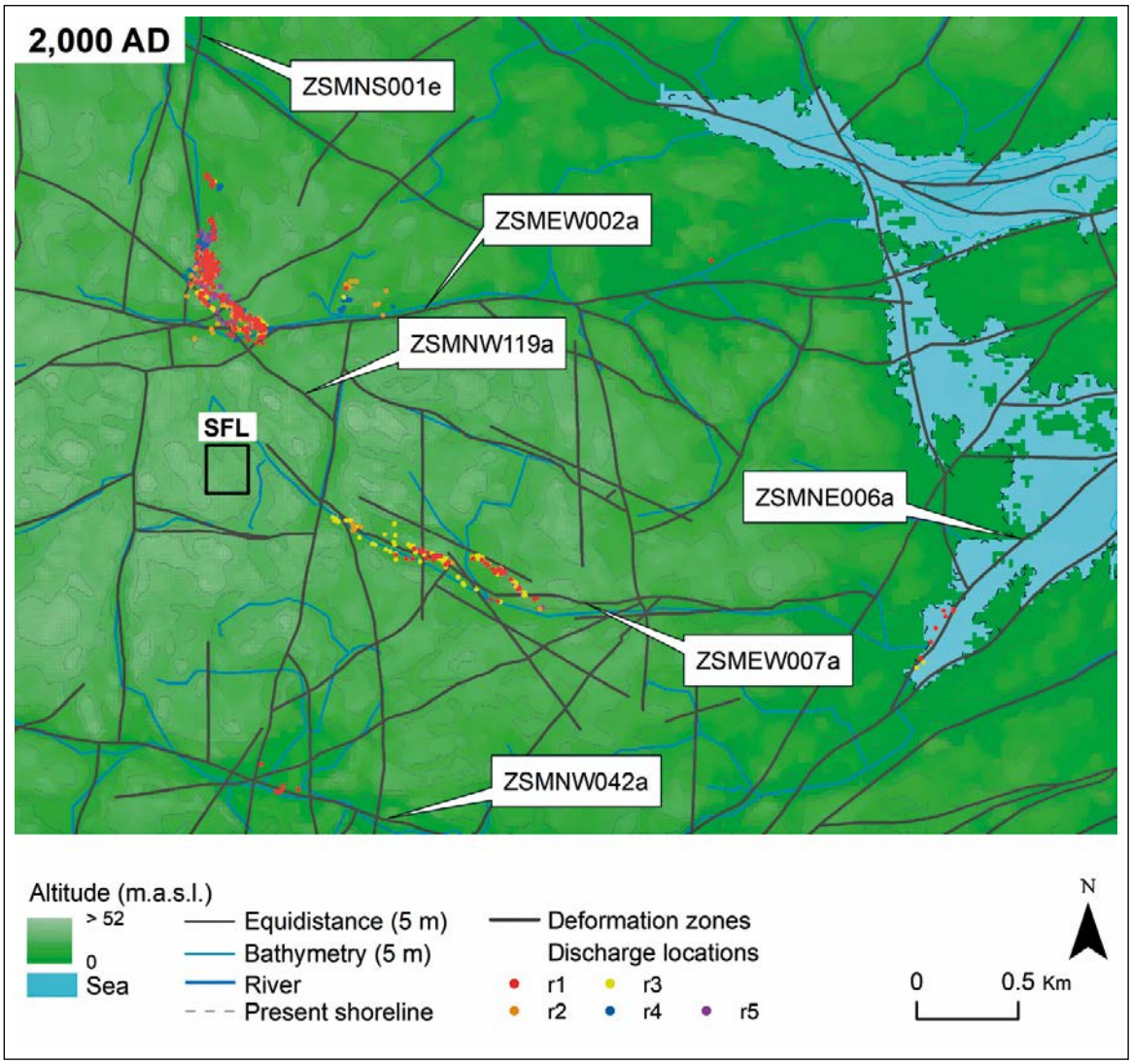

Figure 4-149. *Particle discharge locations at the ground surface for each realisation of Case 1 of the facility focussed model at 2000 AD (r1=red, r2=orange, r3=yellow, r4=blue, r5=purple). The model surface is coloured by elevation (land in green, sea in blue). Rivers (blue), present shoreline (dashed grey), deformation zones at −20 m elevation (dark grey) and the SFL repository location (black) are added for context.*

4.6.5 Effects of groundwater composition and concrete degradation

There were three cases considered for the facility focussed modelling in which the groundwater composition varied due to the effects of chemical reactions (or lack thereof) in the catchment focussed modelling, as described in Section 1.2. Only one realisation of the HRD was used for all cases together with an HCD with deterministic depth-dependent properties. Results are also presented for an additional variant of Case 1 that considers a situation with degraded concrete backfill in the BHK vault, with the hydraulic conductivity of the backfill increased from 8.3×10^{-10} m/s to 1.0×10^{-7} m/s.

Table 4-6 and Figure 4-150 to Figure 4-154 give the performance measure statistics and show the cumulative distribution functions (CDF's) for each of the cases. In general, there appear to be few differences between the results for Cases 1 to 3. The differences in groundwater compositions between these cases are relatively small and so the differences in the flow field are also relatively minor, leading to very similar particle tracking statistics. The only significant difference is a moderate reduction in the proportion of higher F values for Case 2 relative to Cases 1 and 3. This difference is related to small changes in groundwater density that, by chance, give variation in some of the longer paths. The variant with degraded concrete backfill for the BHK vault gives reductions in the median and 10th percentile values for U and Q_{eq}, which is to be expected since these performance measures are most sensitive to changes close to the vaults. The increase in hydraulic conductivity in the BHK vault leads to a greater proportion of the flow passing through the vault rather than through the neighbouring fractures, thus leading to a reduction in U and Q_{eq}. There is also a greater proportion of particles with higher F values for the degraded concrete variant.

Table 4-6. Performance measure statistics for different cases of the facility focussed model, for particles successfully reaching the model top boundary (46–48 %), released at 2000 AD.

Performance measure	Case 1	Case 1 degraded[1]	Case 2	Case 3
$\log_{10}$(U) [m^2/y]				
10th-percentile	−3.592	−4.069	−3.628	−3.625
Median	−2.514	−2.818	−2.517	−2.510
90th-percentile	−1.604	−1.696	−1.603	−1.581
$\log_{10}$(Q_{eq}) [m^3/y]				
10th-percentile	−4.124	−4.381	−4.133	−4.124
Median	−3.399	−3.545	−3.399	−3.395
90th-percentile	−2.720	−2.768	−2.719	−2.696
$\log_{10}$(F) [y/m]				
10th-percentile	4.385	4.405	4.385	4.382
Median	4.782	4.816	4.749	4.768
90th-percentile	5.505	5.883	5.248	5.510
$\log_{10}$(t) [y]				
10th-percentile	1.903	1.923	1.896	1.901
Median	2.249	2.267	2.210	2.235
90th-percentile	2.944	3.061	2.994	2.944
$\log_{10}$(L) [m]				
10th-percentile	3.222	3.215	3.223	3.222
Median	3.328	3.315	3.328	3.330
90th-percentile	3.500	3.518	3.516	3.510

[1] Degraded concrete backfill for the BHK vault

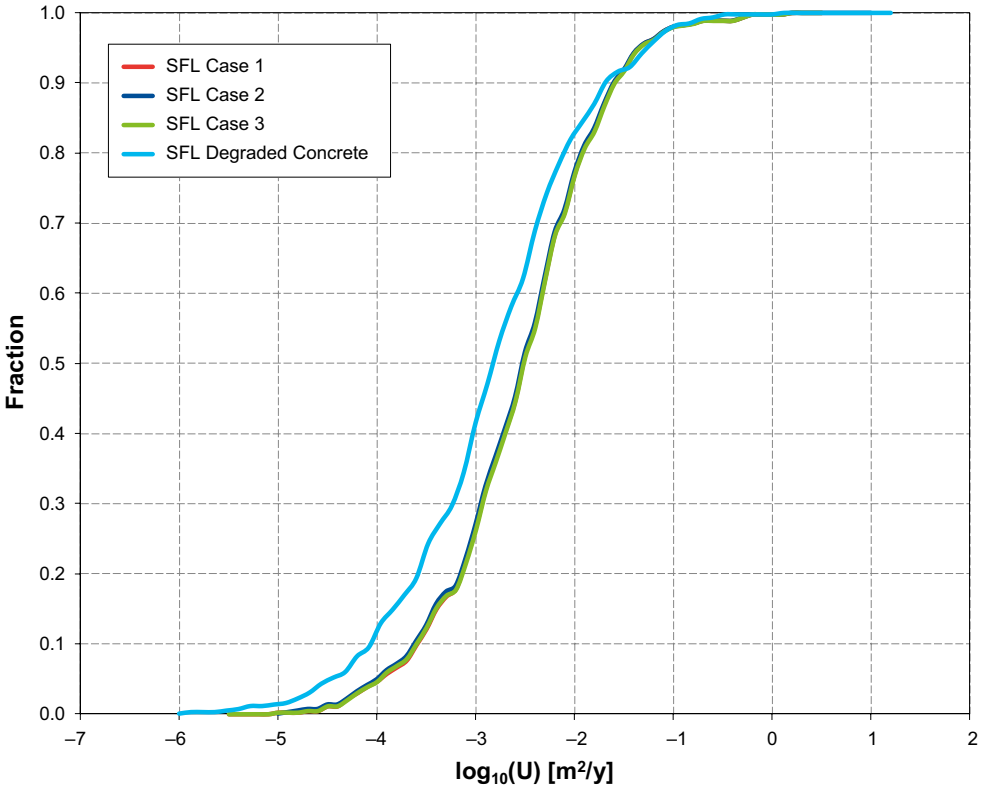

Figure 4-150. *Normalised CDF plots of equivalent flux (U) for different cases of the facility focussed model for particles successfully reaching the model top boundary (46–48 %), released at 2000 AD.*

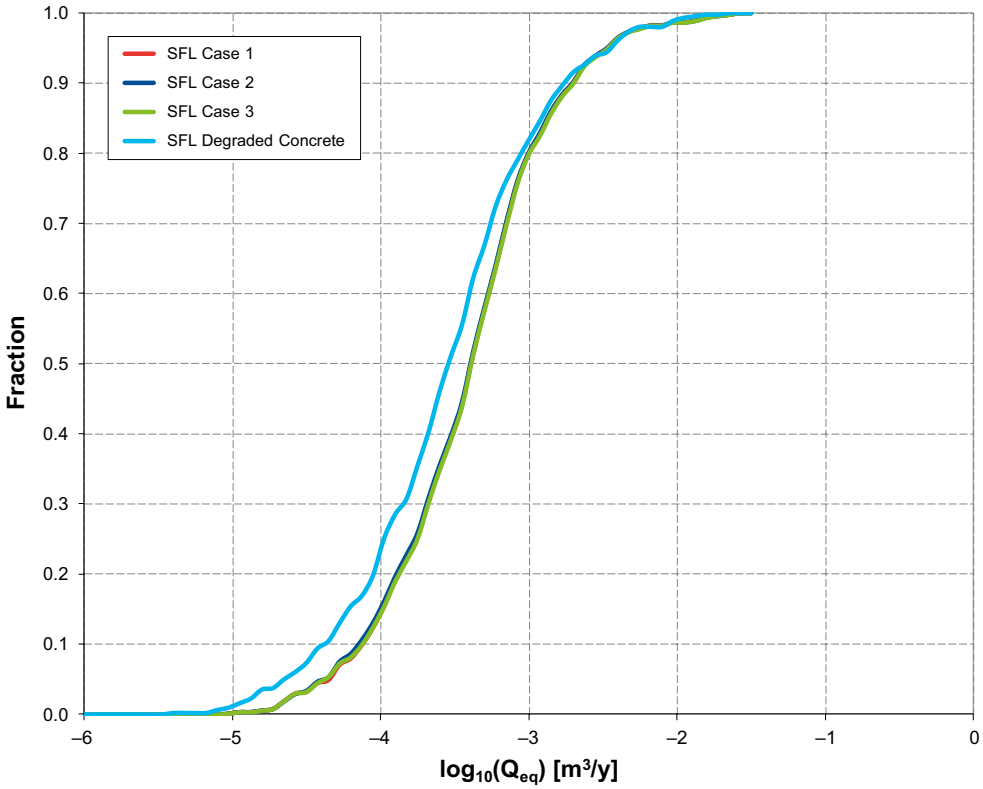

Figure 4-151. *Normalised CDF plots of equivalent flow rate (Q_{eq}) for different cases of the facility focussed model for particles successfully reaching the model top boundary (46–48 %), released at 2000 AD.*

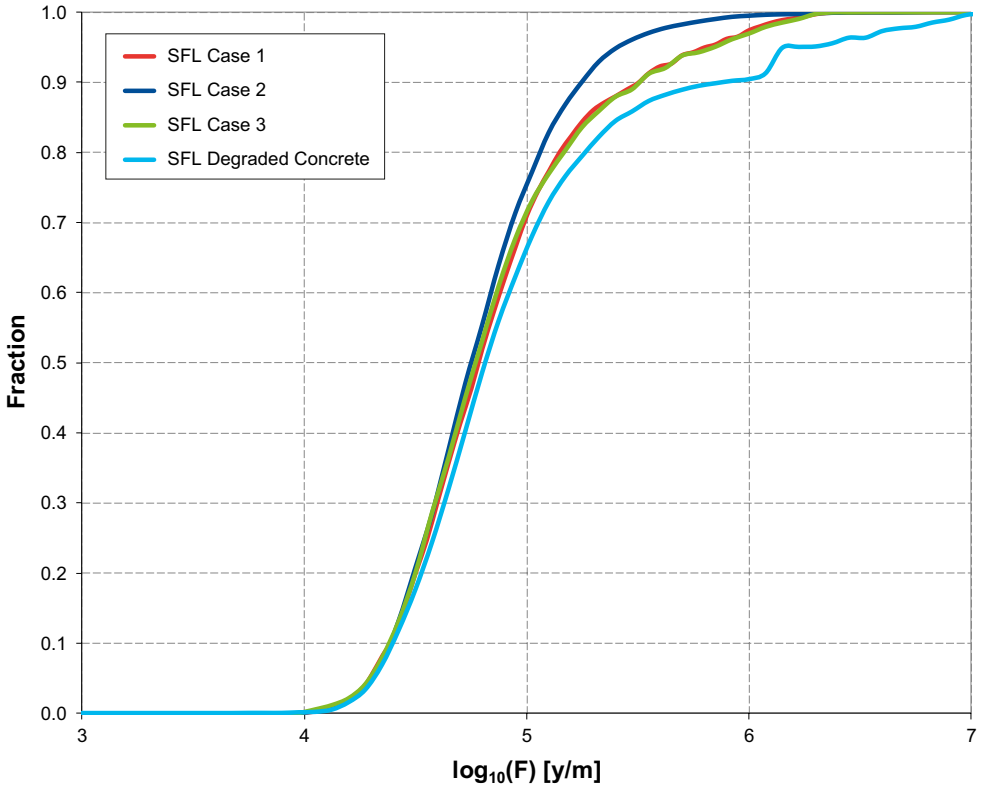

Figure 4-152. *Normalised CDF plots of flow-related transport resistance (F) for different cases of the facility focussed model for particles successfully reaching the model top boundary (46–48 %), released at 2000 AD.*

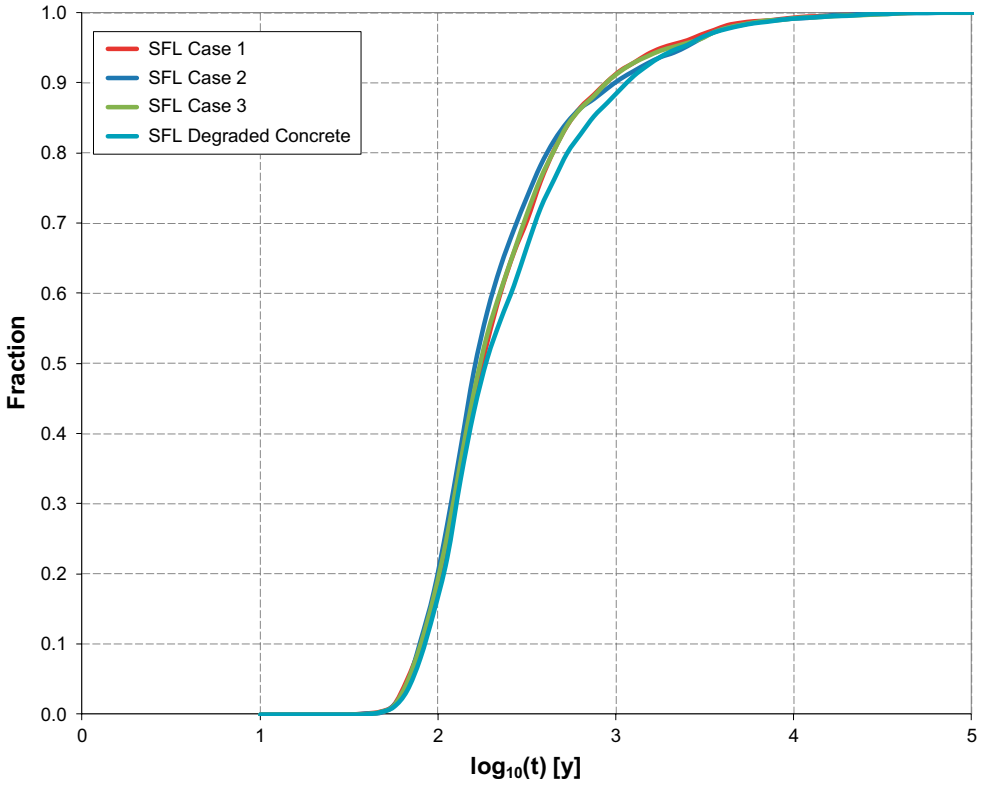

Figure 4-153. *Normalised CDF plots of travel time (t) for different cases of the facility focussed model for particles successfully reaching the model top boundary (46–48 %), released at 2000 AD.*

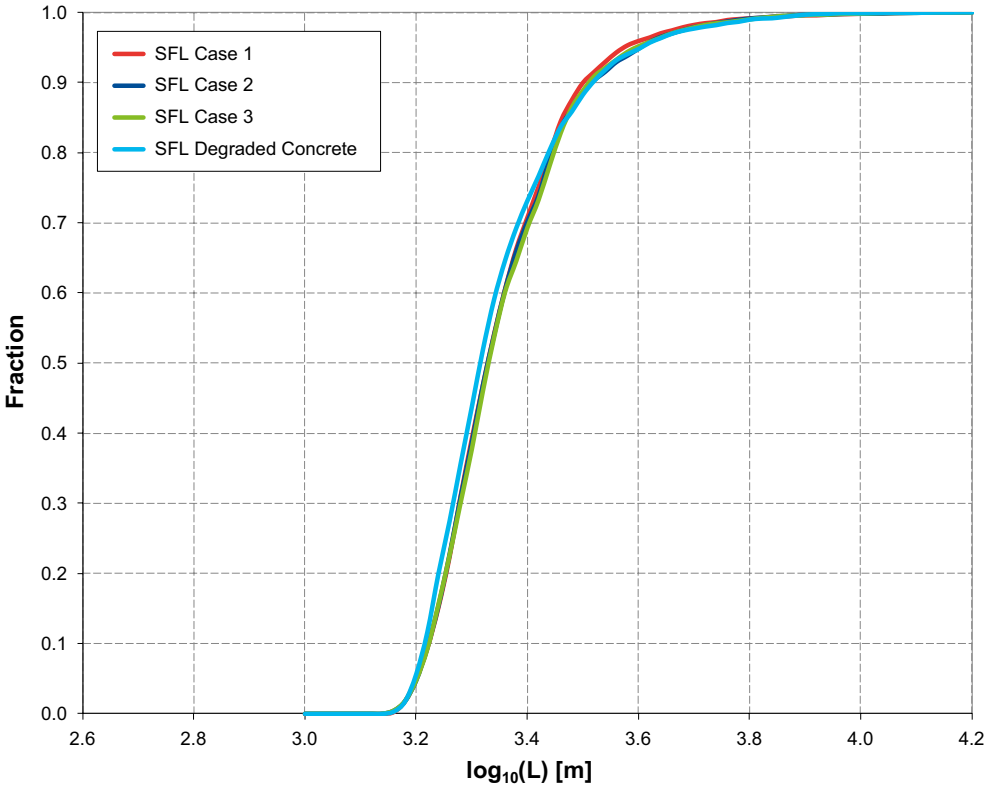

Figure 4-154. *Normalised CDF plots of path length (L) for different cases of the facility focussed model for particles successfully reaching the model top boundary (46–48 %), released at 2000 AD.*

4.7 Effect of water supply wells

4.7.1 Introduction

This section considers the effect of water supply wells on the contaminant discharge pathways from the example SFL vaults. Because water supply wells would be pumped, there will be a localised effect on the groundwater flow field near the well. Depending on the abstraction rate and the proximity of the well to any contaminant plume from SFL, then there is the potential for contaminants to either enter the well or for the plume to be deflected and concentrated, thus resulting in a change to the discharge area for the contaminants. Either of these possibilities would have consequences for the impact of the contaminants on the biosphere.

The work described here considers the effect of individual hypothetical water supply wells on groundwater flow and contaminant discharge pathways calculated by particle tracking. Specifically, the effect of the wells on particle-exit locations is examined.

4.7.2 Model description

Realisation r1 for Case 1 of the facility focussed model described in Section 3.4 was used to evaluate the effects of each well. Five models were considered, each containing a single well in a different location (denoted W1 to W5 and shown in Figure 4-155). Each well location is within a contaminant transport volume identified by the particle-tracking calculations for the particular realisation of the facility focussed model, as reported in Section 4.6.2. The wells extend vertically from the ground surface to a depth of 60 m below the ground surface and are 11.6 cm in diameter. In reality, a well would be drilled to the depth necessary to achieve a sufficient yield, so the model was checked to ensure that the modelled well intersected with a least one fracture in the flowing fracture network. The pumping rate for the abstraction of water was set to a constant 700 litres per day. Steady-state groundwater flow was calculated from the applied boundary conditions and initial conditions that were imported from the catchment focussed model for 2000 AD, as described in Section 3.4.4, with the effects of the pumping well included. Particle tracking was then carried out for particles released from the vault locations, as described in Section 3.4.4. The particles stop when they either reach the ground surface or the well.

4.7.3 Results

Exit locations

Of the five well locations considered, only well W3 was intersected by any particles. For this model, of the 4 660 particles that leave the vaults, 116 (2.5 %) intersect well W3 (Figure 4-156). However, the pumping wells will have an effect on the flow field and may cause a change in the particle pathways and ultimately the exit locations. Figure 4-157 to Figure 4-161 compare the exit locations obtained in Section 4.6.2 for Case 1 of the facility focussed model at 2000 AD (shown in red) with those obtained in the presence of a pumping well (shown in blue). There are no changes generally to the main particle discharge locations. This is to be expected, since the effect of the pumping well will be quite localised. However, there are some differences for individual particles. Particle tracking within a DFN is quite sensitive to even small changes in the groundwater flow field, since even a small perturbation at any point in a particle's path can lead to it following a different branch though the fracture network and hence to quite a different exit location.

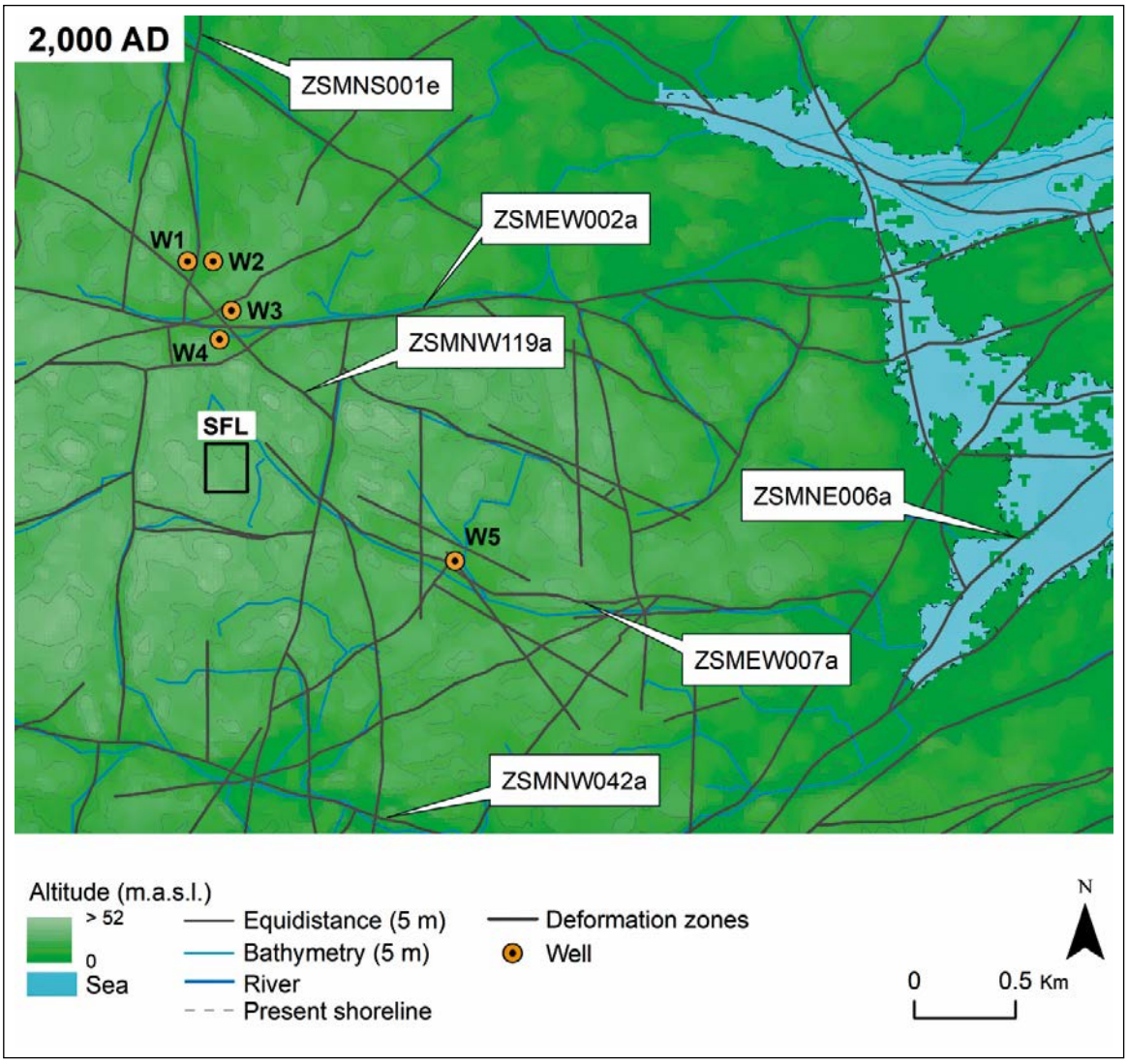

Figure 4-155. *Well locations (orange, labelled W1 to W5) at the ground surface for Case 1 of the facility focussed model at 2000 AD. The model surface is coloured by elevation (land in green, sea in blue). Rivers (blue), present shoreline (dashed grey), deformation zones at −20 m elevation (dark grey) and the SFL repository location (black) are added for context.*

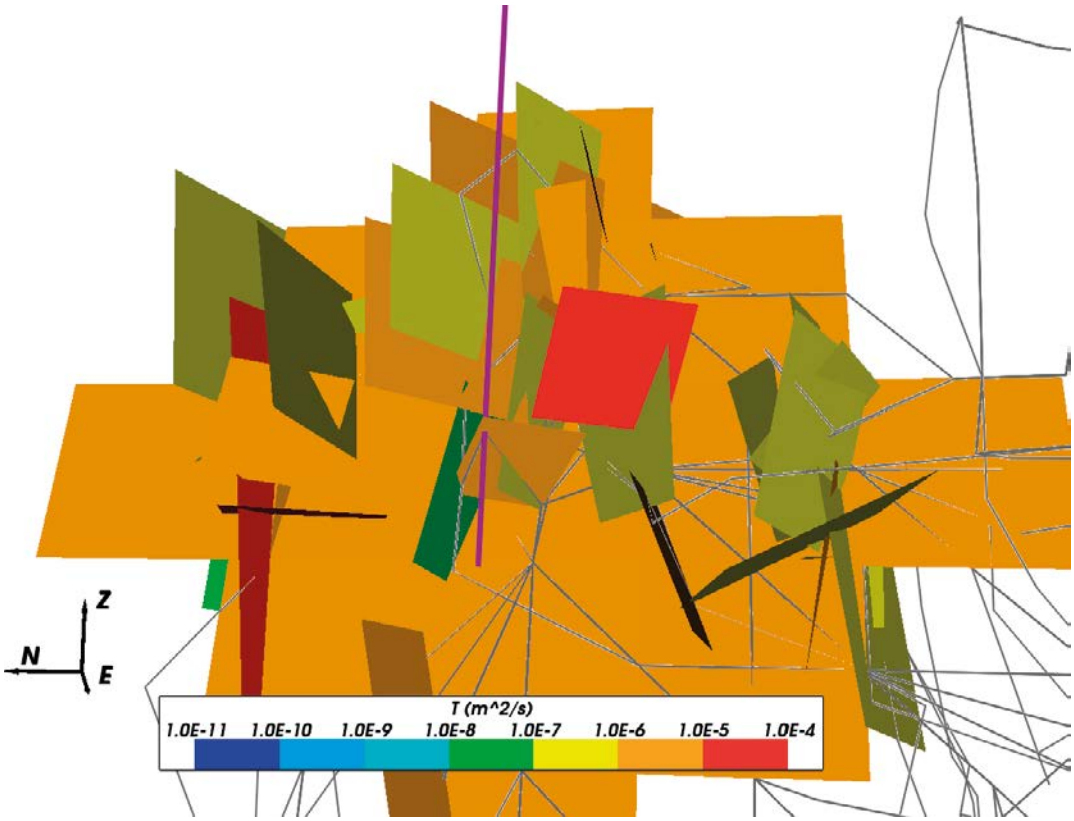

Figure 4-156. *Particle tracks intersecting well w3 (purple). Fractures are coloured by transmissivity, with some removed to reveal the well and some of the paths.*

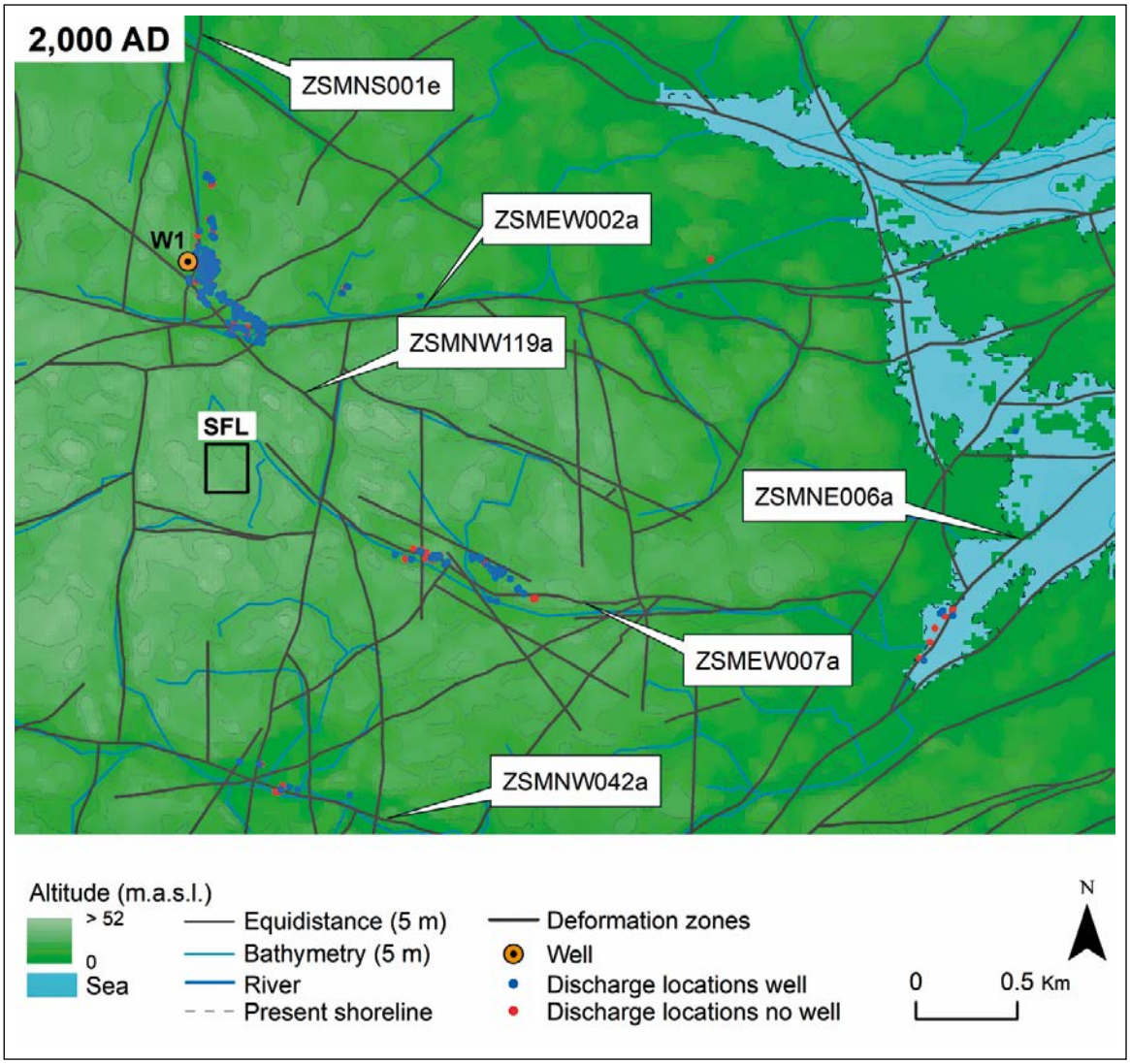

Figure 4-157. *Particle discharge locations with pumping well W1 (blue) and with no well (red) at the ground surface for Case 1 of the facility focussed model at 2000 AD. The model surface is coloured by elevation (land in green, sea in blue). Rivers (blue), present shoreline (dashed grey), deformation zones at −20 m elevation (dark grey) and the SFL repository location (black) are added for context. Well location W1 is in orange.*

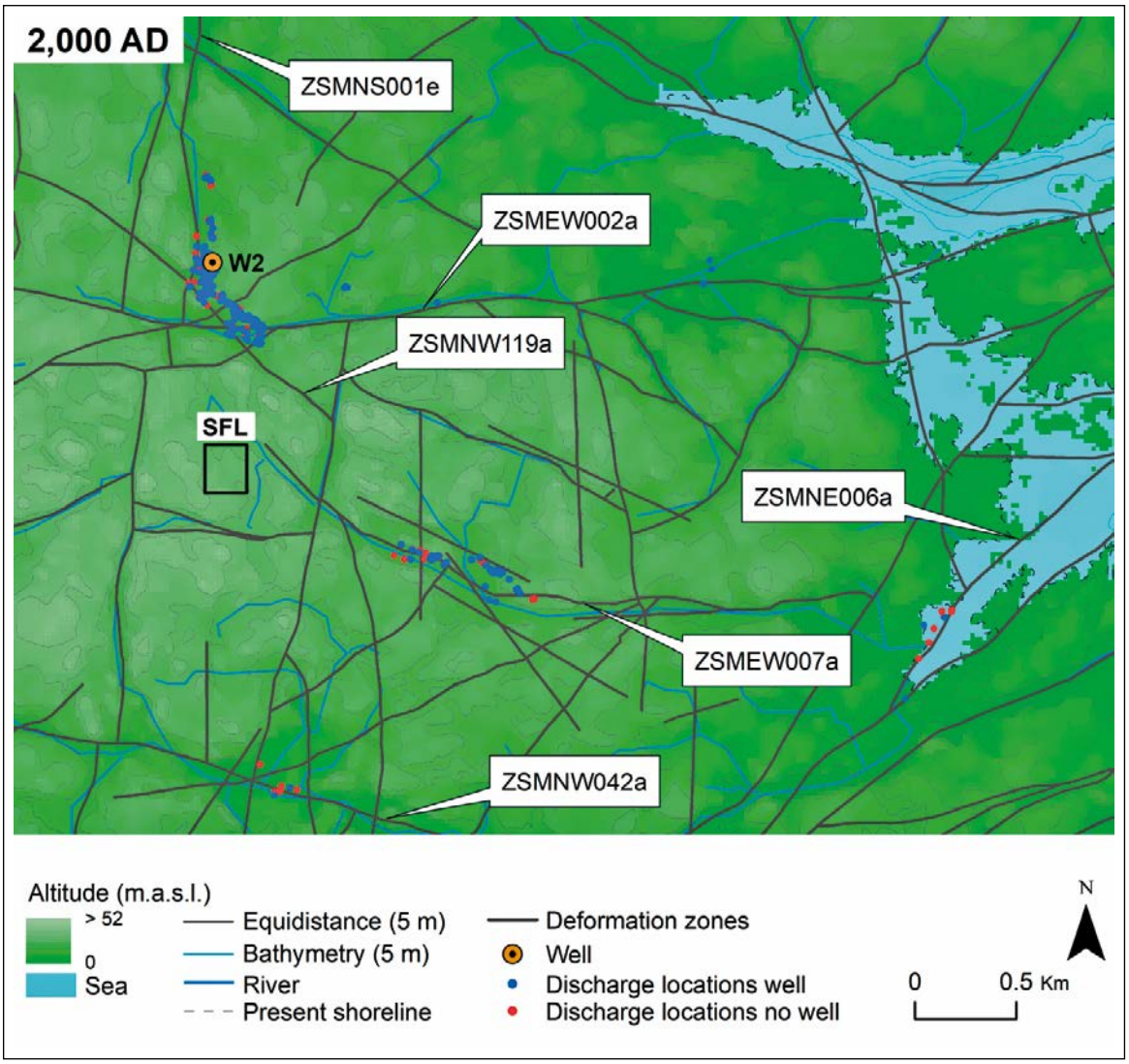

Figure 4-158. *Particle discharge locations with pumping well W2 (blue) and with no well (red) at the ground surface for Case 1 of the facility focussed model at 2000 AD. The model surface is coloured by elevation (land in green, sea in blue). Rivers (blue), present shoreline (dashed grey), deformation zones at −20 m elevation (dark grey) and the SFL repository location (black) are added for context. Well location W2 is in orange.*

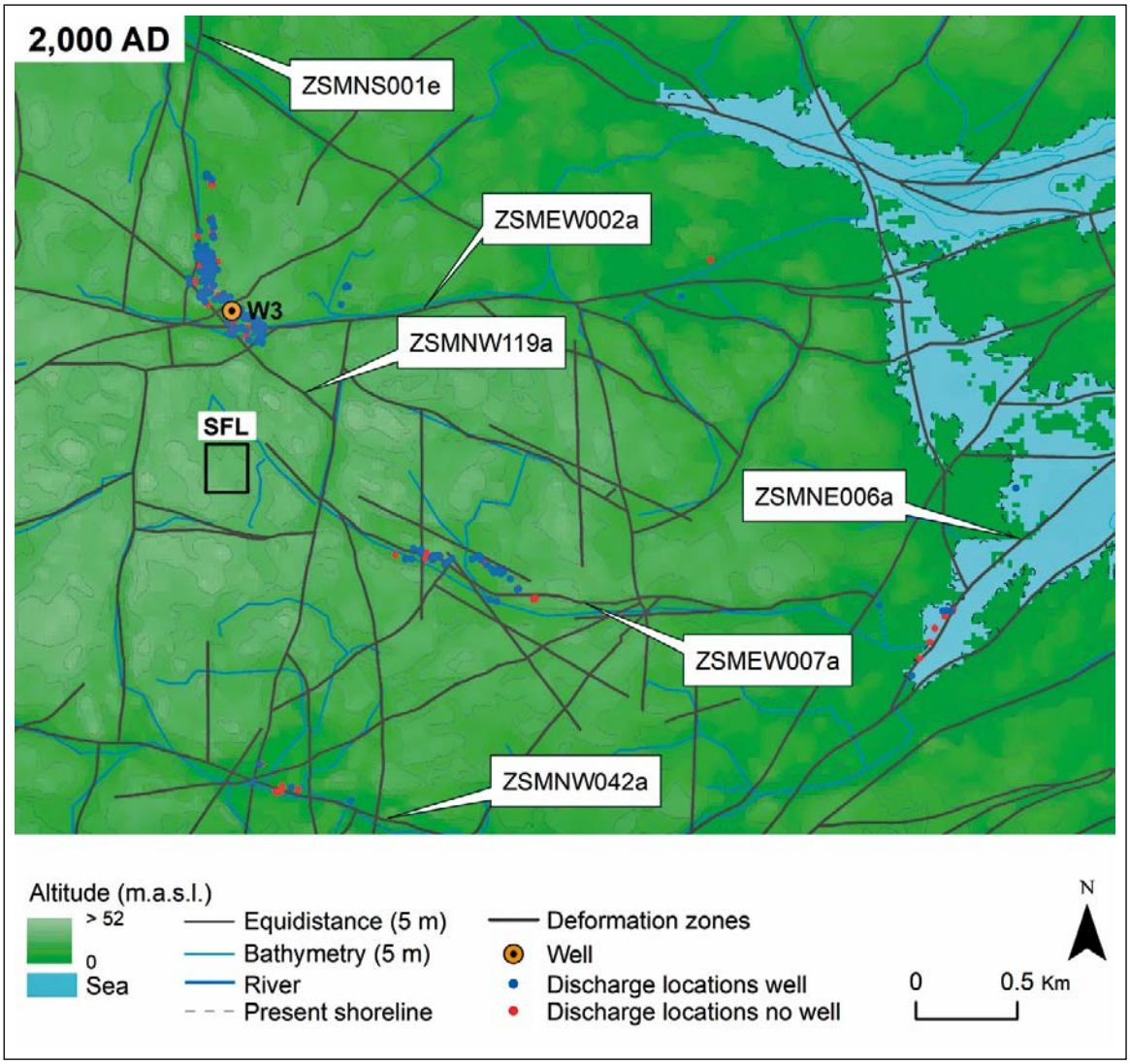

Figure 4-159. *Particle discharge locations with pumping well W3 (blue) and with no well (red) at the ground surface for Case 1 of the facility focussed model at 2000 AD. The model surface is coloured by elevation (land in green, sea in blue). Rivers (blue), present shoreline (dashed grey), deformation zones at −20 m elevation (dark grey) and the SFL repository location (black) are added for context. Well location W3 is in orange.*

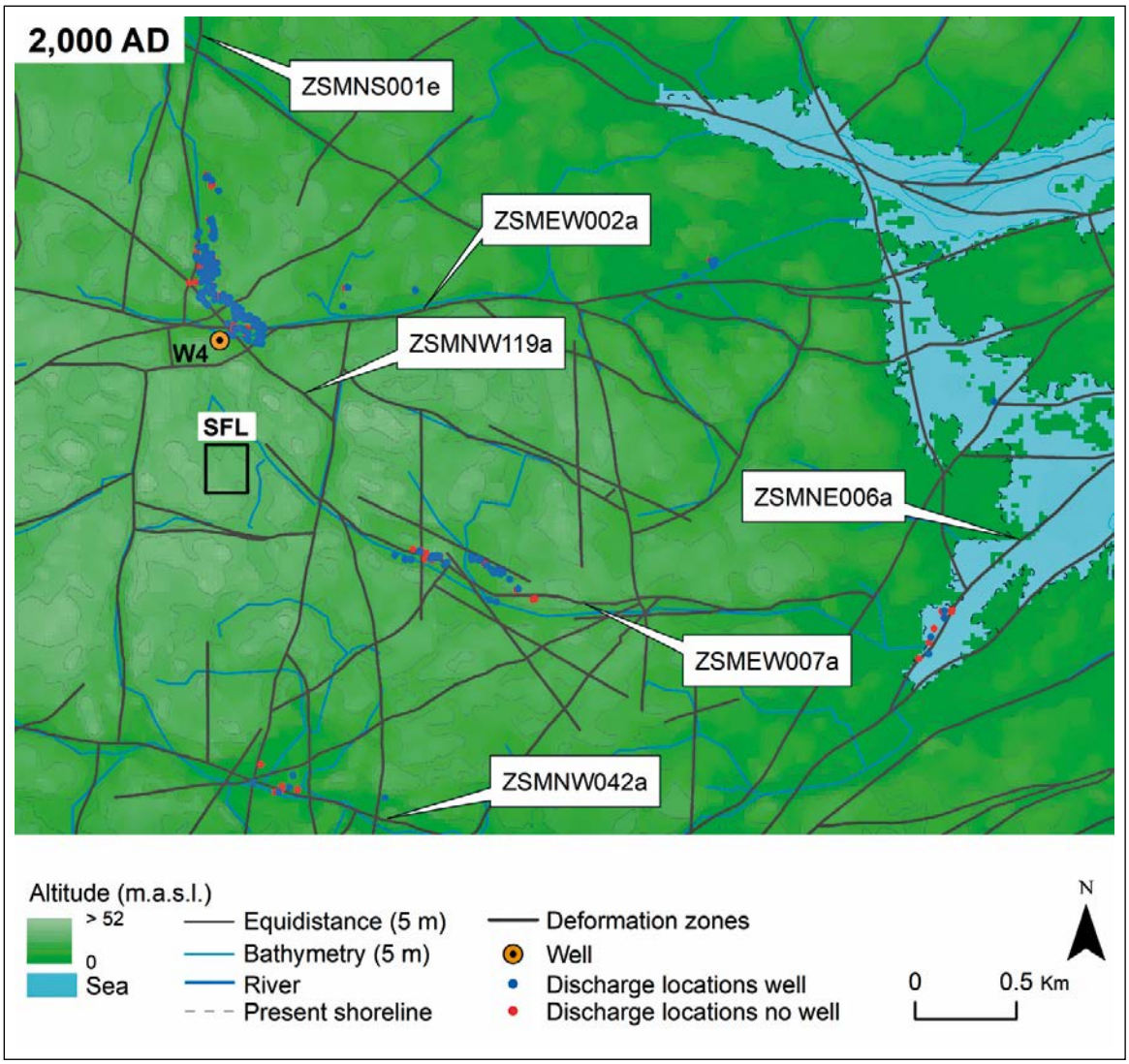

Figure 4-160. *Particle discharge locations with pumping well W4 (blue) and with no well (red) at the ground surface for Case 1 of the facility focussed model at 2000 AD. The model surface is coloured by elevation (land in green, sea in blue). Rivers (blue), present shoreline (dashed grey), deformation zones at −20 m elevation (dark grey) and the SFL repository location (black) are added for context. Well location W4 is in orange.*

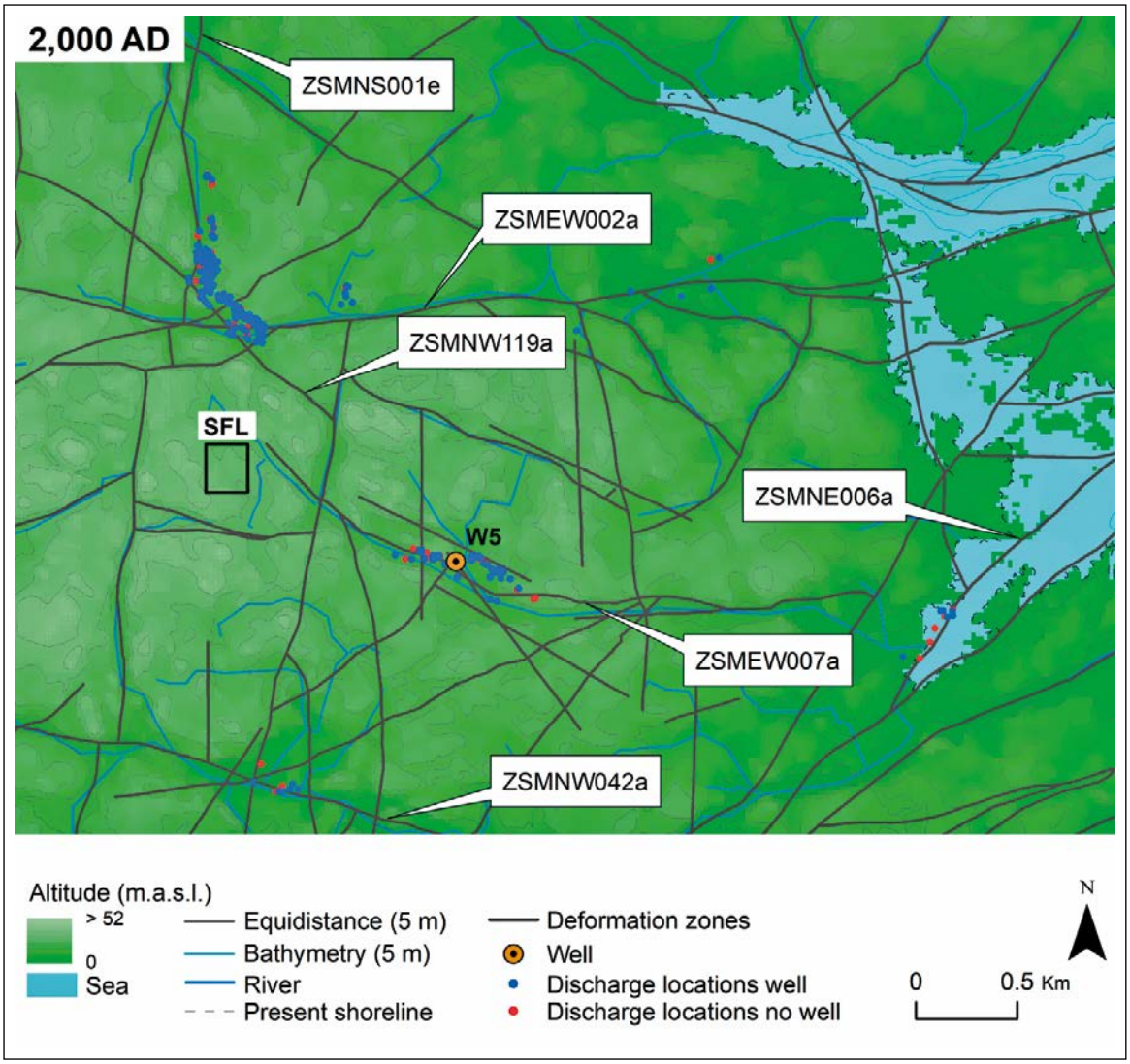

Figure 4-161. *Particle discharge locations with pumping well W5 (blue) and with no well (red) at the ground surface for Case 1 of the facility focussed model at 2000 AD. The model surface is coloured by elevation (land in green, sea in blue). Rivers (blue), present shoreline (dashed grey), deformation zones at −20 m elevation (dark grey) and the SFL repository location (black) are added for context. Well location W5 is in orange.*

Performance measures

Table 4-7 shows the performance measure statistics for the models containing each of the five wells compared with the case without wells. The performance measures are calculated as described in Section 2.2.11. As expected, the presence of a pumping well has negligible effect on the U and Q_{eq} performance measures. These performance measures are dependent on the local groundwater flow conditions around the vaults, which are unlikely to be affected to an appreciable degree by a well that is some distance away from the vaults. There is more effect seen for the F, t and L performance measures, as shown in Figure 4-162 to Figure 4-164, as these are more dependent on groundwater flow conditions distant from the vaults. However, the effects are very minor and largely restricted to the higher value tails of the performance measure distributions. This is because the effects on the groundwater flow patterns of the pumping wells are fairly localised and so are most likely to influence the relatively small proportion of the particles that pass near to a well.

Table 4-7. Performance measure statistics for Case 1, of the facility focussed model with (w1 to w5) and without (r1) a pumping well, for particles successfully reaching the model top boundary or a well, released at 2000 AD.

Performance measure	r1	w1	w2	w3	w4	w5
$\log_{10}$(U) [m^2/y]						
10th-percentile	−3.592	−3.627	−3.626	−3.627	−3.627	−3.626
Median	−2.514	−2.510	−2.510	−2.510	−2.518	−2.514
90th-percentile	−1.604	−1.582	−1.604	−1.593	−1.604	−1.604
$\log_{10}(Q_{eq})$ [m^3/y]						
10th-percentile	−4.124	−4.128	−4.124	−4.128	−4.132	−4.128
Median	−3.399	−3.397	−3.397	−3.397	−3.399	−3.399
90th-percentile	−2.720	−2.720	−2.697	−2.708	−2.720	−2.697
$\log_{10}$(F) [y/m]						
10th-percentile	4.385	4.388	4.392	4.386	4.396	4.392
Median	4.782	4.782	4.766	4.781	4.776	4.807
90th-percentile	5.505	5.312	5.237	5.522	5.244	5.562
$\log_{10}$(t) [y]						
10th-percentile	1.903	1.903	1.889	1.904	1.906	1.910
Median	2.249	2.229	2.213	2.242	2.221	2.263
90th-percentile	2.944	2.996	2.981	2.952	3.027	3.020
$\log_{10}$(L) [m]						
10th-percentile	3.222	3.224	3.222	3.223	3.224	3.227
Median	3.328	3.333	3.330	3.331	3.331	3.333
90th-percentile	3.500	3.519	3.514	3.510	3.519	3.521

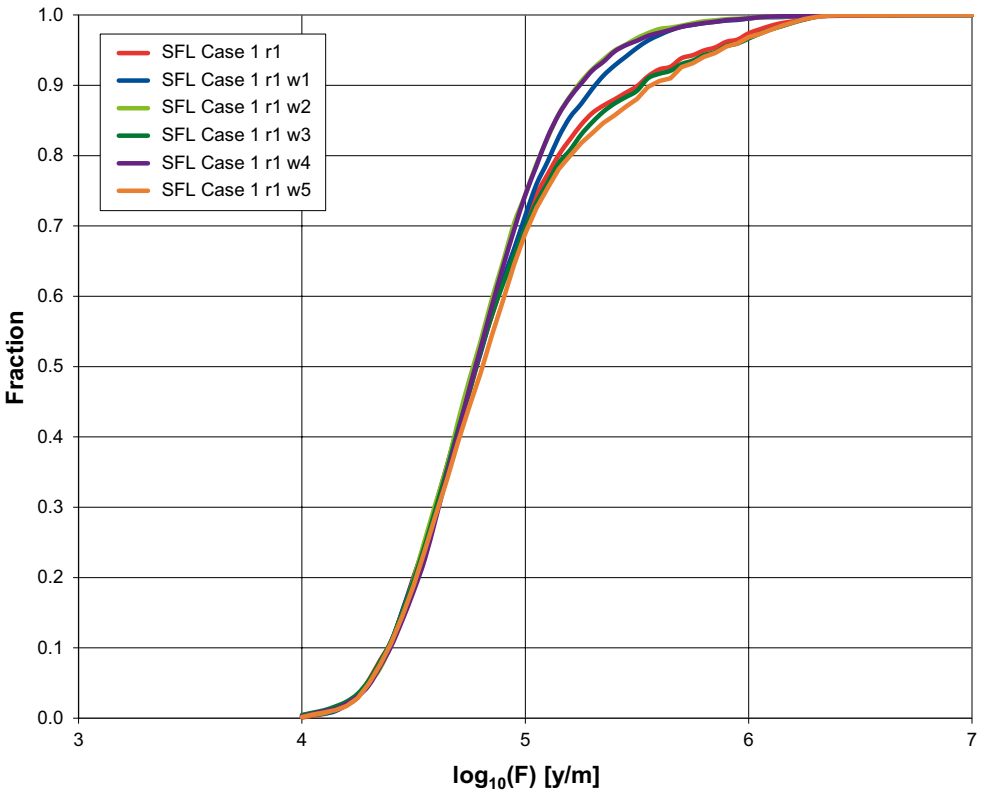

Figure 4-162. *Normalised CDF plots of flow-related transport resistance (F) for Case 1 of the facility focussed model with and without a pumping well for particles successfully reaching the model top boundary or a well, when released at 2000 AD.*

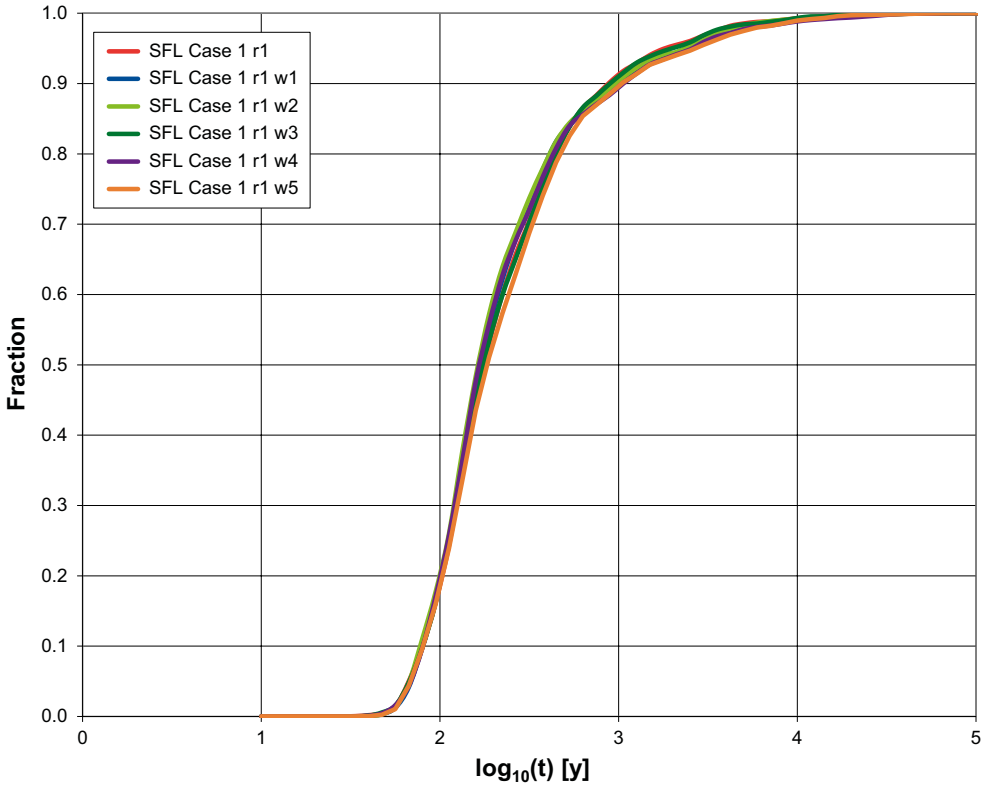

Figure 4-163. *Normalised CDF plots of travel time (t) for Case 1 of the facility focussed model with and without a pumping well for particles successfully reaching the model top boundary or a well, when released at 2000 AD.*

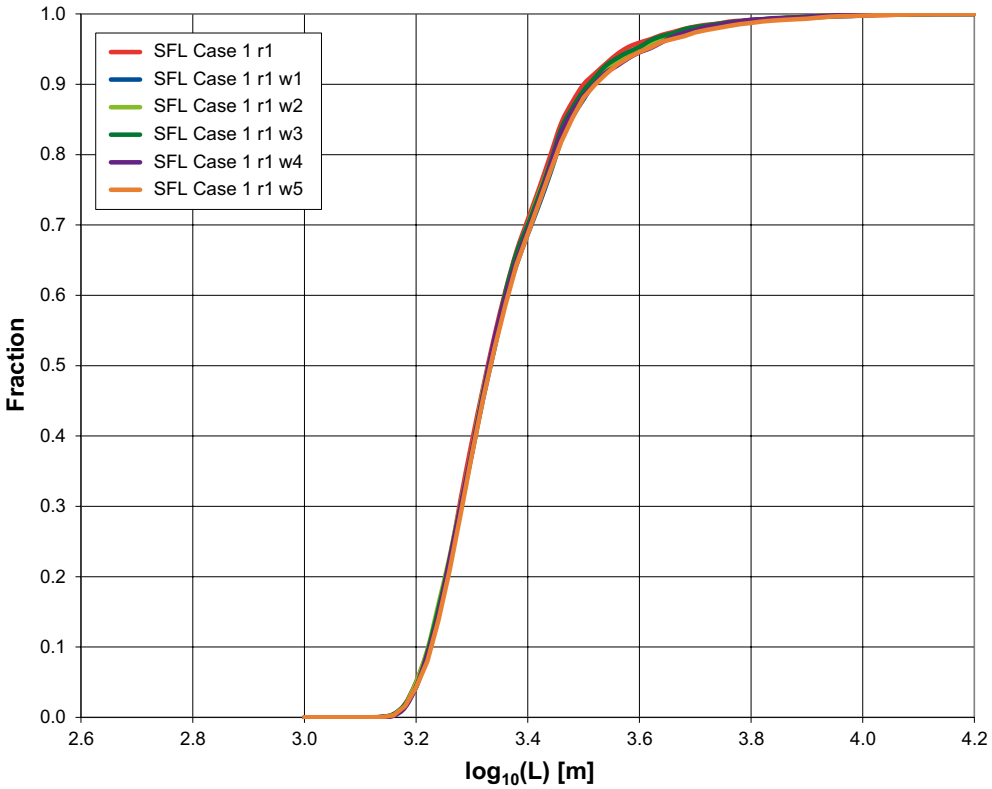

Figure 4-164. *Normalised CDF plots of path length (L) for Case 1 of the facility focussed model with and without a pumping well for particles successfully reaching the model top boundary or a well, when released at 2000 AD.*

4.7.4 Summary

This section has considered the effects on groundwater flow and particle pathways of introducing a pumping well into the SFL facility focussed model in one of five locations. The effects of the well are quite localised, but minor changes can be observed in particle-exit locations and performance measures. In one well location, w3, a small proportion of particles enter the well. The conclusion is that individual water supply wells are not likely to have a significant effect on contaminant transport pathways or discharge locations. However, there is the possibility of small amounts of contamination entering a water supply well, depending on where it is located.

5 Summary and conclusions

5.1 Methodology improvements since SR-Site

Several methodological improvements have been incorporated into SE-SFL relative to SR-Site due to advances in software capability, greater computing capacity and a desire to attain greater integration between disciplines.

The catchment focussed model uses an extended temperate period to account for potential dilution effects arising from prolonged periods of meteoric water infiltration. This prolonged period is a potential scenario resulting from climate change and leading to a delay in the onset of periglacial and glacial conditions (SKB 2010b).

The catchment focussed model also includes the effects of chemical reactions in two of the cases. These allow water-rock interactions to affect the composition of the groundwater. This influences groundwater flow and transport processes, and also the hydrogeochemical environment, which have implications for repository safety functions related to canister corrosion and integrity of engineered barrier systems.

For the facility focussed model, the main change relative to SR-Site is the merging of the site-scale and repository scale models into a single facility focussed model. This model contains the detailed representation of the backfilled repository structures as a CPM, within a surrounding facility scale DFN, which itself is embedded within a catchment scale ECPM model. This approach allows much greater integration between models and simplifies the transfer of data between scales.

The facility focussed model also includes an updated representation of the regolith that honours the layered structure of the Quaternary deposits that is more consistent with near-surface and biosphere models used elsewhere in SE-SFL. This allows particles to be treated consistently when moving from the bedrock to the biosphere. Model hydraulic properties are calibrated against time and spatially varying head measurements using recharge data provided from the surface hydrology and near-surface hydrogeology model (Bosson et al. 2009), again improving the consistency between the models.

5.2 Summary of results

Catchment focussed ECPM modelling was used to simulate the evolution of groundwater composition from 8000 BC to 60 000 AD. It was also used to calibrate and evaluate an alternative HSD model for use in the facility focussed modelling.

A sensitivity analysis was performed using the catchment focussed hydrogeological model to improve the match to the measured mean and transient heads at the locations of the percussion drilled boreholes (HLX) and groundwater monitoring wells (SSM). The results demonstrate which parameters can be modified to influence the match to observations. Within the parameter ranges considered, the potential to improve the match of modelled to measured heads was demonstrated using updated physical properties for the soil and upper bedrock of the hydrogeological model.

The catchment focussed modelling of the evolution of hydrogeochemistry shows that there are only small differences between the modelled cases, arising from differences in hydrogeochemical reactions, suggesting that the hydrogeology is dominating most of the geochemical properties of the system. Cases 2 and 3 differ only to a minor extent from Case 1 where chemical reactions were not considered. Also, no significant differences were seen between Cases 2 and 3, which suggest that the redox pathway that differentiates the two chemistry cases has a limited effect on the general groundwater evolution. The analysed chemical cases are similar enough to not significantly affect the groundwater flows.

There are significant differences between the five simulated HRD realisations that are large enough to change the calculated statistics within the analysed repository volume, see discussion below on stochastic modelling results.

The results from tracer simulations prove to be useful for the analysis of the mixing and evolution of reference waters. This information is valuable in the analysis and understanding of the results from the reactive transport simulations.

The evolution of particle-exit locations and performance measures was examined as a function of particle release time for Case 1 of the facility focussed model. The particle-exit locations are governed by the catchment scale flow pattern, but are constrained by the locations and geometries of larger conductive features, such as deformation zones. The structure of the regolith can also affect the exit locations in the near-surface environment, for instance with particles being diverted around clay volumes before discharging to the surface. Recharge to the vaults originates from above and slightly to the west, with discharge primarily to the north and southeast. Apart from at the earliest times, there are only minor changes to particle-exit locations and performance measures with release time, arising from changes in flow patterns as the shoreline recedes.

Multiple realisations of Case 1 were evaluated and the performance measures obtained from the facility focussed model showed significant variation between realisations. Specifically, the performance measures are sensitive to the presence of large sub-vertical fractures that intersect the vaults. These fractures are not present in every realisation, two of the five realisations contain such structures here, but this includes realisation r1 which was the main realisation considered. In the DFN model, these large fractures are generated as homogeneous fractures open to flow over their entire surface. This is likely a pessimistic representation of the real system, in which large fractures, greater than c. 100 m are more likely to comprise minor deformation zones of individual fractures of varying connectivity and transmissivity. Hence, the occurrence and nature of minor deformation zones is an important input from site characterisation for safety assessment and needs to be factored in operational decisions for locating and constructing vaults.

The other cases considered the effects on groundwater composition of including chemical reactions and the implications for groundwater flow, particle tracking and performance measures. The facility focussed calculations show that the relatively modest changes in groundwater composition caused by chemical reactions have little effect on performance measures. A variant of Case 1 considered the effect of degraded concrete backfill for the BHK vault. This variant did show some changes in the performance measures, particularly for U and Q_{eq}, since these are most affected by changes close to the vaults. The chemical effects of the groundwater composition on the concrete were not included in this case but could be a relevant consideration. Another variant considered the effects of water supply wells on particle pathways and concluded that, although the overall effect on performance measures and exit locations was relatively minor, there is the potential for small amounts of contamination to enter a well, depending on its location.

5.3 Recommendations

The methodology used in this work has shown how the integration between models can be improved by using consistent representations, for instance for the regolith in the groundwater flow and biosphere models. It is suggested that this approach be extended as far as possible to enhance the interfaces between different models and between different scales.

More work can be done on the calibration of the soil model properties. The match to average measured heads can probably be improved for specific boreholes and wells by changing the soil properties individually for separate soil layers and soil types within each layer. The anisotropic properties can also be further investigated to see if a better calibration can be achieved. The uncertainty associated with the characterisation and parameterisation of the upper ~50 m of bedrock due to the borehole casing may suggest the splitting of depth zone 1 into 0–50 m and 50–150 m zones. The use of an automated parameter estimation code, such as PEST (Doherty 2015), would be helpful for improving the calibration. The transient head response is not matching the measured head responses in the SSM wells and HLX boreholes very well. The reason for this is not clear and would need further work.

The numerical stability of the updated soil model needs to be improved to make use of it in the hydrogeochemical model. There are indications that small cell layer thicknesses cause convergence problems and maybe thicker cell layers can improve the numerical stability of the model. This was achieved in the site-scale model, which had greater horizontal resolution, leading to lower cell aspect ratios and reduced distortion.

The discretisation scheme needs to be adjusted for better performance and numerical stability. The facility scale domain with a dense mesh may have given a good resolution for the proposed nuclear waste repository volume considered in SR-Site. Although the SFL repository volume studied in this report is located within the densely meshed volume, it is close to the margin of the coarser catchment scale domain. This gives rise to numerical artefacts in the hydrogeochemical evolution calculations at the dense/coarse mesh interface. The mesh size should be optimised with respect to the repository location and also with respect to hydrogeochemical calculations that may require a greater resolution to produce numerically stable results as compared with the purely hydrogeological transport calculations.

The effects of the temporal resolution (time step size) on hydrogeological calculations and on chemistry in particular, need to be further investigated. Related to this, there are also parameter settings for the solver in iPhreeqc that need more optimization to improve the solution and speed in the chemistry calculations.

The performance measures calculated in the facility focussed model are rather sensitive to stochastic variation and, in particular, to the presence of large sub-vertical fractures that intersect the vaults. It would be desirable to more fully assess the stochastic variability by using more realisations. The effect of alternative representations for large structures could also be examined, for instance by considering depth-dependent properties or spatial heterogeneity, treating them effectively as minor deformation zones. Alternative representations of the deformation zones themselves could also be considered, for example as bands of fractures rather than as single surfaces.

The current work has used the ConnectFlow approximate particle tracking approach for determining particle pathways and performance measures. This method is efficient and robust, but the alternative exact particle tracking method is better able to represent the detailed flow field at a finite-element scale and produce more physically representative pathlines. The method also allows the groundwater fluxes to be examined in the immediate vicinity of the fracture intersections with the vault and produce more accurate calculations of U and Q_{eq}. Therefore, the exact particle tracking method may be a better approach for future work.

Particle tracking approaches in a DFN are useful for quickly assessing flow pathways from the vaults to the ground surface. However, they fail to fully account for mixing processes that can dilute high concentrations of radionuclides. Conversely, advection-dispersion solute transport approaches using ECPM models can overestimate dilution effects through continuous connectivity. A solute transport approach using a DFN model would maintain the limited connectivity and structural controls of a fracture model but allow for mixing of groundwater within the fractures and at fracture intersection lines, thus providing a more physical representation of radionuclide migration from the vaults to the ground surface.

References

SKB's (Svensk Kärnbränslehantering AB) publications can be found at www.skb.com/publications. SKBdoc documents will be submitted upon request to document@skb.se.

Amec Foster Wheeler, 2015. ConnectFlow, version 11.2. Harwell, UK: Amec Foster Wheeler.

Auqué L F, Gimeno M J, Gómez J B, Puigdomenech I, Smellie J, Tullborg E-L, 2006. Groundwater chemistry around a repository for spent nuclear fuel over a glacial cycle. Evoluation for SR-Can. SKB TR-06-31, Svensk Kärnbränslehantering AB.

Bosson E, Sassner M, Gustafsson L-G, J, 2009. Numerical modelling of surface hydrology and near-surface hydrogeology at Laxemar-Simpevarp. Site descriptive modelling SDM-Site Laxemar. SKB R-08-72, Svensk Kärnbränslehantering AB.

Charlton S R, Parkhurst D L, 2011. Modules based on the geochemical model PHREEQC for use in scripting and programming languages. Computers & Geosciences 37, 1653–1663.

Doherty J, 2015. Calibration and uncertainty analysis for complex environmental models: PEST: complete theory and what it means for modelling the real world. Brisbane: Watermark Numerical Computing.

Elfwing M, Evins L Z, Gontier M, Grahm P, Mårtensson P, Tunbrant S, 2013. SFL concept study. Main report. SKB TR-13-14, Svensk Kärnbränslehantering AB.

Fisher R A, 1953. Dispersion on a sphere. Proceedings of the Royal Society of London, Series A 217, 295–305.

Gimeno M, Auqué L, Gómez J, Salas J, Molinero J, 2010. Hydrogeochemical evolution of the Laxemar site. SKB R-10-60, Svensk Kärnbränslehantering AB.

Grenthe I, Stumm W, Laaksoharju M, Nilsson A C, Wikberg P, 1992. Redox potentials and redox reactions in deep groundwater systems. Chemical Geology 98, 131–150.

Hartley L, Joyce S, 2013. Approaches and algorithms for groundwater flow modeling in support of site investigations and safety assessment of the Forsmark site, Sweden. Journal of Hydrology, 500, 200–216.

Jackson C P, Hoch A R, Todman S, 2000. Self-consistency of a heterogeneous continuum porous medium representation of a fractured medium. Water Resources Research 36, 189–202.

Joyce S, Simpson T, Hartley L, Applegate D, Hoek J, Jackson P, Roberts D, Swan D, Gylling B, Marsic N, Rhén I, 2010. Groundwater flow modelling of periods with temperate climate conditions – Laxemar. SKB R-09-24, Svensk Kärnbränslehantering AB.

Joyce S, Applegate D, Appleyard P, Gordon A, Heath T, Hunter F, Hoek J, Jackson P, Swan D, Woollard H, 2014. Groundwater flow and reactive transport modelling in ConnectFlow. SKB R-14-19, Svensk Kärnbränslehantering AB.

Joyce S, Woollard H, Marsic N, Sidborn M, 2015. Future evolution of groundwater composition at Forsmark during an extended temperate period. SKB R-14-26, Svensk Kärnbränslehantering AB.

Kestin J, Khalifa H E, Corrreia R J, 1981. Tables of the dynamic and kinematic viscosity of aqueous NaCl solutions in the temperature range 20–150 ºC and the pressure range 0.1–35 MPa. Journal of Physical and Chemical Reference Data 10, 71-87.

Laaksoharju M, Smellie J, Tullborg E-L, Wallin B, Drake H, Gimeno M, Hallbeck L, Molinero J, Waber N, 2009. Bedrock hydrogeochemistry Laxemar, Site descriptive modelling SDM-Site Laxemar, SKB R-08-93, Svensk Kärnbränslehantering AB.

Parkhurst D L, Appelo C A J, 1999. User's guide to PHREEQC (version 2): a computer program for speciation, batch-reaction, one-dimensional transport, and inverse geochemical calculations. Water-Resources Investigations Report 99-4259, U.S. Geological Survey, Denver, Colorado.

Rhén I, Hartley L, 2009. Bedrock hydrogeology Laxemar. Site descriptive modelling, SDM-Site Laxemar. SKB R-08-92, Svensk Kärnbränslehantering AB.

Rhén I, Follin S, Hermanson J, 2003. Hydrological Site Descriptive Model – a strategy for its development during Site Investigations. SKB R-03-08, Svensk Kärnbränslehantering AB.

Rhén I, Forsmark T, Hartley L, Jackson C P, Roberts D, Swan D, Gylling B, 2008. Hydrogeological conceptualisation and parameterisation. Site descriptive modelling, SDM-Site Laxemar. SKB R-08-78, Svensk Kärnbränslehantering AB.

Rhén I, Forsmark T, Hartley L, Joyce S, Roberts D, Gylling B, Marsic N, 2009. Bedrock hydrogeolology. Model testing and synthesis. Site descriptive modelling, SDM-Site Laxemar. SKB R-08-91, Svensk Kärnbränslehantering AB.

SKB, 2009a. Site description of Laxemar at completion of the site investigation phase. SDM-Site Laxemar. SKB TR-09-01, Svensk Kärnbränslehantering AB.

SKB, 2009b. Thermodynamic database: SKB-09. SKBdoc 1261302 ver 3.0, Svensk Kärnbränslehantering AB.

SKB, 2010a. Comparative analysis of safety related site characteristics. SKB TR-10-54, Svensk Kärnbränslehantering AB.

SKB, 2010b. Climate and climate-related issues for the safety assessment SR-Site. SKB TR-10-49, Svensk Kärnbränslehantering AB.

Sohlenius G, Hedenström A, 2008. Description of regolith at Laxemar-Simpevarp. Site descriptive modelling, SDM-Site Laxemar. SKB R-08-05, Svensk Kärnbränslehantering AB.

Appendix A

Comparison of calculated error values for boreholes

Table A-1 through Table A-4 show comparisons between the base case and Case 6_4c, of the calculated MAE (mean absolute error) and ME (mean error) values, for percussion-drilled boreholes (HLX) (Table A-1 and Table A-2) and groundwater monitoring wells (SSM) (Table A-3 and Table A-4).

Table A-1. A comparison of Mean absolute error (MAE) and Mean error (ME) in the first set of percussion-drilled boreholes (HLX) for the base case and Case 6_4c.

	Base case		Case 6_4c	
ID borehole	MAE	ME	MAE	ME
HAV02.1b	4.27	−4.27	1.57	−1.57
HAV05.1b	5.36	−5.36	2.95	−2.95
HAV06.1	7.01	−7.01	0.90	−0.88
HAV06.2	1.89	1.07	7.08	7.08
HAV07.1	9.67	−9.67	6.19	−6.19
HLX01.1b	3.07	−3.07	2.47	2.47
HLX02.1	0.91	0.83	3.29	3.29
HLX06.1	0.85	0.61	5.70	5.70
HLX07.1	0.26	−0.03	2.94	2.94
HLX08.1	1.93	−1.93	0.68	−0.68
HLX09.1b	0.90	−0.90	0.92	−0.92
HLX09.2b	0.54	0.16	0.55	0.08
HLX11.1	5.40	−5.40	1.54	1.25
HLX11.2	5.41	−5.41	1.67	1.40
HLX13.1	5.63	−5.63	2.13	0.18
HLX14.1	4.52	−4.52	1.11	1.04
HLX15.1	3.95	−3.95	1.73	−1.73
HLX16.1	3.36	−3.36	0.98	0.98
HLX17.1	4.30	−4.30	0.50	−0.05
HLX18.1	4.36	−4.36	0.42	−0.40
HLX18.2	3.96	−3.96	0.30	−0.24
HLX19.1	5.35	−5.35	1.48	−1.48
HLX20.1	0.88	−0.65	4.43	4.30
HLX21.1a	3.24	−3.24	2.74	2.74
HLX21.1b	2.88	−2.88	3.08	3.08
HLX21.1c	3.41	−3.41	2.79	2.79
HLX21.1d	2.49	−2.49	3.57	3.57
HLX21.1e	3.26	−3.26	3.00	3.00
HLX21.2b	3.43	−3.43	2.38	2.38
HLX21.2c	3.22	−3.22	2.58	2.58
HLX22.1b	2.22	−2.22	2.57	2.56
HLX22.1c	2.56	−2.56	3.12	3.12
HLX22.2	4.30	−4.30	1.50	1.48
HLX23.1	4.61	−4.61	1.49	1.49
HLX23.2	4.62	−4.62	1.36	1.36
HLX24.1a	4.91	−4.91	0.73	0.73
HLX24.1b	4.45	−4.45	1.18	1.18
HLX24.1c	4.61	−4.61	1.37	1.37

Table A-2. A comparison of Mean absolute error (MAE) and Mean error (ME) in the second set of percussion-drilled boreholes (HLX) for three different cases.

	Base case		Case 6_4c	
ID borehole	MAE	ME	MAE	ME
HLX24.2b	4.06	−4.06	1.89	1.89
HLX25.1a	5.02	−5.02	0.39	0.39
HLX25.1b	5.68	−5.68	0.85	0.24
HLX25.2b	5.13	−5.13	0.95	0.46
HLX26.1	5.48	−5.48	3.34	−3.34
HLX27.1a	4.64	−4.64	3.75	−3.75
HLX27.1b	4.64	−4.64	3.17	−3.17
HLX27.2	4.24	−4.24	3.31	−3.31
HLX28.1	1.40	1.40	2.52	2.52
HLX30.1a	5.24	−5.24	0.31	−0.30
HLX30.1b	5.59	−5.59	0.44	−0.06
HLX30.2b	5.08	−5.08	0.52	0.27
HLX31.1a	5.20	−5.20	0.22	−0.09
HLX31.1b	5.11	−5.11	0.63	0.20
HLX31.2	4.79	−4.79	0.33	0.14
HLX32.1	4.97	−4.97	4.18	−4.18
HLX33.1	4.81	−4.81	0.60	0.60
HLX33.2	4.71	−4.71	0.44	0.41
HLX34.1	3.84	−3.84	2.59	2.51
HLX35.1	4.10	−4.10	2.06	2.05
HLX35.2	5.48	−5.48	0.75	0.73
HLX36.1a	3.58	−3.58	1.47	−1.47
HLX36.1b	0.31	−0.26	1.77	1.75
HLX36.2	3.72	−3.72	1.45	−1.45
HLX37.1a	1.44	−1.38	1.35	0.58
HLX37.1b	1.44	−1.44	1.36	1.04
HLX37.2	1.05	−1.05	1.34	1.01
HLX37.3	0.67	0.61	2.61	2.61
HLX38.1	5.91	−5.91	4.86	−4.86
HLX39.1	5.13	−5.13	2.08	2.06
HLX40.1	4.88	−4.88	3.00	3.00
HLX41.1	3.25	−3.25	4.50	4.50
HLX43.1	2.52	−2.52	2.45	2.45
HLX43.2	0.71	0.00	5.46	5.46
HSH01.1	1.35	−1.35	0.35	−0.16
HSH01.2	1.39	−1.39	0.34	−0.16
HSH02.1	3.79	−3.79	0.57	−0.49
HSI04.1	1.56	−1.56	2.69	2.69
HSI13.1	1.65	1.65	3.79	3.79

Table A-3. A comparison of Mean absolute error (MAE) and Mean error (ME) in the first set of groundwater monitoring wells (SSM) for three different cases.

	Base case		Case 6_4c	
ID well	MAE	ME	MAE	ME
SSM000001	0.78	−0.78	0.80	0.76
SSM000002	1.85	−1.85	0.17	−0.03
SSM000004	0.84	−0.84	2.35	2.35
SSM000005	1.57	1.57	5.15	5.15
SSM000008	2.81	−2.81	2.17	2.17
SSM000009	3.04	−3.04	1.99	1.99
SSM000011	0.85	−0.82	4.19	4.19
SSM000012	4.36	−4.36	0.60	−0.60
SSM000014	2.41	−2.41	0.77	−0.77
SSM000017	3.15	−3.15	0.18	−0.13
SSM000018	5.43	−5.43	1.60	−1.60
SSM000019	3.49	−3.49	1.27	1.27
SSM000021	5.26	−5.26	0.45	0.35
SSM000022	3.78	−3.78	0.54	0.51
SSM000027	7.72	−7.72	8.54	−8.54
SSM000028	5.63	−5.63	6.12	−6.12
SSM000029	4.28	−4.28	1.32	−1.32
SSM000030	6.87	−6.87	3.55	−3.55
SSM000031	3.91	−3.91	0.21	0.00
SSM000032	2.96	−2.96	1.77	−1.77
SSM000033	0.67	−0.67	1.97	1.97
SSM000034	0.21	−0.09	0.34	−0.33
SSM000035	4.58	−4.58	0.35	−0.30
SSM000037	6.60	−6.60	0.41	−0.40
SSM000039	4.90	−4.90	1.96	1.96
SSM000040	3.72	−3.72	1.32	−1.32
SSM000041	6.83	−6.83	4.93	−4.93
SSM000042	5.45	−5.45	2.34	−2.34
SSM000209	1.66	−1.66	3.64	3.64
SSM000210	0.73	−0.64	4.64	4.64
SSM000211	3.35	−3.35	2.55	2.55
SSM000212	1.18	−1.18	4.99	4.99
SSM000213	1.99	−1.99	4.16	4.16
SSM000215	5.35	−5.35	4.76	−4.76
SSM000218	1.07	0.88	7.60	7.60
SSM000219	1.55	−1.55	5.09	5.09
SSM000220	2.89	−2.89	2.66	2.66
SSM000221	2.89	−2.89	2.64	2.64

Table A-4. A comparison of Mean absolute error (MAE) and Mean error (ME) in the second set of groundwater monitoring wells (SSM) for three different cases.

	Base case		Case 6_4c	
ID well	MAE	ME	MAE	ME
SSM000222	5.85	−5.85	0.41	0.40
SSM000223	5.74	−5.74	0.47	0.45
SSM000224	3.66	−3.66	0.28	0.23
SSM000225	3.65	−3.65	0.28	0.24
SSM000226	2.02	−2.02	2.84	2.84
SSM000227	2.13	−2.13	2.71	2.71
SSM000228	4.73	−4.73	0.70	0.70
SSM000229	3.48	−3.48	1.94	1.94
SSM000230	4.62	−4.62	0.99	−0.99
SSM000237	1.84	−1.84	3.30	3.30
SSM000238	0.34	−0.32	0.38	−0.36
SSM000239	0.85	0.85	0.16	−0.06
SSM000240	0.45	0.44	0.16	−0.07
SSM000241	0.54	−0.54	0.58	−0.58
SSM000242	3.37	−3.37	1.88	−1.88
SSM000243	4.43	−4.43	4.91	−4.91
SSM000244	4.15	−4.15	1.29	−1.29
SSM000245	1.48	−1.48	1.19	−1.19
SSM000246	3.40	−3.40	1.26	−1.26
SSM000249	1.83	1.83	7.78	7.78
SSM000250	0.85	−0.85	4.93	4.93
SSM000252	2.92	−2.92	3.13	3.13
SSM000253	2.88	−2.88	3.15	3.15
SSM000255	6.26	−6.26	6.04	−6.04
SSM000256	4.57	−4.57	0.18	0.15
SSM000257	4.29	−4.29	0.17	0.15
SSM000260	6.82	−6.82	3.36	−3.36
SSM000261	6.80	−6.80	3.41	−3.41
SSM000262	4.70	−4.70	0.57	0.57
SSM000263	6.23	−6.23	4.35	−4.35
SSM000264	0.49	−0.33	5.96	5.96
SSM000265	4.14	−4.14	1.38	1.38
SSM000266	4.13	−4.13	1.42	1.42
SSM000267	1.12	1.12	6.75	6.75
SSM000268	2.94	−2.94	1.25	−1.11
SSM000269	1.12	1.12	3.97	3.97
SSM000270	0.84	−0.84	2.03	2.03
SSM000271	1.80	1.80	4.90	4.90

Appendix B

Derivation of Performance Measure Equations

Analytic solutions can be used in several cases to give good representations of radionuclide migration in regions with small dimensions without incurring the computational costs of a finely discretised numerical model. One such case is that of radionuclide migration from a bentonite or concrete-filled vault into a fracture carrying flow that intersects the vault. This is represented in terms of the following analytic solution.

Radionuclide migration is considered for constant uniform flow u parallel to the x-axis in the region

$0 \le x \le L_f$

$0 \le y \le e_f$

$0 \le z \le \infty$

shown in Figure B-1, which represents a parallel-sided fracture with aperture e_f, with the concentration held at some value c_0 on z=0, which represents the interface between the back-filled vault, where there is no flow, and the water flowing in the fracture.

The equation that represents advection and diffusion of a solute migrating in the domain is

$$\frac{\partial c}{\partial t} + u\frac{\partial c}{\partial x} = D_w\left(\frac{\partial^2 c}{\partial x^2} + \frac{\partial^2 c}{\partial y^2} + \frac{\partial^2 c}{\partial z^2}\right) \qquad \text{(B-1)}$$

where

- u is flow,
- c is concentration,
- t is time,
- D_w is the diffusion coefficient for the solute.

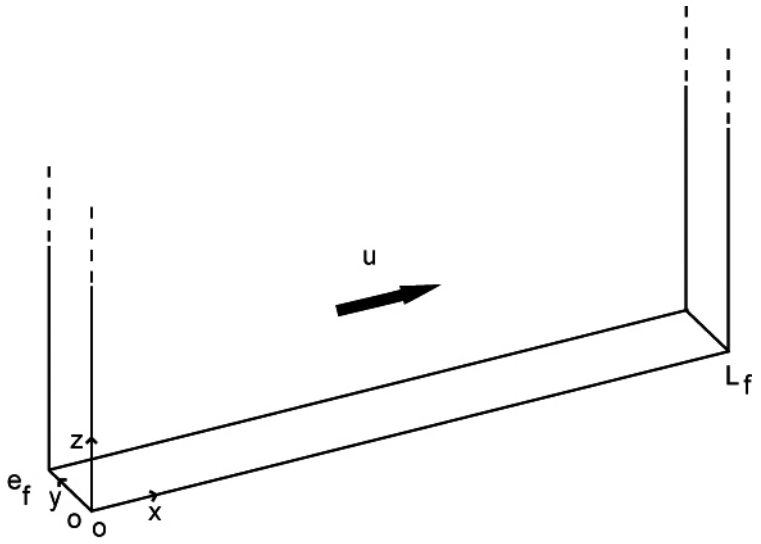

Figure B-1. *Domain for analytic solution.*

In the case of interest, the first term on the right-hand side is relatively small and can be neglected and the second term on the right-hand side is zero. Then, for steady state, the equation reduces to

$$u\frac{\partial c}{\partial x} = D_w \frac{\partial^2 c}{\partial z^2} \tag{B-2}$$

which is essentially the 1D diffusion equation with x/u taking the role of time. The solution to this for the case of interest is well known and is

$$c = c_0 erfc\left(\frac{z}{2\sqrt{D_w\, x/u}}\right) \tag{B-3}$$

where

$$erfc(\xi) = 1 - \frac{2}{\sqrt{\pi}}\int_0^{\xi} e^{-\zeta^2}\, d\zeta$$

is the complementary error function.

The total quantity of solute in the water at $x = L_f$ is

$$\int_0^{\infty} dz e_f c_0 erfc\left(\frac{z}{2\sqrt{D_w L_f/u}}\right) \tag{B-4}$$

On changing variables to

$$\xi = \frac{z}{2\sqrt{D_w L_f/u}}$$

and integrating by parts, this can be written as

$$\left[e_f c_0 2\sqrt{D_w L_f/u}\,\xi erfc(\xi)\right]_0^{\infty} + e_f c_0 2\sqrt{D_w L_f/u}\int_0^{\infty} d\xi\xi\frac{2}{\sqrt{\pi}}e^{-\xi^2} = e_f c_0 2\sqrt{\frac{D_w L_f/u}{\pi}} \tag{B-5}$$

Hence the flux of solute out of the domain can be expressed as $Q_{eq}c_0$, where

$$Q_{eq} = u e_f \sqrt{\frac{4D_w L_f/u}{\pi}} \tag{B-6}$$

Various approximations have been made in this. Firstly, the flow has been taken to be independent of y. In reality, there would be a parabolic variation of the flow with y within a fracture. It can be shown that, asymptotically, diffusion in such a flow field approximates to diffusion in the constant flow field with an enhanced diffusion coefficient (this is so-called Taylor dispersion). The flow field has also been taken to be 1D and unaffected by the presence of the vault. The 1D approximation is reasonable provided that the radius of the vault is large compared to the effective distance over which the solute diffuses.

In this case, several fractures intersect a vault containing waste packages surrounded by bentonite or concrete (Figure B-2). The approximation is made that the concentration on the interface between the backfill and the water flowing in the fracture is the same for all fractures. Taking the fractures to be square, with uniform flow aligned with one of the axes, the flow velocity in a fracture is given by

$$u_f = \frac{Q_f}{e_f\sqrt{a_f}} \tag{B-7}$$

where

- Q_f is the water flux in the fracture [m^3/y];
- a_f is the area of the fracture (and so $\sqrt{a_f}$ is the length of a side) [m^2];
- e_f is the aperture of the fracture [m].

Then, using the analysis derived above, the total flux of solute into the fractures is given by $Q_{eq}c_0$ where

$$\boldsymbol{Q_{eq} = \sqrt{\frac{4D_w \sum_f (q_f L_f e_f)}{\pi}}} \tag{B-8}$$

where L_f is the length of the intersection of the vault with the fracture [m] and q_f is the area weighted flow rate per unit length [m^2/y]

$$\boldsymbol{q_f} = \frac{\sum_i (\boldsymbol{q_i a_i})}{\sum_i \boldsymbol{a_i}} \tag{B-9}$$

The equivalent Darcy flux near the vault is given by

$$\boldsymbol{U} = \frac{\sum_f (\boldsymbol{q_f L_f})}{\sum_f \boldsymbol{L_f}} \tag{B-10}$$

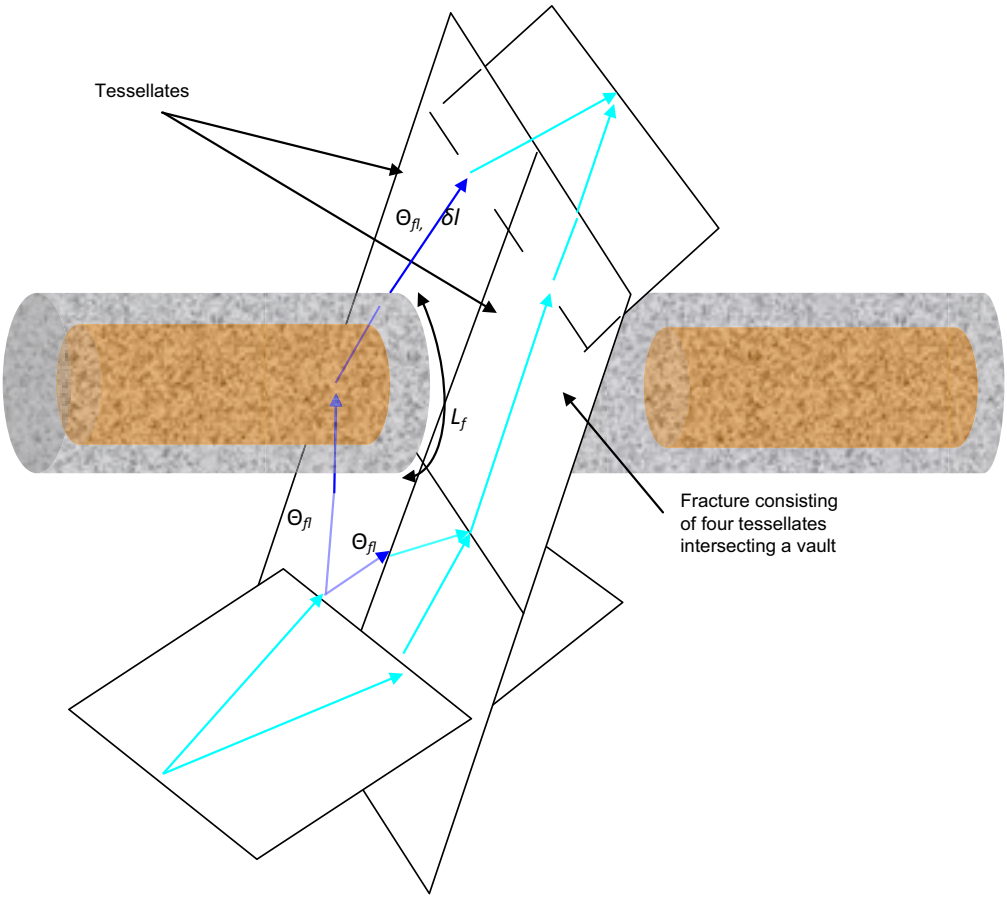

Figure B-2. *Tessellated fracture intersecting a vault. Dark blue arrows are flows included in the calculation of Q_{eq}, but light blue arrows represent flows that are not included.*

Appendix C

Data deliveries

C.1 Catchment focussed model

For the catchment focussed model, the main data deliveries are the model properties and groundwater composition calculated at the centre of each model cell for each case at selected time slices. The exported data is in ConnectFlow *.val* format. This is a simple space-separated text file, where the first line contains the column headers. Each subsequent line contains the coordinates and exported data at one selected point. In this case, the selected points correspond to the centres of the model cells. Each value in the data line is associated with the corresponding column heading. Each column is described in Table C-1.

Table C-1. Description of columns in catchment focussed model data delivery.

Column name	Description
POINT_NUM	The point index number.
X	The X-coordinate of the point [m].
Y	The Y-coordinate of the point [m].
Z	The Z-coordinate of the point [m].
PRES	The residual pressure (see Section 2.2.6) [N/m^2].
TEMP	The temperature [°C].
Al	The mass fraction of aluminium [kg/kgs].
Br	The mass fraction of bromide [kg/kgs].
C	The mass fraction of inorganic carbon [kg/kgs].
Ca	The mass fraction of calcium [kg/kgs].
Cl	The mass fraction of chloride [kg/kgs].
F	The mass fraction of fluoride [kg/kgs].
Fe	The mass fraction of iron [kg/kgs].
K	The mass fraction of potassium [kg/kgs].
Li	The mass fraction of lithium [kg/kgs].
Mg	The mass fraction of magnesium [kg/kgs].
Mn	The mass fraction of manganese [kg/kgs].
Na	The mass fraction of sodium [kg/kgs].
S	The mass fraction of sulphur [kg/kgs].
Si	The mass fraction of silicon [kg/kgs].
Sr	The mass fraction of strontium [kg/kgs].
O	The mass fraction of oxygen not included in H_2O [kg/kgs].
H	The mass fraction of hydrogen not included in H_2O [kg/kgs].
E	Charge balance [-].
pH	Acidity [-].
pE	Negative log of the conventional activity of the electron [-].
RHOF	The fluid density [kg/m^3].
AMU	The fluid viscosity [kg/m/s]
QDARCY	The Darcy flux [m/s].
KXX	The XX-component of the permeability tensor [m^2].
KYY	The YY-component of the permeability tensor [m^2].
KZZ	The ZZ-component of the permeability tensor [m^2].
POROS	Kinematic porosity [-].

C.2 Facility focussed model

C.2.1 Particle summary file

For the facility focussed model, the main data deliveries are the particle-exit locations and path properties. The exported data is in ConnectFlow PTABLE (.ptb) format. This is a simple space-separated text file, starting with a header and then a line containing the column names. Each subsequent line contains the start and end coordinates and path data for each released particle. Each value in the data line is associated with the corresponding column heading. Each column is described in Table C-2 and corresponding performance measures are described in Section 2.2.11. The header lines are:

```
# PARAMETER TABLE FILE FROM CONNECTFLOW
#
# NUMBER OF COLUMNS DEFINED
<number of columns>
# NUMBER OF TIMES THEY ARE USED
<number of rows> <number of rows> <number of rows>
# HOW MANY TIMES THEY COULD BE USED
<number of rows> <number of rows> <number of rows>
# THE PARAMETER TABLE:
```

The column names are:

```
# POINT     XS          YS          ZS          XE          YE
ZE          OKFLAG      T0          U0          QEQ         TW
F           L           TRAPP       TW_TUN      L_TUN       TW_CPM
L_CPM       UR          QEQR        LR_TUN      TR_TUN      FLOW
DIP         STRIKE      INTL        XINTC       YINTC       ZINTC
XINTS       YINTS       ZINTS       XINTE       YINTE       ZINTE
```

Table C-2. Description of columns in the facility focussed PTABLE (.ptb) data delivery.

Column name	Description
POINT	Particle number.
XS, YS, ZS	X, Y, Z-coordinates of start point [m].
XE, YE, ZE	X, Y, Z-coordinates of end point [m].
OKFLAG	Indicates whether or not a particle reached the model boundary: • 0 = reached the top boundary, • 1 = failed to start due to no fracture with an outflow from the vault, • 2 = ran out of time steps, • 3 = stuck, • 4 = oscillating between DFN and CPM, • 5 = reached a side boundary or the bottom boundary.
T0	Release time [y].
U0	Initial equivalent flux [m/y] (Equation (B-7)).
QEQ	Equivalent groundwater flow rate [m^3/y] (Equation (B-6)).
TW	Travel time in the DFN [y].
F	Flow-related transport resistance for the DFN [y/m].
L	Path length in the rock, i.e. the DFN [m].
TRAPP	Initial transport aperture in the first fracture [m].
TW_TUN	Travel time in the vaults and tunnels [y].
L_TUN	Path length in the vaults and tunnels [m].
TW_CPM	Travel time in the ECPM or CPM, i.e. not in the DFN [y].
L_CPM	Path length in the ECPM or CPM, i.e. not in the DFN [m].
UR	Not used.
QEQR	Not used.
LR_TUN	Not used.
TR_TUN	Not used.
FLOW	Darcy flux in the fracture at the release point [m^2/y].
DIP	Dip angle of the fracture [degrees].
STRIKE	Strike angle of the fracture [degrees].
INTL	Length of the intersection between the fracture and the vault [m].
XINTC, YINTC, ZINTC	X, Y, Z-coordinates of the intersection centre [m].
XINTS, YINTS, ZINTS	X, Y, Z-coordinates of one end of the intersection [m].
XINTE, YINTE, ZINTE	X, Y, Z-coordinates of the other end of the intersection [m].

C.2.2 Particle path file

Another output of the facility focussed model is the detailed information for each particle pathway for use in radionuclide transport calculations. The exported data is in ConnectFlow verbose particle (*.ptv)* format. This is a simple space-separated text file, starting with a header. This is followed by a summary lines for each particle and then detailed information for each segment of the particle pathway. The information for each data field is described in Table C-3. The file header lines are:

```
<PACKAGE> <VERSION NUMBER>
<PARTICLES> <REALISATIONS> <TIMESTEPS>
```

The summary lines for each particle pathway are as follows, with the **`STEPS`** line optional:

```
PART <PART INDEX> <REALISATION> <START TIME> <OKFLAG> <XS YS ZS>
<XE YE ZE> <UX UY UZ> <TOT TIME> <TOT LENGTH> <TOT F>

STEPS <NO OF STEPS>
```

Then, if there are any steps, for each path segment in a DFN:

```
<TIME> <POSITION X Y Z> <HYD APERTURE> <TRANS APERTURE> <STEP TIME>
<F> <FLOW POTENTIAL> <ROCK INDEX> <TESSELLATE INDEX> <FRACTURE SET>
<FRACTURE INDEX> <CONCEPT ID=2> <FRACTURE NAME>
```

or in a CPM:

```
<TIME> <POSITION X Y Z> <PERMEABILITY> <POROSITY> <STEP TIME> <F>
<FLOW POTENTIAL> <ROCK INDEX> 0 0 <CELL INDEX> <CONCEPT ID=1>
<FRACTURE NAME>
```

Table C-3. Description of fields in the facility focussed verbose particle (.ptv) data delivery.

Column name	Description
PACKAGE	CONNECTFLOW for an embedded CPM/DFN model.
VERSION NUMBER	ConnectFlow version used to generate the file.
PARTICLES	Total number of particles released.
REALISATIONS	Number of model realisations used.
TIMESTEPS	Number of transient timesteps used (zero for steady-state).
PART INDEX	Particle index.
REALISATION	Realisation index.
START TIME	Particle start time [y].
OKFLAG	Indicates whether or not a particle reached the model boundary: • 0 = reached the top boundary, • 1 = failed to start due to no fracture with an outflow from the vault, • 2 = ran out of time steps, • 3 = stuck, • 4 = oscillating between DFN and CPM, • 5 = reached a side boundary or the bottom boundary.
XS, YS, ZS	X, Y, Z-coordinates of start point [m].
XE, YE, ZE	X, Y, Z-coordinates of end point [m].
UX UY UZ	X, Y, Z components of initial Darcy flux [m/y].
TOT TIME	Total travel time of particle.
TOT LENGTH	Total length of particle pathway.
TOT F	Flow-related transport resistance for the particle pathway [y/m].
NO OF STEPS	Number of steps in the particle pathway.
TIME	Time at the end of the segment [y].
POSITION X Y Z	X, Y, Z-coordinates of the particle at the end of the segment [m].
HYD APERTURE	Hydraulic aperture of the fracture containing the particle segment [m].
TRANS APERTURE	Transport aperture of the fracture containing the particle segment [m].
STEP TIME	The travel time for the path segment [y].
F	Flow-related transport resistance for the path segment [y/m].
FLOW POTENTIAL	The driving force for advective flow along the path segment, equal to the head gradient for freshwater, but includes a buoyancy term for variable density [-].
ROCK NUMBER	The index of the rock containing the path segment [-].
TESSELLATE INDEX	The index of the fracture tessellate containing the path segment [-].
FRACTURE SET	The index of the set of the fracture containing the path segment [-].
FRACTURE INDEX	The index of the fracture containing the path segment [-].
CONCEPT ID	1=CPM, 2=DFN
FRACTURE NAME	The name (if any) of the fracture containing the path segment [-]. Usually, only deformation zone fractures are named.
PERMEABILITY	The permeability of the CPM cell containing the path segment [m^2].
POROSITY	The porosity of the CPM cell containing the path segment [-].
CELL INDEX	The index of the CPM cell containing the path segment [-].

Arkitektkopia AB, Bromma, 2019

SKB is responsible for managing spent nuclear fuel and radioactive waste produced by the Swedish nuclear power plants such that man and the environment are protected in the near and distant future.

skb.se